Spin-Echo Resolved Neutron Scattering from Self-Organised Polymer Interfaces

Max Nülle
Stuttgart, 2010

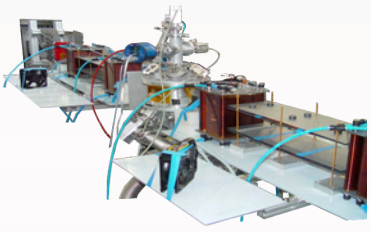

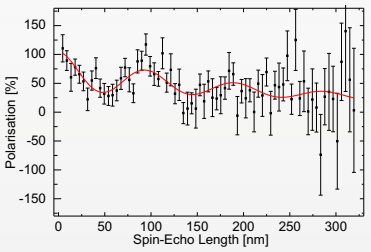

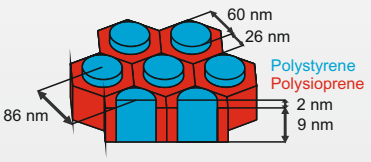

Max-Planck-Institut
für Metallforschung
Stuttgart

Institut für Theoretische
und Angewandte Physik
der Universität Stuttgart

Spin-Echo Resolved Neutron Scattering from Self-Organised Polymer Interfaces

Von der Fakultät Mathematik und Physik der Universität Stuttgart
zur Erlangung der Würde eines
Doktors der Naturwissenschaften (Dr. rer. nat.)
genehmigte Abhandlung

Vorgelegt von

MAX MARIUS NÜLLE
aus Stuttgart

Hauptberichter:	Prof. Dr. H. Dosch
Mitberichter:	Prof. Dr. U. Stroth

Eingereicht am:	01.12.2009
Tag der mündlichen Prüfung:	12.02.2010

Institut für Theoretische und Angewandte Physik
der Universität Stuttgart
Max-Planck-Institut für Metallforschung

2010

Content

0 Deutsche Zusammenfassung

Vielversprechende Anwendungen in der Nanotechnologie führten in der jüngsten Vergangenheit zu einem großen Interesse an lateral strukturierten Diblock-Copolymer-Filmen [Clery'02]. Hierzu zählen zum Beispiel Antireflexion-Beschichtungen [Walheim'99], magnetische Speicher mit hoher Informationsdichte [Thurn-Albrecht'00a, Cheng'01, Liu'01], Nanoelektroden-Arrays [Jeoung'01], sowie Matrixvorlagen für Metall-Nanodrähte [Lopes'01, Lopes'02] und für lithographische Halbleitermasken mit extrem kleinen Strukturen [Park'97, Harrison'98]. Bei lithographischen Methoden zur Herstellung von kleinen Strukturen, zum Beispiel für integrierte Schlatungen, stellt die Wellenlänge von Licht (~380 nm) eine physikalische Schranke dar [Xia'99]. Mittels neuer Nano-Technologien, die auf dem Einsatz von Diblock-Copolymer-Filmen basieren, ist es jedoch möglich, kleinere Strukturen zu erzeugen.

Voraussetzungen für solche Anwendungen sind mikrophasenseparierte Diblock-Copolymer-Filme mit einer Strukturierung parallel zur Film-Oberfläche. Diese Ausrichtung der Mikrophasenseparation kann in einigen Fällen mittels bestimmter Verfahren wie zum Beispiel der Anwendung von elektrischen Feldern [Schäffer'00, Thurn-Albrecht'00b] oder von Oberflächenbehandlungen [Kellogg'96, Huang'98b, Huang'98c], ausgerichtet werden. Eine andere Möglichkeit ist eine selbständige Ausrichtung der Mikrophasenseparation in besonders dünnen Filmen, wie sie die in der vorliegenden Arbeit nachgewiesen werden konnte. Letzerer Mechanismus hat den Vorteil, dass sowohl die Phasenseparation als auch die Ausrichtung der Struktur Selbstordnungsprozesse sind und daher potentiell einfach ohne weitere Arbeitsschritte im großen Maßstab zu realisieren sind.

Kleinwinkel-Neutronenstreuung unter streifendem Einfall hat sich als eine wichtige Methode zur Untersuchung von Grenzflächen bewährt. Neutronenstreuung ist der Röntgenstreuung hinsichtlich der Intensität, Strahldivergenz und Brillanz der modernen Synchrotron-Quellen deutlich unterlegen, jedoch bringt Neutronenstreuung die Möglichkeit des Isotopenaustauschs mit sich, die es erlaubt, bestimmte Moleküle für Streuexperimente zu markieren. Üblich ist es zum Beispiel, Wasserstoff durch Deuterium zu ersetzen was der Neutronenstreuung einen entscheidenden Vorteil für Anwendungen im Bereich der Biophysik und der weichen Materie verschafft. In dieser Arbeit wurde durch Deuterierung ein Teil des untersuchten Diblock-Copolymers markiert.

Die Streuung an Grenzflächen ist durch die geringe Anzahl an streuenden Atomen im Vergleich zur Volumenprobe sehr signalschwach. Hinzu kommt eine starke Limitierung durch die schwache Neutronenintensität und die Notwendigkeit, sowohl den Querschnitt als auch die Divergenz des verwendeten Neutronenstrahls stark zu beschränken, um Strukturen auf großen Längenskalen im

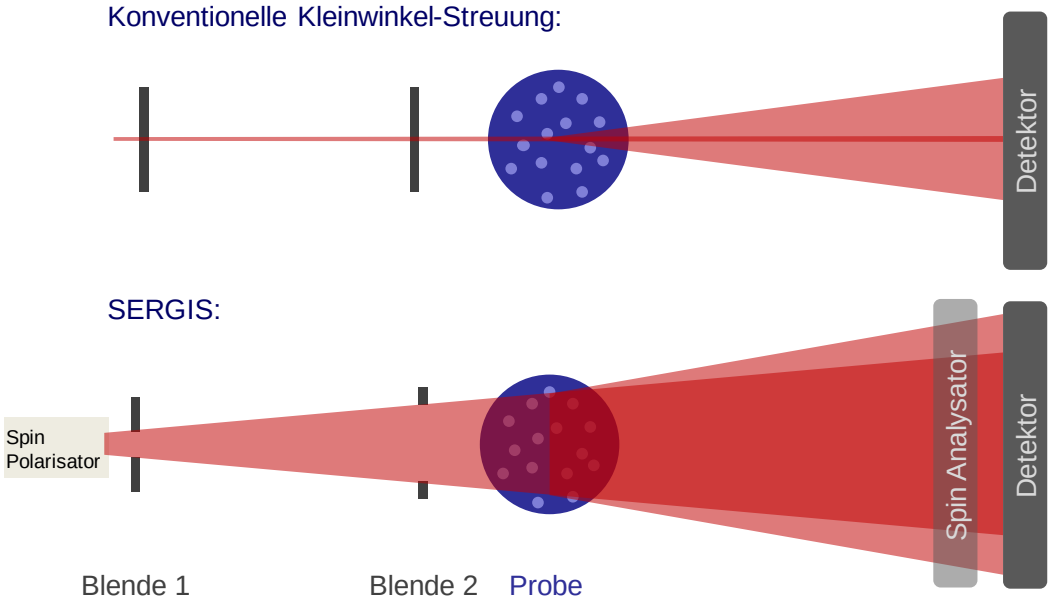

Abb. 0.1: Vergleich zwischen konventioneller (oben) und spinaufgelöster (unten) Kleinwinkel-Neutronenstreuung unter streifendem Einfall. SERGIS ermöglicht eine Entkopplung der Strahldivergenz von der Auflösung. Anstatt den Streuwinkel zu messen, um auf den Impulsübertrag zu schließen, wird bei SERGIS die Depolarisation gemessen.

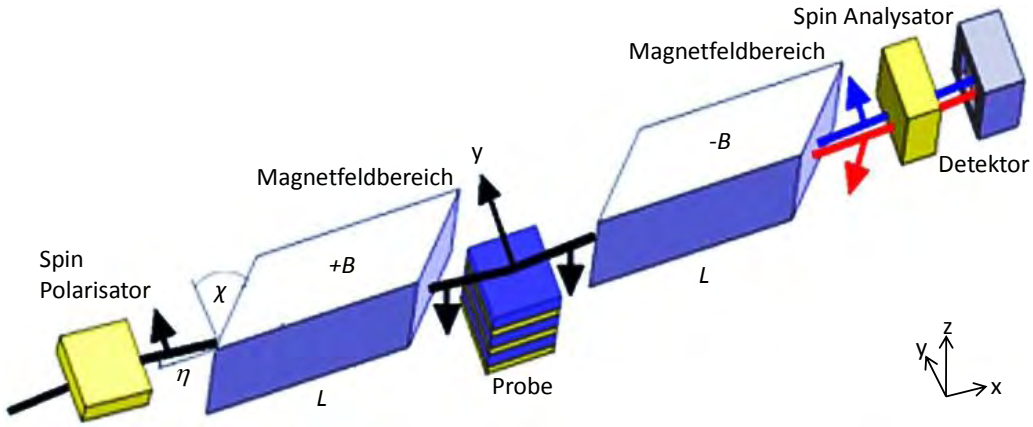

Abb. 0.2: Schematischer Aufbau eines SERGIS Experiments. Hauptbestandteile sind zwei parallelogrammförmige Magnetfeldbereiche der Länge L mit entgegengesetzt ausgerichteter magnetischer Induktion B. Die Normalen-Richtungen der Eintritts- und Austrittsflächen der Magnetfeldbereiche sind um einen Winkel χ gegen die Strahlrichtung gedreht. Der Neutronenstrahl wird am Polarisator polarisiert und mittels Analysator und Detektor detektiert. Der Einfallswinkel des Neutronenstrahls auf die Probenoberfläche ist η. Die Probe befindet sich in der Mitte des Aufbaus zwischen den beiden Magnetfeldbereichen.

Streuexperiment detektieren zu können. Dies macht Kleinwinkel-Neutronenstreuung, bedingt durch die schwache Streuintensität, zu einer instrumentell sehr anspruchsvollen Methode.

Spin-Echo Kleinwinkel-Neutronenstreuung unter streifendem Einfallswinkel (SERGIS) umgeht das Problem der Kopplung von besserer Auflösung und schwacher Strahlintensität, indem der Impulsübertrag nicht wie üblich mittels des Streuwinkels gemessen wird, sondern über den Neutronenspin. Somit ist es möglich, die Strahlbegrenzung und die Auflösung des Experiments in erster Näherung zu entkoppeln, siehe Abb. 0.1.

Der experimentelle Aufbau für ein SERGIS Experiment besteht aus einem Polarisator, zwei parallelogrammförmigen Magnetfeldbereichen, einem Spin-Analysator und einem Detektor, wobei sich die Probe zwischen den beiden entgegengesetzt ausgerichteten Magnetfeldern befindet. Ein schematischer SERGIS-Aufbau ist in Abb. 0.2 gezeigt.

Während des Durchlaufens der beiden Magnetfeldbereiche präzediert der Spin des Neutrons um die Magnetfeldrichtung. Die Präzessionsphase des Neutronen-Spins

nach dem Durchlaufen beider parallelogrammförmigen Magnetfeldbereiche hängt unter anderem von dem Impulsübertrag $\vec{q}$ ab, den ein an der Probe gestreutes Neutron erhält. Bezeichnet man den mittleren Wellenvektor des einfallenden Strahls mit $\vec{\bar{k}}_{\mathrm{i}}$ und die Abweichung des anfänglichen Wellenvektors eines bestimmten Neutrons von diesem Mittelwert mit $\vec{\tilde{k}}_{\mathrm{i}}$), so ist die Präzessionsphase des Neutronen-Spins nach Durchlaufen der beiden Magnetfeldbereiche gegeben durch:

$$\begin{aligned}\varphi = -\frac{m_{\mathrm{n}}\gamma_{\mathrm{n}}}{2\pi h} BL\lambda^2 \left(q_{\mathrm{x}} + q_{\mathrm{y}} \tan\chi - 2\tilde{k}_{\mathrm{i,z}} \frac{\tan\eta}{\cos\chi}\right) \frac{1}{\cos\eta} \\ \times \left[\cos\eta + \frac{\tilde{k}_{\mathrm{i,x}}}{\bar{k}_{\mathrm{i}}} + \frac{\tilde{k}_{\mathrm{i,y}}}{\bar{k}_{\mathrm{i}}} \tan\chi + \left(\sin\eta + \frac{\tilde{k}_{\mathrm{i,z}}}{\bar{k}_{\mathrm{i}}}\right) \frac{\tan\eta}{\cos\chi}\right]^{-1} \\ \times \left[\cos\eta + \frac{\tilde{k}_{\mathrm{i,x}} + q_{\mathrm{x}}}{\bar{k}_{\mathrm{i}}} + \frac{\tilde{k}_{\mathrm{i,y}} + q_{\mathrm{y}}}{\bar{k}_{\mathrm{i}}} \tan\chi + \left(\sin\eta - \frac{\tilde{k}_{\mathrm{i,z}}}{\bar{k}_{\mathrm{i}}}\right) \frac{\tan\eta}{\cos\chi}\right]^{-1},\end{aligned} \tag{0.1}$$

wobei die hier nicht erwähnten Variablen in Kapitel 2 eingeführt werden.

Im Rahmen der Kleinwinkelnäherung ($\frac{\tilde{k}_{\mathrm{i}}}{\bar{k}_{\mathrm{i}}} \ll 1$, $\frac{\tilde{k}_{\mathrm{i}}+q}{\bar{k}_{\mathrm{i}}} \ll 1$ und $\eta \ll 1$) und bei Vernachlässigung der Streuung in x-Richtung erhält man folgendes Ergebnis

$$\varphi \approx q_{\mathrm{y}} Y^{\mathrm{SE}} . \tag{0.2}$$

wobei die sogenannte Spin-Echo-Länge durch

$$Y^{\mathrm{SE}} := -\frac{m\gamma_{\mathrm{n}}}{2\pi h} BL\lambda^2 \tan\chi \tag{0.3}$$

definiert ist. Die Strahlpolarisation am Ort des Analysators ist dann gegeben durch Mittelung des Kosinus der Präzessionsphase φ über den betrachteten Querschnitt des gestreuten Strahls,

$$P := \frac{I_{\uparrow} - I_{\downarrow}}{I_{\uparrow} + I_{\downarrow}} = \langle \cos\varphi \rangle , \tag{0.4}$$

wobei $I_{\uparrow}$ und $I_{\downarrow}$ die Intensität am Detektor mit in y-Richtung bzw. in –y-Richtung präparierter Polarisation sind. Unter der Voraussetzung, dass Impulsüberträge von null bis unendlich in der betrachteten Richtung erfasst werden und die Streuung

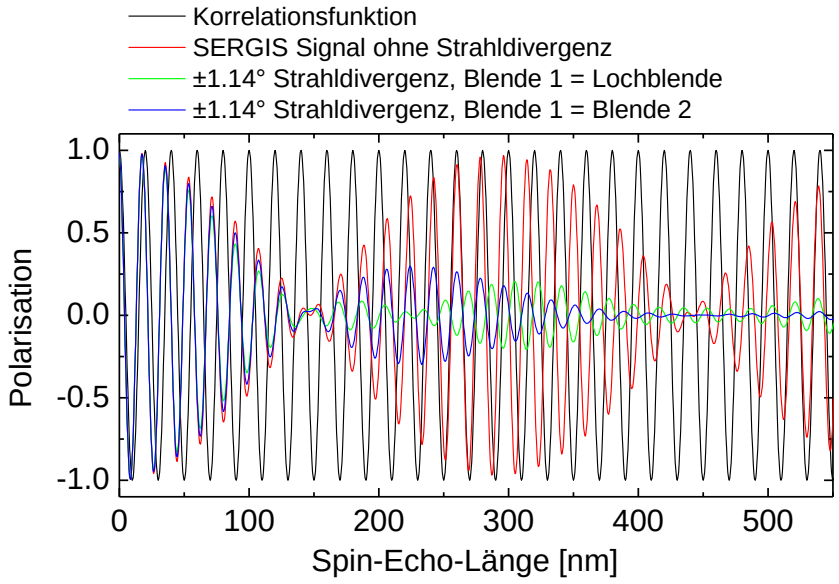

Abb. 0.3: Polarisation als Funktion der Spin-Echo-Länge Y^{SE} für ein Struktur mit sinusförmiger Streulängendichteverteilung einer Periodizität von 18 nm, berechnet mittels Gl. (0.1) für $\chi = 45°$ und $\lambda = 5.5$ Å. Es wurden drei Szenarien simuliert: Einfallender Strahl ohne Divergenz (rote Kurve), mit 1.14° Divergenz wobei Blende 1 eine Lochblende ist und die Divergenz über die Blende 2 eingestellt wird (grüne Linie) und wobei die Divergenz über zwei gleichweit geöffnete Blenden definiert ist (blaue Kurve). Blende 1 befindet sich vor dem Polarisator und Blende 2 vor der Probe. Aus Gleichung (0.2) (nach Näherung) folgt, dass in der Simulation die Polarisation unabhängig von der Strahldivergenz keine Schwebung zeigt (schwarze Kurve), sonder identisch mit der Korrelationsfunktion ist.

mit der kinematischen Theorie beschrieben werden kann, ist die Polarisation proportional zur verallgemeinerten Patterson-Funktion $g(y)$

$$P\left(Y^{SE}(B,L,\lambda,\chi)\right) \approx \frac{g\left(Y^{SE}(B,L,\lambda,\chi)\right)}{g(0)}. \qquad \textbf{(0.5)}$$

In Abb. 0.3 ist die eingeschränkte Gültigkeit der üblichen Näherung verdeutlicht (Vergleich von Gl. (0.1) und (0.2)). Die zu erwartende Polarisation einer SERGIS Messung für ein Struktur mit sinusförmiger Streulängendichteverteilung einer Periodizität von 18 nm wurde als Funktion der Spin-Echo-Länge Y^{SE} simuliert, dabei wurden verschiede Szenarien mit einer unterschiedlichen Divergenz des einfallenden Neutronenstahls berücksichtigt. Die Abweichungen treten bei Vielfachen der Periodizität der Struktur auf und sind bei kleinen Strukturen, wie für Abb. 0.3 zugrunde gelegt wurde, dominanter als bei größeren Strukturen (in

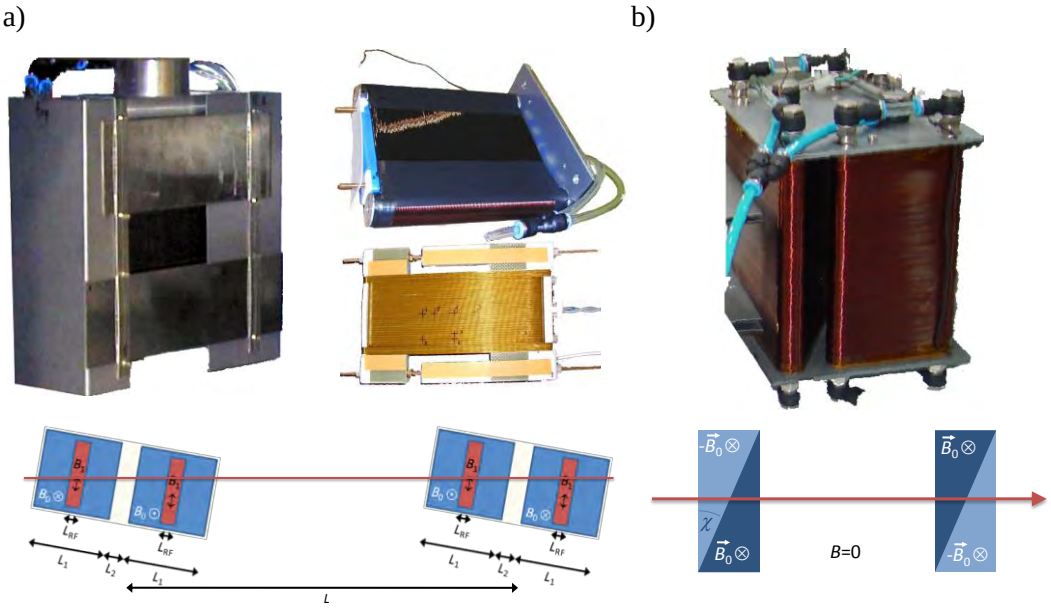

Abb. 0.4: a) NRSE-Spulen-Paar in μ-Metall-Abschirmung bestehend aus zwei Spulen mit konstantem Magnetfeld B_0 und darin jeweils eine Hochfrequenz-Spule B_1. b) Dreieckspulen Paar mit $\chi = 30°$. In der schematischen Zeichnung unter den Fotos ist jeweils die Anordnung zweier Spulenpaare gezeigt, die vor und nach der Probe installiert werden.

der Abbildung nicht gezeigt). Die errechnete Strahlpolarisation ist mit (farbige Linien) und ohne (schwarze Linie) die erwähnten Näherungen dargestellt. Limitierend sind hier die große Strahldivergenz und große Streuwinkel. Das erste Korrelationsmaximum wird jedoch mit guter Genauigkeit reproduziert.

Im Rahmen dieser Arbeit wurden zwei verschiedene technische Umsetzungen der parallelogrammförmigen Magnetfeldbereiche analytisch und experimentell verglichen: Die Neutronen-Resonanz-Spin-Echo Methode (NRSE) [Major'09] (Abb. 0.4a) und doppelbrechende magnetische Prismen (Dreiecksspulen) (Abb. 0.4b). Der Vorteil der NRSE-Methode ist die bauartbedingt relativ große erreichbare Spin-Echo-Länge. Nachteile dieser Methode sind eine hohe Absorption des Neutronenstrahls und eine starke Erhöhung des Untergrunds durch 16 Magnetfeldspulen, die im (Neutronen-)Strahlengang stehen. Desweiteren ist NRSE-Methode wellenlängenspezifisch. Dreieckspulen zeigen weniger Absorption und erzeugen weniger Untergrund. Durch die simplere Bauweise ist die Kühlung dieser Spulen einfacher und effizienter zu realisieren, womit die bauartbedingt zunächst geringeren maximalen Spin-Echo-Längen mit stärkeren

Magnetfeldern kompensiert werden können. Zwei Versionen der Dreieckspulen wurden im Rahmen dieser Arbeit realisiert und getestet: die erste Version mit einer um 45° zum einfallenden Neutronenstrahl geneigten Spulenseite, die zweite Version mit einer um 30° bzw. 60° geneigten Spulenseite. Für die 30°- bzw. 60°-Spulen wurde eine integrierte Wasserkühlung konzipiert, um höhere Magnetfelder und somit größere Spin-Echo-Längen zu erreichen. Die 30°- bzw. 60°-Spulen können auf zwei verschiedene Arten zusammengesetzt werden, um 30° bzw. 60° Spulenpaare zu erhalten.

Zum quantitativen Vergleich der SERGIS-Varianten wurde ein optisches Gitter mit einer Periodizität von 277.7 nm als Referenzprobe genutzt. Da dessen Streusignal sehr stark gerichtet und intensiv ist, stellt das optische Gitter eine ideale Referenzprobe dar. Unter streifendem Einfall ist das Streusignal allerdings aus streutechnischen Gründen auf kleine Winkel beschränkt, somit werden hochfrequente Anteile der Streulängendichteverteilung im Streusignal nicht auftreten. Mit allen vier untersuchten experimentellen SERGIS-Aufbauten (NRSE, 30°-, 45°- und 60°-Spulen) lässt sich die Struktur des optischen Gitters durch das SERGIS-Signal gleich gut reproduzieren, siehe Abb. 0.5. Unterschiedliche Absorption in den Aufbauten wurde durch entsprechend längere Zählzeiten kompensiert.

Als eine erste physikalisch relevante Fragestellung die mit SERGIS untersucht wird, wurde in dieser Arbeit der Selbstanordnungsprozess (engl. Self-assembly) von Diblock-Copolymeren in ultra-dünnen Filmen systematisch untersucht. Daneben wurden zur Charakterisierung als komplementäre Methoden auch Neutronen- und Röntgen-Reflektometrie sowie Raster-Kraft-Mikroskopie (AFM) genutzt. Die Untersuchungen wurden an Diblock-Copolymer-Filmen aus dem Material *Poly(Styrol-block-Isopren)* vorgenommen. Die Styrol-Komponente war dabei im Gegensatz zur Isopren-Komponente deuteriert, um einen hohen Neutronen-Streukontrast zwischen den beiden Komponenten zu erhalten. Bei dem Polymer handelte es sich um ein symmetrisches Diblock-Copolymer mit annähernd identischem Volumen der beiden Teilketten.

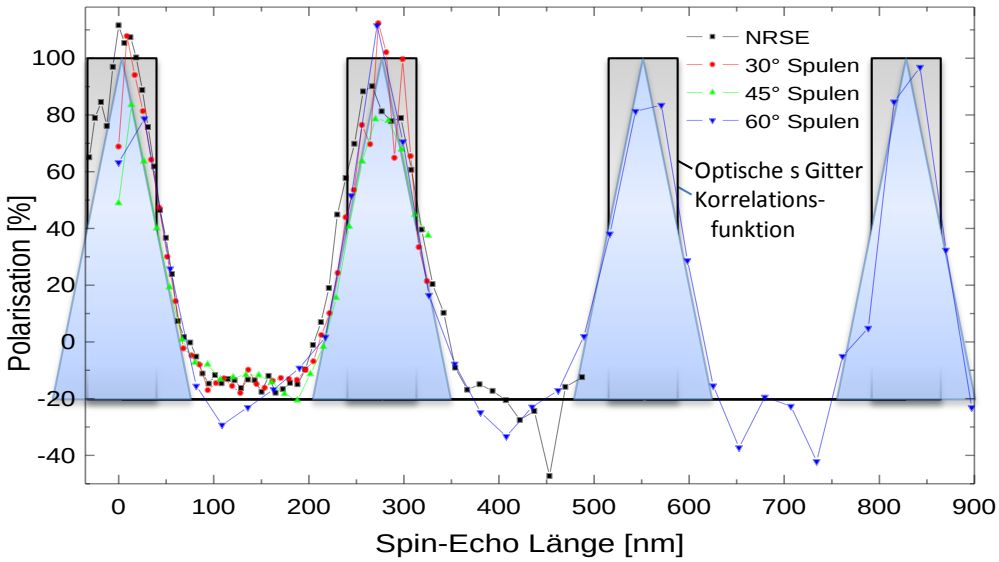

Abb. 0.5: Vergleich der vier untersuchten SERGIS-Varianten. Die nicht vollständig a priori zu bestimmende Korrektur für den Untergrund bei der Messung wurde so gewählt, dass der Polarisationsoffset zwischen den verschieden Messungen amortisiert wurde. Im Hintergrund sind die idealisierte Streulängenverteilung im optischen Gitter (graue Rechtecke) und die zugehörige Korrelationsfunktion (blaue Dreiecke) dargestellt. Der Fehlerbalken beträgt ca. ±5 Prozentpunkte, er wurde der Übersichtlichkeit halber nicht dargestellt.

Bedingt durch die chemische Inkompatibilität der beiden Bestandteile des Diblock-Copolymers kann unter geeigneten Bedingungen eine Phasenseparation der beiden Komponenten Styrol und Isopren stattfinden. Da die beiden Polymerbestandteile chemisch gebunden sind, findet die Phasenseparation auf der Größenordnung eines Polymermoleküls statt, sie wird deshalb Mikrophasenseparation genannt. Das Phasendiagramm in Volumenproben ist gut bekannt. Bei Raumtemperatur befindet sich das untersuchte symmetrische Diblock-Copolymer in der lamellaren Phase. In dünnen Filmen jedoch können die Grenzflächen (bzw. die Wechselwirkung der Polymermoleküle mit dem Substrat und der freien Oberfläche) einen Einfluss auf die Struktur ausüben. Der Einfluss wird besonders dominant, wenn die Filmdicke kleiner ist als die Größe eines Polymermoleküls im Gleichgewichtszustand. Die untersuchten Polymere haben im phasenseparierten Zustand eine Länge von 309 Å senkrecht zur Phasengrenze und einen Durchmesser von 50 Å in der Ebene parallel zur Phasengrenze. In

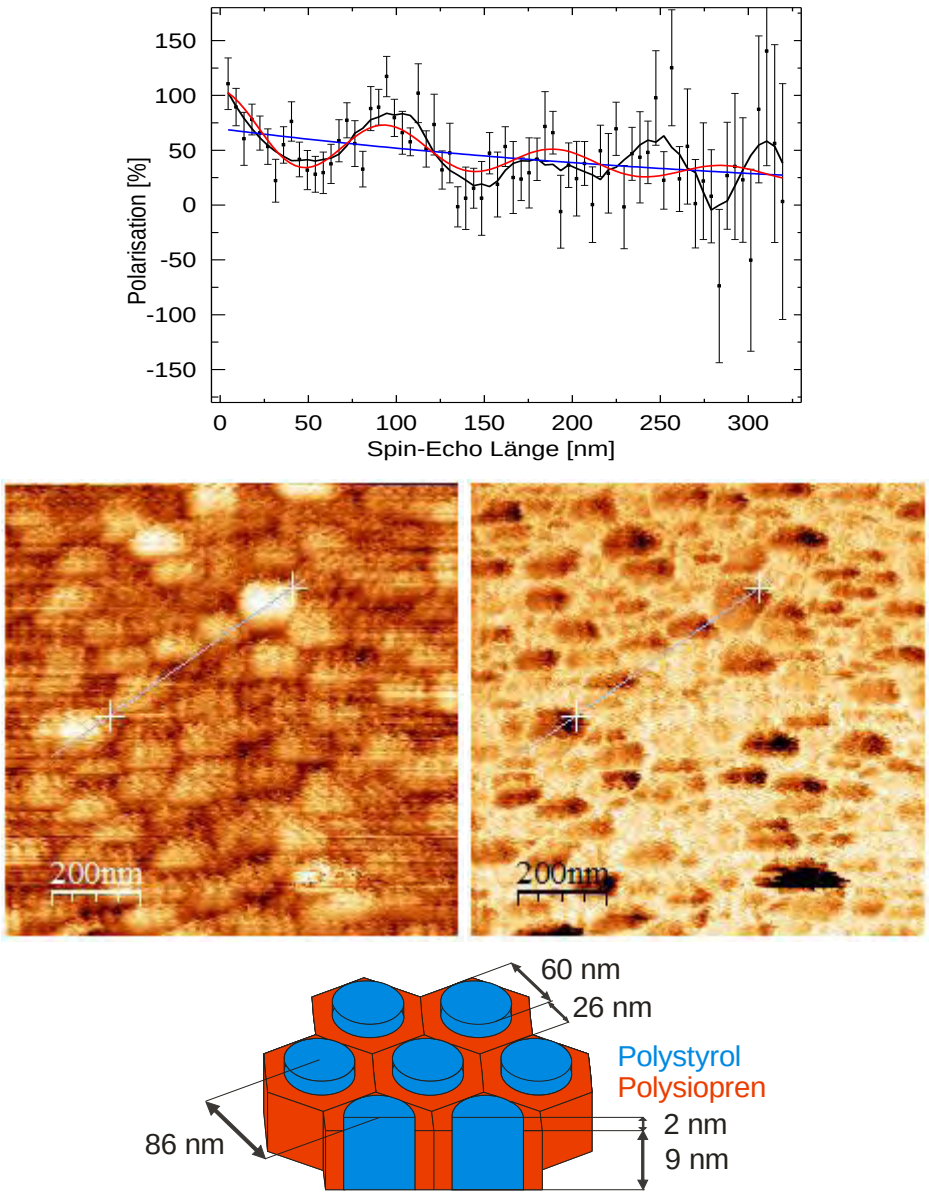

Abb. 0.6: Ergebnisse von SERGIS- und AFM-Untersuchungen an einem ursprünglich 100 Å dicken Poly(Styrol-block-Isopren)-Film nach einstündigem Tempern bei 105°C (SERGIS-Daten) bzw. 145° C (AFM-Daten). Im oberen Teil sind die mittels 30°-Dreieckspulen gemessenen SERGIS-Daten gezeigt (Korrelationsfunktion der Streulängendichte parallel zur Probenoberfläche). Im Mittelteil sind das bei den AFM-Untersuchungen erhaltene Topographie- und Phasen-Signal dargestellt. Der Phasenkontrast lässt auf Polystyrol- bzw. Polyisoprenreiche Bereiche unterschiedlicher Viskosität schließen. Aus diesen experimentellen Ergebnissen kann, abweichend von Volumenproben, auf die Existenz einer hexagonalen Phase in ultra-dünnen Diblock-Copolymer-Filmen geschlossen werden. Im unteren Teil der Abbildung ist diese Phase idealisiert skizziert. Polystyrol-reiche Zylinder stehen hierbei 2 nm über die 9 nm dicke Isopren-Matrix heraus.

dieser Arbeit wurden Filme mit Dicken zwischen 100 Å und 450 Å untersucht. Die Polymerfilme wurden im Rahmen einer Kooperation mit Prof. Hyungjung Kim von der Sogang Universität in Seoul, Südkorea mit Hilfe des Zentrifugalbeschichtungsverfahrens (engl. spin-coating) auf Siliziumsubstraten aufgetragen.

Die frisch präparierten Proben zeigen nahezu keine Phasenseparation. Mildes Tempern führt in ultra-dünnen Filmen (d.h. dünner als die Größe eines Polymermoleküls) mit Dicken von 100 Å bis 150 Å zu einer Phasenseparation von zylinderförmigen Bereichen aus Polystyrol, eingebettet in einer Matrix von Polyisopren, wobei die Phasengrenzen senkrecht zur Substratoberfläche ausgerichtet sind (siehe Abb. 0.6). Die Zylinder stehen etwas aus der Polyisoprenmatrix heraus. Diese Phase mit hexagonaler Symmetrie trat ausschließlich in ultra-dünnen Filmen auf, so dass dieser Effekt offensichtlich auf den Einfluss der Substrat- und Oberflächen-Wechselwirkung als auch auf die beschränkte Filmdicke zurückzuführen ist.

In Filme mit einer Dicke von 450 Å (d.h. dicker als die Größe eines Polymermoleküls) konnte eine lamellare Phase, wie sie auch in Volumenproben auftritt, dokumentiert werden. Die Phasengrenzen hier sind im Gegensatz zu den ultra-dünnen Filmen parallel zur Substratoberfläche. Da die präparierte Filmdicke nicht kommensurabel mit der Lamellenperiode in Volumenproben war, befand sich das Polymer in einem leicht gedehnten Zustand.

Unabhängig von der Filmdicke tritt die Phasenseparation bereits nach mildem Tempern auf. Intensives Tempern führt zu einem Aufbrechen des bis dahin kontinuierlichen Films. In den dickeren Filmen (450 Å) bleibt die Phasenseparation bestehen, in den ultra-dünnen Filmen jedoch konnte keine Ordnung gefunden werden. Abb. 0.7 zeigt eine Zusammenfassung der beobachteten Strukturen.

Es wurde gezeigt, dass ultra-dünne Diblock-Copolymer-Filme selbstordnende, laterale Strukturen auf der Nanometerskala bilden. Damit öffnen sich neue Horizonte hin zu kleineren Strukturen, die sich prinzipiell relativ einfach per Selbstanordnungsprozess auch im großen Maßstab erzeugen lassen sollten.

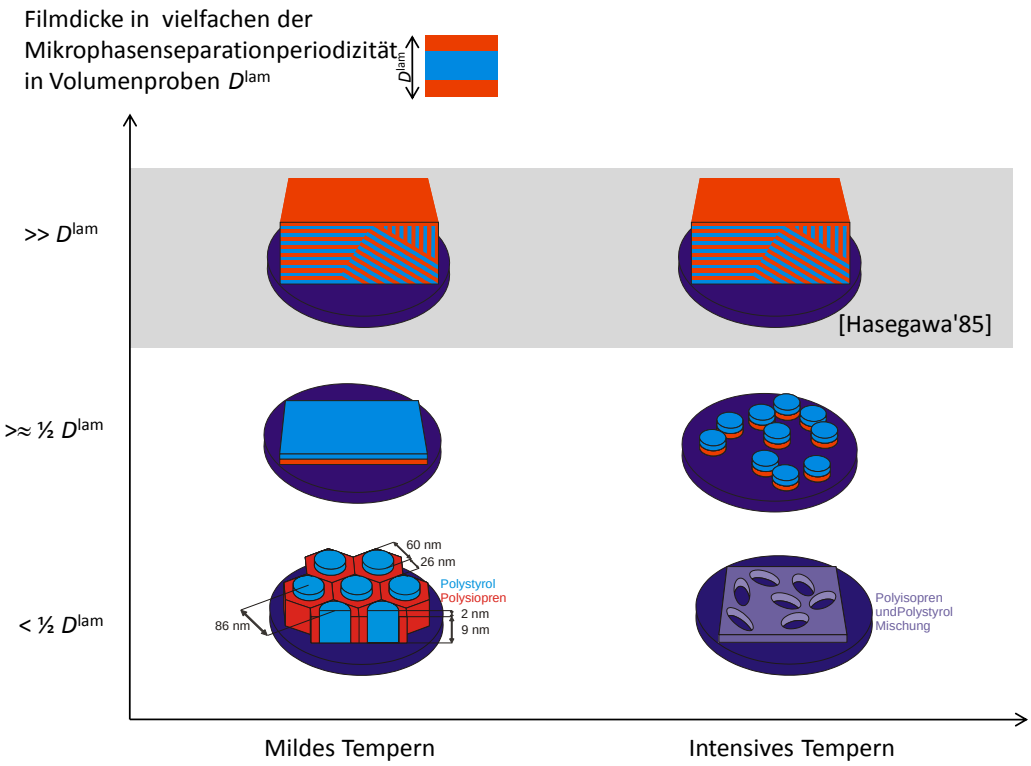

Abb. 0.7: Selbstorganisation von Ppoly(Styrol-block-Isopren) Diblock Copolymer Filmen in Abhängigkeit von der ursprünglich präparierten Filmdicke. Grundlegende Unterschiede bei der Struktur von Filmen mit Dicken kleiner (untere Zeile) und größer (mittlere Zeile) als die Länge eines Polymermoleküls im Gleichgewichtszustand ($½D^{lam}$ = 319 Å) konnten beaobachtet werden. Zum Vergleich ist in der oberen Zeile die Struktur von Volumenproben gezeigt [Hasegawa'85].

In dieser Arbeit wurden erstmals mit SERGIS systematische Untersuchungen an physikalisch relevante Proben durchgeführt. SERGIS eröffnet neue Möglichkeiten zur Untersuchung von lateralen Strukturen (mit Längenskalen bis in den Mikrometerbereich) an Neutronenreflektometern. Durch die relativ einfache Installation und den moderaten Platzbedarf ist SERGIS eine interessante Alternative zu konventionellen oberflächenempfindlichen Neutronen-Kleinwinkel-Streu-Instrumenten.

1 Introduction

Twenty years ago, in 1989, Donald Eigler arranged 35 individual atoms to spell out the three letters of his company's name [Eigler'90]. By writing the letters I-B-M in a length scale that constituted a world record, Eigler made his employer immortal, as the famous microscopy image will remain in the textbooks for centuries. At the end of the twentieth century, it seemed that mankind had achieved the ultimate goal of materials science and engineering: Mastering matter on the most fundamental level imaginable – being able, in principle, to build any structure on an atomic scale. Nanotechnology was born. For photonic crystals, metamaterials, moth-eye structures, high-density data storage media and self-cleaning surfaces, however, we need not millions but billions or trillions of individual laterally structured nano- or microscale units. The grand challenge for materials science and engineering in the 21st century is to produce smart, functional, nanostructured materials in a controlled way that allows at the same time for economical viable production methods. To a certain extent, this may be possible by the top-down approaches – lithography by light, by electron or ion beam. Ultimately, however, we can only succeed by the same principles that nature employs to build incredibly complex systems from molecular building blocks: by self-organisation. Although powerful real-space microscopy may show us how one unit looks like, getting the "big picture" of a material or surface made up from a billion of units we need modern versions of the techniques that have already shown us the structure of matter a century ago: We need advanced scattering techniques. Self-organisation is going to be the key that unlocks the door. Scattering is going to be the lamp that lights the way!

Polymers offer an ideal (play-) ground to understand the link between structure and function in complex self-organised materials, as the chemical anisotropy of

diblock copolymer molecules may lead to a microphase separation of both constituents. The interest on polymers, however, goes beyond their position as model systems. Polymers can enable nanoscale material processing for future generations of nanotechnology devices in microfluidics and electronics. Surface effects and size reduction down to a regime in which a characteristic length scale of a physical phenomenon becomes comparable with the typical length of the nanostructure offer unique properties. The thickness of polymer films can be smaller than the unperturbed size of the macromolecules. In this work such films are called ultrathin films. Confinement influences conformation and intertwining of the molecules. Structural changes induced by the interaction with a solid substrate can affect dynamical aspects as well as adhesion and wetting characteristics. As a consequence, a systematic study of nanostructured thin films is of prime importance.

To design laterally structured films by microphase separation, a well-oriented modulation parallel to the film surface is crucial. Structures can be aligned by an electric field [Schäffer'00, Thurn-Albrecht'00b], structured substrates [Rockford'99], surface treatments to compensate the substrate selectivity [Kellogg'96, Huang'98b, Huang'98c], or, as investigated in the present work, by confinement in ultrathin films.

With decreasing thickness, the stability of liquid films usually decreases and the films tend to dewet. For many applications, stable films are required, while the droplet structure of dewetted films may be of advantage for other applications. In both cases, reliable predictions based on a fundamental understanding of ultrathin film stability play a strategic role. The dewetting of thin homopolymer films has been investigated intensively [Redon'91, Reiter'92, Reiter'93, Xie'98]. The dewetting of diblock copolymer films, on the other hand, is much more complex and up to now not fully understood.

Small angle neutron scattering has been proven in past years to be a powerful non-destructive tool to study micro-structured systems. Surface-sensitive grazing incidence small angle neutron scattering (GISANS), in particular, enables the investigation of buried films and interfaces. A key advantage of neutron scattering

with respect to x-ray scattering for soft-matter and bio-physical systems is the possibility of labelling molecules or atoms by isotope exchange. In this work, isotope labelling is taken advantage of by deuterating one part of the diblock copolymer. This makes it possible to investigate the microphase separation of the two constituents of the polymer, for which the scattering length contrast for x-rays is very weak. The present neutron sources, however, deliver neutron beams with divergence, brilliance, and flux far below typical recent third generation x-ray sources. This fact, combined with the weak scattering signal that originates from the reduced number of atoms involved in the near surface region, but also the necessity of using a narrow, low divergence beam to be able to resolve small scattering angles for the investigation of structures in the micrometre range, makes surface sensitive GISANS experiments very challenging. To overcome these strong limitations, a new revolutionary technique, spin-echo resolved grazing incidence neutron scattering (SERGIS) has been developed, whose improvement is in the focus of the present thesis.

SERGIS is a neutron scattering method that yields real-space information about the near surface region of a sample on the nanometre to micrometre scale. The structural information about the scattering object is resolved by a neutron property unused in conventional non-magnetic neutron scattering experiments, namely the neutron spin. With the neutron spin as fingerprint, the Larmor precession in two parallelogram-shaped magnetic field regions can be used to label the scattering from the sample. In a first approximation, the measured signal, the polarisation of the scattered neutron beam, is proportional to the correlation function of the scattering length density of the sample. SERGIS aims at a decoupling of the instrumental resolution required to characterize large-scale structures in the direction of interest from the available beam intensity, which is normally strongly limited due to beam collimation, as encountered in GISANS experiments (see Fig. 1.1). SERGIS is a non-standard and challenging technique in a development stage and has up to now only been tested on selected strongly scattering test samples. In the framework of this thesis project, SERGIS has been implemented in different versions at the *NREX*$^{+}$ instrument at the new high flux neutron source FRM II in Garching, Germany.

The motivation of this work is twofold: the development of the spin-echo resolved neutron scattering technique for the investigation of buried interfaces and the study of the self-organisation (i.e., microphase separation and dewetting) of ultrathin diblock copolymer films of symmetric poly(styrene-block-isoprene) on the surface of a single crystalline silicon substrate.

The prospects and limitations of the SERGIS technique are investigated by both a detailed analysis of the expected signal without the usual approximations made in literature (Chapter 2) and by experiment (Chapter 9). Two different technical realisations of the basic parallelogram-shaped magnetic field regions, i.e. neutron resonance spin-echo coils and birefringent magnetic prisms, are developed (Chapter 3) and compared quantitatively with an optical grating as test sample (Section 9.1). A detailed study on the dewetting of poly(styrene-block-isoprene) diblock copolymer films including the internal microphase separation was performed with SERGIS and complementary techniques (Section 9.2). Chapters 4 to 7 give an introduction to grazing incidence scattering, the used experimental facilities, properties of the polymer, and the wetting theory. The sample chamber constructed in the framework of this thesis project and the sample preparation process are presented in Chapter 8.

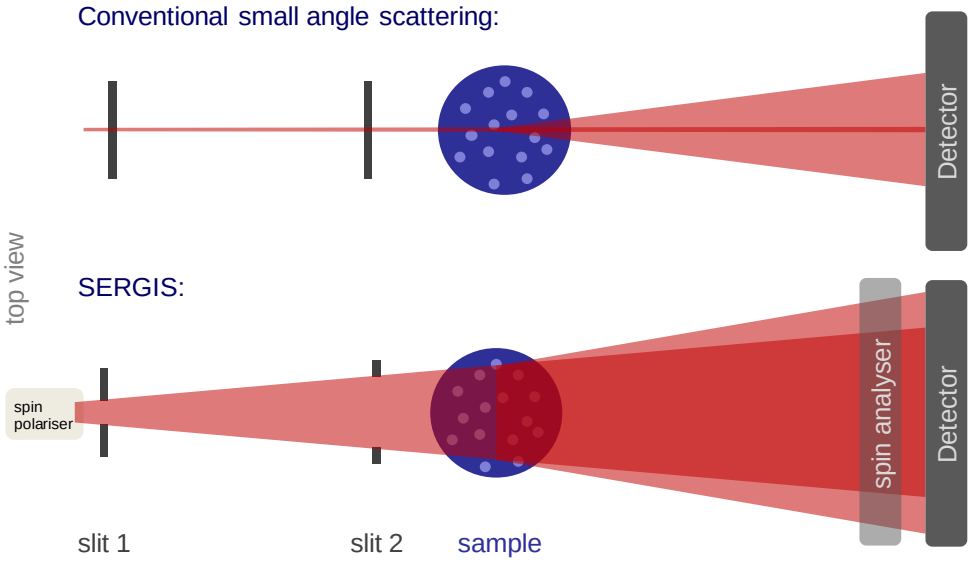

Fig. 1.1: Comparison of GISANS (top) and SERGIS (bottom). With SERGIS, the neutron beam collimation requirements and the measurement resolution can be decoupled. Instead of a position sensitive measurement in GISANS, the total polarisation of the scattered beam is probed in a SERGIS experiment.

2 Spin-Echo Resolved Grazing Incidence Neutron Scattering (SERGIS)

Spin-echo resolved grazing incidence neutron scattering (SERGIS) is a non-standard neutron scattering method yielding real-space information on the near surface region of a sample on the nanometre to micrometre scale. The technique takes advantage of the neutron spin Larmor precision in parallelogram shaped magnetic-field regions to gather information on lateral structures. SERGIS aims in general at the same applications as the conventional grazing incidence small angle neutron scattering technique (GISANS). However, it resolves the momentum transfer by measuring the polarisation of the scattered beam instead of the scattering angle. With GISANS, the measurement resolution increases with decreasing divergence of the incident neutron beam, which has the effect of reducing significantly the intensity of the incident neutron beam. In the case of SERGIS, the resolution related intensity decrease can be overcome by encoding the momentum transfer of each neutron by its spin orientation. This way, SERGIS enables to resolve correlations on the sample beyond the slit-defined transverse coherence length of the neutron beam. The intensity advantage of the so-called Kratky-camera set-up [Kratky'84] is preserved. A good measurement resolution with good counting statistics in a limited time span can be achieved.

A brief review on the history of the technique is given at the beginning of this chapter. In the following, the theoretical background of the spin-echo technique, including the influence of beam divergence and limitations on higher order correlations are discussed in detail. The related background in grazing incidence scattering will be introduced in Chapter 4.

2.1 History and State-of-the-Art of Spin-Echo Resolved Neutron Scattering

Many of the ideas for SERGIS are based on the neutron spin-echo (NSE) technique, that was discovered in 1972 by F. Mezei [Mezei'72, Mezei'78] as a way of achieving very good energy resolution in neutron spectroscopy experiments, without the need for excessive monochromatisation. R. Pynn suggested in 1980 a variation of this method to encode the momentum transfer of an elastic scattering process [Pynn'80].

In 1995 the first spin-echo resolved small angle neutron scattering (SESANS, or sometimes also called SESAME) measurement was published by T. Keller et al. [Keller'95]. In 1996 T. Rekveld discussed the realisation of a dedicated SESANS instrument [Rekveldt'96]. W. Bouwman et al. report in 1999 of the instrument realisation, a SESANS instrument with magnetic foils [Bouwman'99, Bouwman'00] to measure spin-echo small angle neutron scattering. Followed by a dedicated SESANS beamline at ISIS [Plomp'07a]. Further SESANS measurements were published [Bouwman'99, Bouwman'00, Bouwman'04, Pynn'05, Rekveldt'05, Bouwman'08, Pynn'08a] including measurements on magnetic samples [Grigoriev'06, Rekveldt'06, Grigoriev'07]. T. Rekveld showed a modification of the magnetic foil set-up for varying wavelengths by changing the magnetisation in the foil synchronously with the change of the wavelength in a pulsed source set-up [Rekveldt'03b]. J. Major et al. used the NRSE technique in 2003 for SESANS measurements [Major'09]. R. Pynn at al. suggested a modification of this technique for the application at pulsed neutron sources [Pynn'02, Pynn'03, Pynn'05] realised by Kraan et al. [Kraan'03].

The first spin-echo resolved grazing incidence (SERGIS) measurement was published by G.P. Felcher et al. in 2002 [Felcher'02], as sample the authors used a periodic grating. Later, further SERGIS experiments on a strongly scattering periodic grating test sample were performed [Major'03, Plomp'07a, Plomp'07b] and spin-echo lengths up to 18 μm were reached [Bouwman'08].

Variations of the SESANS/SERGIS technique are MIEZE [Gähler'92] and MULTI MIEZE [Arend'04]. Spin-echo neutron reflectivity [Rekveldt'97, Pynn'02,

Rekveldt'03a, Bouwman'08] is suitable for the specular reflectivity measurements on samples with a wavy surface and to discriminate the diffuse contribution to the specular reflected beam. High resolution neutron diffraction [Rekveldt'00, Rekveldt'01] is another technique taking advantage of the neutron spin-echo.

2.2 General Properties of Neutrons

The neutron is a uncharged baryon with spin ½ and a magnetic dipole moment $\mu_n = -9.662\ 36\ 40(23)\ 10^{-26}$ J T^{-1} anti-parallel to its spin. The neutron mass is 0.14% larger than the proton mass. While bound neutrons in stable nuclei are stable, free neutrons are unstable; they undergo a beta decay into a proton, an electron and an electron-antineutrino with a mean lifetime of just under 15 minutes. Thus, neutrons can fly a macroscopic distance even if they are decelerated down to low energies. They have a strong penetrability through matters and are not very much deflected flying through air. The basic properties of slow (thermal and cold) neutrons used in this work will be summarised in this section.

A neutron exhibits both, wave-like and particle-like properties. In scattering experiments, the wave-like properties are predominant. A neutron can be described by a wave vector $\vec{k}$, and the corresponding wavelength λ, with

$$k = \frac{2\pi}{\lambda}, \tag{2.1}$$

where the modulus of a vector is written as $k \coloneqq |\vec{k}|$, as in the following of this thesis. The kinetic energy of the neutrons E is given by

$$E = \frac{\hbar^2 k^2}{2m_n} = \frac{1}{2} m_n v_n^2 , \tag{2.2}$$

where $m_n = 1.67492716(13)\ 10^{-27}$ kg is the mass of the neutron and $\hbar = h/2\pi = 6.62606896(33)\ 10^{-34}$ J s is the reduced Planck constant. The rest mass of a free neutron corresponds to $E_0 = m_n c^2 = 939.565330(38)$ MeV. Consequently, neutrons which are usually used for condensed matter physics with energies in the range of 25 meV and below show no relativistic effects since their velocity is much smaller than the velocity of light in vacuum $c = 299\ 792\ 458$ m/s. From

relations (2.1) and (2.2) one can obtain the velocity v_n of the neutron as a function of its wavelength

$$v_n(\lambda) = \frac{h}{m_n \lambda}. \tag{2.3}$$

Since neutrons are fermions, it is convenient to write their wave function as a superposition of two eigenstates of the spin Hamiltonian

$$\psi(\vec{r},t) = \phi_+(\vec{r},t)|\uparrow\rangle + \phi_-(\vec{r},t)|\downarrow\rangle, \tag{2.4}$$

where the weights are the eigenfunctions of the spatial Hamiltonian. In the absence of a magnetic field, both states are degenerated.

2.3 A Neutron in a Magnetic Field

2.3.1 Classical Picture

In the presence of a magnetic-field the spin of the neutron precesses around the direction of the magnetic field, see Fig. 2.1. This effect is named Larmor precession, after an Irish physicist Joseph Larmor. The angular precession frequency is

$$\omega_L = -\gamma_n B, \tag{2.5}$$

where, γ_n = -1.83247185(43) 10^8 s^{-1} T^{-1} is the gyromagnetic ratio of the neutron and B the magnitude of the magnetic induction. $\omega_L/2\pi$ is called Larmor frequency.

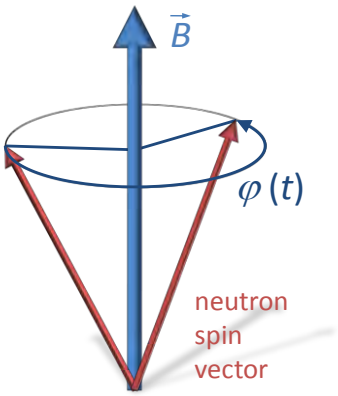

Fig. 2.1 Neutron spin precession around the direction of the magnetic field.

In a neutron scattering experiment, where a neutron beam is used, the neutron spin can only be measured as an ensemble average. The spatial changes of the magnetic-field can be expressed as time dependent changes since the neutrons are flying with a speed v_n. Changes of the magnetic-field may have an influence on the beam polarisation. Slow changes of the magnetic-field direction with

$$\left|\frac{\mathrm{d}(\vec{B}/B)}{\mathrm{d}t}\right| \ll \omega_L\,, \tag{2.6}$$

lead to an ideal adiabatic process. In this extreme case, the spin precession axis follows the changes of the magnetic-field direction. The spin component parallel to the magnetic-field remains constant. The perpendicular spin component with respect to the magnetic-field direction precesses with the Larmor frequency.

If the change of the magnetic-field direction is fast, i.e.

$$\left|\frac{\mathrm{d}(\vec{B}/B)}{\mathrm{d}t}\right| \gg \omega_L\,, \tag{2.7}$$

the beam polarisation might be lost or reduced. In the other extreme of two constant magnetic-field areas with a narrow interface region that Eq. (2.7) is fulfilled, the precession around the first magnetic-field direction changes instantaneously into the precession around the second magnetic field. The parallel spin component in the second magnetic-field depends on the exact spin state at the end of the first magnetic field. E.g. the neutron is travelling through two adjacent different magnetic-field areas with a spin (y- and z-component) precessing around the direction of the first magnetic-field in x-direction. Adjacent to this field another magnetic-field in y-direction exists, after traversing the thin magnetic-field border region, the y-component of the spin in the first magnetic-field at the position of the interface will be constant in the next field region and the x- and z-component of the spin will precess around the direction of the new magnetic field. Since only one component of the spin is preserved, a part of the beam polarisation might be lost. This transition is called strictly non-adiabatic.

Both kinds of magnetic-field transitions can be taken advantage of in a SERGIS set-up. A magnetic-field transition in the medium range leads to a uncontrolled depolarisation of the neutron beam and is usually undesired.

The precession angle of a neutron spin after passage of a homogenous magnetic-field of length *l* and strength *B* is

$$\varphi = -\frac{m_\mathrm{n}\gamma_\mathrm{n}}{\hbar}\frac{Bl}{k}\,. \tag{2.8}$$

2.3.2 Quantum Mechanical Description

The presence of a magnetic-field breaks the degeneracy of the spin eigenstates of the Hamiltonian of the neutron, see Eq. (2.4). The propagation of the neutrons can be expressed by a wave function interacting with the potential

$$V(\vec{r}) = \frac{2\pi\hbar}{m_\mathrm{n}}\rho(\vec{r}) - \vec{\mu}\vec{B}(\vec{r})\,, \tag{2.9}$$

where the first term of the potential describes the interaction with the nuclei (strong interaction) via their scattering length density $\rho(\vec{r})$, while the second term arises from the interaction of the magnetic moment $\vec{\mu}$ of the neutron with the magnetic induction $\vec{B}(\vec{r})$, called Zeeman interaction. The magnetic-field can arise from the magnetic moments of the molecules and/or from an external magnetic field.

The magnetic-field acts as spin quantisation axis. The one stationary state $|\uparrow\rangle$ will be referred to as the spin configuration parallel to the magnetic field, and the other one $|\downarrow\rangle$ as the spin configuration anti-parallel to the magnetic field. If, in the classical picture, the spin is oriented perpendicular to the direction of the magnetic field, in the quantum-mechanical description this corresponds to the wave function of a neutron before the magnetic-field area

$$\psi(\vec{r},t) = \mathrm{e}^{\mathrm{i}(\vec{k}_0\vec{r}-\omega_0 t)}\frac{|\uparrow\rangle + |\downarrow\rangle}{\sqrt{2}}, \tag{2.10}$$

with the wave vector of the neutron $\vec{k}_0$ and $E/\hbar = \omega_0$ outside the magnetic-field area.

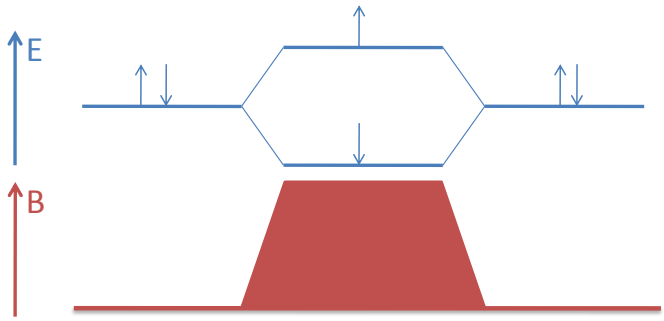

Fig. 2.2: Energy levels of the different neutron spin components in a magnetic field.

In the magnetic-field area the wave function of the neutron becomes [Golub'94]

$$\psi(\vec{r},t) = \mathrm{e}^{\mathrm{i}(\vec{k}_0\vec{r}-\omega_0 t)}\,\frac{\mathrm{e}^{-\frac{\mathrm{i}B\gamma_\mathrm{n}x}{2v_0}}\,|\uparrow\rangle + \mathrm{e}^{+\frac{\mathrm{i}B\gamma_\mathrm{n}x}{2v_0}}\,|\downarrow\rangle}{\sqrt{2}}, \qquad \textbf{(2.11)}$$

where x is the flight path length in the magnetic-field region. The beating of the two parts of the wave function can be seen as the analogy to the classical picture where the spin performs Larmor precessions. The spin precession of 2π in the classical picture corresponds to a relative phase shift of the two wave functions of 2π in the quantum-mechanical picture.

Due to the Zeeman interaction, neutrons with their spin parallel and anti-parallel with respect to the direction of the magnetic-field have different energies

$$E_{\uparrow\downarrow} = \frac{\hbar^2}{2m_\mathrm{n}}\left(\frac{2\pi}{\lambda} \mp \frac{m_\mathrm{n}\lambda\gamma_\mathrm{n}B}{4\pi\hbar}\right)^2, \qquad \textbf{(2.12)}$$

as depicted in Fig. 2.2, and hence different wave vectors

$$k_{\uparrow/\downarrow} = k_0 \mp \frac{m_\mathrm{n}\gamma_\mathrm{n}B}{2\hbar k_0}. \qquad \textbf{(2.13)}$$

These different wave vectors lead to different refraction angles at the magnetic-field boundaries [Just'73, Badurek'79]. Their direction of propagation (represented by the wave vector $\vec{k}$) can be expressed by Snell's law in analogy to the refraction of visible light, provided the angle of incidence in the magnetic-field region is larger than the critical angle of total reflection at the interface, with

$$\frac{\sin\chi}{\sin\alpha_{2\uparrow/\downarrow}} = \frac{k_{\uparrow/\downarrow}}{k_0}, \tag{2.14}$$

as depicted in Fig. 2.3. With respect to $\vec{k}_0$, $\vec{k}_\uparrow$ respectively $\vec{k}_\downarrow$ are diffracted by

$$\begin{aligned}\beta = \alpha_{2\uparrow/\downarrow} - \chi &= -\chi + \arcsin\frac{k_0 \sin\chi}{k_{\uparrow/\downarrow}} \\ &= -\chi + \arcsin\frac{\sin\chi}{1 \mp \frac{m_n \gamma_n B}{2\hbar k_0^2}}.\end{aligned} \tag{2.15}$$

For the refraction of the plane wave fronts at the magnetic-field border exists no analogue in the classical picture. For many other applications this refraction can be omitted since for typical magnetic inductions and neutron energies the refraction angle is in the order of 10^{-5}° (χ = 55°, B = 0.01 T, λ = 0.55 nm).

2.4 Neutron Spin-Echo

The neutron spin-echo principle is based on the precession of the neutron spin in two identical magnetic-field regions with opposite magnetic-field directions before and after the sample. In case of no scattering event at the sample, the spin precessions in the first and second magnetic-field regions cancel each other and the initial spin orientation is retrieved (echo condition), independently of the wavelength and direction of the individual neutron. The measured quantity in a neutron spin-echo experiment is the polarisation of the neutron beam at the detector position, usually one component of it, e.g. a scalar quantity. If scattering events at the sample take place, the neutron spin orientation after the second magnetic-field region depends on the momentum and energy transfer. The

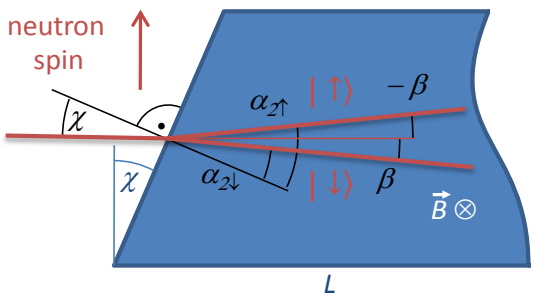

Fig. 2.3: Spin dependent neutron refraction at a magnetic-field border.

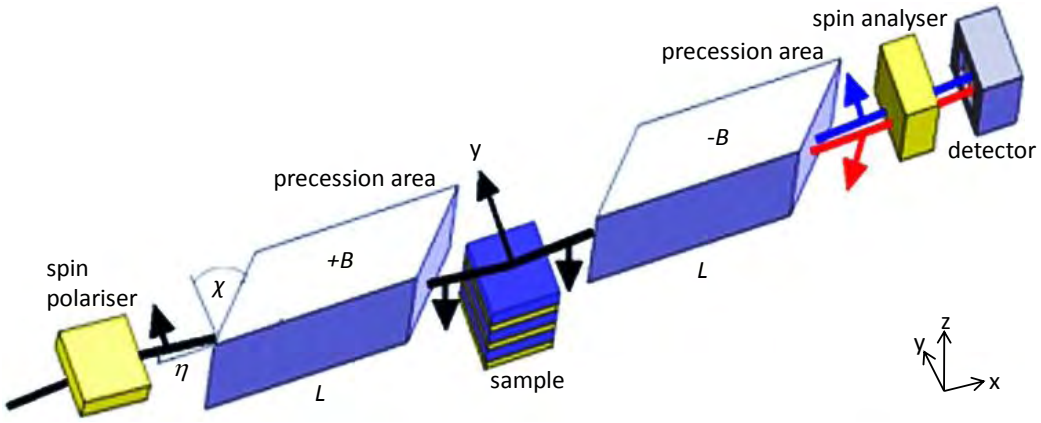

Fig. 2.4: General sketch of a SERGIS set-up. L is the length of the magnetic-field area with a magnetic induction B and χ the inclination of the magnetic field area as indicated. The blue and red arrows stand for different polarisations of the scattered neutrons. The angle η describes the deviation in vertical direction of the incident neutron beam from the surface normal of the magnetic-field border for $\chi = 0$.

classical spin-echo set-up aims to resolve the energy transfer; the magnetic-field borders are orientated perpendicular to the direction of the neutron propagation. To measure SERGIS or more general SESANS (spin-echo resolved small angle neutron scattering) [Rekveldt'96] one has to assume an elastic scattering process and can resolve one component of the momentum transfer with inclined magnetic-field borders.

The SERGIS spin-echo set-up consists of two parallelogram-shaped regions with magnetic fields of magnitude B, see Fig. 2.4. In the set-up as depicted, in one region the magnetic-field is directed in the vertical direction upwards and in the other magnetic-field region in the vertical direction downwards. The mean direction of the incoming neutrons is in the vertical plane parallel to the x-direction. The incoming neutrons are polarised with the spin oriented in the y-direction. The front and end faces of the precession devices make an angle χ with the mean beam direction. The latter coincides with the average transmission direction in both magnetic-field regions of the neutron beam (x-direction). In the following two sections the phase change of the neutron spin as a function of its momentum transfer at the sample and the neutron beam divergence will be calculated in detail.

2.4.1 Classical Picture

Within a precession region, the neutron spin undergoes Larmor precession. The number of precessions depends on the magnetic-field strength, and on the dwell time needed for the passage of this region, which is itself a function of the trajectory and the velocity of the neutron.

The wave vector of a neutron before and after the sample position is

$$\begin{aligned} \vec{k}_\mathrm{i} &:= \vec{\bar{k}}_\mathrm{i} + \vec{\tilde{k}}_\mathrm{i}\,, \\ \vec{k}_\mathrm{f} &:= \vec{k}_\mathrm{i} + \vec{q} = \vec{\bar{k}}_\mathrm{i} + \vec{\tilde{k}}_\mathrm{i} + \vec{q}\,, \end{aligned} \tag{2.16}$$

where $\vec{\bar{k}}_\mathrm{i}$ is the average wave vector of the incoming divergent neutron beam, and $\vec{\tilde{k}}_\mathrm{i}$ accounts for the deviation of $\vec{\bar{k}}_\mathrm{i}$ due to the divergence of the beam and the degree of monochromatisation. $\vec{q}$ is the momentum transfer induced by the sample. Since the scattering process is assumed to be elastic $k_\mathrm{i} = k_\mathrm{f}$.

The distance vector $\vec{d}$ of the two inclined field borders of one spin-echo arm is

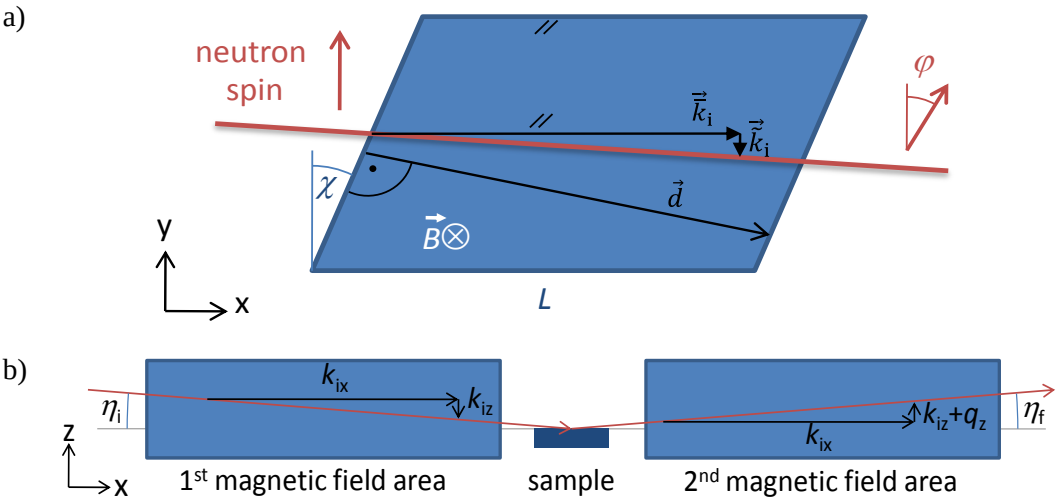

Fig. 2.5 a) Top view of the parallelogram shaped magnetic-field area. The distance vector $\vec{d}$ of the magnetic-field borders is oriented parallel to the x-y-plane. $\vec{k}_\mathrm{i} = \vec{\bar{k}}_\mathrm{i} + \vec{\tilde{k}}_\mathrm{i}$ b) Side view of the parallelogram shaped magnetic-field area. To minimize disadvantageous effects on the neutron spin phase, the magnetic-field regions and the neutron beam have to be set-up to satisfy $\eta_\mathrm{i} \approx \eta_\mathrm{f}$ or $q_\mathrm{z} \approx -2k_\mathrm{iz}$, respectively. $\eta_\mathrm{i/f}$ is the deviation of the average neutron propagation direction from the x-direction. For clarity the angles $\eta_\mathrm{i/f} \approx 0.8°$ are overdrawn.

parallel to $\vec{\bar{k}}_\mathrm{i}$ if $\chi = \eta_\mathrm{i} = 0$ (see Fig. 2.5). The projection of $\vec{k}_\mathrm{i}$ respectively $\vec{k}_\mathrm{f}$ on $\vec{d}/d$, is

$$\begin{aligned} k_{\mathrm{i,d}} &= \left(\vec{\bar{k}}_\mathrm{i} + \vec{\tilde{k}}_\mathrm{i}\right)\begin{pmatrix}\cos\chi_\mathrm{i}\cos\eta_\mathrm{i}\\ \sin\chi_\mathrm{i}\cos\eta_\mathrm{i}\\ \sin\eta_\mathrm{i}\end{pmatrix} \\ &= \begin{pmatrix}\bar{k}_\mathrm{i}\cos\eta_\mathrm{i} + \tilde{k}_\mathrm{i,x}\\ \tilde{k}_\mathrm{i,y}\\ \bar{k}_\mathrm{i}\sin\eta_\mathrm{i} + \tilde{k}_\mathrm{i,z}\end{pmatrix}\begin{pmatrix}\cos\chi_\mathrm{i}\cos\eta_\mathrm{i}\\ \sin\chi_\mathrm{i}\cos\eta_\mathrm{i}\\ \sin\eta_\mathrm{i}\end{pmatrix} \\ &= \bar{k}_\mathrm{i}\cos\chi_\mathrm{i}\cos\eta_\mathrm{i} \\ &\quad\times\left[\cos\eta_\mathrm{i} + \frac{\tilde{k}_\mathrm{i,x}}{\bar{k}_\mathrm{i}} + \frac{\tilde{k}_\mathrm{i,y}}{\bar{k}_\mathrm{i}}\tan\chi_\mathrm{i} + \left(\sin\eta_\mathrm{i} + \frac{\tilde{k}_\mathrm{i,z}}{\bar{k}_\mathrm{i}}\right)\frac{\tan\eta_\mathrm{i}}{\cos\chi_\mathrm{i}}\right] \end{aligned} \tag{2.17}$$

and

$$\begin{aligned} k_{\mathrm{f,d}} &= \left(\vec{\bar{k}}_\mathrm{i} + \vec{\tilde{k}}_\mathrm{i} + \vec{q}\right)\begin{pmatrix}\cos\chi_\mathrm{f}\cos\eta_\mathrm{f}\\ \sin\chi_\mathrm{f}\cos\eta_\mathrm{f}\\ \sin\eta_\mathrm{f}\end{pmatrix} \\ &= \bar{k}_\mathrm{i}\cos\chi_\mathrm{f}\cos\eta_\mathrm{f}\left[\cos\eta_\mathrm{f} + \frac{\tilde{k}_\mathrm{i,x} + q_\mathrm{x}}{\bar{k}_\mathrm{i}} + \frac{\tilde{k}_\mathrm{i,y} + q_\mathrm{y}}{\bar{k}_\mathrm{i}}\tan\chi_\mathrm{f}\right. \\ &\quad\left. + \left(\sin\eta_\mathrm{f} + \frac{\tilde{k}_\mathrm{i,z} + q_\mathrm{z}}{\bar{k}_\mathrm{i}}\right)\frac{\tan\eta_\mathrm{f}}{\cos\chi_\mathrm{f}}\right]. \end{aligned} \tag{2.18}$$

In one spin-echo arm the precession angle changes by

$$\varphi = -\frac{m_\mathrm{n}\gamma_\mathrm{n}B_\mathrm{i/f}}{\hbar}\frac{d_\mathrm{i/f}}{k_\mathrm{i/f,d}}. \tag{2.19}$$

The precession phase accumulated in both spin-echo arms with a momentum transfer $\vec{q}$ at the sample is

$$\varphi = -\frac{m_\mathrm{n}\gamma_\mathrm{n}}{\hbar}\left(\frac{B_\mathrm{i}d_\mathrm{i}}{k_\mathrm{i,d}} + \frac{B_\mathrm{f}d_\mathrm{f}}{k_\mathrm{f,d}}\right). \tag{2.20}$$

With $d_\mathrm{i/f} = L_\mathrm{i/f}\cos\chi_\mathrm{i/f}$, $\eta_\mathrm{i} = -\eta_\mathrm{f} := \eta$ and $q_\mathrm{z} = -2k_\mathrm{iz}$, where q_z is the z-component of the momentum transfer at the sample in the coordinate system of the set-up (Fig. 2.5b), eventually the sample surface normal has to be tilted to fulfil $\eta_\mathrm{i} = -\eta_\mathrm{f}$. Under these conditions the phase of the neutron spin after the two magnetic-field regions is

$$\varphi = -\frac{m_\mathrm{n}\gamma_\mathrm{n}}{\hbar}\left(\frac{\cos\chi_\mathrm{i}\, B_\mathrm{i} L_\mathrm{i}}{k_\mathrm{i,d}} + \frac{\cos\chi_\mathrm{f}\, B_\mathrm{f} L_\mathrm{f}}{k_\mathrm{f,d}}\right). \tag{2.21}$$

Since both spin-echo arms are identical with an anti-parallel magnetic-field $B_\mathrm{i} = -B_\mathrm{f} := B$, $L_\mathrm{i} = L_\mathrm{f} := L$ and $\chi_\mathrm{i} = \chi_\mathrm{f} =: \chi$, one obtains

$$\begin{aligned}\varphi = -\frac{m_\mathrm{n}\gamma_\mathrm{n}}{2\pi h} BL\lambda^2 \left(q_\mathrm{x} + q_\mathrm{y}\tan\chi - 2\tilde{k}_\mathrm{i,z}\frac{\tan\eta}{\cos\chi}\right)\frac{1}{\cos\eta} \\ \times\left[\cos\eta + \frac{\tilde{k}_\mathrm{i,x}}{\bar{k}_\mathrm{i}} + \frac{\tilde{k}_\mathrm{i,y}}{\bar{k}_\mathrm{i}}\tan\chi + \left(\sin\eta + \frac{\tilde{k}_\mathrm{i,z}}{\bar{k}_\mathrm{i}}\right)\frac{\tan\eta}{\cos\chi}\right]^{-1} \\ \times\left[\cos\eta + \frac{\tilde{k}_\mathrm{i,x} + q_\mathrm{x}}{\bar{k}_\mathrm{i}} + \frac{\tilde{k}_\mathrm{i,y} + q_\mathrm{y}}{\bar{k}_\mathrm{i}}\tan\chi + \left(\sin\eta - \frac{\tilde{k}_\mathrm{i,z}}{\bar{k}_\mathrm{i}}\right)\frac{\tan\eta}{\cos\chi}\right]^{-1}.\end{aligned} \tag{2.22}$$

With $\cos\eta \approx 1$, $\left|\left(\sin\eta \pm \tilde{k}_\mathrm{i,z}/\bar{k}_\mathrm{i}\right)\tan\eta / \cos\chi\right| \ll 1$ and $\left|2\tilde{k}_\mathrm{i,z}\tan\eta / \cos\chi\right| \ll q_\mathrm{x} + q_\mathrm{y}\tan\chi$, i.e.

$$\varphi \approx -\frac{m_\mathrm{n}\gamma_\mathrm{n}}{2\pi h} BL\lambda^2 \left(q_\mathrm{x} + q_\mathrm{y}\tan\chi\right) C_\mathrm{corr}\ , \tag{2.23}$$

with

$$C_\mathrm{corr} = \left(1 + \frac{\tilde{k}_\mathrm{i,x}}{\bar{k}_\mathrm{i}} + \frac{\tilde{k}_\mathrm{i,y}}{\bar{k}_\mathrm{i}}\tan\chi\right)^{-1}\left(1 + \frac{\tilde{k}_\mathrm{i,x} + q_\mathrm{x}}{\bar{k}_\mathrm{i}} + \frac{\tilde{k}_\mathrm{i,y} + q_\mathrm{y}}{\bar{k}_\mathrm{i}}\tan\chi\right)^{-1}. \tag{2.24}$$

E.g. for a divergence in z-direction of the incident beam of ±0.076°, λ = 5.5 Å, $\chi = 45°$, $\eta = 0.8°$, and $q_\mathrm{y} = 6\cdot10^{-5}$ Å^{-1} the phase information is lost since the divergence of the incident beam in z-direction attributes to the neutron spin phase in the same order of magnitude as the scattering at the sample $\left|2\tilde{k}_\mathrm{i,z}\tan\eta / \cos\chi\right| = q_\mathrm{y}\tan\chi$. Under these conditions only real space structures with a size well below 10 µm can by reproduced.

For a typical set-up (Chapter 3) $\left|\vec{\tilde{k}}_\mathrm{i} + \vec{q}\right| / \bar{k}_\mathrm{i} < 0.06$, hence the term C_corr in Eq. (2.23) and (2.24) may lead to a considerable effect, especially for small structures and larger spin-echo lengths, the according decay of polarisation has to be calculated in detail according to the exact experimental set-up and for each momentum transfer. Neglecting these corrections

$$\begin{aligned}\varphi \;&\approx -\frac{m\gamma_\mathrm{n}}{2\pi h} BL\lambda_i^2 \left(q_\mathrm{x} + q_\mathrm{y} \tan\chi\right) \\ &= q_\mathrm{x} X^\mathrm{SE} + q_\mathrm{y} Y^\mathrm{SE}\end{aligned} \tag{2.25}$$

with

$$\begin{aligned}X^\mathrm{SE} &:= -\frac{m\gamma_\mathrm{n}}{2\pi h} BL\lambda^2 \,, \\ Y^\mathrm{SE} &:= -\frac{m\gamma_\mathrm{n}}{2\pi h} BL\lambda^2 \tan\chi \,.\end{aligned} \tag{2.26}$$

In case of a non-divergent incident beam, i.e. $\tilde{k}_\mathrm{i} = 0$, the phase accumulated in both spin-echo arms as calculated in (2.22) can be simplified to

$$\begin{aligned}\varphi = &\left(q_\mathrm{x} X^\mathrm{SE} + q_\mathrm{y} Y^\mathrm{SE}\right) \frac{1}{\cos\eta} \\ &\times \left(\cos\eta + \sin\eta \frac{\tan\eta}{\cos\chi}\right)^{-1} \left(\cos\eta + \frac{q_\mathrm{x}}{\bar{k}_\mathrm{i}} + \frac{q_\mathrm{y}}{\bar{k}_\mathrm{i}} \tan\chi + \sin\eta \frac{\tan\eta}{\cos\chi}\right)^{-1} .\end{aligned} \tag{2.27}$$

Eq. (2.27) is valid for elastic as well as for inelastic scattering processes. If $\chi = 0$ only the energy transfer of the neutron can be resolved (cf. a conventional neutron spin-echo spectrometer [Mezei'72]). Usually the total precession phase of a SERGIS experiment is represented in the form

$$\varphi \approx q_\mathrm{y} Y^\mathrm{SE} \,. \tag{2.28}$$

where Y^SE is the spin-echo length. According to (2.22) and its derivation, this is an approximation which is only valid as long as q_x is negligible compared to $q_\mathrm{y} \tan\chi$, the last two factors in brackets in (2.22) can be approximated by one, and the divergence of the incident beam in z-direction as well as η are sufficiently small.

2.4.2 Quantum Mechanical Picture

As described in Section 2.3.2, the two wave packages traverse the field regions in analogy to light in a birefringent medium. After the first magnetic-field region the wave function is [Golub'94]

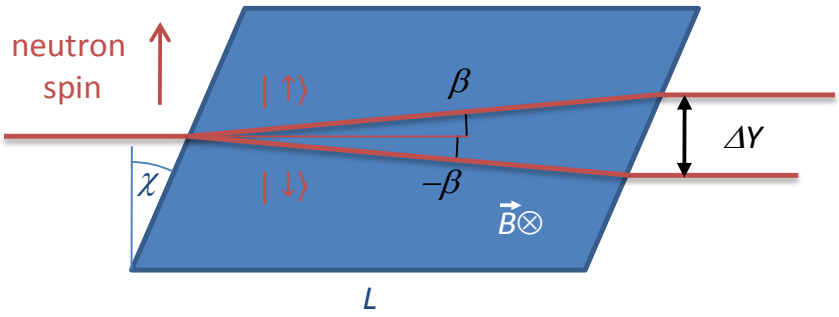

Fig. 2.6 Neutron propagation in a parallelogram shaped magnetic-field area. The coherent splitting in energy of the spin-up and spin-down states leads to their macroscopic spatial separation, as a function of the experimental parameters.

$$\psi(\vec{r},t) = \mathrm{e}^{\mathrm{i}(\vec{k}_0\vec{r}-\omega_0 t)}\frac{\mathrm{e}^{-\frac{\mathrm{i}B\gamma_\mathrm{n}L}{2v_0}}|\uparrow\rangle + \mathrm{e}^{+\frac{\mathrm{i}B\gamma_\mathrm{n}L}{2v_0}}|\downarrow\rangle}{\sqrt{2}}. \qquad \textbf{(2.29)}$$

Using (2.14), and (2.15), the spatial separation of the wave packages can be calculated as

$$\Delta Y = 2L\tan\beta = 2L\tan\left(\arcsin\frac{4\pi h\sin\chi}{4\pi h - m_\mathrm{n}\gamma_\mathrm{n}B\lambda^2} - \chi\right), \qquad \textbf{(2.30)}$$

which, within the approximation used for the classical picture, turns out to be identical to

$$Y^{\mathrm{SE}} = \frac{m_\mathrm{n}\gamma_\mathrm{n}}{2\pi h}L\lambda^2 B\tan\chi\,, \qquad \textbf{(2.31)}$$

assuming $\frac{2m_\mathrm{n}\gamma_\mathrm{n}}{\pi h}L\lambda^2 B\tan\chi \ll 1$. For illustration see Fig. 2.6.

The lateral separation of two plane wave fronts can only be justified assuming a limited lateral coherence of the neutron beam. Then ΔY is the shift of two coherent regions with respect to each other. After the second spin-echo arm the separation of the two wave packages is reverted and the wave packages will interfere. This way the coherence length can be significantly larger than the slit defined coherence length.

From this point on, the derivation of the wave function after the sample and the second magnetic-field region is analogue to the classical picture, as shown in Section 2.4.1, keeping in mind that in the classical picture the relative phase shift

of the two wave packages is represented by the Larmor precession of the neutron spin.

2.4.3 Interpretation of the Polarisation – the Generalised Patterson Function

The polarisation P of a neutron beam is defined as

$$P = \langle \cos\varphi \rangle = \frac{I_\uparrow - I_\downarrow}{I_\uparrow + I_\downarrow}, \tag{2.32}$$

where $I_\uparrow$ and $I_\downarrow$ are the measured intensities at the detector with the spin prepared in y and $-y$ direction. $I_0 = I_\uparrow + I_\downarrow$ is the intensity downstream of the spin polariser. In this chapter, the technical efficiencies of the devices are neglected.

The neutron intensity at the detector is

$$I_{\uparrow/\downarrow} = I_0 \int_{\vec{q}} \frac{\mathrm{d}\sigma}{\mathrm{d}\Omega}(\vec{q})(1 \pm \cos\varphi)\mathrm{d}\vec{q} \tag{2.33}$$

with the scattering cross section $\mathrm{d}\sigma/\mathrm{d}\Omega(\vec{q})$ of the sample. Taking into account Eq. (2.23) the intensity is

$$I_{\uparrow/\downarrow} = I_0 \int_{\vec{k}_\mathrm{i}} \int_{\vec{q}} \frac{\mathrm{d}\sigma}{\mathrm{d}\Omega}(\vec{q})\{1 \pm \cos[(q_\mathrm{x}X^\mathrm{SE} + q_\mathrm{y}Y^\mathrm{SE})C_\mathrm{corr}]\}\mathrm{d}\vec{k}_\mathrm{i}\mathrm{d}\vec{q} \tag{2.34}$$

and the polarisation as a function of the scattering cross section is

$$\begin{aligned} P = & \int_{\vec{k}_\mathrm{i}} \int_{\vec{q}} \frac{d\sigma}{d\Omega}(\vec{q}) \cos[(q_\mathrm{x}X^\mathrm{SE} + q_\mathrm{y}Y^\mathrm{SE})C_\mathrm{corr}]\, \mathrm{d}\vec{k}_\mathrm{i}\mathrm{d}\vec{q} \\ & \times \left(\int_{\vec{k}_\mathrm{i}} \int_{\vec{q}} \frac{d\sigma}{d\Omega}(\vec{q})\mathrm{d}\vec{k}_\mathrm{i}\mathrm{d}\vec{q} \right)^{-1}. \end{aligned} \tag{2.35}$$

As an example, the polarisation as a function of the spin-echo length for four structures with a sinusoidal scattering length density distribution along the y-direction, i.e. $\mathrm{d}\sigma/\mathrm{d}\Omega(q_\mathrm{y}) = \delta(q_\mathrm{y} - 2\pi/l_{period})$ of different periodicity l_period

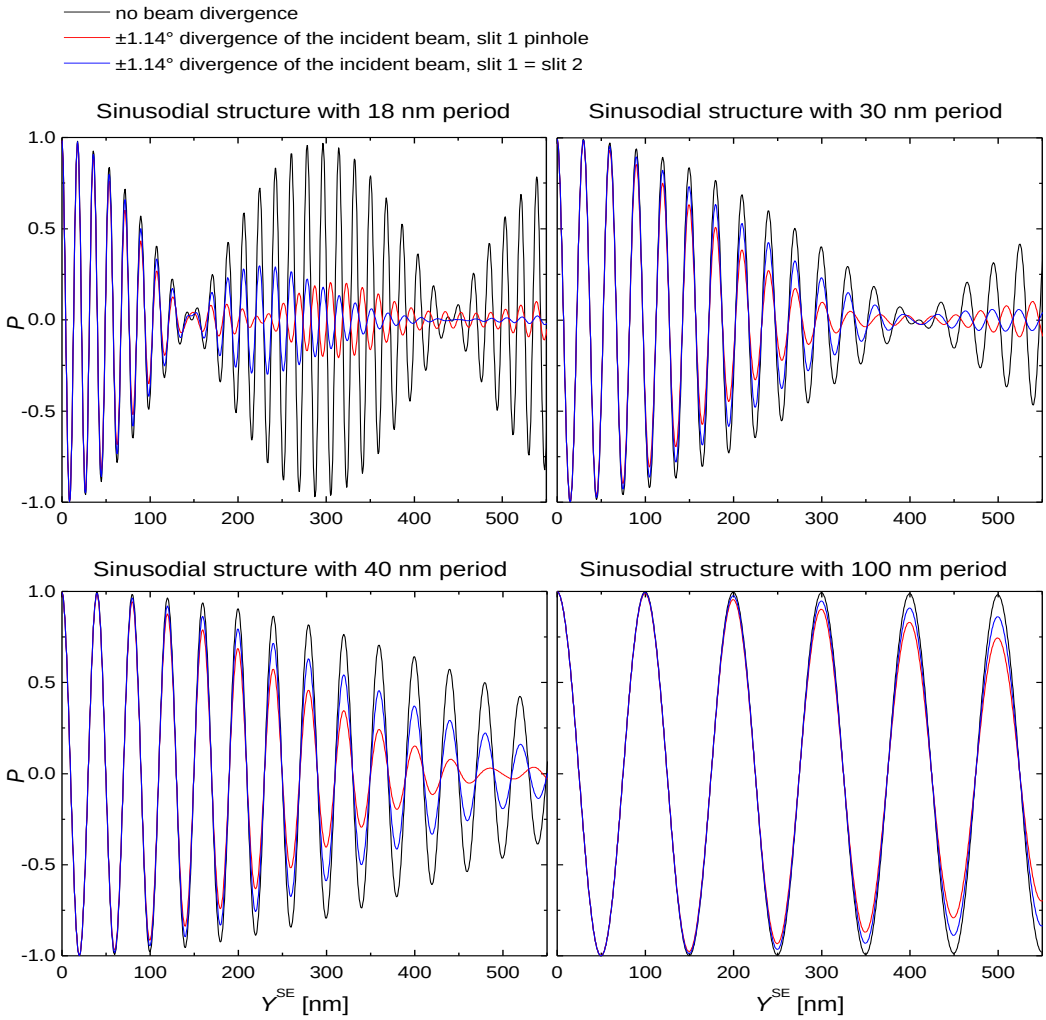

Fig. 2.7: Polarisation as a function of the spin-echo length Y^{SE} for four structures with a sinusoidal scattering length distribution in y-direction and homogeneous scattering length distribution in x-direction, as calculated from Eq. (2.35) with: $\bar{k}_i$ = 11.4 nm^{-1} and χ = 45°. Both slit 1 and slit 2 are situated in front of the sample. If the first slit is very small (pinhole) the distribution of the intensity on the different propagation directions is uniform. In case of both slits having the same size, a weighting function $(2 - 2|\tilde{k}_{i,y}/\bar{k}_i|/\tan^{-1} 1.14°)$ is introduced to simulate the intensity distribution on the propagation direction.

and homogeneous scattering length density distribution in x-direction, as calculated from Eq. (2.35) with $\tilde{k}_i = 0$ and $\tilde{k}_{i,x}/\bar{k}_i \leq 0.0002$, $\tilde{k}_{i,y}/\bar{k}_i \leq 0.02$, $\bar{k}_i$ = 11.4 nm^{-1}, χ = 45°, is plotted in Fig. 2.7. The $\tilde{k}_i/\bar{k}_i$ values correspond to a beam divergence at the sample position of ±1.14° in y-direction. A divergent beam can be created with two slits before the sample position. If the first slit is

very small it can be approximated by a pinhole, the divergence is then only defined by the second slit (and or by the intensity divergence in the beam, as defined by the monochromator mosaicity and the divergence of the neutron in the guide). In the other case when both slits are of comparable size, the divergence is defined by both slits and the intensity distribution with respect to the propagation direction is a function of the deviation of the average propagation direction of the neutron beam. If the slits have the same dimensions and the intensity distribution before the first slit is homogenous, the intensity distribution as a function of $\tilde{k}_{\mathrm{i,y}}$ is $2 - 2\left|\tilde{k}_{\mathrm{i,y}}/\bar{k}_{\mathrm{i}}\right|/\tan^{-1}\alpha$, with the divergence ±α. The described instrumental reduction of the polarisation cannot be accounted for with the normalisation by a reference beam (see Section 3.3.2). For small structures and small spin-echo length Y^{SE} the dependency of the correction factor, Eq. (2.24), on + $\vec{q}_{\mathrm{y}}$ respectively -$\vec{q}_{\mathrm{y}}$ are dominant. The fractions of the neutrons scattered to the left and right about +$\vec{q}_{\mathrm{y}}$ and -$\vec{q}_{\mathrm{y}}$ lead to a beating of the polarisation signal of the total beam as function of the spin-echo length. In case of no beam divergence, i.e. $\tilde{k}$ = 0 and q_{x} = 0, the polarisation is

$$P\left(Y^{\mathrm{SE}}\right) = \cos\left(q_{\mathrm{y}} Y^{\mathrm{SE}}\left(1 - \frac{q_{\mathrm{yl}}^2}{\bar{k}_{\mathrm{i}}^2}\right)^{-1}\right)\cos\left[\frac{q_{\mathrm{y}} Y^{\mathrm{SE}}}{2}\left(\left(1 - \frac{q_y}{\bar{k}_{\mathrm{i}}}\right)^{-1} - \left(1 + \frac{q_y}{\bar{k}_{\mathrm{i}}}\right)^{-1}\right)\right] \approx \cos\left[q_{\mathrm{yl}} Y^{\mathrm{SE}}\right]\cos\left[q_{\mathrm{yl}} Y^{\mathrm{SE}}\frac{q_{\mathrm{yl}}}{\bar{k}_{\mathrm{i}}}\right]. \quad \textbf{(2.36)}$$

The second cosine function in Eq. (2.36) describes the beating of the amplitude, whereas the first cosine function represents the Fourier transform of the sample morphology. For small $q_y/\bar{k}_{\mathrm{i}}$ and limited Y^{SE} the second cosine function can be approximated by unity. However for very small $q_y \ll 10^{-4}\text{Å}^{-1}$ (in a typical set-up), Eq. (2.34) has to be deduced from Eq. (2.22) instead from Eq. (2.23). In this case a considerable depolarisation due to the divergence of the incident neutron beam in *z*-direction for large structures and large spin-echo lengths Y^{SE} (both >> 1 µm) can be observed, which will not be discussed here further.

For $q/\bar{k}_{\mathrm{i}}$, q_{x} and Y^{SE} limited to sufficiently small values, one can write Eq. (2.35) as

$$P\left(Y^{\mathrm{SE}}\right) \approx \frac{\int \frac{d\sigma}{d\Omega}(q)\cos\left(q_y Y^{\mathrm{SE}}\right)\mathrm{d}q_y}{\int \frac{d\sigma}{d\Omega}(q)\mathrm{d}q_y}. \tag{2.37}$$

As shown in [Squires'96] the Fourier transform of the scattering cross section is identical to the pair-correlation function of the scattering length density distribution. Since the pair correlation function is an even function, the conventional Fourier transform can be replaced by the cosine Fourier transform. We then obtain

$$\begin{aligned}\int \frac{\mathrm{d}\sigma}{\mathrm{d}\Omega}(q)\cos\left(q_y Y^{\mathrm{SE}}\right)\mathrm{d}q_y &= \int_y \tilde{\varrho}_b(y)\tilde{\varrho}_b\left(y + Y^{\mathrm{SE}}\right)\mathrm{d}y \\ &\coloneqq g\left(Y^{\mathrm{SE}}(B, L, \lambda, \chi)\right)\end{aligned} \tag{2.38}$$

and the polarisation [Gähler'96b, Krouglov'03, Pynn'03]

$$P\left(Y^{SE}(B, L, \lambda, \chi)\right) \approx \frac{g\left(Y^{\mathrm{SE}}(B, L, \lambda, \chi)\right)}{g(0)}. \tag{2.39}$$

The function $g(y)$ is also called the generalised Patterson function, since it includes the contributions of the Bragg-diffracted and also of the diffuse intensities [Egami'03].

3 SERGIS Experimental Set-Up and Data Analysis

In this chapter, the experimental realisation of the SERGIS set-up will be explained. In Section 3.1 different ways to build the well-defined magnetic-field regions will be discussed. The other necessary instrumental devices are discussed in Section 3.2, followed by the data analysis, which will be introduced in Section 3.3.

3.1 Precession Devices

Upstream and downstream of the sample, two parallelogram-shaped magnetic-field regions are situated, which are also called precession devices. In the next

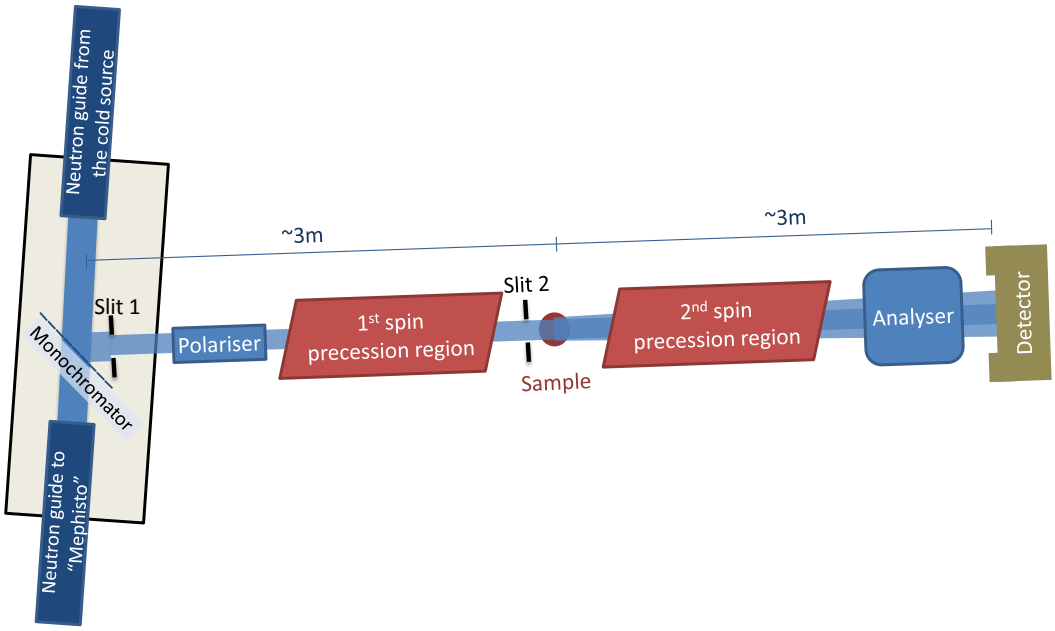

Fig. 3.1: General SERGIS set-up. On the left, the neutron guide is displayed. The neutrons are filtered with respect to the wavelength and polarisation at the monochromator and polariser. The sample is situated at the centre of the figure. Before and after the sample position, magnetic regions for the neutron spin precession are installed. Finally, the neutrons get analysed and detected.

subsections, some general experimental aspects to build a precession device are discussed, followed by different realisations of such device.

3.1.1 General Aspects of Precession Devices

3.1.1.1 Resolution

The resolution of a SERGIS experiment can be limited in two different ways. The first limitation is in real space. The smallest distance in the measured auto-correlation function, where changes in the scattering length density can still be resolved is defined as resolution limit. The limitation arises from the distribution of incident angles at the magnetic-field border due to the divergence of the incident neutron beam, and of the instrumental *q*-limitation (see next section). This definition is in analogy with the definition of resolution of an optical microscope and will be called real-space resolution.

The resolution can also be limited in reciprocal space, where the smallest momentum transfer respectively scattering angle, which can be measured, defines the resolution. This is limited by the accuracy of the magnetic-field borders, since the separated neutron spin wave packages should undergo a magnetic-field exactly as described be the ideal parallelogram shaped field regions. The further those wave packages are separated, the more it is difficult to fulfil this requirement, since the magnetic-field has to be homogeneous on larger length scales [Major'03]. This will be referred to as reciprocal-space resolution. Limitations in the reciprocal-space resolution limit the maximal accessible spin-echo length. In literature, this is also called instrumental resolution.

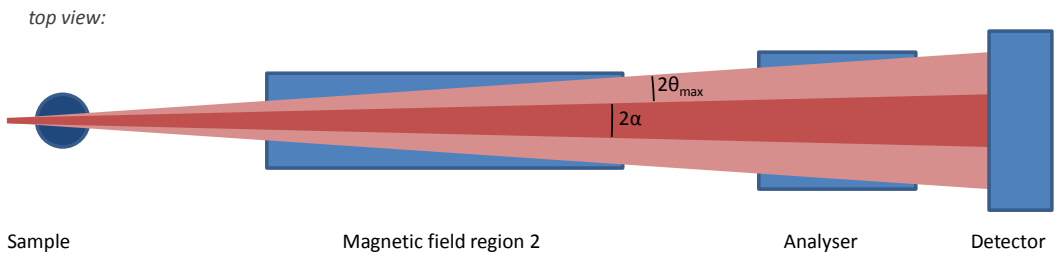

Fig. 3.2: Schematic overview of the SERGIS set-up from the sample to the detector. The maximum scattering angle $2\theta_{max}$ (light red shaded area) and the divergence of the beam 2α (dark red shaded area) are depicted.

3.1.1.2 **Instrumental *q*-Limitation**

To estimate the experimental accessible real space resolution of a SERGIS set-up the maximum scattering angle, which is still transmitted through all components, has to be calculated taking the incident divergence of the neutron beam into account. The maximal scattering angle allows concluding to minimal modulation of scattering length density in real space, which is still correctly reproduced. The transmission of neutrons, which are scattered on smaller structures, is due to the divergence and width of the neutron beam, partly transmitted. E.g. neutron originating from the right side of the neutron beam can be scattered a larger angle to the left without being absorbed, then a neutron in the left side of the beam. Finally there is a second limit which arises from the scattering from one extremity of the incident beam to the opposite extremity of the free beam path in the set-up. Structures below the corresponding real space limit are not reproduced at all. The instrumental limitation of the beam size acts as a low pass filter on the measured correlation function in real space.

For example, to achieve a real-space resolution of r = 50 nm with a neutron beam of width w_i = 40 mm at the sample position, divergence $\alpha = \pm 0.76°$, and wavelength λ = 5.5 Å, the end of the second magnetic-field region, in a distance d = 2 m from the sample position, should have a free path width of at least $2d\tan(\alpha + 2\arcsin(\lambda/2r)) + w_i = 137$ mm . The size of the neutron spin analyser and the detector (each 200 mm) are limiting the resolution in the same way taking in account their distance from the sample position. The set-up with the free neutron beam path is shown in Fig. 3.2.

3.1.2 Neutron Resonance Spin-Echo

R. Golub and R. Gähler suggested neutron resonance spin-echo (NRSE), as a method to enlarge the effective magnetic-field for spin-echo measurements in 1987 and 1995 [Gähler'88, Gähler'96a]. The NRSE technique was first employed by T. Keller et al. [Koppe'99] for NRSE spectroscopy. The method was used by the authors to resolve the inelastic scattering, but can be used for SERGIS as well [Major'03, Major'09].

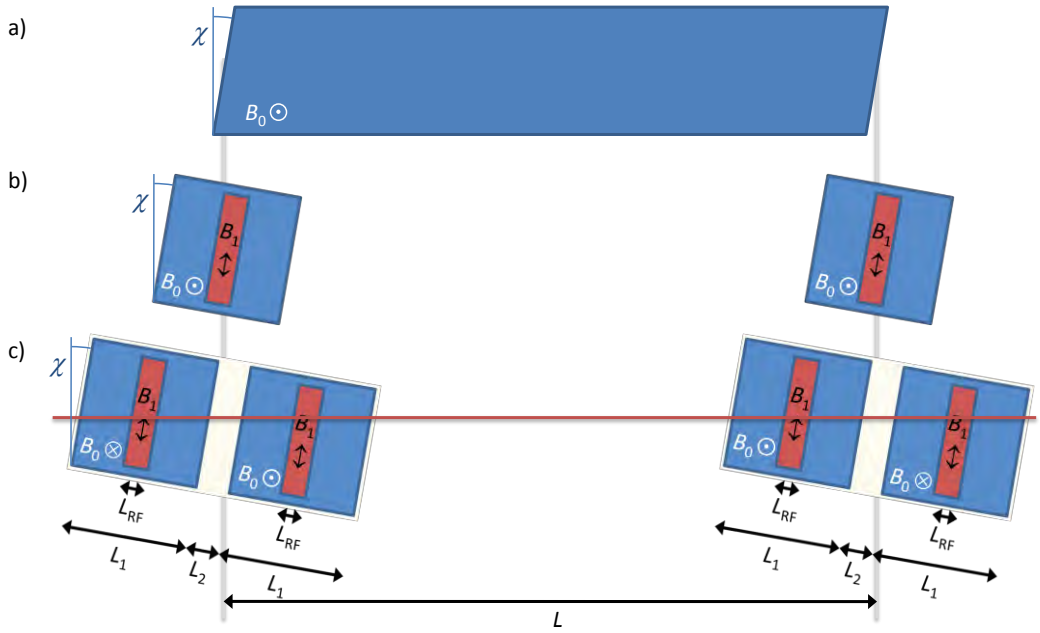

Fig. 3.3: NRSE set-up to mimic one conventional precession region. The blue areas are region with constant (DC) magnetic fields, in the red area a radio frequency (RF) magnetic-field in a perpendicular direction is applied in addition. a) Conventional magnetic-field region. b) Simple NRSE. The χ rotation axis is the centre of the DC field. c) Bootstrap NRSE. Two DC/RF coils are mounted in μ-metal shielding. The χ rotation axis is located in the centre of a coil pair. In b) and c) L is the distance of the rotation axes, in a) the length of the magnetic-field region.

3.1.2.1 **Definition of the Magnetic-Field Regions**

The precession devices are realised in NRSE by a combination of a constant (DC) magnetic-field with a magnetic induction B_0 and an alternating (radio frequency, RF) magnetic field with a magnetic induction amplitude B_1, see Fig. 3.3b. The magnetic B_0 coils have a rectangular shape. Inside the B_0 coil a rectangular coil for the generation of an RF field is mounted with its magnetic-field perpendicular to the B_0 field. The borders of both rectangular field regions are parallel to each other.

In the classical picture, the effect of the NRSE set-up can be described as follows. The neutron is initially polarised in the plane perpendicular to the B_0 field. The neutron enters the B_0 field region and precesses with the Larmor angular frequency

$$\omega_1 = -\gamma_n B_0 \tag{3.1}$$

in the so called precession plane perpendicular to the magnetic-field. Then, still inside the B_0 field region it enters in a weak RF magnetic field. The oscillating field can be regarded as a superposition of two counter-rotating fields [Ramsey'56], each with a magnitude $B_1^{\pm} = \mathrm{B}_1/2$, one of which (depending on the direction of B_0) will rotate in the same direction as the neutron spin precession (e.g. B_1^+). The angular frequency of the oscillating field is set equal ω_1. The neutron spin will precess around B_1^+ with a constant angle between the neutron spin and the B_1^+ field. The other counter-rotating B_1 component (B_1^-) has only a negligible effect on the behaviour of the neutron spin, which is called "Bloch-Siegert shift" [Bloch'40] and amounts to

$$\frac{\Delta\omega_1}{\omega_1} = \left(\frac{B_1^-}{4B_0}\right)^2 . \tag{3.2}$$

For the typical SERGIS set-up, the Bloch-Siegert shift is in the order of 10^{-3} due to the strong B_0 and weak B_1 field and can be omitted.

The amplitude of the (B_1^+) rotating field is set to

$$B_1^+ = -\frac{\pi v_n \cos\chi}{\gamma_n L_{RF}}, \tag{3.3}$$

where L_{RF} is the length, perpendicular to the field borders, of the circular polarised magnetic-field area (see Fig. 3.3c). The amplitude and length of the circular polarised magnetic-field is chosen, that the neutron spin performs a π precession around the direction of the circular polarised magnetic field. Hence, when leaving the RF field region the neutron spin will be again in the initial precession plane defined by $\vec{B}_0$. The RF field amplitude is to be set to

$$B_1 = -2\frac{\pi v_n \cos\chi}{\gamma_n L_{RF}}. \tag{3.4}$$

In case of a divergent neutron beam, Eq. (3.3) is only fulfilled for the average propagation direction of the neutrons. The part of the beam with a deviation of the average propagation direction and hence a different incident angle on the

magnetic-field borders $\chi + \Delta\chi$ will not exactly perform a π precession and not coincide with the initial precession plane any more, i.e. a spin component in the direction of the B_0 magnetic-field will occur. The precession angle around the axis of B_1^+ is

$$\frac{\cos(\chi + \Delta\chi)}{\cos\chi}\pi\,. \tag{3.5}$$

With increasing χ this effect becomes more dominant.

3.1.2.2 **Impact on the Neutron Spin**

To describe the effect of the NRSE in detail (Fig. 3.3), it is convenient to perform a transformation to a rotating coordinate system in which the rotation of the B_1^+ field and also the Larmor spin precession in the B_0 field, see Eq. (3.1), are compensated. The surface normal of the magnetic-field border is inclined about χ with respect to the average incident neutron beam. A neutron enters the B_0 field region with an arbitrary phase shift ψ with respect to the phase of the circular polarised field. Within the B_0 field region the phase remains constant. In the RF field region the phase gets inverted to -ψ (by a π precession). In the area between the two B_0 fields the spin is precessing with respect to the rotating coordinate system about $-\omega_1/v_n(L - L_1/\cos\chi)$. In the second NRSE coil, the spin does not precess in the B_0 magnetic field (in the rotating coordinate system). The second B_1 field then leads to a phase inversion from $-\psi - \omega_1/v_n(L - L_1/\cos\chi)$ to $\psi + \omega_1/v_n(L - L_1/\cos\chi)$. The phase change is thus

$$\psi + \frac{\omega_1}{v_\mathrm{n}}\left(L - \frac{L_1}{\cos\chi}\right) - \psi = \frac{\omega_1}{v_\mathrm{n}}\left(L - \frac{L_1}{\cos\chi}\right), \tag{3.6}$$

which is independent of the initial phase shift ψ. The transformation from the rotating coordinate system back to the laboratory system gives rise to $\omega_{1\square}/v_\mathrm{n}(L + L_1/\cos\chi)$ precessions while the neutron is passing the double coil set-up. The total phase shift of the neutron spin is thus

$$\frac{\omega_1}{v_\mathrm{n}}\left(L - \frac{L_1}{\cos\chi}\right) + \frac{\omega_1}{v_\mathrm{n}}\left(L + \frac{L_1}{\cos\chi}\right) = 2\frac{\omega_1}{v_\mathrm{n}}L. \tag{3.7}$$

This phase shift is twice larger than in the conventional constant magnetic-field set-up for the same field B_0. The length of the effective magnetic-field region is to be measured from the middle of each B_0 coil.

The position and length of the B_1 magnetic-field in the area of the B_0 field has no impact on the phase of the neutron spin.

The enhancing effect on the spin-echo length can be increased by using more NRSE coil pairs [Gähler'88], see Fig. 3.3c). The magnetic-field in the first and the second DC coil pair have opposite direction and in our case the coil pair is rotated as a whole to set the angle χ between the magnetic-field border normal and the average incident neutron beam direction. The effect on the polarisation can be calculated in the rotating coordinate system, similar to the single coil case. The spin enters with an arbitrary phase shift of ψ with respect to the B_1^+ field in the first DC field region. In the RF field, the spin is inverted to -ψ. At the end of the gap between the two first NRSE coils of length L_2 the phase will be $-\psi - \omega_1/v_n(L_2/\cos\chi)$. In the second and third DC magnetic region, the field is oriented in opposite direction with respect to the fist and fourth DC magnetic region. The neutron spin precesses in the opposite direction. The phase change of the neutron spin will be treated in the coordinate system compensating the Larmor precession in this region and afterwards the transformation back in the first rotating coordinate system will be performed. In the second RF field region the phase of the neutron spin gets inverted to $\psi + \omega_1/v_n(L_2/\cos\chi)$. The middle field free region leads to a phase change of $\omega_1/v_n(L - 2L_1 - L_2/\cos\chi)$. The third RF coil leads again to a phase inversion to $-\psi - \omega_1/v_n(L - L_2/\cos\chi)$. The transformation back to the first rotating coordinate system leads to a phase change of $-2\omega_1/v_n(L - L_2/\cos\chi)$, since the relative angular velocity of the two rotating coordinate systems is $2\omega_1$. Hence the phase at the end of the third NRSE coil is $-\psi - \omega_1/v_n(3L - 2(L_1 + L_2)/\cos\chi)$. The gap between the last NRSE coils leads to a phase of $-\psi - \omega_1/v_n(3L - (2L_1 + 3L_2)/\cos\chi)$, which is then inverted in the last RF coil and amounts to $\psi + \omega_□/v_n(□3L - (2L_1 + 3L_2)/\cos\chi)$. The transfer to the laboratory frame ($\omega_□/v_n(□L + (2L_1 +$

$L_2)/\cos\chi))$ leads to a final phase of $\psi + \omega_1/v_n(4L - L_2/\cos\chi))$. The total change of the neutron spin precession is thus

$$\psi + \omega_1/v_n\left(4L - \frac{L_2}{\cos\chi})\right) - \psi = 4\frac{\omega_1}{v_\mathrm{n}}\left(L - \frac{L_2}{2\cos\chi}\right), \tag{3.8}$$

and the effective length is

$$L_{\mathrm{eff,BS\ NRSE}} = L - \frac{L_2}{2\cos\chi}. \tag{3.9}$$

If L_2 << L, the effective length can be approximated to

$$L_{\mathrm{eff,BS\ NRSE}} \approx L\,. \tag{3.10}$$

The bootstrap NRSE set-up is hence equivalent to a parallelogram shaped magnetic-field region of length $4L - 2L_2/\cos\chi$ or approximately $4L$ in the case of L_2 << L. One constraint is an additional depolarisation in case of a divergent beam originating from non-exact π flips in the RF coils as described by Eq. (3.5). The angular deviation of the initial precession plane leads to a depolarisation. In case the effect is adding up in each coil, it can amount to

$$P_{\mathrm{loss}}^{n\ \mathrm{RF}} = 1 - \cos\left[2n\left(1 - \frac{\cos(\chi + \Delta\chi)}{\cos\chi}\right)\right] \tag{3.11}$$

for n RF coils, where in a bootstrap set-up $n = 8$. Taking this additional depolarisation into account Eq. (2.22) can be applied to yield the phase of a neutron spin. In Fig. 3.4 the influence on the loss of polarisation due to the imperfect π precession in eight RF coils in the bootstrap set-up is plotted for a part of the neutron beam with a deviation of 0.5°, 1°, and 1.14° of the average propagation direction.

In the bootstrap set-up (Fig. 3.3c), the adjacent DC coils have B_0 magnetic-fields in opposite direction, with the consequence that the stray fields of the two neighbouring DC coils cancel each other in first approximation outside of each B_0 coil pair. The spin-echo length for the NRSE bootstrap set-up is

$$Y_{\mathrm{BS\ NRSE}}^{\mathrm{SE}} = -\frac{2m_\mathrm{n}\gamma_\mathrm{n}}{\pi h} L_{\mathrm{eff,BS\ NRSE}} \lambda^2 B_0 \tan\chi\,. \tag{3.12}$$

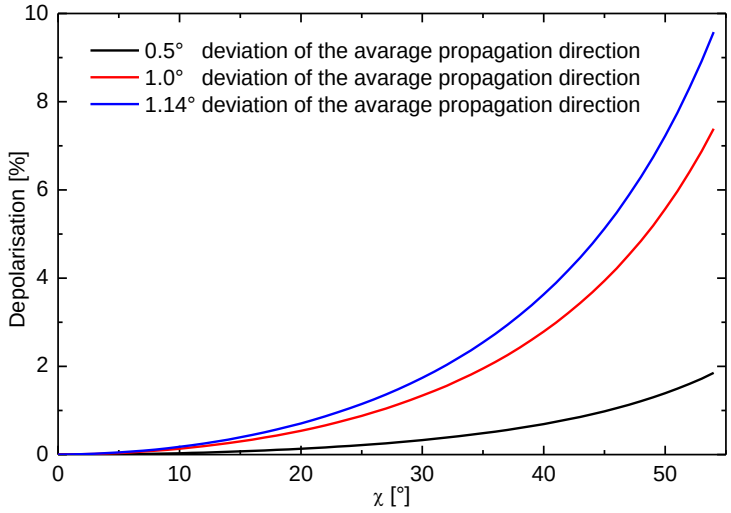

Fig. 3.4: Eq. (3.3) is only fulfilled for the average propagation direction. In the graph the maximal loss of polarisation due to $n = 8$ RF coils in the set-up is plotted as calculated by Eq. (3.11) for the part of the beam with a deviation of 0.5° (black line), 1° (red line), and 1.14° (blue line) in the x-y-plane.

3.1.2.3 **NRSE Set-Up**

The NRSE set-up is depicted in Fig. 3.5. After monochromatisation, the average neutron beam propagates in the x-z-plane and will be polarised in y-direction at the polariser (see Section 3.2.1). The coupling coil (see Section 3.2.4) with its vertical magnetic-field leads to a $\pi/2$ rotation of the neutron spin in the vertical plus or minus z-direction, depending on the sign of the magnetic-field in the coupling coil. From here on until the next coupling coil before the spin analyser, the neutron beam path is shielded by a μ-metal housing. Before and after being reflected on the sample, the neutrons pass two pairs of NRSE bootstrap coils with the DC field pointing in the horizontal direction and inclined about the angle χ with respect to the y-direction. The RF field always points in the vertical direction. At the second coupling coil, the z-component of the neutron spin is rotated in y-direction. The analyser (see Section 3.2.2) filters the spin component in -y-direction and the transmitted neutrons with spin component in y-direction are detected by the two dimensional detector (see Section 3.2.5).

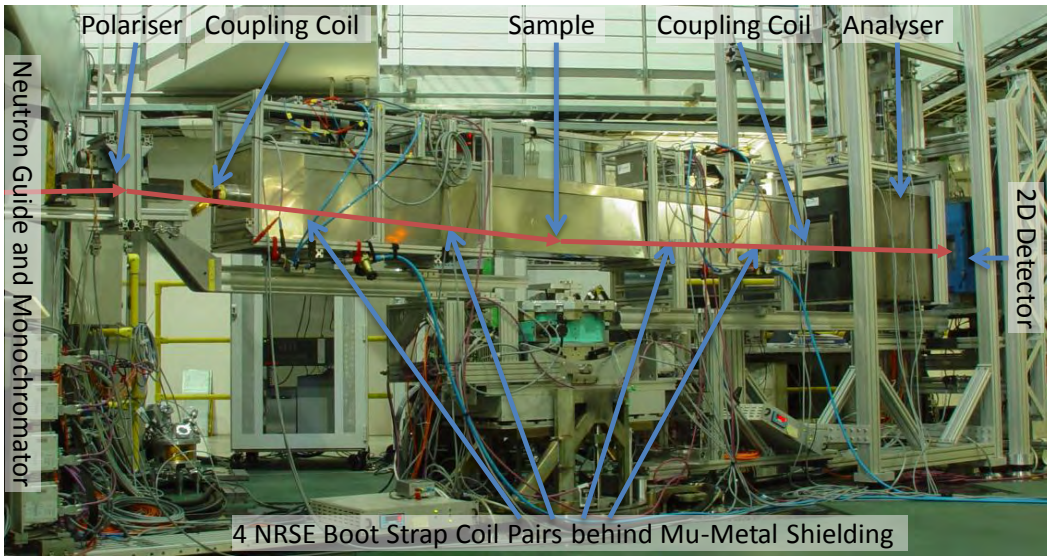

Fig. 3.5: NRSE bootstrap set-up at the instrument *N-REX*$^{+}$, FRM II. The neutron flight path is indicated with the red arrow.

3.1.2.4 **NRSE Coil Assembly**

Both the DC and RF coil are made from aluminium wire, in order to minimise the absorption and the small angle scattering. The isolation of the wire of the RF coils (diameter: 0.91 mm) is made of thin Kapton^{TM}, that of the DC coils (diameter: 1.38 mm) of enamel. The dimensions (length x width x thickness) of the RF coils are 81 mm x 178 mm x 16 mm, and those of the DC coils are 200 mm x 200 mm x 30 mm. The angle χ between the neutron beam direction and the surface normal of the coils, as depicted in Fig. 3.6, can be varied between -5° and +54° with a minimum clearance due to geometric effects. The limitation arises from the single RF coil, the arrangement of the two RF coils, and the μ-metal shielding, which is mounted around the coil pair to limit the stray fields. The spin precession plane is perpendicular to the DC field B_0 and rotates together with the coils as a function of χ. In the μ-metal shielding, two DC coils are mounted horizontally with opposite magnetic-field direction in one unit in which the DC fields were shorted by μ-metal pieces in order to minimize external stray fields and increase the field homogeneity. The homogeneity of the RF coil field is improved by a second wire layer covering about 9% of the full coil length at the ends of each coil. In one coil assembly there is a gap L_2 = 2 mm between the B_0 field regions. The four compact coil assemblies with shielding, electric leads, and air cooling are mounted on

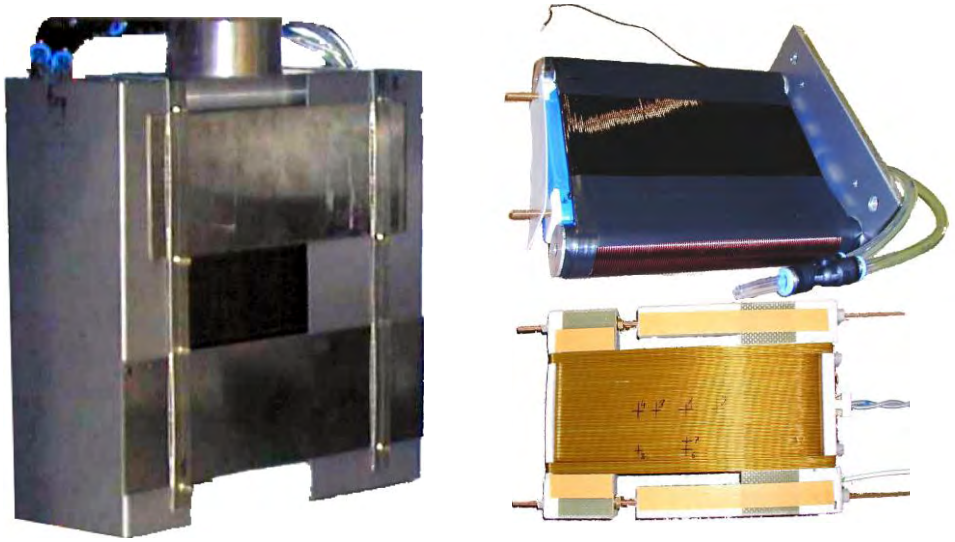

Fig. 3.6: From left to right, top to bottom: One pair of NRSE bootstrap spin-echo coils with μ-metal shielding, B_0 coil with B_1 coil inside (only the supporting rods of the B_1 coil are visible), B_1 coil. The coils were constructed in the framework of the Diploma Thesis of R. Maier [Maier'04].

standard motor-driven rotation stages, and one coil pair assembly in each arm is coupled to a motorized linear stage for adjustment and variation of the effective length of the precession device. All rotation and translation stages and motors are positioned outside of the magnetic shielding. Each DC coil is cooled by an airstream from the interior of the coil trough gaps between the wires. The borders of the field regions are (nearly exactly) defined by current sheets, so that the condition of perfectly flat field borders as required for SERGIS can be very well fulfilled. The coils were constructed in the framework of the Diploma Thesis of Ralf Maier [Maier'04].

In the NRSE-SERGIS set-up with bootstrap configuration described above, four pairs of resonance coils (see Fig. 3.6) are in the neutron path. At a neutron wavelength of 5.5 Å the entire set of coils reduces the primary beam intensity by about 75 %.

There are three possibilities to change the spin-echo length: First, the B_0 field can be ramped and the amplitude and frequency of the RF field accordingly (χ and L_{eff} are kept constant). Second, the effective length of the precession device can be changed, which has to be done very accurately in both spin-echo arms (χ and B_0 are kept constant). Or third, each coil can be rotated with respect to the neutron

beam (L_{eff} and B_0 are kept constant). Experimentally it is easier to change the incident angle of the neutron beam on the magnetic-field borders (third method) as will be shown in the following. The third method allows to set the spin-echo length to relatively small values, under the condition that $q_{\mathrm{x}} \ll q_{\mathrm{y}} \tan \chi$ is fulfilled (at a wavelength of λ = 5.5 Å this yields a lower limit in spin-echo length of approximately Y^{SE} = 20 nm). Then Eq. (2.25) can be approximated by Eq. (2.28). The other two methods are more limited in this respect.

The eight radio-frequency coils are connected serially to each other and are driven by a single amplifier, which is connected to a RF decade generator with adjustable frequency and amplitude. A high-voltage capacitor is connected to each pair of RF-coils for electrical resonance. The RF current output is monitored by a low-inductance 0.1 Ω resistor, a digital voltmeter, and an oscilloscope. Likewise, the eight coils for the static magnetic fields are also connected serially and were driven by a single DC current source. By these means, a constant frequency and magnetic-field amplitude could be insured in all coils. The static magnetic-field B_0 achievable with this NRSE system was limited to about 80 Gauss by the efficiency of the applied air-cooling. Within this B_0 range, the radio-frequency field B_1 could be easily adjusted to B_0 according to the resonance conditions Eq. (3.1), for a neutron wavelength of λ = 5.5 Å, i.e. the radio frequency output was limited neither by the power amplifier nor by the cooling system. The B_0 fields where set to a value as high as the cooling capacity allowed.

3.1.2.5 **Real Space Resolution with the NRSE Set-Up**

The real space resolution is on the one hand limited by the divergence of the incident beam (Section 2.4.3) and on the other hand, by the maximal transmitted scattering angle by the set-up which results in a transmitted q_{max}. In this section, the influence of the instrumental limitation by the NRSE set-up will be discussed.

In the case of the NRSE set-up the maximal transmitted scattering angle is a function of inclination of the magnetic-field borders χ. In the cross section of the neutron beam the coil has a rectangular shape. The free path width for the neutron beam is limited as depicted in Fig. 3.4. In reciprocal space, the maximal

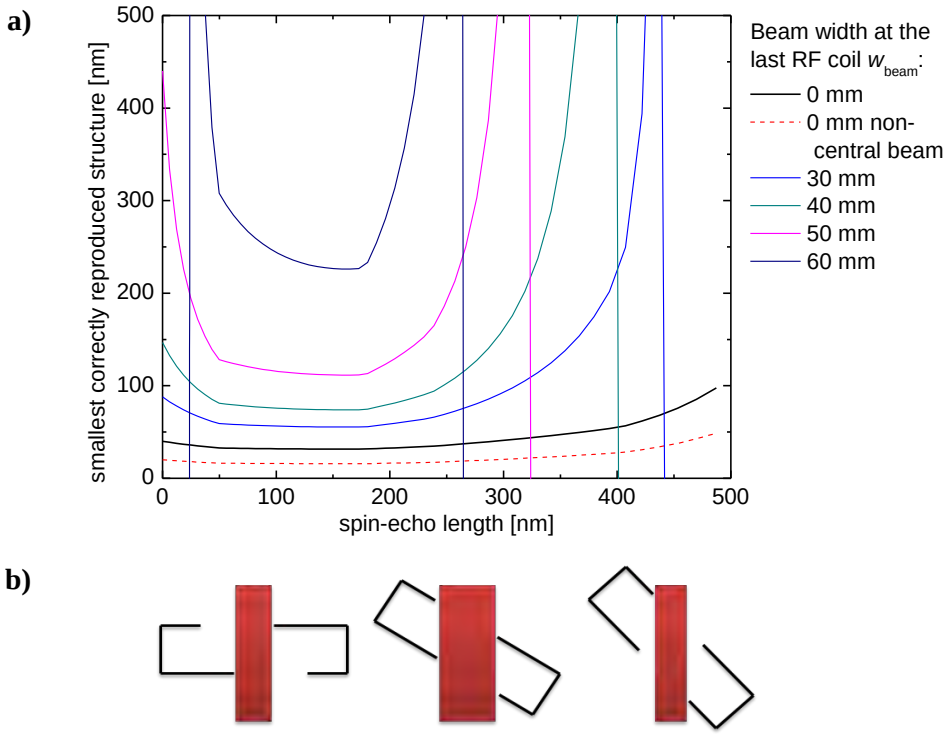

Fig. 3.7: a) Resolution limit in real space. The curves show the scattering of the smallest correlation on the sample which is 100% transmitted through the instrument for different direct beam widths at the last NRSE coil pair. It is assumed that the beam is aligned in the centre of the NRSE coil pairs (full line), and from one extremity of the first slit to the opposite extremity of the second slit (dashed line). The spin-echo length is calculated for $L_{\mathrm{eff}} = 0.5$ m and $B_0 = 0.05$ T as a function of $Y^{\mathrm{SE}}(\chi)$. The distance of the sample position to the last NRSE coil pair is $d_1 = 2000$ mm. The width of zero stands for a negligible width. b) Sketch of the μ-metal shielding of the coils reducing the free path width at different inclination χ.

momentum transfer q_{max} is a function of the beam size at the position of the last coil.

$$q_{\mathrm{max}} = \frac{4\pi}{\lambda}\sin\left(\frac{1}{2}\arctan\left(\frac{w_{\mathrm{eff.coil}} - w_{\mathrm{beam}}}{2d_1}\right)\right), \qquad \textbf{(3.13)}$$

where $w_{\mathrm{eff.coil}}$ is the horizontal free path width of the last coil pair due to limitation of the μ-metal shielding, w_{beam} the width of the non scattered beam at this position, and d_1 the distance from the sample position to the last coil pair. In real space q_{max} can be expressed as the smallest correctly reproduced structure

$$l_{\mathrm{min}} = \frac{\lambda}{2}\arcsin\left[\frac{1}{2}\arctan\left(\frac{w_{\mathrm{eff.coil}} - w_{\mathrm{beam}}}{2d_1}\right)\right]. \qquad \textbf{(3.14)}$$

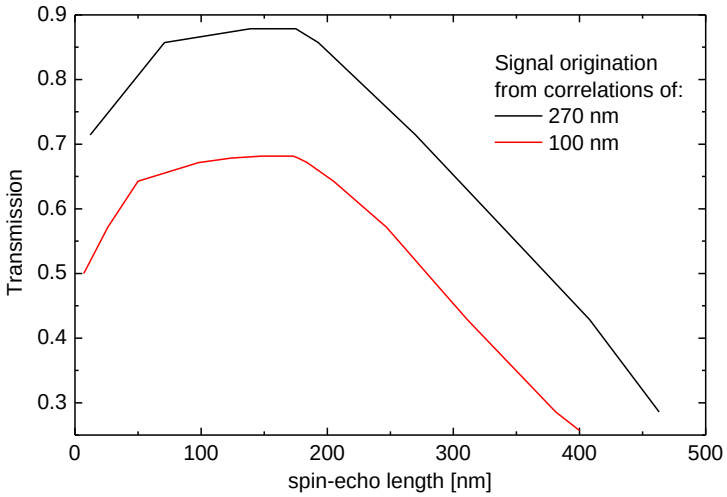

Fig. 3.8: Instrumental transmission of a 70 mm wide beam at the last RF coil as a function of the spin-echo length. The spin-echo length is calculated for L_{eff} = 0.5 m and B_0 = 0.05 T as a function of $Y^{\mathrm{SE}}(\chi)$.

The smallest structures of length l_{min} whose scattering signal is fully transmitted through the instrument is plotted in Fig. 3.7 for different width of the unscattered neutron beam at the position of the last NRSE coil pair. For the calculation, the beam was assumed as centred with its main axes parallel to the spin-echo arms (full curve) besides one simulation where the beam was assumed to be situated at one extremity of the first slit and at the opposite extremity of the second slit to calculate which scattering signal are completely blocked by the instrument (dashed curve). All full curves depicted show the limit where 100% of the scattered signal is transmitted, below a fraction of the signal is absorbed. The vertical lines in the plot mark the spin-echo length where the direct beam is of identical size as the clearance of the NRSE coils.

Assuming a homogeneous angular intensity distribution in the limits of the beam divergence at the position of the sample the transmission of a signal originating from a structure with a certain periodicity can be calculated. In Fig. 3.8 this is shown for a structure with 100 nm and 270 nm periodicity. The assumption that the angular distribution of the intensity of the direct beam at the sample position is constant is not the case in a real set-up it might resemble more a Gaussian distribution, so this calculation is only elucidating the problem, but cannot be used for the mathematical treatment of this effect. By this in detail unknown

attenuation of small frequency Fourier components the decay of correlations which are attenuated cannot be measured with this set-up.

3.1.3 Birefringent Magnetic Prisms (Triangular Coils)

R. Pynn suggested triangular coils to mimic the parallelogram shaped precession devices [Pynn'08a]. The triangular-coil set-up is a less complex solution for SERGIS than the NRSE set-up and will be introduced in the following sections.

3.1.3.1 Impact on the Neutron Spin

The triangular coils are arranged that they act in analogy to optical prisms. The phase change of a neutron spin traversing a triangular-coil set-up, as depicted in Fig. 3.11, can be calculated as a sum of the phase change in three overlapping regions. Two magnetic-field regions with rectangular field borders and one magnetic-field region with inclined field borders and an opposite magnetic-field direction with twice the magnitude, as depicted in Fig. 3.9, are required to simulate the triangular set-up. The phase accumulated in each of the field regions can be calculated using Eq. (2.22) and summed up to yield the total phase change

$$\begin{aligned}\varphi \;=& -\frac{m_\mathrm{n}\gamma_\mathrm{n}}{\pi h} BL\lambda^2 \left(q_\mathrm{x} + q_\mathrm{y}\tan\chi - 2\tilde{k}_{\mathrm{i,z}}\frac{\tan\eta}{\cos\chi}\right) \\ &\times \frac{1}{\cos\eta}\left[\cos\eta + \frac{\tilde{k}_{\mathrm{i,x}}}{\bar{k}_\mathrm{i}} + \frac{\tilde{k}_{\mathrm{i,y}}}{\bar{k}_\mathrm{i}}\tan\chi + \left(\sin\eta + \frac{\tilde{k}_{\mathrm{i,z}}}{\bar{k}_\mathrm{i}}\right)\frac{\tan\eta}{\cos\chi}\right]^{-1} \\ &\times \left[\cos\eta + \frac{\tilde{k}_{\mathrm{i,x}} + q_\mathrm{x}}{\bar{k}_\mathrm{i}} + \frac{\tilde{k}_{\mathrm{i,y}} + q_\mathrm{y}}{\bar{k}_\mathrm{i}}\tan\chi + \left(\sin\eta - \frac{\tilde{k}_{\mathrm{i,z}}}{\bar{k}_\mathrm{i}}\right)\frac{\tan\eta}{\cos\chi}\right]^{-1} \\ &+ \frac{m_\mathrm{n}\gamma_\mathrm{n}}{\pi h} BL\lambda^2\left(q_\mathrm{x} - 2\tilde{k}_{\mathrm{i,z}}\tan\eta\right) \\ &\times \frac{1}{\cos\eta}\left[\cos\eta + \frac{\tilde{k}_{\mathrm{i,x}}}{\bar{k}_\mathrm{i}} + \left(\sin\eta + \frac{\tilde{k}_{\mathrm{i,z}}}{\bar{k}_\mathrm{i}}\right)\tan\eta\right]^{-1} \\ &\times \left[\cos\eta + \frac{\tilde{k}_{\mathrm{i,x}} + q_\mathrm{x}}{\bar{k}_\mathrm{i}} + \left(\sin\eta - \frac{\tilde{k}_{\mathrm{i,z}}}{\bar{k}_\mathrm{i}}\right)\tan\eta\right]^{-1}\end{aligned} \tag{3.15}$$

in a triangular coil set-up. The effective length is to be measured from the centre of the triangular-coil pairs. With respect to a parallelogram shaped precession region as described by Eq. (2.22), the dependency of the neutron spin precession on q_x and $\tilde{k}_{\mathrm{i,x}}$ is reduced for the triangular shaped set-up. The field integral in one

coil pair is zero and stray fields cancel each other in a first approximation because of the symmetry of the set-up.

The spin-echo length of this set-up is

$$Y^{\mathrm{SE}}_{\mathrm{triangular}} = -\frac{m_{\mathrm{n}}\gamma_{\mathrm{n}}}{\pi h} L\lambda^2 B \tan\chi. \qquad \textbf{(3.16)}$$

3.1.3.2 **Triangular-Coil Assembly**

The triangular coils are wound from aluminium wire, in order to minimise the absorption and the small angle scattering. The isolation of the wire of the coils

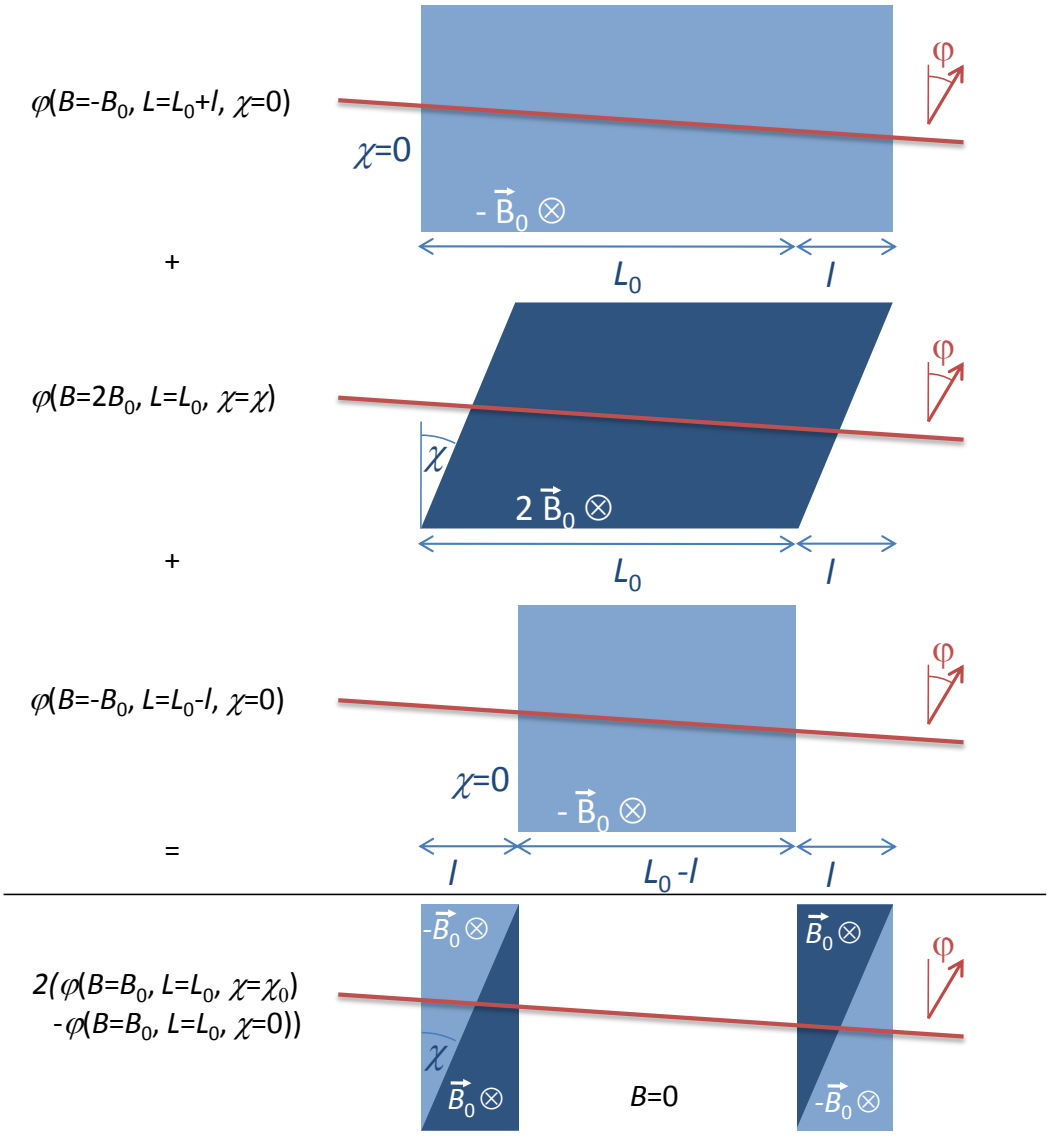

Fig. 3.9: Neutron spin phase accumulated in a triangular coil set-up.

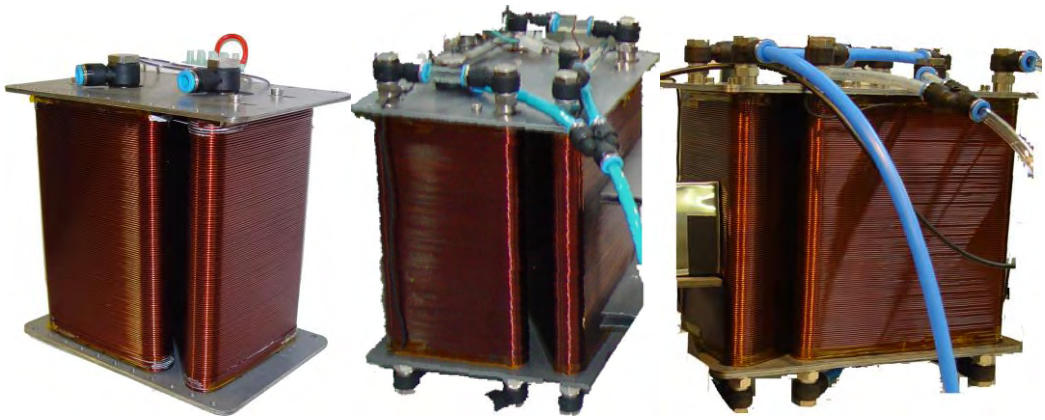

Fig. 3.10: Triangle coil pair with $\chi = 45°$, 30°, and 60°. The neutron beam is passing from left to right entering and leaving the coil pair through the side without the gap. The blue connectors on top serve for the air-cooling and additional water cooling in case of the 30° and 60° coils.

(diameter: 1.38 mm) is made of enamel. During this work two sets of triangle coils were built, which allow three different set-ups. The construction is made out of three supporting brass rods of 20 mm diameter. The dimensions (length x width x height) of the coils are 100 mm x 100 mm x 200 mm ($\chi = 45°$) (see Fig. 3.10), 100 mm x 200 mm x 200 mm ($\chi = 30°$), and 200 mm x 100 mm x 200 mm ($\chi = 60°$). To allow for maximal horizontal path width of the neutron beam, the coils are aligned in the direction of the beam as depicted in Fig. 3.11. The 30° / 60° coils can be mounted in two different ways to form an angle of 30° or 60°, respectively. The gap between the coils has to be kept as small as possible to maintain a well-defined magnetic-field and on the other hand large enough to allow cooling of the coils. A gap of few millimetres proved to be most suitable. In the two coils of a coil pair, a magnetic-field with opposite direction is applied. In each coil pair, the magnetic fields are shorted by 10 layers of 0.5 mm thick transformer sheet (silicon iron) at the top and bottom of the coil pair in order to minimise external stray fields and increase the field homogeneity. In a first approximation, the remaining stray field of both coils cancels outside of the coil pair.

The minimal accessible structure size depends on the width of the coils, which is limiting the scattering angle and can be obtained as described in Section 3.1.1.2.

The dissipated thermal power of a triangular-coil is

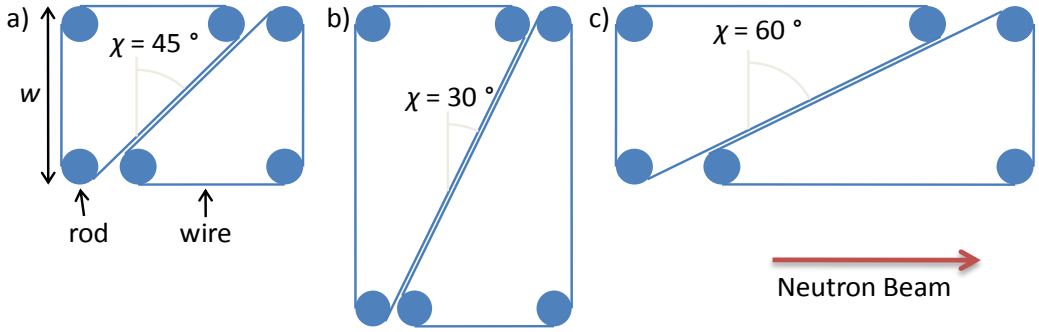

Fig. 3.11: Top view of a triangular coil pair: a) $\chi = 45°$ b) $\chi = 30°$ c) $\chi = 60°$. The neutron propagation direction is from left to right. The short non diagonal sides are 100 mm, the long non diagonal sides are 200 mm and the diameter of the rods is 20 mm. The free horizontal path width for the neutron beam is 60 mm and 160 mm, respectively. The coils with $\chi = 30/60°$ are identical, but mounted differently in a pair to allow for maximum clearance.

$$P_{\text{coil}} = I^2 \frac{\rho}{A} n_{\text{windings}} \cdot l_{\text{circumference}} = I^2 \frac{\rho}{A} n_{\text{windings}} w \left(1 + \tan\chi + \frac{1}{\cos\chi}\right), \tag{3.17}$$

with $\rho = 2.82 \ \ 10^{-8} (1 + 0.0039°\text{C}^{-1} (T - 20°\text{C}))\ \Omega\text{m}$ the specific resistance of aluminium, w the width of the coil along the wire and perpendicular to the beam direction, the current I, n_{windings} the number of windings of the wire in the coil, the circumference of the coil $l_{\text{circumference}}$, the voltage U, and the area cross section of the wire A.

Since B is proportional to I, the dissipated thermal power as a function of the spin-echo length is proportional to

$$P_{\text{coil}} \sim \left(\frac{Y^{\text{SE}}}{L\lambda^2 \tan\chi}\right)^2 \rho w \left(1 + \tan\chi + \frac{1}{\cos\chi}\right). \tag{3.18}$$

For constant temperature, e.g. ideal cooling, the heat dissipation for triangular coils with different χ, but identical w is plotted in Fig. 3.12 normalised to the heat dissipation of a 45° coil for a given spin-echo length Y^{SE}.

The heat transfer away from the coil occurs by air-cooling and in the case of the second version (30°/60° coils) in addition by water-cooling of the supporting rods. The heat dissipation due to the air-cooling is proportional to the surface of the

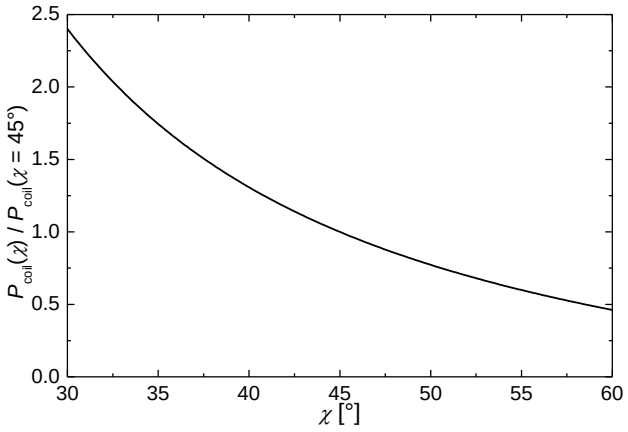

Fig. 3.12: Dissipated thermal power as a function of χ, normalised to the dissipated thermal power of a 45° coil and constant temperature to access a given spin-echo length Y^{SE}.

coils. Considering only the air-cooling, the temperature of the coil is independent of its circumference or width, since the increase in heat dissipation (3.18) and cooling power cancel each other. In a triangular-coil pair, the cooling of the diagonal face of a triangular-coil, which is mounted adjacent to the other coil, is most crucial. Hence, if high magnetic fields should be reached the gap between the coils should allow a minimal airstream. By water cooling of the supporting rods the cooling efficiency of the coils can be increased significantly. The effect of the water-cooling becomes slightly less dominant for larger coils since a smaller fraction of the wire is in contact with the supporting rods, although the limiting factor of the water-cooling is the limited heat transfer through the isolation of the wire and the limited heat conduction in long and thin wires.

For an effective air-cooling, air is blown in the coils through a hole in the top plate and exhausted between the wires. The water-cooling in the 30°/60° coils is done by pumping 20°C chilled water through the cooling channels located in the supporting rods of the coil.

To prevent overheating, the average temperature of the coils is monitored by the temperature dependent resistance of the aluminium wire. The temperature was approximated by

$$T \approx 300\ \mathrm{K} \frac{U}{I} \frac{I_{300\mathrm{K}}}{U_{300\mathrm{K}}}, \qquad \textbf{(3.19)}$$

and monitored through the whole experiment. This estimation can be justified by the thermal resistance change of the wires, supposed that the wire of the coils were made of unalloyed or low-alloyed aluminium, i.e. small resistance at low temperatures. The temperature has been double-checked with an infrared thermometer. The average temperature value corresponds to the estimation, whereas some local deviation due to different airflow close to the coils where measured. The temperature determination only serves to avoid overheating, the temperature threshold was set with some additional margin, hence a modest temperature measurement accuracy is sufficient. The temperature threshold was chosen in the experiment to 90°C.

3.1.3.3 **Triangular-Coil Set-Up**

The triangular-coil set-up, as depicted in Fig. 3.13, will be introduced in this section. At the polariser, the neutron beam is polarised in y-direction and if necessary, the spin will be flipped by π at the spin flipper (see Section 3.2.3). To insure an ideally adiabatic transition at the triangular coils, adjacent to the triangular coils at the beginning and the end of both spin-echo arms a coupling coil is mounted (see Section 3.2.3). The magnetic-field transition from the coupling coil to the triangular-coil might be adiabatic or ideally non-adiabatic, but in both cases the *y*-component of the spin is conserved. The first and the last coupling coil, in the neutron propagation direction, have a magnetic-field oriented perpendicular to the magnetic-field in the triangular coils and parallel to the initial polarisation in *y*-direction. The coupling coils close to the sample position are oriented with a magnetic-field parallel to one adjacent triangle coil and anti-parallel to the other adjacent triangular coil. All four triangular coils are mounted as depicted in Fig. 3.14. At the sample position, a non ferromagnetic vacuum chamber can be mounted. The leaking magnetic-field of the coupling coils will act as a weak guide field. There is no influence of weak external magnetic fields, e.g. the earth magnetic field, at the sample position due to the adiabatic magnetic-field transition. The size of the triangular coils has to be adapted on the size of the neutron beam, notably the last coupling coil has to be large enough to insure the passage of the divergent and scattered neutron beam. A pair of slits directly before

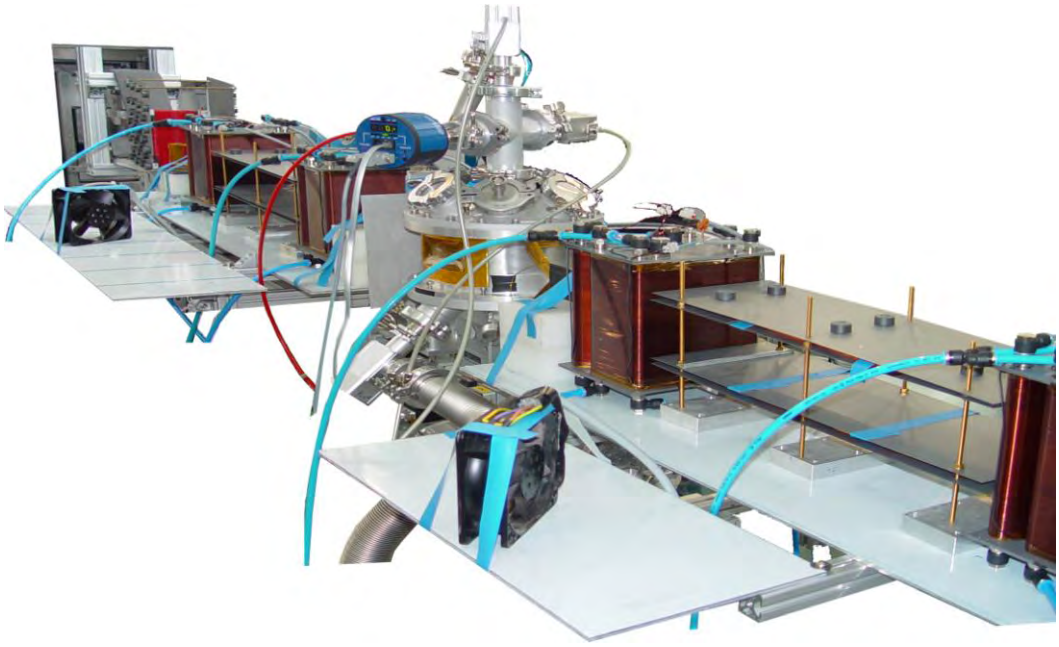

Fig. 3.13: Triangular coil set-up. The neutron beam is monochromatised and polarised before it passes the spin-flipper (red coil in the rear left of the picture). Each spin-echo arm consists of two 30° triangular coil pairs (dark red). The sample chamber is situated in the centre of the image. One of four coupling coils at the beginning and at the end of both spin-echo arms is visible (yellow coil after the sample chamber). The analyser and the detector situated on the right of the picture are not shown. The fans provide an additional air stream at the coils for cooling.

the sample chamber reduces the beam size to fit the dimensions of the sample. In addition, small angle scattering from the coils before the slits is mostly absorbed.

The ideally flux free regions in the first and second spin-echo arm are shielded by a vertical guide field with magnetic-field vectors parallel to the magnetic-field in the adjacent triangular coils, see Fig. 3.14. Both guide fields being in opposite direction and with perpendicular field borders with respect to the mean neutron beam. The magnetic induction in the guide fields $B_{\text{guide field}}$ is low with respect to the maximal field in the triangular coils to insure a weak dependence on inelastic scattering and scattering in the x-direction, as well as to minimise the stray fields. Eq. (3.15) then becomes

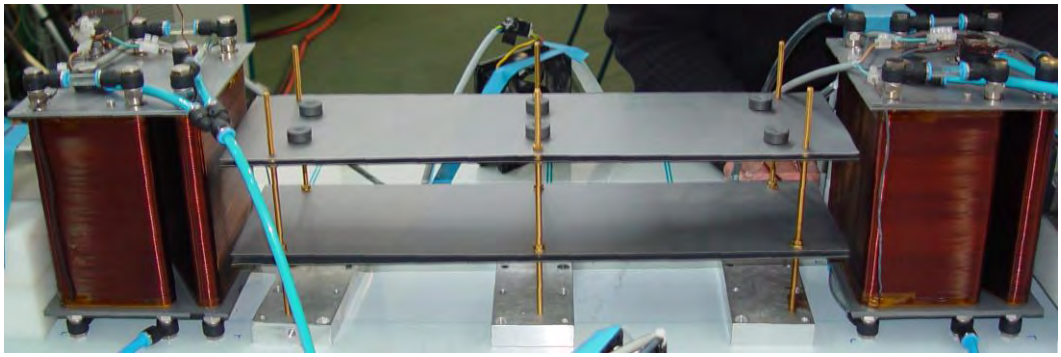

Fig. 3.14: 30° triangular coils spin-echo arm: One spin-echo arm with two pair of triangular coils and a guide field between them is depicted. The triangular coils are cooled by air in a central nozzle and water cooled through their three supporting rods.

$$
\begin{aligned}
\varphi \; = & -\frac{m_{\mathrm{n}}\gamma_{\mathrm{n}}}{2\pi h} BL\lambda^2 \left(q_{\mathrm{x}} + q_{\mathrm{y}} \tan\chi - 2\tilde{k}_{\mathrm{i,z}} \frac{\tan\eta}{\cos\chi}\right) \\
& \times \frac{1}{\cos\eta} \left(\cos\eta + \frac{\tilde{k}_{\mathrm{i,x}}}{\bar{k}_{\mathrm{i}}} + \frac{\tilde{k}_{\mathrm{i,y}}}{\bar{k}_{\mathrm{i}}} \tan\chi + \left(\sin\eta + \frac{\tilde{k}_{\mathrm{i,z}}}{\bar{k}_{\mathrm{i}}}\right) \frac{\tan\eta}{\cos\chi}\right)^{-1} \\
& \times \left(\cos\eta + \frac{\tilde{k}_{\mathrm{i,x}} + q_{\mathrm{x}}}{\bar{k}_{\mathrm{i}}} + \frac{\tilde{k}_{\mathrm{i,y}} + q_{\mathrm{y}}}{\bar{k}_{\mathrm{i}}} \tan\chi + \left(\sin\eta - \frac{\tilde{k}_{\mathrm{i,z}}}{\bar{k}_{\mathrm{i}}}\right) \frac{\tan\eta}{\cos\chi}\right)^{-1} \\
& + \frac{m_{\mathrm{n}}\gamma_{\mathrm{n}}}{\pi h} \left(BL - B_{guide\ field}(L - l)\right) \lambda^2 \left(q_{\mathrm{x}} - 2\tilde{k}_{\mathrm{i,z}} \tan\eta\right) \\
& \times \frac{1}{\cos\eta} \left(\cos\eta + \frac{\tilde{k}_{\mathrm{i,x}}}{\bar{k}_{\mathrm{i}}} + \left(\sin\eta + \frac{\tilde{k}_{\mathrm{i,z}}}{\bar{k}_{\mathrm{i}}}\right) \tan\eta\right)^{-1} \\
& \times \left(\cos\eta + \frac{\tilde{k}_{\mathrm{i,x}} + q_{\mathrm{x}}}{\bar{k}_{\mathrm{i}}} + \left(\sin\eta - \frac{\tilde{k}_{\mathrm{i,z}}}{\bar{k}_{\mathrm{i}}}\right) \tan\eta\right)^{-1} .
\end{aligned}
\tag{3.20}
$$

To reduce the small angle scattering the direct beam is blocked after the sample position directly before the second spin-echo arm by a cadmium plate. Only a small tail of the direct beam with the intensity in the order of the Yoneda peak (see Section 4.2) might pass over the cadmium sheet to serve as a reference beam for the polarisation analyses. Four pairs of spin-echo coils and four Forte coils (Section 3.2.4) have a transmission of 65% and increase the background by about 200%. The background at the detector is mainly produced at the coils after the sample position since the slit before the sample position is shielding most of the background originating from the coils upstream of the sample position. The attenuation of the signal is influenced by all coils. In Fig. 3.15 a comparison of the

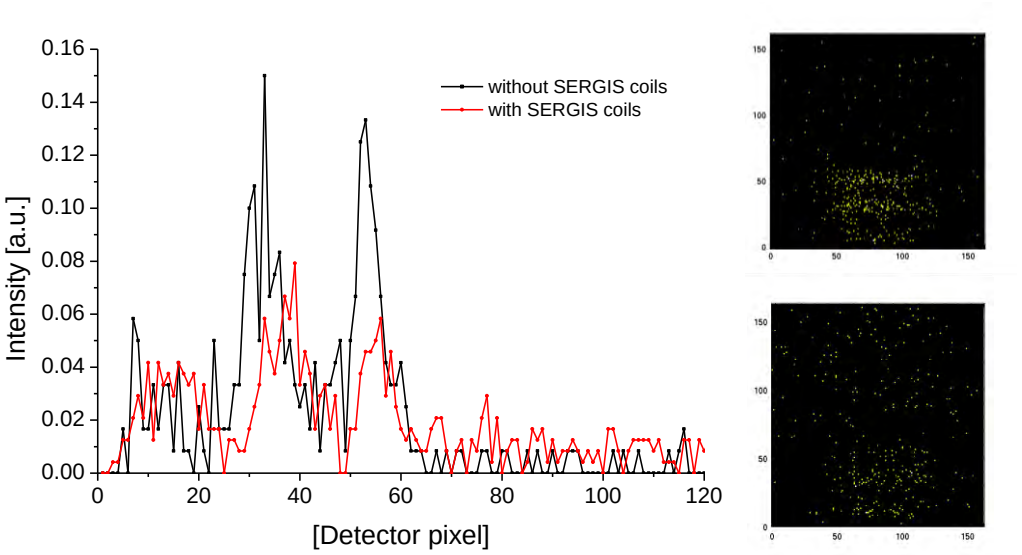

Fig. 3.15: Specular reflected beam and Yoneda peak of a spin polarised neutron beam. Comparison with and without SERGIS coils (triangular and Forte coils). On the left side: vertical line cut of columns 42 to 122, the intensity is normalised in seconds. At pixel 53 the specular reflected beam is visible and at pixel 33 the Yoneda peak is visible. At detector pixel 5 to 25 the background is elevated due to the direct beam. Below detector pixel 5 the signal is shielded. On the left: Detector images of both scenarios with 120s counting time. The top image was taken without SERGIS coils and the bottom image with Forte and triangular coils in the path of the neutron beam. A decrease of the peak intensities and increase of the background with the SERGIS set-up is visible. The small shift in peak positions in detector units is due non-perfect reproduced height of the detector.

reflected signal with and without SERGIS coils is shown. The measurements were both performed with a spin polarised neutron beam without analyser.

Besides the direct cooling of the coils as described in Section 3.1.3.2, additional air-cooling can be provided by fans blowing air through the gap of a coil pair to prevent overheating. The fans have to be positioned far enough from the neutron flight path to avoid an influence of the magnetic field of the electric motors on the neutron spin. Two pairs of triangular spin-echo coils with the described cooling and a magnetic guide field in between them are depicted in Fig. 3.14.

3.1.4 Further Options to Increase the Signal to Background Ratio

The limited magnetic-field of the coils could be improved trough coils with iron core and a gap at the height of the neutron beam. The advantages are twofold, much higher magnetic fields are reached and the absorption and small angle

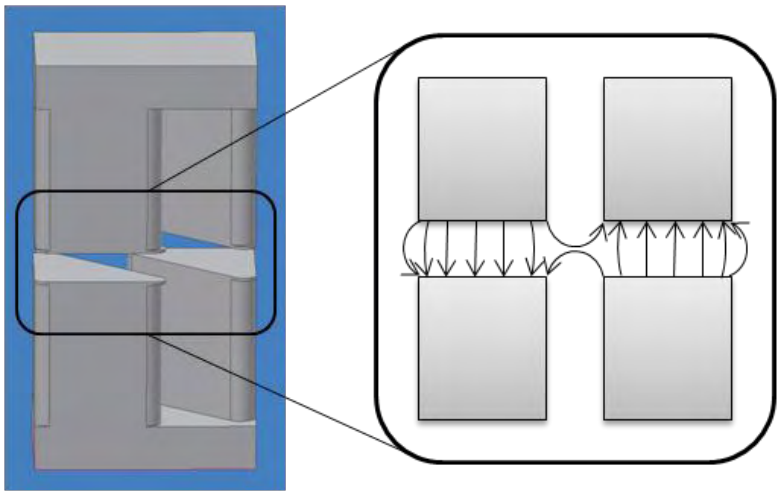

Fig. 3.16: A pair of triangular coils with iron core and a gap for the neutron beam. The magnetic-field lines in the area of the gap are depicted on the right side of the figure. The horizontal components of the magnetic-field are different for different sections of the neutron beam and hence will lead to an unwanted depolarisation.

scattering at the wires is eliminated. The drawbacks are the bad definition of the field boundaries. The fields with opposite direction of the adjacent coils in a spin-echo coil pair are leading to a horizontal magnetic-field with strongly height dependent magnitude and direction, see Fig. 3.16. The magnetisation of the iron core follows a hysteresis curve, which makes it more difficult to set the magnetic-field correctly.

To avoid the interception of the magnetic-field in a coil pair, single coils can be used. The limitation on 50% of the accessible spin-echo length as with respect to the triangular-coil pair set-up can be compensated by the larger accessible magnetic fields due the iron core. When single coils are used field inhomogeneities have to be compensated by correction coils.

R. Pynn also suggested a modification of the triangular coils as introduced in Section 3.1.3, but with a gap in the face through which the neutron beam passes at right angle [Pynn'08b], see Fig. 3.17. Small angle scattering and attenuation only occurs on one face of the triangular-coil and hence is reduced by 50%. The influences of the magnetic-field inhomogeneities of the two coils in a coil pair on the neutron spin cancel each other in a first approximation.

Fig. 3.17: Triangular coil pair as suggested by R. Pynn. On one side of a coil a gap is located to allow passage of the neutron beam. At the side adjacent to the other coil the neutron beam has to pass a layer of aluminium wires. Reproduced from [Pynn'08b].

3.1.5 Comparison of the Different SERGIS Set-Ups

For a given magnetic induction and length of the set-up the highest spin-echo length can be achieved with the NRSE bootstrap set-up (four times as large as the standard set-up introduced in Chapter 2), but this set-up also leads to the highest background to signal ratio in the detector and strongest attenuation of the signal. 17 layers of ~1 mm thick Al wire before and 17 layers after the sample are intercepting the beam path. Due to the adjustment of the RF-coils, the NRSE bootstrap set-up is only suitable for a monochromatised neutron beam, for the application in a time of flight experiment, complicated modifications of the set-up are necessary. A divergent neutron beam leads to an additional depolarisation in the RF coils. With the NRSE bootstrap set-up realised with rotating coils to set the spin-echo length, the real-space resolution is depending on the angle χ, which is used to set the spin-echo length. As all methods where the neutron beam is intercepting the magnetic coils through the wire, the magnetic-field borders are well defined. This set-up is especially suitable for measurements in transmission through the sample where usually a strong scattering signal is obtained or for grazing incidence measurements with strongly scattering samples.

The triangular-coil pair set-up reduces the sensitivity to the inelastic scattering contribution, if present, as well as the elastic scattering in x-direction with respect to the NRSE bootstrap and the standard set-up. In the triangular-coil set-up, the restriction on a monochromatic beam can be slightly relaxed, and this set-up can

be used without modifications at pulsed neutron sources in a time of flight system. In a triangular set-up without windows for the neutron beam 14 layers of 1mm thick Al wire before and ten layers after the sample are intercepting the beam path. The weaker background and attenuation of the signal make the triangular-coil pair set-up more suitable for SERGIS on weakly scattering systems. The 50% smaller accessible spin-echo length for a given magnetic induction and length of the set-up can be compensated by the higher maximal magnetic induction of the triangular coils due to the better cooling possibilities.

A set-up with triangular-coil pairs with iron core and gap is not attenuating the neutron beam nor leading to any additional background, but the magnetic-field borders are badly defined. If single iron core coils with gaps are used, the accessible spin-echo length is identical to the standard set-up as introduced in Chapter 2. The magnetic line integrals have to be corrected with external coils and the sensitivity for inelastic scattering or elastic scattering is as strong as in the standard set-up.

A good compromise for weakly scattering samples seems to be the triangular-coil pair with one gap set-up leading to a moderate background and a weakly attenuated signal. Ten layers of 1 mm thick Al wire before and six layers after the sample are intercepting the beam path. The magnetic-field borders are fairly well defined.

3.2 Other SERGIS Components

The necessary devices, besides the magnetic-field area, for a spin resolved measurement will be summarized in the following sections. The general set-up is depicted in Fig. 3.1.

3.2.1 Polarising Mirror

To be able to use polarised neutrons for an experiment the appropriate spin component has to be filtered from the non-polarised beam. A polarising mirror has a spin dependent neutron reflectivity. The critical angle of total reflection, see also Section 4.1, for one spin component is considerably larger than for the other spin component, see Fig. 3.18. To increase the critical angle of total reflection of

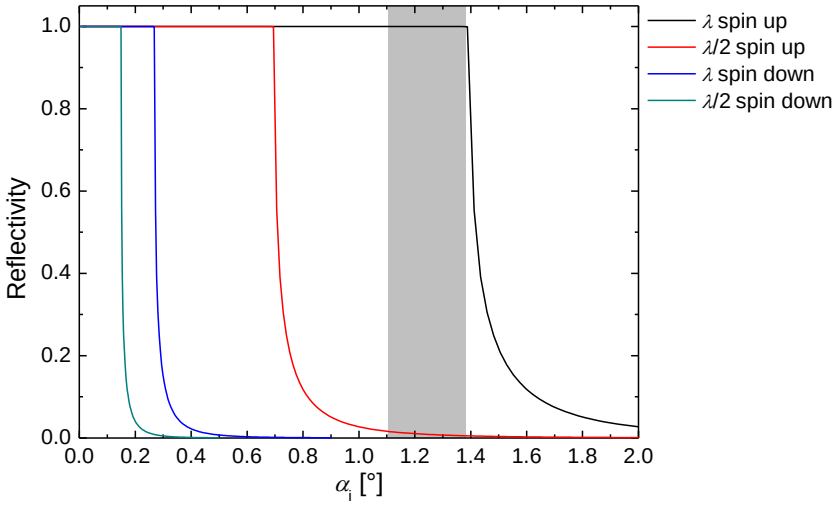

Fig. 3.18: Spin and wavelength dependent reflectivity curves of a neutron spin polariser (calculated). In the grey shaded angular range, the polarising mirror can be used as a spin and wavelength selective device simultaneously. The vertical scale is linear.

the favourable spin component a magnetic multi layer mirror (supermirror) [Schaerpf'89] is used. From the monochromator not only neutrons of the suitable wavelength λ are refracted but also higher harmonics e.g. $\lambda/2$ and $\lambda/3$. To suppress the higher harmonics the polarising mirror is installed in reflection geometry. The transmitted beam is absorbed in a beam dump and the reflected beam is led to the sample. The total reflection edge for neutrons with spin up and wavelength λ is at reasonably higher angles than those for wavelength $\lambda/2$ or shorter wavelengths and/or neutrons with spin down, see Fig. 3.18. Since the neutron is a spin-1/2 particle and the wave function is a superposition of two spin states, compare Eq. (2.11), polarizing a neutron beam costs only about 50% in intensity.

The spin dependent reflectivity of the neutron spin polariser used in the frame of this work is plotted in Fig. 3.19.

3.2.2 Neutron-Spin Analyser

A neutron spin analyser works after the same principle as a neutron spin polariser. One spin component is transmitted, and the other is absorbed. The requirements though are different; the direct beam is well collimated (approximately 1 mm x 6 cm) whereas the neutrons reaching the detector cover a larger angular distribution and larger area has to be analysed (ideally the size of the detector

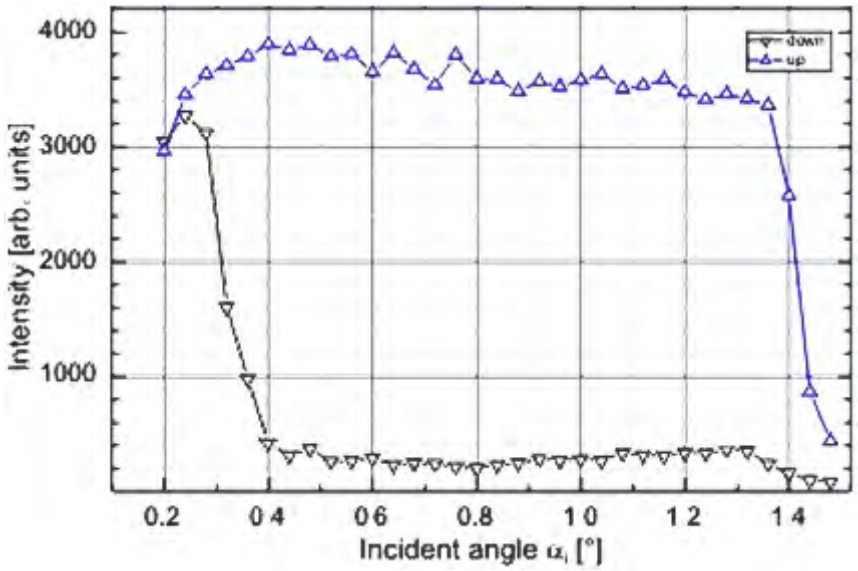

Fig. 3.19: Spin dependent neutron reflectivity of the polariser mirror. The vertical scale is linear.

19 cm x 19 cm). A magnetised mirror or a spin polarised ^{3}He gas, e.g. can act as analyser. Both possibilities were used in the framework of this work and will be described in the following sections.

3.2.2.1 **Supermirror Analyser**

The simplest option to analyse the polarisation of a neutron is a single supermirror analyser. The disadvantage is that only a small vertical angular segment of the neutron beam can be covered by this analyser due to the limited angular range of spin up/down reflectivity difference. And since the angle of inclination against the neutron beam has to be very small (approximately 0.3° - 1.3°) the length of the mirror has to be in accordance very large. With this mirror, it is only possible to analyse a very small region of interest. This single analysing mirror has only been used once in the framework of this work due to the lack of availability of the more sophisticated neutron analysers.

3.2.2.2 **Two-Dimensional Multi Mirror Neutron-Spin Analyser**

Since the detector sees only neutrons originating from the sample position, the spin detection can be done with a neutron spin analyser consisting of a set of single supermirrors [Falus'06]. The construction is illustrated in Fig. 3.20. Neutrons with the unfavourable spin component get reflected on the polarising

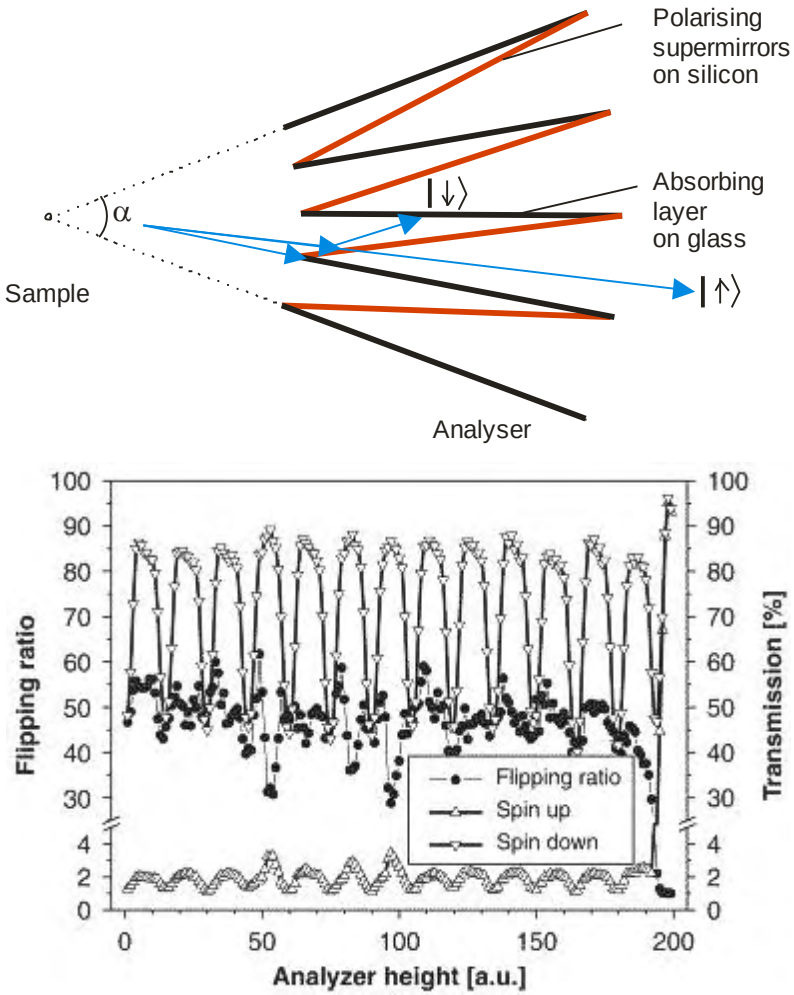

Fig. 3.20: Top: The analyser set-up with channel walls of absorbing glass radial pointing towards the sample and polarising supermirrors on Si wafers diagonally inserted into these channels. A neutron beam impinging the supermirror surface is partially transmitted and reflected depending on the neutron spin. The reflected beam is absorbed. Only a small fraction of the beam is completely blocked due to the finite thickness of the supermirror and absorbing layers. Bottom: Spin dependent neutron transmission and flipping ratio of the two-dimensional multi mirror neutron spin analyser. Reproduced from [Falus'06].

supermirror sheets and then absorbed at absorption layers which point to the sample position. Neutrons originating from the sample position have an angle of incidence on the polarising supermirror sheets between the critical total reflection angle of the spin up and spin down component. The neutrons with the favourable spin component are transmitted through the supermirror. Only a small fraction of the neutron beam is blocked by the thickness of the absorbing sheets. The spin dependent neutron transmission trough the multi supermirror neutron spin

analyser is shown in the bottom of Fig. 3.20. It has to be taken care that the absorbing sheets are not blocking important features of the scattered beam. The multi mirror analyser can be turned slightly around the sample position to tune the positions of the absorbing layers. Eventually measurements can be done with different analyser positions. In the frame of this work the position of the analyser was optimised once before the SERGIS scan to avoid the time consuming measurement at two analyser positions.

3.2.2.3 **Polarised ^{3}He Gas Analyser**

Polarised ^{3}He gas analysers consist of polarised ^{3}He gas, which absorbs neutrons of one spin component. The polarised gas is filled in high purity quartz container and kept under a homogenous magnetic field [Masalovich'07], see Fig. 3.21. The reaction

$$\mathrm{n} + {}^3\mathrm{He} \rightarrow {}^3\mathrm{H} + {}^1\mathrm{H} + 0.764\ \mathrm{MeV} \qquad \textbf{(3.21)}$$

is highly spin selective. The homogenous magnetic-field is needed for the conservation of the ^{3}He spins which makes polarisation analyses possible. The pressure and thickness attribute to the absorption properties (a so called opaque cell, which almost completely suppresses the transmission of one spin component of the neutron beam while another spin component has noticeable, even if relatively low, transmission; or ideal cell where the ratio of the spin up component to the spin down component is optimised).

The transmission $T_{\pm}$ for both spin orientations, the neutron spin parallel and anti-parallel to the ^{3}He spin, through a cell with polarised ^{3}He is given by

$$T_{\pm} = \mathrm{e}^{-(1\mp P_{\mathrm{He}})n_{\mathrm{He}}\sigma_0 l_{\mathrm{cell}}}, \qquad \textbf{(3.22)}$$

where P_{He} is the polarisation of the helium gas, n_{He} the number density of ^{3}He atoms, σ_0 the absorption cross section for unpolarised neutrons (σ_0 [barn] $\approx 3000\ \lambda$ [Å]) and l_{cell} is the length of the spin filter cell [Heil'99]. The application of ^{3}He spin filter is already established in spin resolved off-specular neutron scattering experiments [Nickel'01].

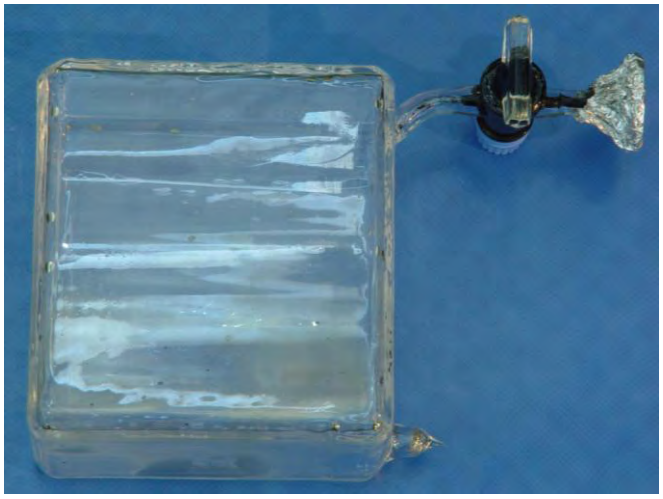

Fig. 3.21: Polarised ^{3}He gas neutron spin filter cell (20 cm x 20 cm) provided by Helios FRM II [Masalovich'07].

Neutron spin filters based on a hyperpolarized ^{3}He gas may compete in polarisation efficiency with such common devices as magnetized single crystals or supermirrors.

3.2.3 π Flipper

To invert the direction of the neutron spin a so called π flipper or Mezei flipper [Mezei'72] is used in the triangular-coil set-up, see Fig. 3.22. The principle of this magnetic coil is to rotate the spin of the incoming neutron about π. This is performed with a magnetic coil with the magnetic-field perpendicular to the neutron spin and the flight direction of the neutrons. The magnetic induction has to be adapted to the wavelength to satisfy the condition of a π spin rotation while the neutron is traversing the coil. Around this coil, a second coil is wound to compensate the guide field. The neutron spin experiences ideally non-adiabatic transitions (see Section 2.3.1) before and after the rotation.

3.2.4 Coupling Coils

To inject or eject neutrons from a more or less arbitrary field region in a zero field area or in another magnetic-field region a coupling coil can be used. A coupling coil, or also called Forte coil [Forte'80], consists of a rectangular shaped coil, where on one side the wire of the coil are bent open, as depicted in Fig. 3.23. The neutron flight path passes through the open side of the coil and then trough the

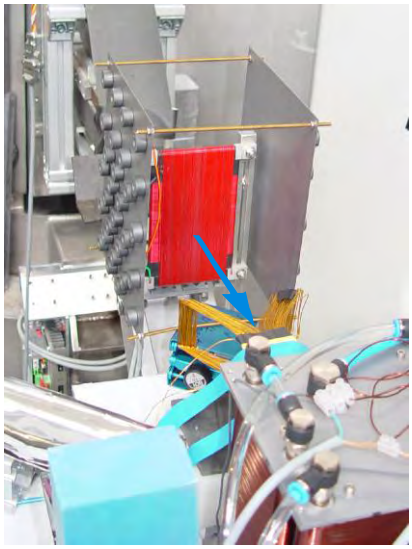

Fig. 3.22: The neutron spin flipper is depicted in the centre of the picture. The red coil with the magnetic-field in the horizontal direction is fully visible. Inside this coil another coil wound with red wire exists where only the side parts are visible. Around the neutron spin flipper a horizontal guide field is installed. The neutron flight path is indicated with a blue arrow.

opposite side through the layer of wires where they are still at their original position. The neutron trajectory can also be in the opposite direction. At the open side, the magnetic-field is leaking out of the coil allowing an ideally adiabatic spin transition. At the other closed side, the field transition is very well defined. If the magnetic-field inside and outside the coupling coil are not aligned an ideally non-adiabatic transition will occur. To suppress the stray field around the closed end of the coil a thin μ-metal shielding is wound around the coil. The coupling coil is mounted with its closed side pointing to the zero field area respectively to the well-defined magnetic-field region where the neutron should be injected or ejected, respectively.

3.2.5 Detector

For the detection of the neutron beam, a two-dimensional (2D) wire chamber of 19 cm × 19 cm entrance area and a spatial resolution of 2 mm (FWHM) was used in all neutron experiments presented. The relatively large tail of the signal broadening handicaps the measurement of weak intensities in the vicinity of high intensity peaks. The chamber is filled with unpolarised ^{3}He gas and a stopping

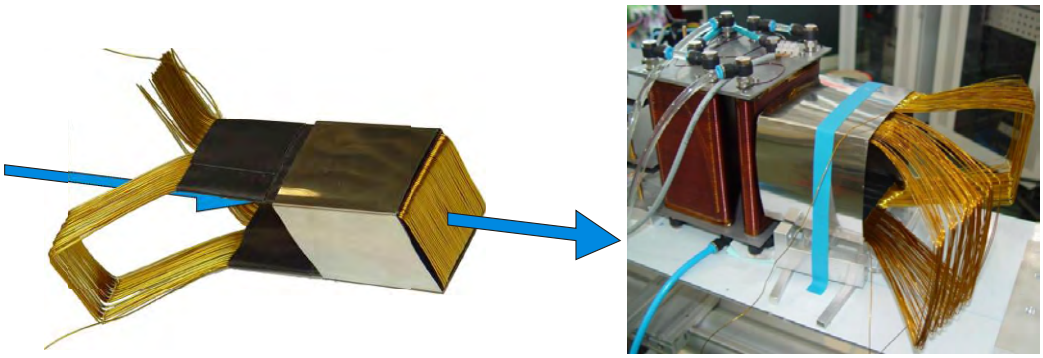

Fig. 3.23: Left image: Standard Forte coil. The neutron trajectory is depicted by the blue arrow, or is pointing in the opposite direction, respectively (size perpendicular to the neutron beam 6 cm x 6 cm). To suppress the field around the closed end of the coil a μ-metal shielding is wound around the coil. To stabilise the coil some black tape is used. Right image: Large forte coil used after the last triangular coil to allow transmission of scattered neutrons (size perpendicular to the neutron beam 14 cm x 14 cm).

gas. The same reaction as the ^{3}He spin analyser (see Section 3.2.2.3) takes place. Since the ^{3}He gas is not polarised, the process is not spin selective. The neutron is converted through the nuclear reaction into charged particles tritium (^{3}H) and proton (^{1}H), which then are detected by their charge cloud induced in the gas, compare Eq. (3.21).

3.3 Data Analysis

The data analysis is in general identical for the different SERGIS options. If differences exist, they will be especially referred to in the text.

3.3.1 Measurement of the Polarisation

The phase of the neutron spin is very sensitive to the instrumental magnetic-field distribution. Hence it is very difficult to set-up the instrument with the required precision and shield all magnetic stray fields to be able to measure the polarisation of the Yoneda peak directly, but small deviation in the magnetic line integral ($\int B\,\mathrm{d}x$) can be compensated by a magnetic field- or length-offset of the magnetic-field in one spin-echo arm. In case of a triangular-coil measurement, a magnetic-field offset scan (of the guide-field in the second spin-echo arm) is used and in case of a NRSE spin-echo measurement a scan of the length of the second spin-echo arm is performed. The scan to compensate the magnetic line integrals

was performed at every spin-echo length, since stray fields were changing with the set spin-echo length.

The polarisation of the unscattered beam at the detector has a cosine like dependency of the magnetic-field or length offset and the amplitude is called P_0. With increasing spin-echo length the requirements on the field homogeneity are increasing, consequently P_0 may decrease. The same effect occurs to the scattered beam, but cannot be measured independently of the depolarisation due to the scattering length distribution on the sample. If one inserts Eq. (2.21) with $k_{\mathrm{i,d}} = k_{\mathrm{f,d}}$, in Eq. (2.33) with $\mathrm{d}\sigma/\mathrm{d}\Omega = \delta(q)$) in (2.32), taking into account the polarisation loss by magnetic-field inhomogeneities, one obtains for the polarisation of the unscattered neutron beam

$$P = P_0 \left(\int_{\vec{\tilde{k}}_\mathrm{i}} \mathrm{d}\vec{\tilde{k}}_\mathrm{i} \right)^{-1} \times \int_{\vec{\tilde{k}}_\mathrm{i}} \cos\left(\frac{-m_\mathrm{n}\gamma_\mathrm{n}\lambda(B_\mathrm{i}L_\mathrm{i} - B_\mathrm{f}L_\mathrm{f})}{h\cos\eta_\mathrm{i}\left(\cos\eta_\mathrm{i} + \frac{\tilde{k}_{\mathrm{i,x}}}{\bar{k}_\mathrm{i}} + \frac{\tilde{k}_{\mathrm{i,y}}}{\bar{k}_\mathrm{i}}\tan\chi_\mathrm{i} + \left(\sin\eta_\mathrm{i} + \frac{\tilde{k}_{\mathrm{i,z}}}{\bar{k}_\mathrm{i}}\right)\frac{\tan\eta_\mathrm{i}}{\cos\chi_\mathrm{i}}\right)} \right) \mathrm{d}\vec{\tilde{k}}_\mathrm{i} \,. \tag{3.23}$$

After a adjustment to fulfil $\chi_\mathrm{i} = \chi_\mathrm{f}$ and $L_\mathrm{i} = L_\mathrm{f}$ as good as possible, the adjustment of $B_{\mathrm{i/f}}$ or $L_{\mathrm{i/f}}$ is done by maximisation of the polarisation amplitude. At every spin-echo length the magnetic fields need to be adjusted by scanning $B_{\mathrm{i/f}}$ or $L_{\mathrm{i/f}}$, respectively, since the depolarisation and phase shift of the neutron spin is specific for every spin-echo length.

The polarisation of the scattered beam is

$$P = P_0 \int_{\vec{\tilde{k}}_\mathrm{i}} \int_{\vec{q}} \frac{\mathrm{d}\sigma}{\mathrm{d}\Omega}(\vec{q}) \cos w \, \mathrm{d}\vec{\tilde{k}}_\mathrm{i} \mathrm{d}\vec{q} \left(\int_{\vec{\tilde{k}}_\mathrm{i}} \int_{\vec{q}} \frac{\mathrm{d}\sigma}{\mathrm{d}\Omega}(\vec{q}) \mathrm{d}\vec{\tilde{k}}_\mathrm{i} \mathrm{d}\vec{q} \right)^{-1} , \tag{3.24}$$

with

$$w = -\frac{m_\mathrm{n}\gamma_\mathrm{n}}{h}\lambda\left[\frac{B_\mathrm{i}L_\mathrm{i}}{\cos\eta_\mathrm{i}\left(\cos\eta_\mathrm{i}+\frac{\tilde{k}_{\mathrm{i,x}}}{\bar{k}_\mathrm{i}}+\frac{\tilde{k}_{\mathrm{i,y}}}{\bar{k}_\mathrm{i}}\tan\chi_\mathrm{i}+\left(\sin\eta_\mathrm{i}+\frac{\tilde{k}_{\mathrm{i,z}}}{\bar{k}_\mathrm{i}}\right)\frac{\tan\eta_\mathrm{i}}{\cos\chi_\mathrm{i}}\right)}-\frac{B_\mathrm{f}L_\mathrm{f}}{\cos\eta_\mathrm{i}\left(\cos\eta_\mathrm{i}+\frac{\tilde{k}_{\mathrm{i,x}}+q_\mathrm{x}}{\bar{k}_\mathrm{i}}+\frac{\tilde{k}_{\mathrm{i,y}}+q_\mathrm{y}}{\bar{k}_\mathrm{i}}\tan\chi_\mathrm{f}+\left(\sin\eta_\mathrm{i}+\frac{\tilde{k}_{\mathrm{i,z}}}{\bar{k}_\mathrm{i}}\right)\frac{\tan\eta_\mathrm{i}}{\cos\chi_\mathrm{f}}\right)}\right]. \quad \textbf{(3.25)}$$

If the scan of the magnetic field- or length-offset is performed in the first spin-echo arm, the period of the cosine function will be identical in the case of the scattered and unscattered beam. The phase of the polarisation is slightly different, since $q_\mathrm{x}/k_\mathrm{i} + q_\mathrm{y}\tan\chi\,/k_\mathrm{i} \ll 1$ also the phase can be approximated as identical to the phase of the unscattered beam. Although for experimental reasons, the shown data were measured with the magnetic-field offset in the second spin-echo arm. With the same approximation as for the measurement of the phase, the period of the scattered and the unscattered signal can be treated as identical.

As unscattered reference beam, in principle the direct beam or the specular reflected beam can be used. Experimentally at $Y^{\mathrm{SE}} \approx 0$ the phase of the specular reflected beam is matching better the phase of the Yoneda peak then the direct beam, see Fig. 3.24. Since the beam path of the Yoneda beam is spatially closer to the beam path of the specular reflected beam, the specular reflected beam is most suitable as reference beam. This can be explained e.g. by an undesired vertical magnetic-field gradient leading to an additional phase shift in the direct beam with respect to the Yoneda peak.

To evaluate the polarisation of the Yoneda peak, in a first step a cosine function is fitted to the polarisation of the specular reflected beam as reference beam. The amplitude P_0, the phase and the offset are determined.

In a second step the phase, the period and the offset of the cosine function of the reference beam are taken as fixed parameters to fit the polarisation amplitude of the Yoneda peak. The fit with the parameter of a reference beam is necessary for two reasons. First, the sample might introduce a phase shift to the neutron spin,

which would be balanced if the phase in the fit would be set as free parameter. In case of a sample with a lateral non-isotropic scattering length distribution; e.g. a sinusoidal scattering length distribution in one direction and homogeneous in the perpendicular direction, the scattering intensity as a function of scattering angle will be asymmetric and follow a delta function (see Fig. 3.25); all scattered neutrons in the Yoneda peak follow the same pathway and the spin will still be in phase at the detector position, independent of the spin-echo length. In this case the maximal polarisation is not at $B_i L_i = B_f L_f$, see Eq. (3.24). The structural information will be encoded in the phase of the polarisation. And second, if the phase shift of the ensemble of the scattered neutrons can be neglected, at higher spin-echo lengths the polarisation-amplitude of the Yoneda peak is only in the order of the error bar of the polarisation at each measured point in the offset scan, see the lower part of Fig. 3.24. The error of the polarisation amplitude fit is

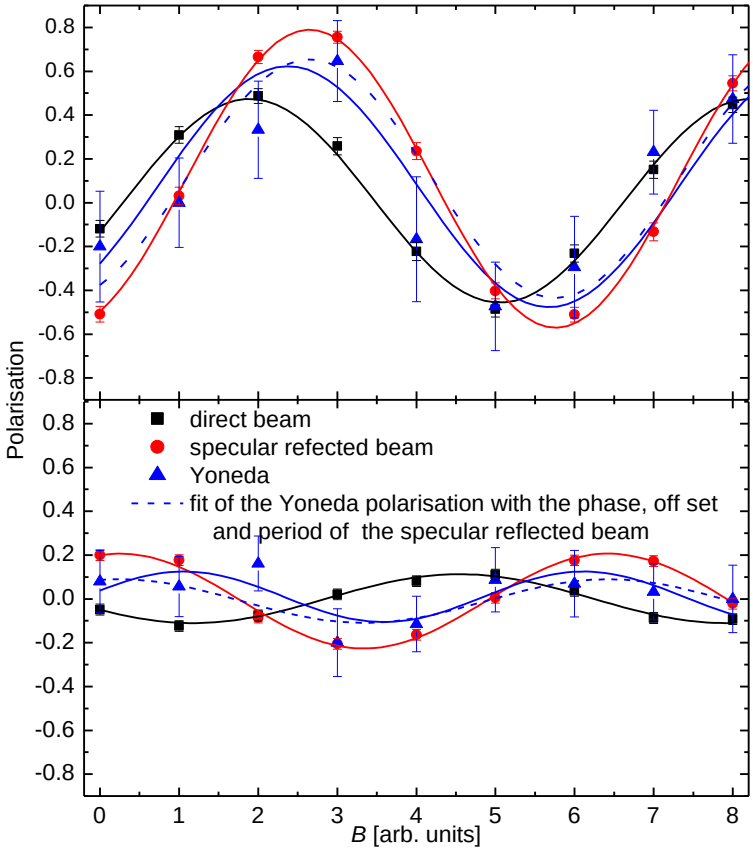

Fig. 3.24: Polarisation measurement of the direct beam (black lines), specular reflected beam (red lines) and Yoneda peak (blue lines) at spin-echo lengths Y^{SE} = 4.5 nm (top) and 279 nm (bottom). The Yoneda peak polarisation is fitted with free variables (blue dashed lines) and with the phase and offset fixed as obtained by the fit of the specular reflected beam (blue full lines).

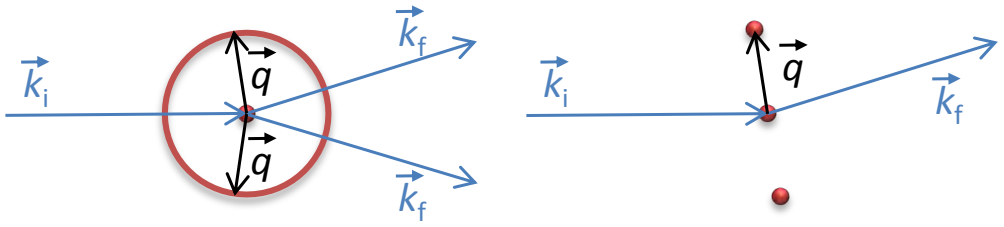

Fig. 3.25: Reciprocal space illustration with the incident and scattered beams. Left: In case of an isotropic scattering length distribution two scattered beams exist. Right: In the special case of a sinusoidal scattering length distribution in one direction and homogenous in the perpendicular direction only one scattered beam may exist. The forward scattering is omitted since in the DWBA (see Chapter 4.2.2) it doesn't contribute to the Yoneda peak.

significantly decreased by using the phase, the period, and the offset of the fit obtained from the reference beam.

In a final step, the polarisation of the Yoneda peak is normalised by the polarisation of the specular reflected beam. This becomes necessary since the polarisation of the incident beam is not exactly 100% and additional depolarisation occurs even on the not scattered beam at not perfectly defined magnetic-field borders.

At the triangular-coil set-up there are no guide fields installed at the position of the triangular coils. This makes a measurement at $Y^{SE} = 0$ difficult since the neutron beam gets depolarised. For the NRSE set-up, the measurement for small spin-echo length is not feasible since the approximation performed in Chapter 2 do not apply for very small values of χ.

3.3.2 Data Corrections

At the two dimensional detector, see Fig. 3.26, a region of interest (ROI) is defined to evaluate the SERGIS signal. The ROI boundaries are set where the diffuse intensity fades into the general background intensity respectively at the minimum between the diffuse intensity and the wing of the specular reflected intensity or the wing of the direct beam. The definition of the ROI can be done after the SERGIS measurement with the summed up detector exposures to guarantee good counting statistics. The ROI intensity I_{ROI} has three contributions: the diffuse intensity I_d (usually the Yoneda peak intensity) which contains

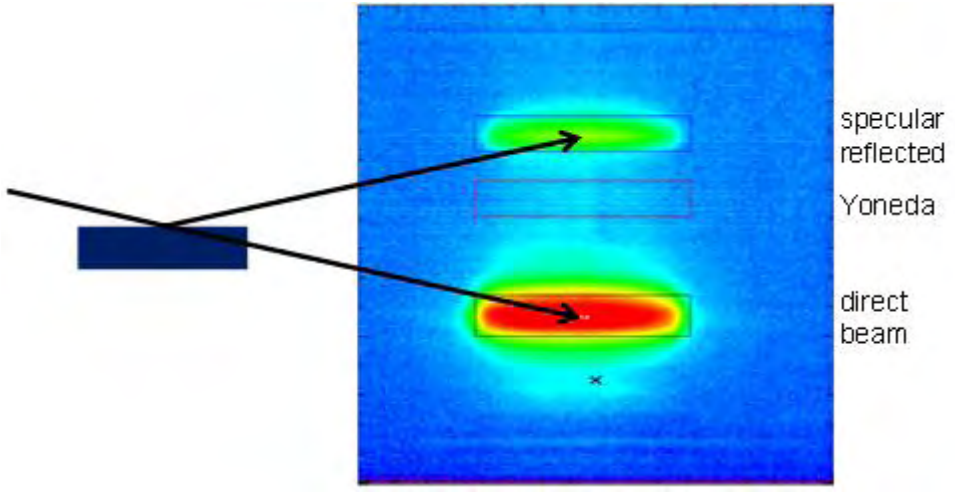

Fig. 3.26: Typical detector image. The intensity is summed up over one SERGIS scan (sum of the measurements at different spin-echo length). The rectangular boxes represent regions of interest (ROI) for the data analyses.

information on the scattering length distribution of the sample, the background due to small angle scattering on the coils I_r, which is in good approximation polarised as the reference beam, and the non-polarised general background I_{back}. The product of the ROI intensity and polarisation can be fragmented in the parts

$$I_{ROI}P_{ROI} = I_dP_d + I_rP_r + I_{back}P_{back}\,, \qquad \textbf{(3.26)}$$

where the instrumental depolarisation has to be taken into account by determining P_{ROI} as described in the previous section and afterwards setting $P_r = 1$. Hence the polarisation of the diffuse scattered signal is

$$P_d = \frac{I_{ROI}P_{ROI} - I_rP_r - I_{back}P_{back}}{I_d} = \frac{P_{ROI} - \frac{I_r}{I_{ROI}}P_r - \frac{I_{back}}{I_{ROI}}P_{back}}{\frac{I_d}{I_{ROI}}}. \qquad \textbf{(3.27)}$$

The three quantities I_r / I_{ROI}, I_{back} / I_{ROI}, and I_d / I_{ROI} have to be estimated from the peak shape of the tail of the direct and specular reflected beam and the level of the general background, with the condition that the sum over the pre-factors is equal one.

The final result is the polarisation P_d as a function of the spin-echo length Y^{SE}, which is in the limitations discussed in Chapter 2, proportional to the generalised Patterson function.

3.3.3 Statistical Error

Reviews on physical data analysis can be found e.g. in [Bevington'69, Brandt'99]. In the following, the main results will be presented. In a scattering experiment, the distribution of the measured counts can be approximated by a normal distribution, also called Gaussian distribution. If the number of counts is not too small (> 30), the width of the distribution is assumed to be the statistical error. With a probability of 68.27% the measured value and the mean value of infinitively many measurements coincide in the margin of the 1σ error

$$\Delta I = \sqrt{I}\,. \tag{3.28}$$

Using Eq. (2.32) and taking into account that the errors of both count rates $I_\uparrow$ and $I_\downarrow$ are statistically independent, the statistical error of the polarisation is

$$P_{\mathrm{err}} = \sqrt{\left(\frac{\partial P}{\partial I_\uparrow}\Delta I_\uparrow\right)^2 + \left(\frac{\partial P}{\partial I_\downarrow}\Delta I_\downarrow\right)^2} = \sqrt{\frac{1-P^2}{I_\uparrow + I_\downarrow}}\,. \tag{3.29}$$

By taking the error of the single polarisation measurements into account, the error of the spin-echo polarisation amplitude is determined within the fit.

3.3.4 Probability Density Function

For the comparison of the data with different model systems, the following procedure is used. To estimate the probability that the expectation value μ_i as calculated from the model and the data X_i coincide within the statistical accuracy, a quantity, the so-called $\chi^2_{\mathrm{red.}}$-Distribution

$$\chi^2_{\mathrm{red.}} = \frac{1}{DoF}\sum_{i=1}^{n}\left(\frac{X_i - \mu_i}{\sigma_i}\right)^2 \tag{3.30}$$

with *DoF* = (*n*-*p*-1) degrees of freedom and *n* number of data points, *p* number of parameters is calculated.

The probability density function of the $\chi^2_{\mathrm{red.}}$ distribution [Bevington'69] is

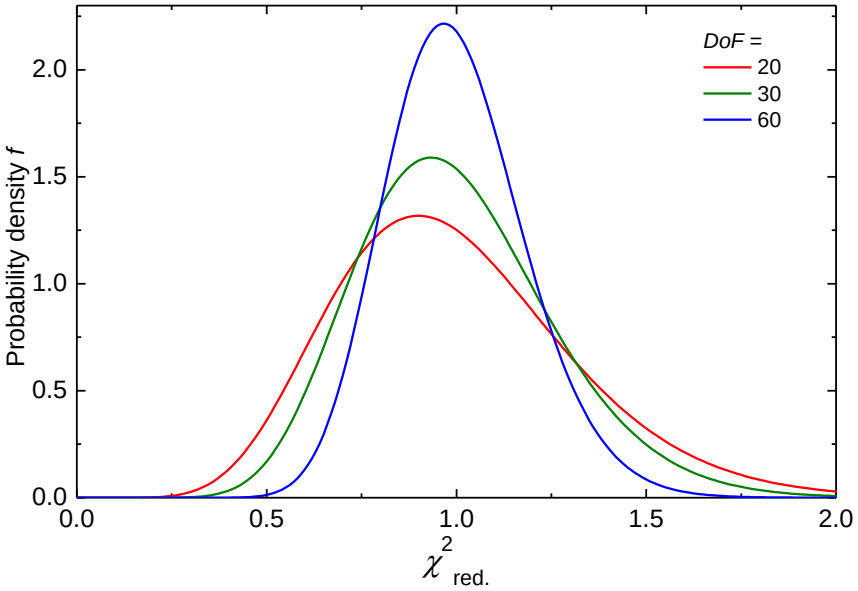

Fig. 3.27: Probability density function (Eq. (3.31)) for *DoF* = 20 (red line), 30(green line), and 60 (blue line) degrees of freedom.

$$f\left(\chi^2_{red.}, DoF\right) = \frac{\left(\chi^2_{red.}\, DoF\right)^{\left(\frac{DoF}{2}-1\right)} \mathrm{e}^{-\frac{\chi^2_{red.}\, DoF}{2}}}{2^{\frac{DoF}{2}}\, \Gamma\left(\frac{DoF}{2}\right)} \qquad \textbf{(3.31)}$$

for $\chi^2_{red.} > 0;\ 0\ otherwise$,

where Γ denotes the Gamma function, which has closed-form values at the half-integers. The expectation value for $\chi^2_{\mathrm{red.}}$ is one. The variance is $2/n$ and the maximum is located at $(n\text{-}2)/n$. The probability density function is plotted in Fig. 3.27 for different *DoF*.

3.4 Impact of the Basic SERGIS Design Parameters

The main design parameters in a SERGIS experiment, with respect to the presented SERGIS options, are presented in Table 4.1 with their advantages respectively disadvantages, and will be summarised in this section. The neutron wavelength has the following influence. Neutrons with short wavelengths λ are fulfilling the approximation $C_{\mathrm{corr}} \approx 1$ (Eq. (2.24)) better than neutrons with longer wavelengths, which is of importance to reproduce small structures. Further the Yoneda peak, see Chapter 4, occurs at smaller angles for smaller wavelengths, which allows the angle η with respect to the horizontal axis to be reduced and the

parameter	**for small parameter value**	**for large parameter value**
wavelength λ	resolve small real space correlations	reach large Y^{SE}
beam divergence	little instrumental polarisation loss and resolve small real space correlations	good statistics, but more instrumental polarisation loss and convolution of spin-echo lengths
$\Delta\lambda/\lambda$	works for all set-up	good statistics, only suitable for triangle coils, convolution of spin-echo lengths
magnetic induction *B*	little instrumental polarisation loss	reach large Y^{SE}, but more instrumental polarisation loss
width of the coils	reach large Y^{SE}, due to easier cooling	resolve small real space correlations / good statistics
inclination of the field border χ	less sensible to the beam divergence	reach large Y^{SE}
number of coils	little background and absorption	reach large Y^{SE}

Table 3.1: Impact of the basic SERGIS design parameters. For a detailed explanation, see text.

approximation to deduce Eq. (2.23) from Eq. (2.22) is better fulfilled. The spin-echo length is proportional to λ^2. Hence, to reproduce large structures, large wavelengths are suitable. For a low beam divergence, the approximation to deduce Eq. (2.23) from Eq. (2.22) is better fulfilled and in addition, the part of the beam deviating from the average propagation direction penetrates the magnetic-field borders not exactly at the angle χ. Hence, a convolution of the signal at different spin-echo length proportional to the beam divergence occurs. The width of the wavelength distribution is crucial for the SERGIS NRSE set-up, whereas the wavelength does not need to be defined very well for the triangle set-up yielding better counting statistics, due to a higher neutron flux with a relaxed monochromatisation. Although, in both cases for a precise definition of the spin-echo length, the wavelength has to relatively well defined. Weak magnetic inductions produce only relatively small stray fields and consequently the

reference polarisation is relatively large. The data points do not need to be normalised by a large factor and hence the statistical error is relatively small. The disadvantage is that only relatively small spin-echo length can be addressed with weak magnetic fields. The width of the coils is limiting, the width of the incident beam as well as its divergence and the maximal scattering angle. Since the heat dissipation scales with the circumference of the coils, the maximal accessible spin-echo length is larger for narrower coils. On the one hand, a higher inclination of the magnetic-field borders χ permits to address larger spin-echo length. On the other hand the approximation to deduce Eq. (2.23) from Eq. (2.22) and $C_{\mathrm{corr}} \approx 1$ (Eq. (2.24)) is better fulfilled for small inclinations of the magnetic field regions. In addition, in the SERGIS NRSE set-up in case of a divergent beam, the π condition (Eq. (3.5)) is better fulfilled for small values of χ. In the presented SERGIS options, the accessible spin-echo length scales with the number of magnetic coils in the neutron beam, but the absorption and background are also increasing. For weakly scattering samples, small background and absorption are essential and a trade-off between maximal spin-echo length due to further coils and the signal quality has to be carefully balanced.

For the mentioned design parameters, no general optimal values exist. The parameters have to be chosen in function of the sample features under investigation.

4 Grazing Incidence Scattering of Neutrons and X-rays

The aim of this chapter is to give an introduction into the basic principles of neutron and x-ray scattering. X-ray and neutron specular reflectivity are used to resolve the structure normal to the sample surface. The neutron off-specular reflectivity explains the scattering of the sample, which is transformed by SERGIS in a real space signal (Section 2.4.3).

Extensive reviews of x-ray and neutron scattering can be found e.g. in [Dosch'92a, Tolan'99, Smith'06]. Here a brief introduction to the techniques is given. In the first section, the specular reflectivity will be presented, followed in the next section by a relaxation of the specular condition to off-specular scattering. Both neutron and x-ray scattering will be discussed.

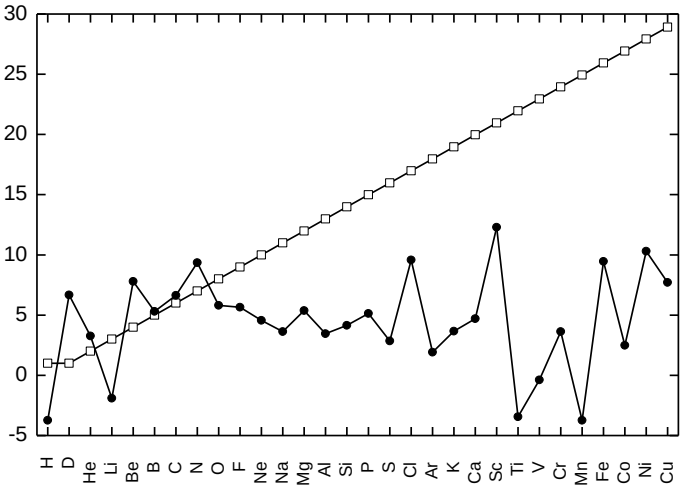

Fig. 4.1: Neutron coherent scattering length [fm] (black circles) [Sears'92] and x-ray atomic scattering factor (white squares) [Henke'93]. The relatively large scattering cross-section makes neutron scattering also suitable to investigate light atoms. In addition hydrogen atoms (H) can be substituted with deuterium atoms (D) without a significant change in the chemical or biological properties, allowing to set a ’marker’ on a molecule.

X-ray and neutron methods offer specific advantages. For the specular reflectivity measurements in the framework of this thesis both kind of radiation were taken advantage of. Due to the much higher flux and brilliance of x-ray sources, x-ray radiation is most commonly employed. In the case of low x-ray scattering contrast or high adsorption of the radiation, neutron scattering becomes an attractive alternative, as e.g. in the case of soft-matter and biologic sample. For x-rays the scattering cross section is increasing with the atomic charge, whereas for neutrons the scattering cross section is isotope dependent and does not depend on the atomic charge. For neutron scattering, this allows not only the labelling of certain atoms by replacing them with an isotope, but also the sensitivity to atoms with a low electric charge. A comparison of the element specific scattering power of neutrons and x-rays is shown in Fig. 4.1. References on grazing incidence scattering instrumentation can be found e.g. in [Usta'91, Dosch'92b, Usta'92].

This chapter will focus on reflectivity and off-specular scattering. In both cases, the scattering vector q is small. Hence, a detailed description of the atomic properties can be omitted. Instead, the average local properties in one area have to be considered.

4.1 Reflectivity

Neutron and x-ray reflectivity are powerful techniques to study thin film systems. Specular reflectivity is only sensible to the scattering length density distribution perpendicular to the sample surface, averaged in the direction parallel to the sample surface.

In this chapter an introduction to the basic principles of reflectivity is given. First general aspects are explained to be followed by the special application of x-rays and neutrons.

4.1.1 Index of Refraction

Consider a homogeneous material consisting of N different atom types with the respective number densities N_j. The index of refraction of this material can be written as

$$n = 1 - \delta + \mathrm{i}\beta \tag{4.1}$$

with, for x-rays,

$$\delta_{\mathrm{x}} = \frac{\lambda^2}{2\pi} r_{\mathrm{e}} \sum_{j=1}^{N} N_j \left(f_j^0 + f_j'(\lambda) \right) \tag{4.2}$$

and

$$\beta_{\mathrm{x}} = \frac{\lambda^2}{2\pi} r_{\mathrm{e}} \sum_{j=1}^{N} N_j f_j''(\lambda) = \frac{\lambda}{4\pi} \mu \,, \tag{4.3}$$

where μ represents the absorption coefficient and $r_{\mathrm{e}} = 2.818\ 10^{-11}$ m the classical electron radius. The x-ray form factor is

$$f_j = f_j^0 + f_j'(\lambda) + \mathrm{i} f_j''(\lambda), \tag{4.4}$$

where $f_j'(\lambda)$ and $f_j''(\lambda)$ account for dispersion and absorption corrections, respectively. Tabulated values for f_j can be found in [Smith'06]. A good approximation (far from absorption edges) is $f_j^0 \approx Z_j$ (Z_j being the atomic number), and thus

$$\delta_{\mathrm{x}} \approx \frac{\lambda^2}{2\pi} r_{\mathrm{e}} \sigma_{\mathrm{e}} \,, \tag{4.5}$$

where σ_{e} denotes the laterally averaged electron density.

For neutrons the dispersion term is

$$\delta_{\mathrm{n}} = \frac{\lambda^2}{2\pi} \sum_{j=1}^{N} N_j \sqrt{b_{c,j}^2 - \left(\frac{\sigma_{\mathrm{r},j}}{2\lambda} \right)^2} \tag{4.6}$$

with the coherent nuclear scattering length b_{c} and the total cross section

$$\sigma_{\mathrm{r}} = \sigma_{\mathrm{a}} + \sigma_{\mathrm{i}} \,, \tag{4.7}$$

σ_{a} and σ_{i} being the absorption and incoherent cross section. For paramagnetic materials an additional contribution has to be taken into account [Zabel'94], which will not be discussed here. The imaginary part of the index of refraction is

	δ_x [10^{-6}]	δ_n [10^{-6}]	β_x [10^{-8}]	β_n [10^{-10}]
*d*PS	3.37	28.91	0.46	4.06
PI	2.44	0.96	0.31	169.83
SiO_2	7.12	16.73	9.22	0.17
Si	7.57	9.98	17.23	0.0088

Table 4.1: Some values for δ and β. The values for x-rays are given for λ = 1.54 Å and in the case of neutrons for λ = 5.5 Å. For x-rays exists only a small scattering contrast between the two polymers, whereas for neutrons the scattering contrast is strong. *d*PS and PI are polymers investigated in this work.

$$\beta_{\mathrm{n}} = \frac{\lambda}{4\pi} \sum_{j=1}^{N} N_j \sigma_{\mathrm{r},j} \,. \qquad \textbf{(4.8)}$$

Values for b_c, σ_a, and σ_i are tabulated in [Sears'92].

Some values of δ and β for neutrons and x-rays used in this work are displayed in Table 4.1.

4.1.2 Reflection at an Ideal Interface

The incoming neutron or x-ray beam can be represented by a plane wave front. In case of x-rays it is an electromagnetic wave with an electric field *E* and can be described by the Helmholtz equation

$$\nabla^2 E + k^2 n^2 E = 0 \,. \qquad \textbf{(4.9)}$$

For neutrons, it is a particle wave, which can be described by the Schrödinger equation

$$-\frac{\hbar}{2m_{\mathrm{n}}} \nabla^2 \psi(\vec{r}) + (V - E_0)\psi(\vec{r}) = 0, \qquad \textbf{(4.10)}$$

where E_0 is the energy at rest and *V* the potential in which the wave field $\psi(\vec{r})$ propagates. In the following text the electromagnetic case will be discussed, the treatment of the particle wave is analogous.

A plane wave $E_{\mathrm{i}}(\vec{r}) = E_{\mathrm{i}}^0 \exp\left(\mathrm{i}\vec{k}_{\mathrm{i}}\vec{r}\right)$ with wave vector $\vec{k}_{\mathrm{i}}$ and amplitude E_{i}^0 impinging on an interface at a grazing incidence angle α_{i} splits into a reflected wave ($\alpha_{\mathrm{f}} = \alpha_{\mathrm{i}}$, amplitude E_f^0) and a refracted wave transmitted at the

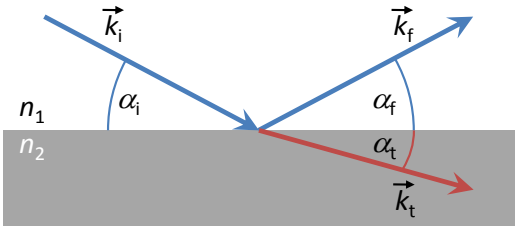

Fig. 4.2: Reflection and refraction of a plane wave front.

grazing angle α_t (see Fig. 4.2). The angle of the refracted wave is linked to the angle of the incident wave by Snell's law:

$$\frac{\cos(\alpha_i)}{\cos(\alpha_t)} = \frac{n_2}{n_1}, \tag{4.11}$$

with n_1 and n_2 the respective indices of refraction, for the media of the incoming wave and the transmitted wave. For $\alpha_i \leq \alpha_c$ total external reflection will occur, with the critical angle of total reflection

$$\alpha_c = \arccos\left(\frac{1-\delta_2}{1-\delta_1}\right) \approx \sqrt{2(\delta_2 - \delta_1)}\,. \tag{4.12}$$

No transmitted wave is created, and only an evanescent wave field penetrates in the second medium. Apart from small losses due to absorption, all incoming radiation is reflected. The critical angle is only defined for $\delta_2 > \delta_1$. This means that total reflection can only occur, when the medium on the side of the incoming wave is optically denser.

The reflection coefficients r for the components of the electric field parallel $\parallel$ and perpendicular $\perp$ to the interface are

$$r_{\parallel/\perp} = \frac{E^0_{f\parallel/\perp}}{E^0_{i\parallel/\perp}}. \tag{4.13}$$

They can be calculated using the fact that the tangential components of the electric and perpendicular component of the magnetic-field have to be continuous at the interface. If n is close to unity, like in the case of x-rays and neutrons, the reflection and transmission coefficient can be expressed as

$$r = \frac{k_{i,z} - k_{t,z}}{k_{i,z} + k_{t,z}} = \frac{n_1 \sin\alpha_i - n_2 \sin\alpha_t}{n_1 \sin\alpha_i + n_2 \sin\alpha_t} \tag{4.14}$$

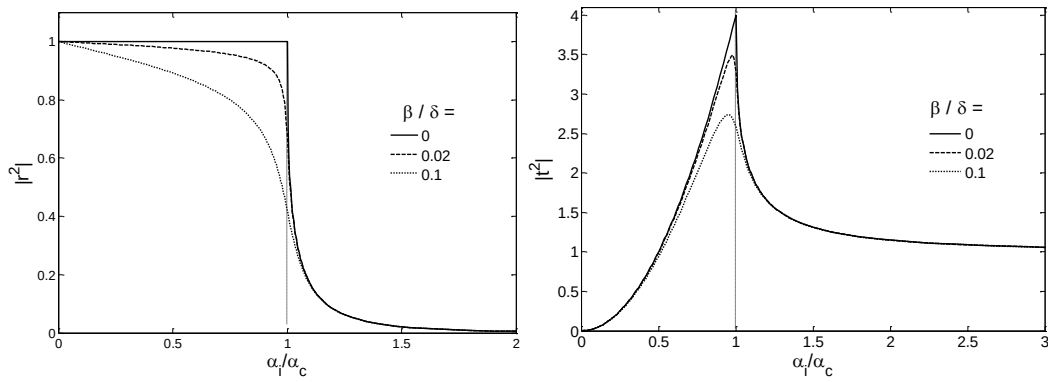

Fig. 4.3: Fresnel reflectivity (left) and transmission (right) versus the angle of incidence $\boldsymbol{\alpha_i}$ normalized by the critical angle $\boldsymbol{\alpha_c}$. Several ratios of β/δ are plotted. The influence of β is only dominant in the vicinity of $\boldsymbol{\alpha_c}$.

and

$$t = \frac{2k_{\mathrm{i,z}}}{k_{\mathrm{i,z}} + k_{\mathrm{t,z}}}, \tag{4.15}$$

where $k_{\mathrm{i,z}} = k \sin\alpha_{\mathrm{i}}$ and $k_{\mathrm{t,z}} = k\frac{n_2}{n_1}\sin\alpha_{\mathrm{t}}$ are the z-components of the wave vector of the incident and transmitted wave, respectively. The intensity of the reflected wave, the so-called Fresnel reflectivity, is given by

$$R_{\mathrm{F}} = |r|^2 = \frac{(\alpha_{\mathrm{i}} - p_+)^2 + p_-^2}{(\alpha_{\mathrm{i}} + p_+)^2 + p_-^2}, \tag{4.16}$$

with

$$p_{+/-}^2 = \frac{1}{2}\left(\sqrt{(\alpha_{\mathrm{i}}^2 - \alpha_{\mathrm{c}}^2)^2 + 4\beta^2} \pm \left(\alpha_{\mathrm{i}}^2 - \alpha_{\mathrm{c}}^2\right)\right). \tag{4.17}$$

The Fresnel reflectivity and transmission $T_{\mathrm{F}} = |t|^2$ are plotted in Fig. 4.3 for a silicon wafer measured with x-ray radiation at a wavelength $\lambda = 1.54$ Å for different ratios of β/δ. The penetration depth is

$$\Lambda = \frac{\lambda}{\sqrt{2}\pi}\left(\sqrt{(\alpha_{\mathrm{i}}^2 - \alpha_{\mathrm{c}}^2)^2 + 4\beta^2} - \left(\alpha_{\mathrm{i}}^2 - \alpha_{\mathrm{c}}^2\right)\right)^{-1/2}. \tag{4.18}$$

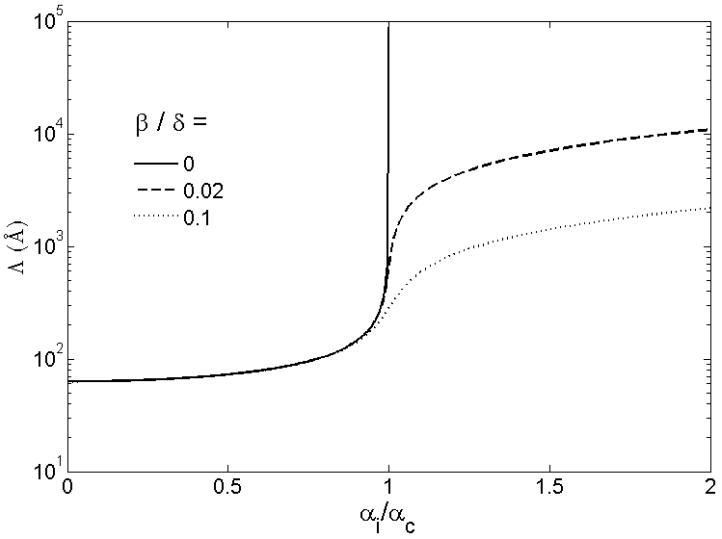

Fig. 4.4: Penetration depth of x-rays with $\lambda = 1.54$ Å in silicon for different ratios of β/δ.

In Fig. 4.4 the penetration depth is plotted as an example for a silicon wafer measured with x-ray radiation at a wavelength $\lambda = 1.54$ Å for different ratios of β/δ.

4.1.3 Multiple Interfaces

Most systems have more then only one interface in the vicinity of the surface. The reflection from all interfaces contributes to the total reflection. A sketch of a systems consisting of N+1 layers is shown in Fig. 4.5. The layer number is j with its refractive index n_j, thickness d_j, and position z_j. The layers 1 and N+1 are semi-infinite and usually the first layer is the vacuum and $z_j = 0$ at the interface between the vacuum and the following layer.

Two waves are created at each interface: a 'reflected' wave (R_j) propagating in the layer j and a 'transmitted' wave (T_j+1) propagating in the layer j +1. However, unlike at a single interface, there are also two incoming waves at each interface: the transmitted wave from the interface $j-1$ (T_j) and the reflected wave from the interface j+1 (R_j+1). The amplitude of the incoming wave in the semi-infinite layer 1 is normalized to unity, $T_1 = 1$, and no reflected wave is propagating through the last layer, $R_{N+1} = 0$. The Parratt formalism [Parratt'54] connects the R_j and T_j:

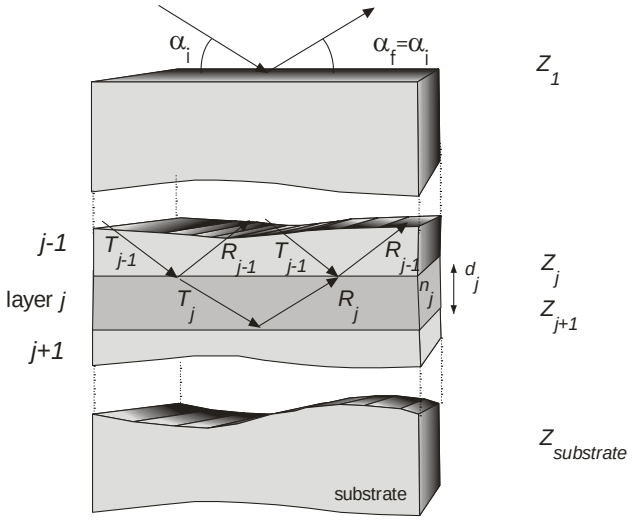

Fig. 4.5: Reflection and refraction of a plane wave at a system of multiple interfaces. The system shown in this figure consists of N+1 layers with refractive indices n_j and thicknesses d_j separated by N interfaces. A recursive approach allows calculating the reflectivity (see text).

$$X_j = \frac{R_j}{T_j} = \mathrm{e}^{-2\mathrm{i}k_{z,j}z_j}\,\frac{r_{i,j+1} + X_{j+1}\mathrm{e}^{-2\mathrm{i}k_{z,j+1}z_j}}{1 + r_{i,j+1}X_{j+1}\mathrm{e}^{-2\mathrm{i}k_{z,j+1}z_j}}\,, \qquad \textbf{(4.19)}$$

with

$$r_{i,j+1} = \frac{k_{z,j} - k_{z,j+1}}{k_{z,j} + k_{z,j+1}}\,. \qquad \textbf{(4.20)}$$

Recursive application of (4.19) with $R_{N+1} = X_{N+1} = 0$ yields after N iterations the reflectivity

$$R = |X_1|^2 = |R_1|^2\,. \qquad \textbf{(4.21)}$$

4.1.4 Interface Roughness

In practice, the abrupt jump of the index of reflection cannot be observed since interface roughness occurs at basically every interface leading to a reduced reflectivity. If the deviation of the average interface follows a Gaussian distribution, Eq. (4.20) has to be substituted with the modified Fresnel coefficients

$$\tilde{r}_{i,j+1} = r_{i,j+1}\mathrm{e}^{-2k_{z,j}k_{z,j+1}\sigma_j^2}\,, \qquad \textbf{(4.22)}$$

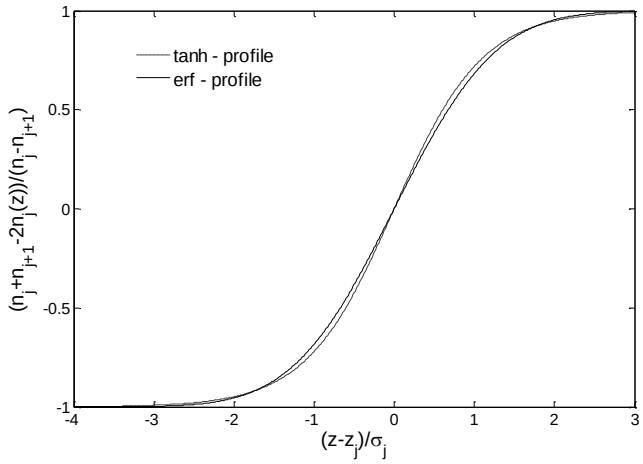

Fig. 4.6: Normalized Gaussian (solid line) and hyperbolic tangent function (dashed line) roughness induced refractive-index profiles $n_j(z)$. The two profiles are very similar with the difference always being less than 5%. The probability density corresponding to the Gaussian profile is $P_j(z) \sim \exp(-z^2)$, and that corresponding to the tanh profile is $P_j(z) \sim \cosh^{-2}(z)$.

where σ_j is the full width of half maximum of the Gaussian height distribution around the average interface position. For immiscible polymers a hyperbolic-tangent function form of the roughness distribution is reported [Helfand'72, Helfand'89, Broseta'90, Tang'91, Schubert'96] which is given by

$$n_j(z) = \frac{n_j + n_{j+1}}{2} - \frac{n_j - n_{j+1}}{2} \tanh\left(\frac{\pi}{2\sqrt{3}} \frac{z - z_j}{\sigma_j}\right) \qquad \textbf{(4.23)}$$

and the Fresnel coefficient from Eq. (4.20) becomes

$$\tilde{\tilde{r}}_{i,j+1} = \frac{\sinh\left[\sqrt{3}\sigma_j\left(k_{z,j} - k_{z,j+1}\right)\right]}{\sinh\left[\sqrt{3}\sigma_j\left(k_{z,j} + k_{z,j+1}\right)\right]}. \qquad \textbf{(4.24)}$$

The differences in these two models are relative small (<5%), see Fig. 4.6, and in this work the interface roughness of polymer films are fitted with Eq. (4.22).

The surface morphology of a dewetted film can be described in approximation by a discrete distribution of heights [Pukite'85]. In a simple model, on the silicon substrate there are disc shaped droplets of uniform height d. In the coherent reflection curve, a surface region perturbed in this way acts as a thin, homogeneous layer with a reduced optical density $\delta = p_1\delta_1$ and $\beta = p_1\beta_1$ with the surface fraction of island coverage p_1 [Sinha'94, Stommer'96, Holy'99]. The

interfaces on the top of the islands and the substrate give rise to interference fringes corresponding to the island height *d*. This surface morphology does not give rise to a surface roughness of the layer in the reflectivity fit, which originates from a Gaussian distribution of heights. At the interfaces additional Gaussian roughness can occur which will damp the reflectivity as shown in Eq. (4.22). The reflectivity is [Holy'99]

$$R = \left|\mathrm{e}^{\mathrm{i}(1-p_1)k_z d}\left(\tilde{r}p_1 + \tilde{r}(1-p_1)\mathrm{e}^{\mathrm{i}k_z d}\right)\right|^2 . \qquad \textbf{(4.25)}$$

4.2 Off-Specular Scattering

As shown in Section 4.1.4, surface or interface roughness damps the intensity in the specular reflected beam. The missing intensity is diffusely scattered in other directions, i.e. in off-specular directions. The diffusely scattered intensity provides information about lateral inhomogeneities. Extensive reviews about off-specular scattering can be found e.g. in [Holy'99, Tolan'99]. Usually the off-specular intensity is measured by grazing incidence small angle x-ray / neutron scattering (GISAXS / GISANS) [Levine'89]. In other words, GISAXS / GISANS is small angle x-ray / neutron scattering in transmission (SAXS/SANS) [Glatter'82] sensitive to the interface region. The SERGIS technique (Chapter 2) translates the information of the angular intensity distribution in one dimension to a neutron polarisation amplitude, which is under certain conditions proportional to the generalised Patterson function in real space (see Section 2.4.3).

To treat the off-specular scattering, it is convenient to write the scattering length or electron density as the sum of the laterally averaged density $\varrho(z) = \langle\varrho(\vec{r})\rangle_{(\mathrm{x,y})}$ and fluctuations $\delta\varrho(\vec{r})$

$$\varrho(\vec{r}) = \varrho(z) + \delta\varrho(\vec{r}) , \qquad \textbf{(4.26)}$$

with the z-component of $\vec{r}$ pointing in the direction perpendicular to the sample surface. The vertical profile of the laterally averaged density $\varrho(z)$ gives rise to the specular reflectivity and $\delta\varrho(\vec{r})$ to the diffuse scattering. The two contributions are illustrated for the case of a microphase separated dewetted polymer film in Fig. 4.7.

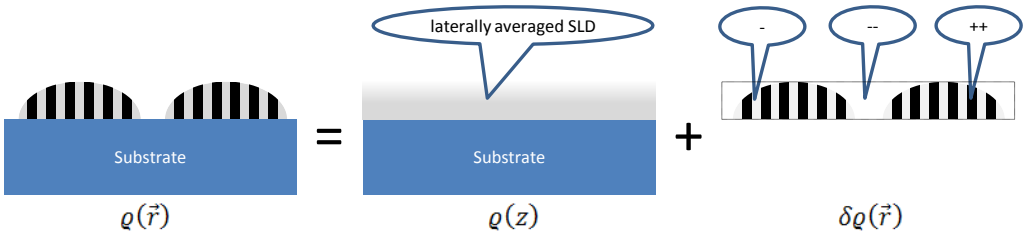

Fig. 4.7: The scattering length density (SLD) of microphase separated diblock copolymer droplets can be modelled by a film with laterally averaged scattering length density plus deviations. The film structure gives rise to the specular reflectivity and the lateral deviations to the diffuse scattering. In the DWBA, the laterally homogeneous film is treated dynamically and the deviations are treated as small perturbations.

In the next subsection, the kinematical formulation of surface scattering is outlined for a single surface. The extension to multilayer is given afterwards within the framework of the more complex distorted wave Born approximation (DWBA).

4.2.1 Kinematical Theory

In the kinematical theory multiple scattering and attenuation effects are neglected. The scattering function $S(\vec{q})$ is the squared modulus of the spatial Fourier transform of the scattering-length density $\varrho(\vec{r})$. This is equivalent to [Liang'88]

$$S(\vec{q}) = \iint \varrho(\vec{r})\varrho(\vec{r}')\mathrm{e}^{\mathrm{i}\vec{q}(\vec{r}-\vec{r}')}\mathrm{d}r\,\mathrm{d}r' \,. \qquad \textbf{(4.27)}$$

The scattering cross section and hence the scattering intensity is proportional to $S(\vec{q})$.

4.2.2 Distorted Wave Born Approximation

The first order distorted wave born approximation was first applied by G. Vineyard in 1982 [Vineyard'82]. S. Sinha et al. calculated the scattering of a rough surface in DWBA [Sinha'88] in 1988, later R. Pynn described the scattering of a single rough layer on a rough substrate in DWBA [Pynn'92]. The DWBA for GISAXS from a diblock copolymer film is discussed in [Busch'06].

The treatment of the diffuse scattering is similar to that of the specular reflectivity. The transmission coefficients are, c.f. Eq. (4.15),

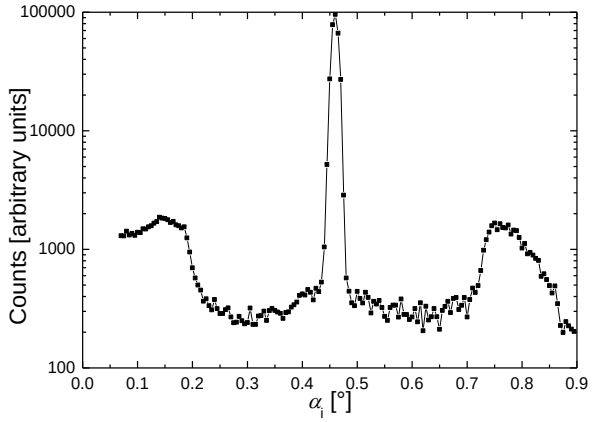

Fig. 4.8: Rocking scan recorded at $\alpha_i + \alpha_f = 0.9°$ with x-ray radiation ($\lambda = 1.54$ Å) on an initially 500 Å thick dewetted diblock copolymer film (poly(styrene-block-isoprene)). The maxima at $\alpha_i = 0.15°$ and 0.75° are the Yoneda peaks. The central peak is due to the specular reflection.

$$t_{\mathrm{i}}(\alpha_{\mathrm{i}}) = \frac{2k_{\mathrm{i,z}}}{k_{\mathrm{i,z}} + k_{\mathrm{t,z;i}}}, \tag{4.28}$$

and

$$t_{\mathrm{f}}(\alpha_{\mathrm{f}}) = \frac{2k_{\mathrm{f,z}}}{k_{\mathrm{f,z}} + k_{\mathrm{t,z;f}}}. \tag{4.29}$$

The diffuse scattering from a single rough surface is given by [Sinha'88]

$$I_{diff} \sim |t_{\mathrm{i}}(\alpha_{\mathrm{i}})|^2 S(\vec{q}) |t_{\mathrm{f}}(\alpha_{\mathrm{f}})|^2 \tag{4.30}$$

with

$$S(\vec{q}) = \frac{(\Delta\varrho)^2}{\left|q_{\mathrm{z,t}}\right|^2} e^{-\left[(q_{\mathrm{z,t}})^2 + (q_{\mathrm{z,t}}^*)^2\right]\frac{\sigma^2}{2}} \iint \left[e^{|q_{\mathrm{z,t}}|^2 C(\vec{R})} - 1\right] e^{-\mathrm{i}\vec{q}_{\parallel}\vec{R}} \mathrm{d}\vec{R}\,, \tag{4.31}$$

where the "*" denotes the complex conjugate. Here $\vec{R}$ is a vector in the plane of the sample surface and $C(\vec{R})$ is the height-height correlation function of the rough surface with roughness σ. Local maxima of the diffuse scattering are observed for $\alpha_i \approx \alpha_c$ or $\alpha_f \approx \alpha_c$. These maxima arise from the transmission functions (Eq. (4.28) and (4.29)) and are named after Y. Yoneda who reported them first in in 1963 [Yoneda'63]. A rocking scan recorded at $\alpha_i + \alpha_f = 0.9°$ with x-ray radiation ($\lambda = 1.54$ Å) on an initially 450 Å thick dewetted diblock copolymer

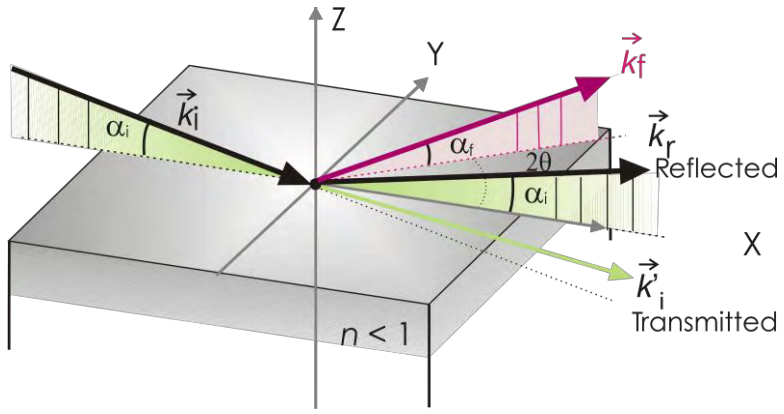

Fig. 4.9: Scattering geometry of a grazing incidence experiment.

film is displayed in Fig. 4.8. The Yoneda peaks appear at $\alpha_i = 0.15°$ and $\alpha_i = 0.75°$, where the latter value corresponds to $\alpha_f = 0.15°$.

The diffuse scattering intensity is proportional to the square of the scattering length density contrast $(\Delta\varrho)^2$. In the case of interfaces of two different polymers, the diffuse scattering is usually difficult to measure with x-ray radiation, since the electron densities in many polymers are similar. Therefore, polymer characterisation is a typical application for neutron scattering.

4.3 Application of the Scattering Theory to SERGIS

The scattering geometry of a grazing incidence experiment is displayed in Fig. 4.9. For intensity reasons, to measure SERGIS it is convenient to take advantage of the signal amplification at the critical angle, also called Yoneda peak (Section 4.2.2). This signal amplification occurs at $\alpha_i \approx \alpha_c$ and at $\alpha_f \approx \alpha_c$. To achieve a good discrimination of the scattering signal (located, e.g., at the Yoneda position at $\alpha_f \approx \alpha_c$) and the reflected beam (located at $\alpha_f \approx \alpha_i$), the incident angle should in principle be chosen large enough such that the two signals are well separated on the detector and, if possible, of comparable intensity. Also, with increasing incident angle the fraction of the direct beam that interacts with the sample increases linearly. In practice, however, the steep decrease of both the reflected and the scattered intensity with increasing incident angle turns out to be more important, so that for intensity reasons the incident angle often needs to be chosen as small as possible. For experimental reasons it is convenient to choose

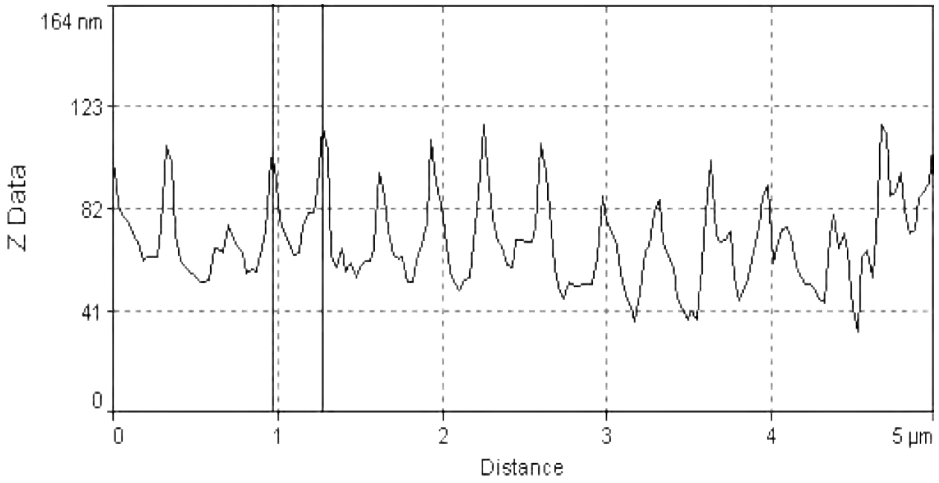

Fig. 4.10: Atomic force microscope (AFM) line scan of the optical grating with a super-sharp tip to minimise smearing due to convolution effects with the tip shape. Reproduced from [Wahl'02].

$\alpha_i = \alpha_c + 0.1° \ldots 0.2°$. This usually allows to discriminate the specular reflection and the Yoneda peak sufficiently well in the detector images.

4.3.1 Scattering Signal from an Optical Grating

In the course of this work, a 1D-periodic grating was used repeatedly as a test sample for a comparative study of different SERGIS options and later as a reference sample for SERGIS studies on dewetted block-copolymer films. The grating consists of parallel grooves of ~ 60 nm depth in a gold layer of 800 nm thickness. The nominal groove density is 3600 lines / mm, resulting in a grating period of 278 nm. The exact shape of the grating is unknown. The height profile is specified as sinusoidal by the manufacturer. In contrast to these specifications, the AFM measurement in Fig. 4.10 shows sharp steep walls with wide spacings in-between. The AFM linescan only gives a lower limit of the steepness of the walls and width of the grooves, since the tip used to scan the surface is not infinitively thin and has a pyramidal shape-giving rise to a flattening of any steep features.

In the following, the scattering at the optical grating will be discussed in DWBA. The one-dimensional periodic structure gives rise to a row of Bragg rods perpendicular to the sample surface. The elongation perpendicular to the sample surface is inversely proportional to the height of the grating and can be assumed infinite for the following discussion. The Ewald construction yields several

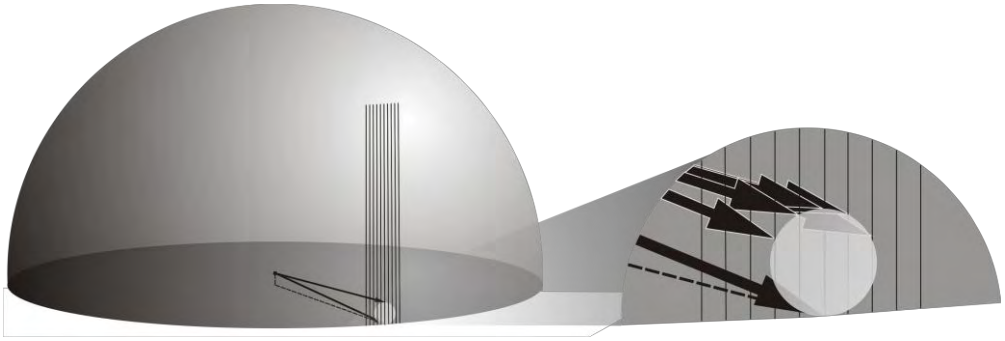

Fig. 4.11: Ewald construction. The optical grating gives rise to Bragg rods perpendicular to the substrate surface. For grazing incidence diffraction, the Ewald sphere only intersects a few times with the Bragg rods.

diffraction peaks, see Fig. 4.11. If the grating is oriented with the walls parallel to the x-direction, the intersection of the Ewald sphere with the plane defined by the Bragg rods (the x-z-plane) is a circle with the radius k_{iz}. With increasing incident angle, i.e. increasing k_{iz}, the number of intersections of the Ewald sphere and the Bragg rods increases. At small incident angles the Ewald construction only gives access to a quite limited q_y range, defined by the condition $q_y < k_{iz}$. (Note that contributions from q_y values equal or very close to k_{iz} are negligible since under this condition the outgoing angle α_f and hence the corresponding transmission function would be zero.) This limitation of the q_y range contributing to the scattering signal has to be kept in mind when interpreting SERGIS data in detail, because cutting off high frequency contributions in reciprocal space can lead to a smearing of features in the final real-space SERGIS data set.

Under ideal experimental conditions (perfect wavelength resolution, negligible beam divergence, infinite sample size, etc.), at any given outgoing angle (or q_z value) only one specific q_y value contributes to the scattering signal. For a SERGIS measurement, in which as many Fourier components as possible should be collected, this implicates the necessity to expand the region of interest to a larger range spanning from $\alpha_f = 0$ to $\alpha_f \sim \alpha_i$. Yet, this introduces a complication for the data analysis since one integrates over scattering intensities (or Fourier components) that carry transmission functions evaluated for different α_f values as a weight factor, see Eq. (4.29).

In a thorough analysis, both the limitations of the contributing q_y range and the α_f dependence of contributing intensity weight factors have to be taken into account. Both effects can be summarized in the following way: A SERGIS data set cannot always be directly interpreted as the real-space autocorrelation function of the scattering length density, because different Fourier components of the ideal scattering signal may be differently weighted or completely cut off in the data recording.

In Fig. 4.12, the scattering signal of the optical grating is displayed for different incident angles. In contrast to the SERGIS measurements discussed later, in these conventional GISANS measurements, no coil material was in the neutron beam path. The white vertical line corresponds to $q_y = 0$. The other vertical lines correspond to the expected Bragg rod positions of the grating and thus exhibit a relative spacing of $2\pi / 278\ \mathrm{nm}^{-1}$ in reciprocal space. Due to the divergence of the incident neutron beam in y-direction, the Bragg peaks are smeared out in z-direction (as a consequence of the Ewald construction, cf. Fig. 4.11). The amplification due to the Yoneda maximum in the transmission function is clearly visible.

4.3.2 Scattering Signal from a Thin Film Structure

In this paragraph, the scattering signal of a thin film on a substrate will be discussed. Locally the scattering length distribution in the film can be arbitrary and might have a certain preferred orientation, for example a lamellar structure. It is assumed, however, that averaged over the sample surface many domains with random orientations exist. Hence, the scattering signal shall be smeared out into a feature with circular symmetry in reciprocal space. The structure in the film can thus be compared to a two-dimensional powder. It is further assumed that the film is very thin and the incident angle comparatively small ($2\pi/d >> q_z$), so that the structure factor can be approximated by cylinders perpendicular to the sample surface. In Fig. 4.13 the Ewald construction is shown for three cylinders of different diameters. It elucidates that at a given q_z value (defined by a certain combination of λ, α_i, and α_f), all in-plane momentum vectors $q_{\|}$ fulfilling

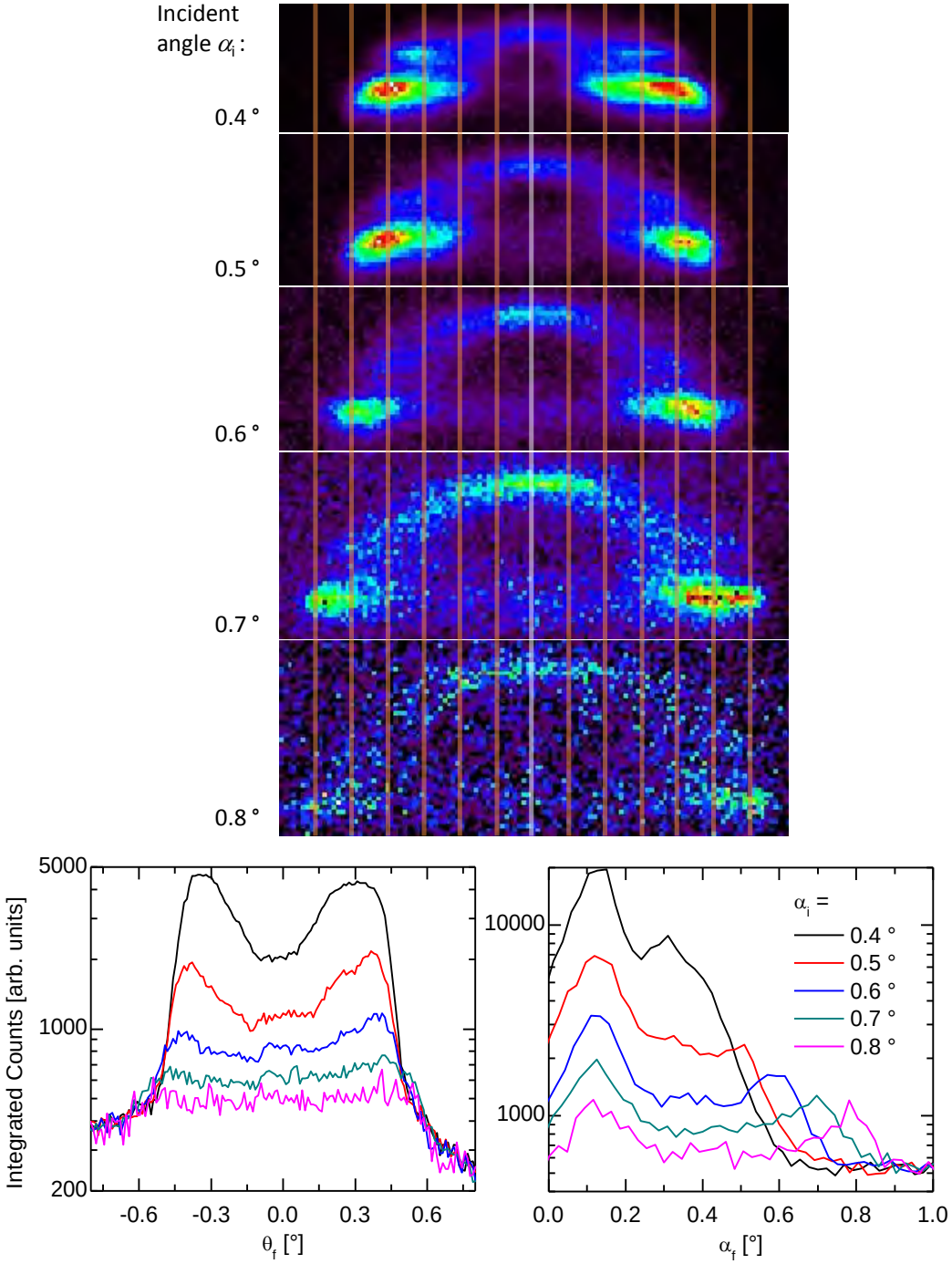

Fig. 4.12: Top: Conventional GISANS scattering signal of the optical grating for different incident angles. The vertical white line corresponds to no scattering in x-direction. The other lines denote the reciprocal lamella spacing (270 nm). The grooves are aligned in x-direction and the average beam direction of the incident beam lies in the x-z-plane. Bottom: Vertically and horizontally integrated intensity.

$k_i(\cos\alpha_f - \cos\alpha_i) < q_\parallel < k_i(\cos\alpha_i + \cos\alpha_f)$ can be addressed. For $\lambda = 5.5$ Å, $\alpha_i = 0.4°$, and $\alpha_f = 0.2°$ this corresponds to $0.00021\ \mathrm{nm}^{-1} < q_\parallel < 23\ \mathrm{nm}^{-1}$.

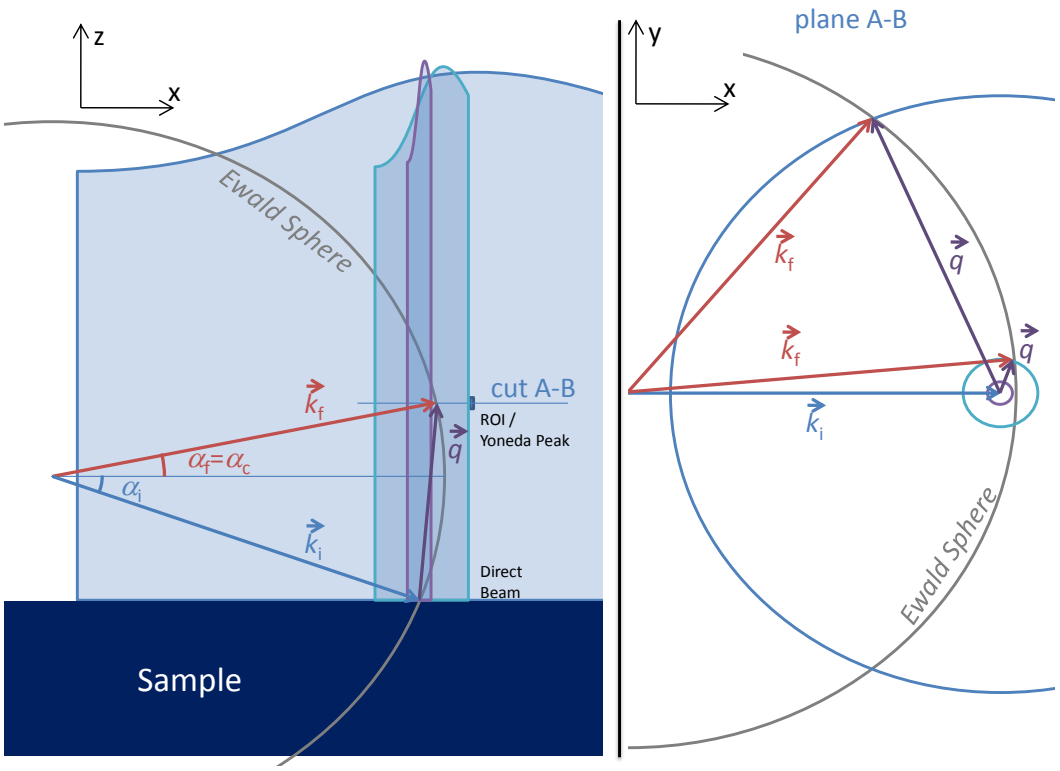

Fig. 4.13: Ewald construction for three cylinders of different diameter in reciprocal space, each of which represents a collection of Bragg rods of a two-dimensional powder. For clarity the incident and outgoing angles α_i and α_f are chosen larger than in reality. Very large structures give rise to cylinder shaped powder rings with a small radius in reciprocal space that do not intersect with the Ewald sphere at the chosen α_f value, which is smaller than α_i. Note that this situation is quite relevant in practice, since in a SERGIS experiment α_f also has to be sufficiently smaller than α_i in order to be able to discriminate the specular reflected and the diffuse intensity. This condition poses an upper limit to the length scales about which information can be obtained in a SERGIS measurement.

To measure SERGIS on isotropic surface morphologies, α_f can be restricted to a narrow region close to the critical angle α_c (Yoneda peak). In this case, the α_f dependence of the transmission function and the q_z dependence of the scattering function become irrelevant for the SERGIS analysis, because they cancel in the calculation of the polarisation from the scattering intensity. For medium size structures as represented by the medium size cylinder in Fig. 4.13, the $q_{\parallel}$ vectors at the intersection of the cylinder and the Ewald sphere are approximately parallel to the y-direction, i.e. $q_{\parallel}$ can be identified with q_y. For very large and very small structures, however, the scattering can no longer be considered to be mainly in

y-direction, hence structures of these length scales are not reproduced correctly by SERGIS. For λ = 5.5 Å, α_i = 0.4, and α_f = 0.2, the $q_\parallel$ vectors compatible with the Ewald construction are approximately parallel to the y-direction to within $\pm 15°$ ($\pm 1°$) under the condition $0.00081\ \mathrm{nm}^{-1} < q_\parallel < 5.91\ \mathrm{nm}^{-1}$ ($0.012\ \mathrm{nm}^{-1} < q_\parallel < 0.041\ \mathrm{nm}^{-1}$). Translated in real space, this means that correlations between 1 nm and 7790 nm (15 nm and 540 nm) can be reproduced. If the scattering cross section is weak, the kinematical theory can be applied and the generalised Patterson function in one dimension can be measured with SERGIS.

4.3.3 Comparison of the Scattering Signal from a 1D and 2D Structure

In the following the scattering of an optical grating as described in Section 4.3.1, yet with a rectangular profile, and the scattering of a two-dimensional powder-like structure as described in Section 4.3.2 will be compared with respect to the intensity of the scattered signal. In both cases, the structure is characterised by a lamellar type of order. In the case of the optical grating, this structure extends over the whole sample. In the powder like sample, the lamellar structure is restricted to domains of circular shape. The orientation of the structure in each domain is random. This model allows a simplified description of dewetted microphase separated diblock copolymer films with the lamella period vector parallel to the sample surface. The scattering cross section in this model is normalized to one. Both structures are depicted in the top panel of Fig. 4.14. In the middle part of this figure, the Fourier transformation, i.e. the simulated intensity distribution in the plane of the sample surface, is shown, based on a kinematic scattering approach. In the bottom panel of Fig. 4.14 the scattering function along the y-axis is displayed. For the optical grating, the local maxima at $q_\parallel \neq 0$ are approximately 1.5 orders of magnitude higher than for the powder-like sample, where the intensity is smeared out over an in-plane angle of 360°. Due to the much higher intensity, the optical grating is a suitable sample for proof of principle SERGIS experiments, although the generalized Patterson function cannot be correctly reproduced (as discussed in Section 4.3.1).

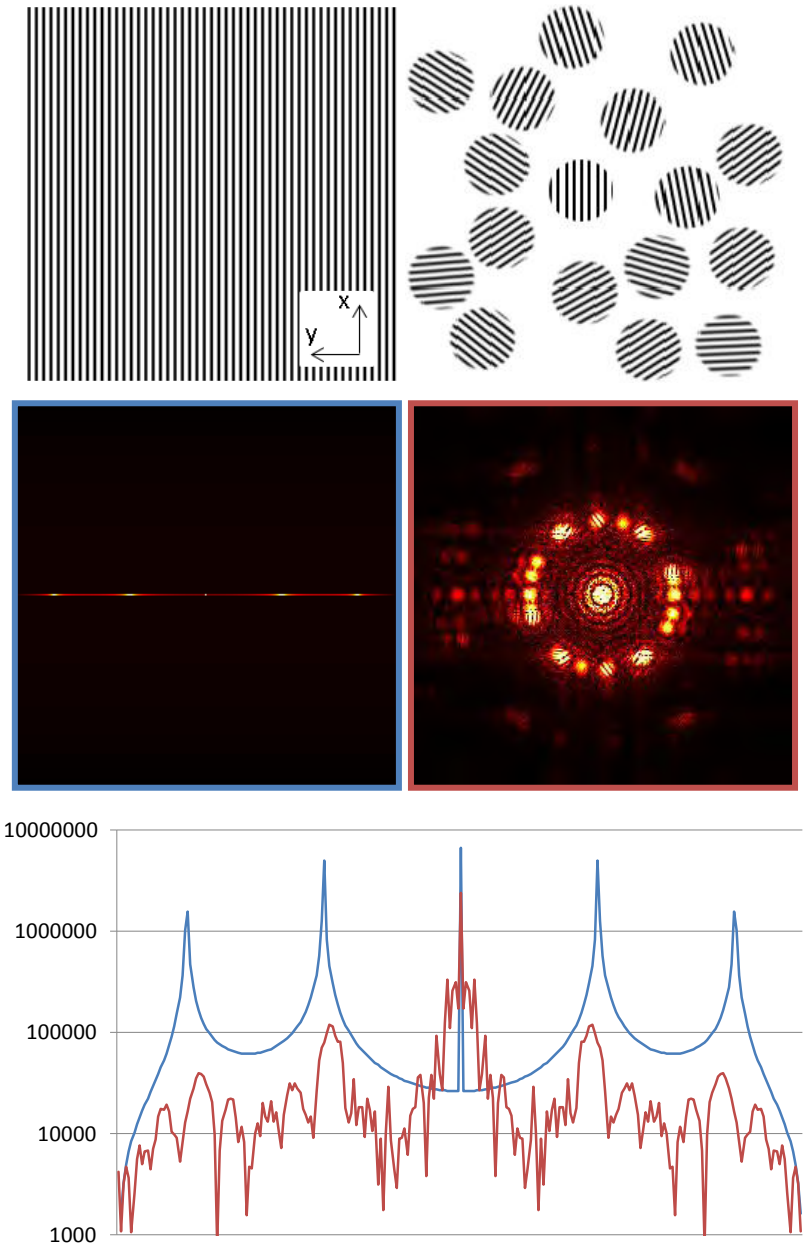

Fig. 4.14: Real space model (top) and FFT (middle) of the optical grating (left) and a model of droplets with microphase separation (right). Magnitude of the Fourier transform i.e. scattered intensity of the optical grating (blue line) and the droplets with microphase separation (red line) in y- direction (bottom).

5 Experimental Facilities and Techniques

In this chapter a brief introduction in the experimental facilities and techniques besides SERGIS will be given. First the neutron source will be discussed followed by the x-ray source and the atomic force microscope (AFM).

5.1 Neutron Source

The generation of low energy neutrons is described in this section. The neutron measurements in the frame of this work were conducted at the research neutron reactor FRM II (Fig. 5.1) in Garching bei München.

5.1.1 Neutron Reactor

The reactor core of FRM II is very small, it is a compact core, but its power density of more than 1MW per litre nuclear volume is larger than that of a nuclear plant. Although the thermal power is limited to 20 MW, a maximum unperturbed

Fig. 5.1: Research neutron source Heinz Meier-Leibnitz (FRM II). The big central building hosts the reactor core. The flat neighbouring building on the right is the neutron guide hall where *N-REX*$^{+}$ is located. © W. Schürmann / FRM II, TU München

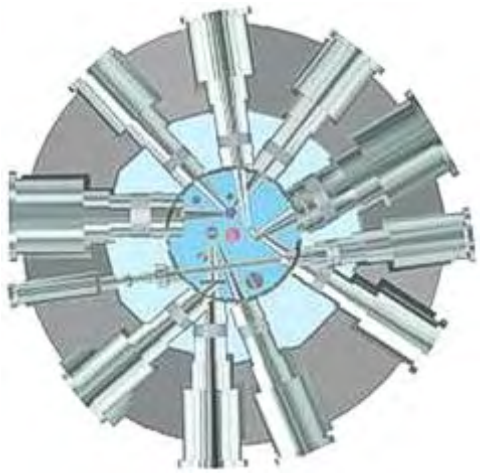

Fig. 5.2: Horizontal cross-section (simplified) through the reactor pool filled with H_2O. The fuel element is located in the centre. © FRM II / TU München

thermal neutron flux of approximately 8 x 10^{14} $cm^{-2}s^{-1}$ is obtained.

The reactor design of the FRM II, see Fig. 5.2, results in extremely favourable background conditions. The basis for this is the particularly compact reactor core, consisting of only one fuel element with a mass of 8 kg which is cooled with light water H_2O. The fuel element is arranged centrally in a large moderator tank which is filled with heavy water D_2O. The moderator tank has a diameter and height of approximately 2.5 m. The whole installation is inside the reactor pool with an internal diameter of approximately 5 m. Due to the low absorption levels of D_2O, in comparison with light water, and the high level of leakage of fast neutrons from the compact core, a pronounced maximum of thermal neutron flux density builds up outside the core. This maximum is located approx. 12 cm from the core surface, which makes it very readily accessible for experimental use. The secondary neutron sources (cold and hot sources) are also to be found in this area.

5.1.2 Cold Source

The cold neutron source is a cooled auxiliary moderator, in which a spectrum of low-energy neutrons is generated with a Maxwell distribution centred on approximately 5 meV. The moderator consists of cold, liquid deuterium. It offers the highest gain factor for cold neutrons due to the low neutron absorption rate for deuterium.

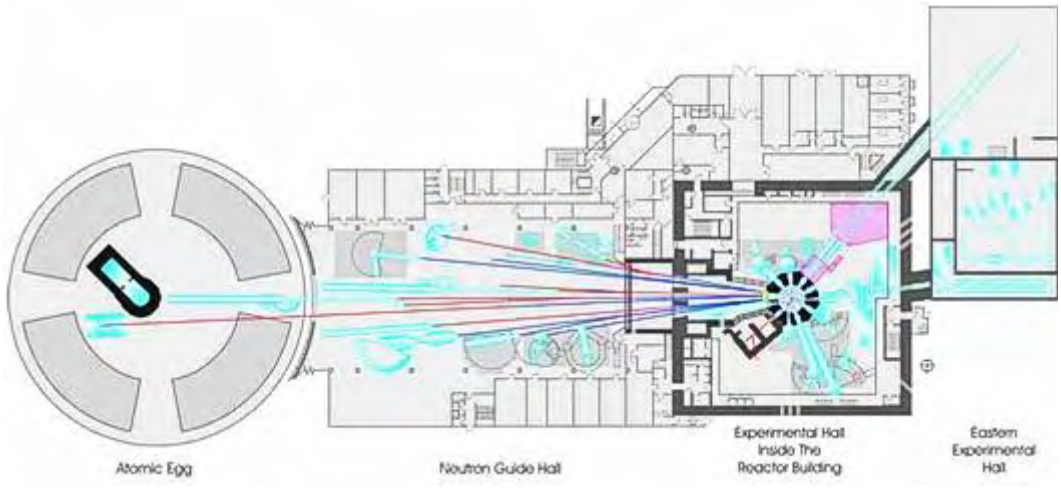

Fig. 5.3: Beam tubes and neutron guides are used for supplying the experiments with neutrons. © FRM II / TU München

The cold neutrons produced in the cold source are fed to the neutron instruments by means of six beam tubes with neutron guides (see next section). A special vertical beam tube is immersed directly in the moderator vessel and allows particularly cold neutrons with energies of around 200 μeV to flow out in an upwards direction. The average integral neutron flux density in the cold source is approximately $3x10^{14}$ $cm^{-2}s^{-1}$ (at a nominal reactor power of 20 MW; perturbed by flux depression), resulting in a cold neutron flux density of $1x10^{13}$ $cm^{-2}s^{-1}$.

5.1.3 Neutron Guide

From the cold source the neutrons are guided in a so called neutron guide to the instruments in the neutron guide hall. The optical properties of the neutron guide walls lead to a total reflection of thermal to cold neutrons. The instruments can hence be situated some distance away from the reactor core. The path of a neutron may be modified within certain limits by varying the reflection conditions on the guide walls. The inner wall of the neutron guide (NL-1) supplying neutrons for *N-REX*$^+$ (Fig. 5.4) is coated with a $m = 2$ supermirror, which means that the measured mirror constant $\alpha_c = 0.2° \lambda$ [Å] is twice the calculated mirror constant of a conventional neutron guide coated with nickel, which is $\alpha_c = 0.1° \lambda$ [Å] ($m = 1$ mirror).

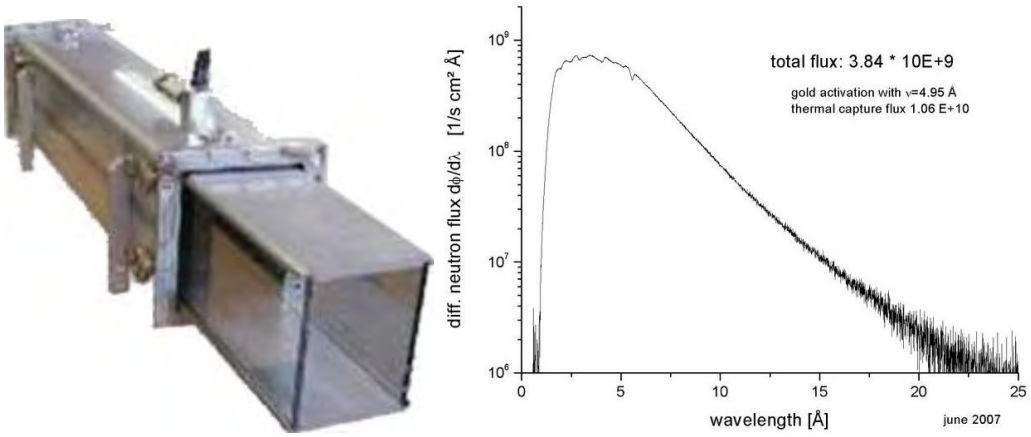

Fig. 5.4: Neutron guide without shielding: The rectangular glass tube guiding neutrons by total reflection. Reproduced from: http://www.frm2.tum.de/en/technik/beamguidance-of-the-neutrons/neutron-guides/index.html and flux measurement at the end of the neutron guide NL-1. Reproduced from [Klenke'08]

5.2 Neutron Reflectometer *N-REX*$^+$

The SERGIS and neutron reflectivity experiments were conducted at the instrument *N-REX*$^+$ (

Fig. 5.5) [Rühm'06], which is operated by the Max Planck Institute for Metals Research in Stuttgart in the framework of the focused neutron research imitative of the Max Planck Society. *N-REX*$^+$ is a "Tanzboden" instrument in the neutron guide hall of the FRM II and uses a monochromatic beam extracted from the cold source via the neutron guide NL-1. The instrument is equipped with a horizontally focussing highly oriented pyrolithic graphite (HOPG) monochromator providing a wavelength resolution of 1 - 2%. A single monochromator crystal provides a divergence of $\pm$ (0.3 - 0.4)° full width at half maximum, or $\pm$ (0.6 - 0.8)° full width. A two-dimensional ^{3}He wire chamber serves as neutron detector (Section 3.2.5). As additional equipment a compact add-on x-ray reflectometer (Section 5.3) and the spin-echo equipment (Chapter 3) is available. Various different sample environments are available, e.g. horizontal or vertical sample orientation, magnetic fields up to 7.5 T, cryostats with low temperatures down to 4 K or less, low pressure atmosphere of various gases or vapours (T < 300°C), large diameter silicon liquid film cell, active anti-vibration device for experiments

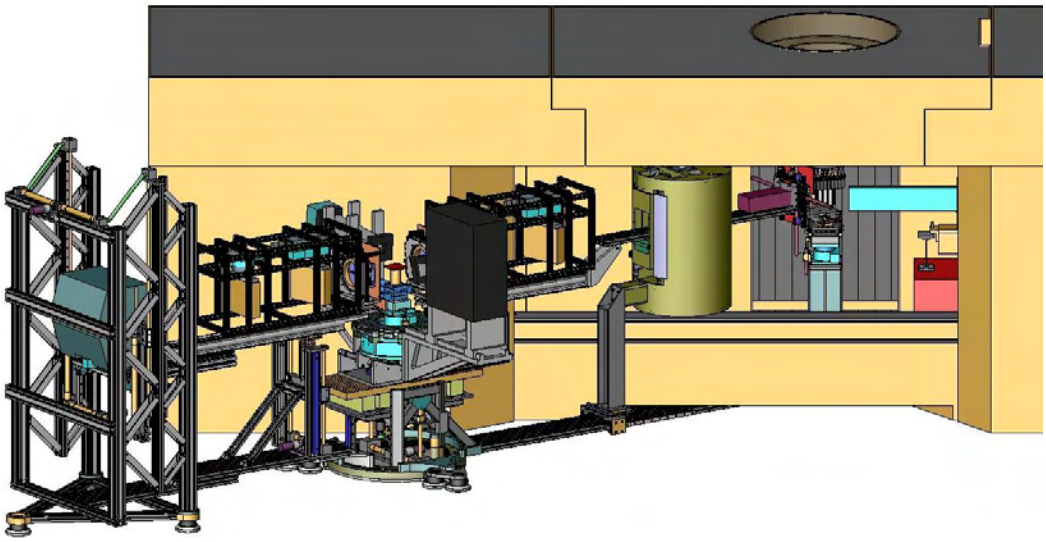

Fig. 5.5: **Neutron reflectometer *N-REX*$^+$.**

on free liquid surfaces, liquid thermostat for cooling and heating to medium temperatures, and a medium pressure (p < 10 bar) gas cell with silicon substrate.

The technical instrument parameters are a wavelength range of 2 – 6 Å, a maximal incidence angle of 5° (this restriction only applies for the liquid mode, where the sample is always kept horizontal and the incident beam can be tilted downwards), a maximal exit angle of 20°, a maximal out-of-plane q (specular) of 0.55 Å^{-1}, a maximal q within the reflection plane of 1.35 Å^{-1}, a maximal in-plane q (grazing angle diffraction) >5.4 Å^{-1}, a total flux at the monochromator of 4x10^9 neutrons/(cm^{2}s), a maximum flux at the monochromator of $4 \cdot 10^8$ neutrons/(cm^{2}sÅ) (at 4 Å), and a monochromatic flux for reflectometry at the sample position of $3 \cdot 10^6$ neutrons/(cm^{2}s) (estimated).

The beam size and divergence is defined by two motor controlled pairs of silts. The first pair of slits is situated directly behind the monochromator and the second pair directly before the sample position. For the presented experiments, a dedicated filter for the higher harmonics being scattered by the monochromator was missing. To avoid the higher harmonics a silicon mirror or the polarising mirror was used at sufficient high angle where reflection of the undesired wavelength was negligible. If the aforementioned was not possible, a special fit routine was used to include the higher order wavelength contribution in the data analysis. The higher order contribution was especially dominant when the

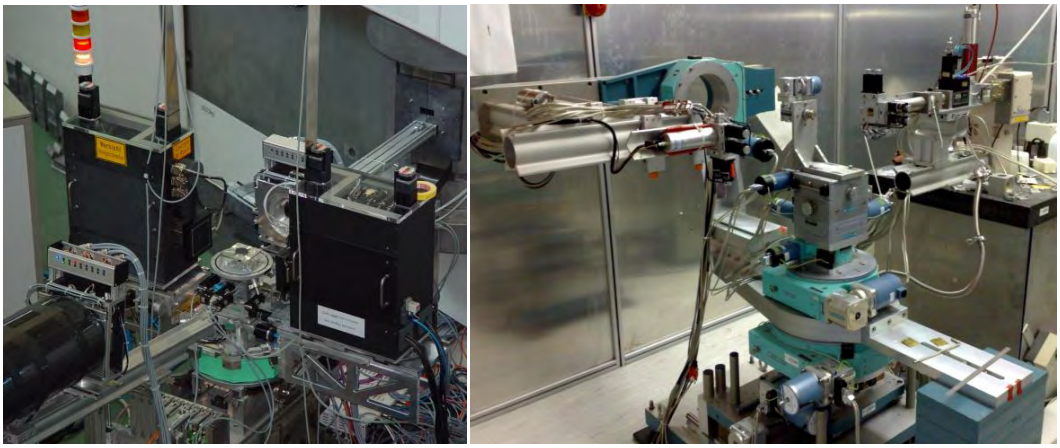

Fig. 5.6: X-ray diffractometer: left two circle diffractometer at *N-REX*$^+$, right six circle diffractometer at the Max-Planck-Institute for Metals Research.

absorber was used, since the absorption cross section is proportional to the wavelength λ and hence neutrons with the wavelength λ were absorbed twice stronger than those with $\lambda/2$.

5.2.1 Neutron Reflectivity Set-Up

The specular and off-specular neutron reflectivity experiments were realised in horizontal sample geometry. This means that the incident beam is ideally horizontal. The incident angle is set by tilting the sample around a horizontal axis perpendicular to the incident beam direction at an angle α_i. The in-plane and out-off-plane angle can be set independently by rotating the detector on a large scale in the vertical and horizontal direction around the sample position or defining a region of interest on the detector to cover the small angle deviation from a position of the detector. To block the direct beam after the sample position a motor controlled cadmium absorber can be installed in order to suppress an elevated background by i.e. air scattering of the direct beam.

5.3 X-Ray Facilities

The x-ray reflectometers (Fig. 5.6) are situated at the *N-REX*$^+$ instrument in Garching and at the Max-Planck-Institute for Metals Research in Stuttgart. These x-ray facilities were equipped with copper targets and the analysers were set to filter $K_{\alpha 1}$ (8047 eV) at a wavelength of 1.54 Å (MPI-MF), at *N-REX*$^+$ due to the

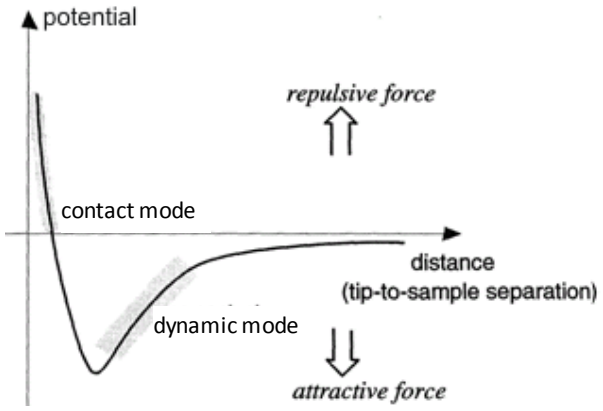

Fig. 5.7: Force distance curve as a function of the tip to sample separation. The potential is a sum of the short range interaction (Morse potential) and long range (van der Waals) potential and in the case of a conductive tip and sample, an electrostatic potential difference.

very compact set-up $K_{\alpha 1}$ and $K_{\alpha 2}$ (8027 eV) cannot be discriminated. The advantage of the two-circle x-ray reflectivity add-on at *N-REX*$^+$ is the easy combination of x-ray reflectivity and neutron measurements, especially when the sample is modified on the diffractometer. The advantage of the six-circle set-up in Stuttgart is the more sophisticated instrument with a better monochromator, a higher flux and lower background, a less divergent beam and the possibility to measure also off-specular x-ray reflectivity to a limited degree.

5.4 Atomic Force Microscopy

The atomic force microscope (AFM) can measure forces in the order of 1 µN to 1 nN between the AFM tip and the sample surface. Typical lateral resolutions are in the range of 5 – 20 nm. The AFM was developed in 1985 by Binnig et al. [Binnig'86] and is an offspring of the scanning tunnelling microscope [Binning'82]. In an AFM, the force between the sample and tip is detected. By scanning the sample or in the case of large area scanners the cantilever the morphology of an area can be mapped by feedback of the distance dependent force. An overview article can e.g. by found in [Giessibl'06].

The AFM can be used either in a static or dynamic mode. In the static mode, also referred to as repulsive mode or contact mode [Binnig'86], a sharp tip at the end of a cantilever is brought in contact with a sample surface. The deflection of the

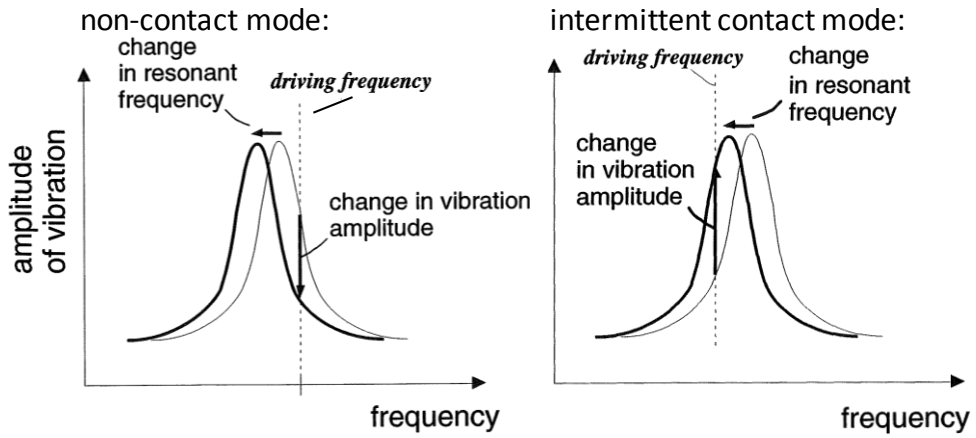

Fig. 5.8: In dynamic AFM operation mode the cantilever is driven at a fixed frequency above (non-contact) or below (intermittent contact) resonance. In non-contact mode (left), the oscillation amplitude is decreasing and in intermittent contact mode (right), the oscillation amplitude is increasing by approaching the sample.

cantilever, which is a result of repulsive forces acting between the tip and the sample surface, is sensed (Fig. 5.7).

In the dynamic AFM operation mode, also referred to as attractive force imaging, the tip is brought at a distance few nanometres from the sample (Fig. 5.7). Very weak van der Waals forces are present in the close vicinity of the sample interface. The advantage of this technique is that it is non-destructive, because of the weak interaction. However, this mode is usually slower than the contact mode. Here, AFM images are obtained in such a way that the cantilever is driven at a fixed frequency near resonance, and changes in its amplitude are detected (amplitude modulation mode [Martin'87]). Two methods to measure in dynamic AFM operation mode exist. In non-contact mode a drive frequency slightly higher than the free-space resonance frequency of the cantilever is selected so that the amplitude decreases significantly as the cantilever is brought closer to the sample surface (Fig. 5.8 left panel). In the so-called tapping mode or intermittent contact mode, a cantilever drive frequency slightly inferior to the free-space resonance frequency is chosen and hence the oscillation amplitude increases by approaching the sample (Fig. 5.8 right panel) and the oscillating tip slightly taps the surface. The oscillating amplitude is kept large enough so that the tip does not get captured by the surface due to capillary forces. The tapping mode is a compromise between

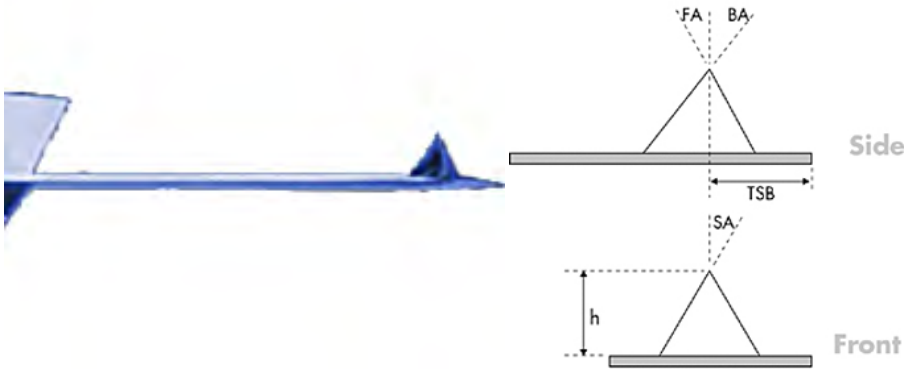

Fig. 5.9: Tip specification: tip height (h): (15 – 20) µm, front angle (FA): (15 ± 2)°, back angle (BA): (25 ± 2)°, side angle (SA): (17.5 ± 2)°, tip radius: (8 ± 2) nm, tip setback (TSB): (15 ± 10) μm. Cantilever specification: Material: (0.5 - 2) Ωcm phosphorous (n) doped silicon, thickness (t): (4 ± 0.5) μm, back side coating: (40 ± 10) nm aluminium, length (L): (125 ± 10) μm, width (w): (35 ± 5) μm, frequency: (300 ± 100) kHz, spring constant: (40 ± 20) N/m.

the non-contact and contact mode. It is used in topography measurements to minimize effects of friction and other lateral shear forces. In this work, the non-contact mode is used to avoid any damage of the partially liquid polymer film.

In the dynamic mode, a change in the phase shift between the driving frequency and the actual frequency of the cantilever indicates a change in the elastic constant of the sample material. In such a way, the phase contrast between e.g. the glassy phase at room temperature of polystyrene and the melt phase at room temperature of polyisoprene at the sample surface can be identified.

The sample is mounted on a lead zirconate titanate (PZT) tube scanner which consists of separate electrodes to scan precisely the sample in the x-y plane and to move the sample in the vertical z-direction. A sharp tip at the free end of a flexible cantilever (Fig. 5.9) is brought in the vicinity to the sample.

A laser beam from a diode laser is pointing on the back of a cantilever near its free end. The reflected beam from the cantilever is directed through a mirror onto a quad photo detector. The difference of the signal from the top and bottom photodiodes provides the AFM signal, which is a sensitive measure of the cantilever vertical deflection. This cantilever deflection will change the direction of the reflected laser beam, changing the intensity difference between the top and

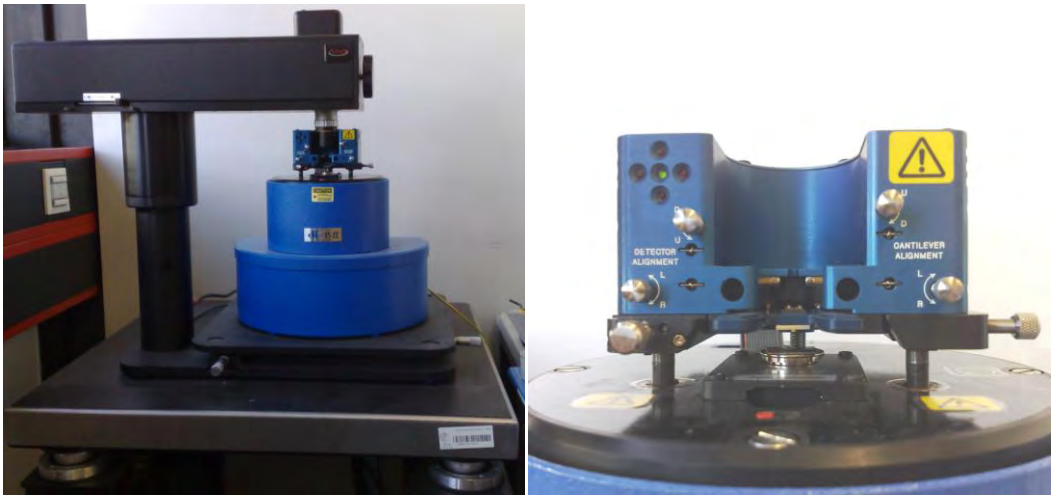

Fig. 5.10: AFM (Veeco Digital Instruments, di CP-II)

bottom sets of photo detectors. For topographic imaging, a feedback circuit is used to adjust the height of the PZT scanner as a function of the cantilever vertical deflection during scanning. The PZT height variation is thus a direct measure of the surface topography of the sample.

In this work a Veeco di CP-II AFM (Fig. 5.10) with a large area (90 x 90 μm^2) piezo electric scanner and a microscope stage of 8 x 8 mm^2 allowing a maximal sample size of 50 x 50 x 20 mm^3 was used.

6 Polymers

Polymers are the main constituent of plastics and are hence omnipresent in our daily environment. Also in not so obvious applications, they are used. They also can be found in nature e.g. as cellulose, which is the main constituent of wood and paper.

The first completely synthetic polymer (Bakelite) was not made until 1905 and polymers only became important for industry in the middle of the 20^{th} century.

A polymer is built of many building blocks called monomers. One monomer represents a chemical unit. If there is only one kind of monomer, linearly bound one to the other the polymer is called homopolymer. Two different homopolymer chemically bound together form a diblock copolymer. Besides many other forms of branched polymers exist e.g. star polymers and triblock polymers.

Block copolymers are found in many products as upholstery foam, adhesive tape and asphalt adhesives. This class of macromolecules is produced by joining two or more chemically distinct polymer blocks, each a linear series of identical monomers that may be thermodynamically incompatible. Segregation of these blocks on the molecular scale (5 - 100 nm) can produce astonishingly complex nanostructures, such as the “knitting pattern” [Breiner'98]. This striking pattern reflects a free-energy minimization that is common to all block copolymer materials. The microphase separation in thin dewetted films as self-assembled structure with two different length scales (those of the droplets and the microphase separation) could e.g. be used as a template for microelectronic structures, but until now, the mechanisms are not fully understood.

In this chapter the general principle will be explained, more detailed information about soft matter can be found e.g. in [Hamley'05] and references therein.

Polymers can be glassy, this means the structure is amorphous or semi crystalline or liquid. When polymers melt, they become viscoelastic, a phase in which a combination of elastic and viscous behaviour occurs depending on the time scale of observation.

6.1 Homopolymer

A homopolymer consists of many identical monomers as building blocks. The monomers can be arranged linearly or from manifold junctions. In the following only linear polymer chains will be considered.

6.1.1 Single Chain Properties

The simplest way to understand the basic properties of a polymer chain is to look at the polymer as randomly orientated linked monomers. The contour length of the polymer chain is then $N \cdot b$ with N the number of monomers in the chain and b the length of one monomer. The mean square end-to-end distance without restriction in bond angle is

$$\langle R^2 \rangle = b^2 N. \tag{6.1}$$

In case of a fixed bond angle θ_b between the monomers

$$\langle R^2 \rangle = b^2 N \frac{1 - \cos\theta_b}{1 + \cos\theta_b}, \tag{6.2}$$

for C-C (carbon) bonds with θ = 109°28’ respectively cos θ_b = -1/3 this gives

$$\langle R^2 \rangle = 2b^2 N\,. \tag{6.3}$$

In case the polymer has a bulky side group, like e.g. polystyrene, which hinders the neighbouring monomers to take all configurations the end to end distance has to be identified experimentally.

The end-to-end distance is difficult to measure. Instead, the radius of gyration, R_g, is often used since this quantity can be measured by scattering techniques. The mean-square value of the radius of gyration can be related to the mean-square value of the end-to-end distance by

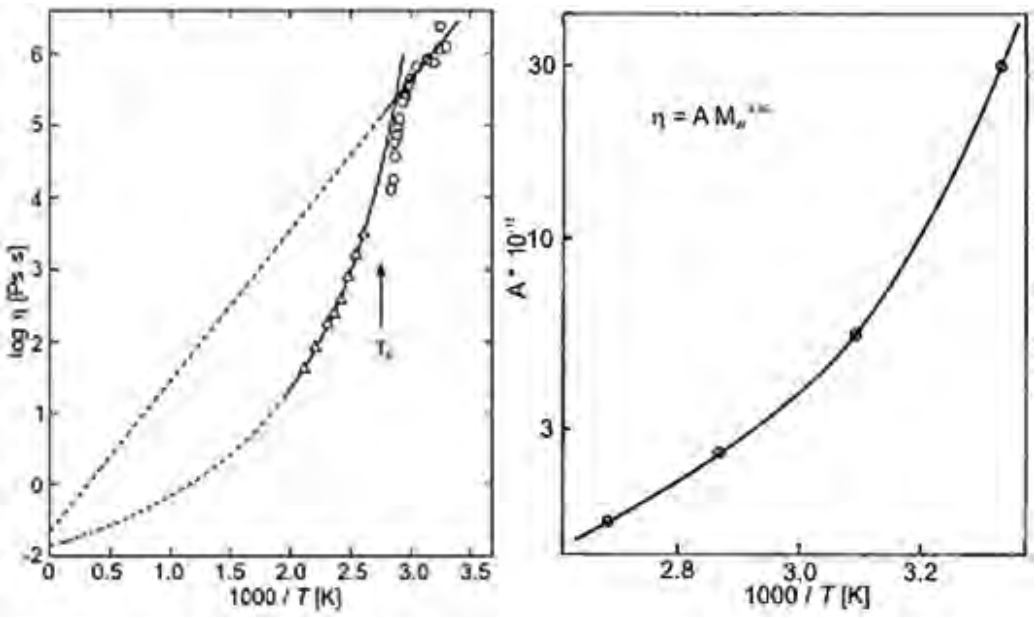

Fig. 6.1: Bulk viscosity of polystyrene [Kobayashi'05] (left) and of polyisoprene [Holden'65] (right).

$$\langle R_g^2 \rangle = \frac{\langle R^2 \rangle}{6}. \tag{6.4}$$

The radius of gyration is the average distance from the centre of gravity to the chain segments. In a solvent, the radius of gyration R_g can be larger (good solvent), identical (θ-solvent), or smaller (bad solvent) than in the melt. In this work toluene is used as a solvent which is in good approximation a θ-solvent for poly(styrene-block-isoprene) [Huang'98a].

Synthetic polymers always show a distribution in molecular weights with a given number average

$$M_n = \frac{\sum n_i M_i}{\sum n_i} \tag{6.5}$$

and weight average

$$M_w = \frac{\sum w_i M_i}{\sum w_i} = \frac{\sum n_i M_i M_i}{\sum n_i M_i}, \tag{6.6}$$

where n_i and w_i are the number and weight fractions, respectively, of molecules with molar mass M_i. The polydispersity index is given by M_w/M_n.

6.1.2 Polymer Melt

The viscosity of a polymer can be described by the Rouse model [Rouse'53] for unentangled and the reptation model [de Gennes'71] for entangled polymers. High molecular weight molecules as employed in this work can be simulated with the reputation model. With increasing temperature, the polymer chains become more mobile and hence the viscosity is decreasing. The bulk viscosity of polystyrene and polyisoprene as a function of temperature are displayed in Fig. 6.1. The glass transition temperature is defined by the maximum in the second derivative of the viscosity. For polystyrene the glass transition temperature is $T_g = 100°C$ [Rieger'96] and for polyisoprene $T_g = -72°C$ [Wood'63].

6.1.3 Polymers in Solution

Polymers in a solvent are usually less viscous with respect to the melt. The solvent molecules occupy some volume between the polymer chains and hence the entanglement of adjacent polymers is reduced. For polystyrene in a toluene solution the viscosity coefficient η increases exponentially with increasing concentration of polystyrene in toluene at a given pressure [Claesson'83]. The glass transition temperature as a function of the solvent weight fraction ω_s is

$$T_g = T_g(\mathrm{dPS}) - A_s\omega_s\,, \qquad \textbf{(6.7)}$$

with the constant A_s that is polymer/solvent dependent (500 K for PS in toluene [Laschitsch'99]). Consequently, a solvent fraction of 15% by weight of toluene is sufficient to lower the glass transition temperature of polystyrene to room temperature. Also the pressure is influencing the viscosity, with increasing pressure the intrinsic viscosity of polystyrene in toluene solution increases [Claesson'83]. Due to the volume occupied by the solvent molecules, the film is swelling by adding solvent. By removing the solvent, de-swelling will be significantly slower, than the swelling process [Müller-Buschbaum'06, Müller-Buschbaum'07].

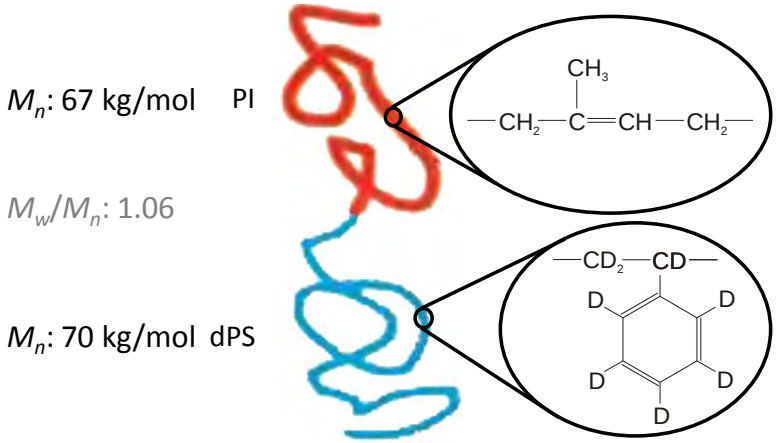

Fig. 6.2: Poly(styrene-block-isoprene). The values indicate the number averaged molar mass of both polymer constituents. The isoprene (PI) component is coloured in red and the deuterated styrene (dPS) component in blue.

6.2 Diblock Copolymers

Two different linear homopolymers covalently bound together form a diblock copolymer. In this work poly(styrene-block-isoprene) with the parameters as displayed in Fig. 6.2 and Table 6.1 is used.

The phase diagram for diblock copolymers was first calculated in 1980 [Leibler'80] and was improved in 1987 [Fredrickson'87b].

The volume fraction of polymer A and B in the diblock copolymer can be calculated by

$$f = \frac{\frac{M_{\mathrm{n.A}}}{\varrho_{\mathrm{A}}}}{\frac{M_{\mathrm{n.A}}}{\varrho_{\mathrm{A}}} + \frac{M_{\mathrm{n.B}}}{\varrho_{\mathrm{B}}}}. \tag{6.8}$$

The overall degree of polymerisation of a diblock copolymer is

$$N = \frac{\frac{M_{\mathrm{n.A}}}{\varrho_{\mathrm{A}}} + \frac{M_{\mathrm{n.B}}}{\varrho_{\mathrm{B}}}}{\sqrt{\frac{M_{0,\mathrm{A}}}{\varrho_{\mathrm{A}}}\frac{M_{0,\mathrm{B}}}{\varrho_{\mathrm{B}}}}}, \tag{6.9}$$

with the molar mass of a monomer M_0.

Density [g/cm^3]		Length [Å]		Volume [10^{-28} m^3]		Number density [10^{27} m^{-3}]		Molar mass [g/mol]	
ρ_{PS}	0.969	b_{PS}	6.7	V_{PS}	1.78	c_{PS}	5.61	$M_{0,PS}$	104
ρ_{PI}	0.83	b_{PI}	6.5	V_{PI}	1.36	c_{PI}	7.35	$M_{0,PI}$	68

Table 6.1: Properties of polystyrene (PS) and polyisoprene (PI) monomers at a temperature T = 140° C [Buzza'99].

The segment-segment interaction energy between the monomer A and B of the diblock copolymer, also called the "Flory-Huggins interaction parameter" [Flory'41, Huggins'41], is defined as

$$\chi_{AB} = \frac{Z_n}{k_B T}\left[\varepsilon_{AB} - \frac{1}{2}(\varepsilon_{AA} + \varepsilon_{BB})\right], \qquad \textbf{(6.10)}$$

which describes the free energy cost per monomer in units of the thermal energy of contacts between A and B monomers. Z_n is the number of nearest neighbour monomers to a copolymer configuration cell and ε_{AB} is the interaction energy between A and B monomers. If χ_{AB} is positive the diblock copolymer will microphase separate, whereas a negative value indicates a free energy drive towards mixing. A macroscopic phase separation cannot occur since two different monomers are chemically bound in a diblock copolymer. A phase diagram of the diblock copolymer poly(styrene-block-isoprene) is displayed in Fig. 6.3. The Flory-Huggins parameter for poly(styrene-block-isoprene) [Mori'85] is

$$\chi_{PS-PI)}(T) = \frac{66\ \mathrm{K}}{T} - 0.0937\,. \qquad \textbf{(6.11)}$$

In the lamellar phase (Fig. 6.3 L) the period can be approximated [Hashimoto'80] by

$$D^{lam} = 0.024\ \mathrm{M}_{n,PS-PI}^{2/3}\ \mathrm{nm}\,. \qquad \textbf{(6.12)}$$

The correlation length in bulk is in the order of 5 to 24 lamellae [Papadakis'97]. In thin microphase separated films with phase boundaries parallel to the substrate (lamellar phase), the correlation length is often increased [Kampf'70, Fredrickson'87a, Russell'89]. The order disorder transition in the bulk occurs at [Buzza'00]

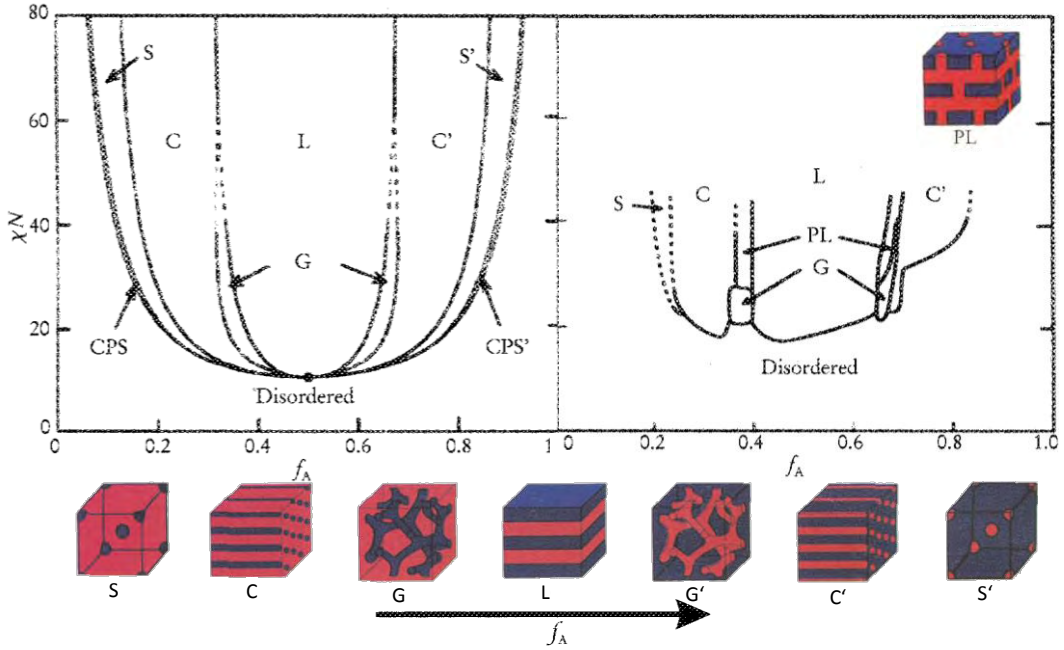

Fig. 6.3: Phase diagram of poly(styrene-block-isoprene) reproduced from [Bates'99]. a) The self consistent mean-field theory predicts four equilibrium morphologies [Matsen'94a, Matsen'94c, Matsen'94b, Matsen'96]: spherical (S), closed packed spheres (CPS), cylindrical (C), gyroid (G), and lamellar (L) as a function of the composition f and the combination parameter $\chi_{AB}N$. b) experimental phase diagram [Khandpur'95] with an additional meta-stable perforated layer (PL) phase.

$$(\chi_{AB}N)_{ODT} = 10.5 + 41\frac{b^6}{V^2}N\,, \qquad \textbf{(6.13)}$$

with the average bond length $b = ½\,(b_A^2+b_B^2)$ and the volume $V = (V_A V_B)^{1/2}$. Already at lower values of $\chi_{AB}N$ (> 5) local concentration fluctuations appear, see Fig. 6.4. This state is called the weak segregation limit (WSL). At $(\chi_{AB}N)_{ODT}$ long range fluctuations appear. For high values of $\chi_{AB}N$ the concentration profile of the two diblock copolymer constituents becomes box like. This regime is called the strong segregation limit (SSL).

In bulk, the diblock copolymer as depicted in Fig. 6.2 with the parameters as in Table 6.1 has an order disorder transition temperature of 592.32 K or 319.17°C, respectively and with f_{PS} = 0.47 is in the lamellar phase at room temperature, see Fig. 6.5. Experiments on polyisoprene-polystyrene hetero-star diblock copolymers in atmospheric conditions indicate a considerable degradation of the polymer at temperatures ≥ 200°C [Johnson'95]. Presumably, these measurements were

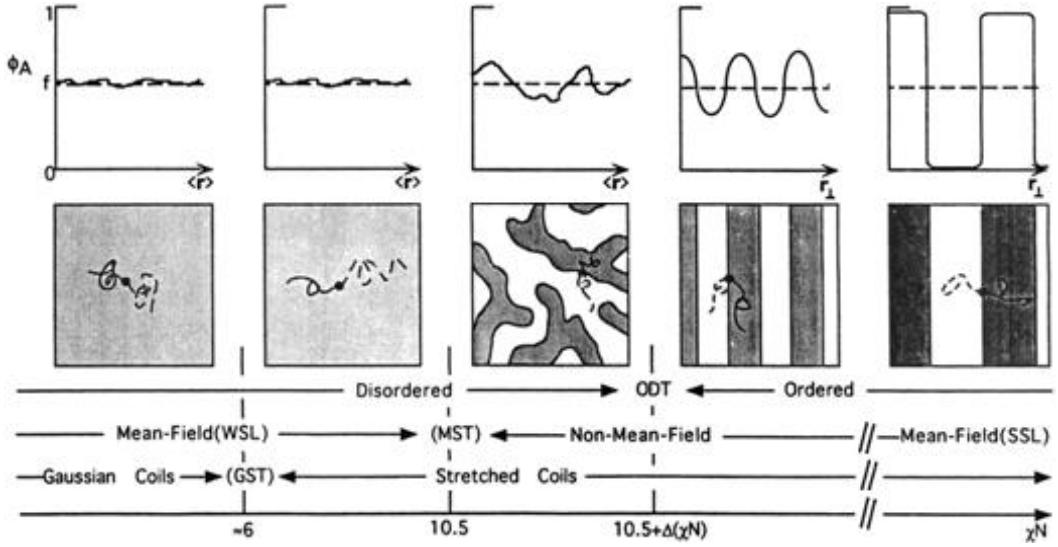

Fig. 6.4: Diblock copolymer chain conformation in the different stages of ordering. Reproduced from [Rosedale'95]. The transition from the weak segregation limit to the strong segregation limit is displayed for $f = 0.5$. In the first line the relative concentration of one component of the diblock copolymer is shown.

performed at ambient conditions. In vacuum, the temperature limit might be higher due to the absence of oxygen. Although, it is expected that the order disorder transition temperature cannot be addressed because of the degradation of the polymer.

The ordering of polymers is generally intermediate between that of a crystalline solid and that of a liquid [Hamley'05]. This lack of order leads to the soft mechanical response of the materials.

6.3 Thin Polymer Films

If the film thickness is below the radius of gyration of the polymer, the polymer chain conformation is compressed in the direction perpendicular to the substrate surface and the mass density is reduced with respect to the bulk value [Reiter'94]. As well the viscosity and the glass transition temperature of very thin polymer films are decreasing with decreasing film thickness [Keddie'94, Masson'02].

6.3.1 Diblock Copolymer Thin Films

In thin films, the boundary conditions have an additional effect on the diblock copolymer. Three theoretical aspects of this boundary layer of fluid are significant in the vicinity of the substrate [Pickett'93].

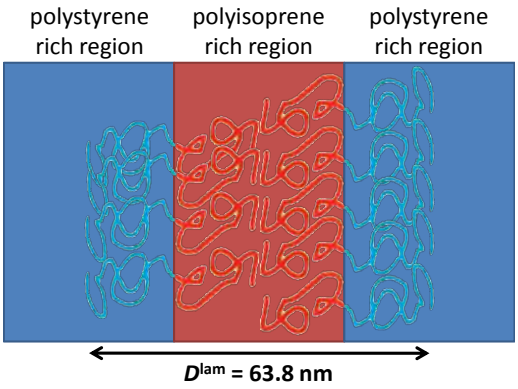

Fig. 6.5: Lamellar micro phase separation of polystyrene block polyisoprene. The values are given for the total molecular weight of 137 kg/mol.

First, the chemical composition of each part of the diblock copolymer can lead to different surface tension with respect to the substrate. If a difference in surface tension of the two constituents of the diblock copolymer with respect to the substrate exists, a parallel lamellar orientation gives a favourable energetic contribution. In poly(styrene-block-isoprene) both building block are rather non-polar, whereas the silicon dioxide layer on the silicon substrate is polar. Hence, a potential significantly different substrate polymer interactions can be excluded for poly(styrene-block-isoprene) on a silicon substrate with a natural silicon dioxide layer.

Second, the substrate, representing a hard wall, induces a nematic ordering on nearby segments, causing them to lie in the plane of the wall, but otherwise disordered in their orientation. In bulk lamellae, stress is inhomogeneously distributed. In planes adjacent to the A-B interfacial planes, the polymer is maximally stressed perpendicular to the A-B interface, whereas in the planes in the middle of two A-B interfaces the stress vanishes. In case of the perpendicular orientation the substrate surface intersects with high stress regions of the lamellae and the nematic ordering attributes to the stretching of the polymer chains, leading to a lowering of the surface energy. For the parallel orientation, at the substrate, a region in the polymer is adjacent to the substrate where the stress vanishes. Hence, no influence can be attributed.

Third, the area density of free chain ends in the boundary layer can affect the interfacial energy. In the microphase separated state, chain ends are expelled from

the vicinity of the A-B interface planes and congregate near the midplane interfaces. The molecular weight dependent interfacial energy between an unstructured melt and a neutral surface is given by $\gamma = \gamma_0 - A_E/M_n$, where A_E is a constant, when the interaction of the chain end groups is the same than that of the interior monomers of the chain [Theodorou'88]. It is expected that there are many more free chain ends in the proximity of the surface in the parallel than in the perpendicular orientation, hence this effect favours a parallel lamellar orientation.

In addition, the interface to the vacuum influences the free energy of the system. The surface tension to the vacuum is lower for polyisoprene (31 mN/m at 20°C [Lee'67]) than for polystyrene (40.7 mN/m at 20°C and M_w = 40 kg/mol [Wu'70, Lau'72, Lau'73, Lau'74]). This effect favours a parallel lamellar orientation with polyisoprene in the top layer adjacent to the vacuum.

The last energetic contribution arises from the dimensions of a single diblock copolymer chain in comparison with the film thickness. In a rough approximation the average conformation in the bulk lamellar phase can be approximated by a cylinder, see Fig. 6.6. The height of the cylinder is approximately $D^{lam} / 2 = 31.9$ nm. The diameter of the cylinder can be estimated by the volume of the cylinder, which is approximated by the monomer length to the power of three times the degree of polymerisation of the diblock copolymer. Here, it is assumed that neighbouring chains do not interpenetrate. In realty this is not the case, but it can be to a certain extend justified by segment swapping from the statistically even distributed interpenetrating segments of neighbouring chains [Silberberg'82]. An energetically favourable state minimises the deformation of the equilibrium chain conformation. Hence, for films of thickness below $D^{lam} / 2 = 31.9$ nm the perpendicular lamellar arrangement leads to an energetically favourable contribution in comparison to the parallel lamellar orientation. For film thickness of approximately $D^{lam} / 2$ and above, the structure with the smallest relative distortion is giving a favourable contribution to the total free energy. For thicker films (many times the thickness of the size of one polymer in the melt), the relative distortion of the polymer conformation becomes negligible and the influence of this effect vanishes.

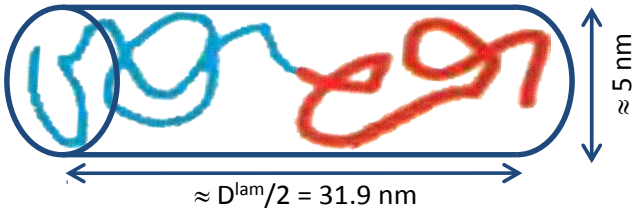

Fig. 6.6: Molecular dimensions of the investigated poly(styrene-block-isoprene) in the bulk lamellar phase. A cylindrical shape is assumed. The length of the cylinder can be estimated from the lamella period assuming that different polymer molecules do not interpenetrate each other. The diameter of the cylinder can subsequently be obtained from the length and the volume of the cylinder, where the latter is approximated by the monomer length to the power of three, multiplied by the number of monomers in the diblock copolymer. The molecular dimensions specified in the figure only represent a rough estimation.

A study on a very thick (0.35 mm) film of poly(styrene-block-isoprene) [Hasegawa'85] reveals that the lamella close to the free film surface are mainly parallel oriented with polyisoprene in the top layer, but also occasionally regions with a perpendicular lamellar orientation including one parallel layer of polyisoprene at the free film surface exist. Thickness induces morphology changes can be observed in copolymer films [Morkved'97, Knoll'02]. A change of a parallel arrangement for thicker films to a perpendicular arrangement for thinner films is reported. In ultra thin ($< 2R_g$) diblock copolymer films of poly(styrene-block-paramethylstyrene) dewetted in air / toluene atmosphere, droplets with a lamellar structure perpendicular to the substrate were reported, measured with conventional GISANS [Müller-Buschbaum'05]. The lamellar period is 60% stretched with respect to the bulk value. In this system $\chi N \approx 24$, whereas for poly(styrene-block-polyisoprene) $\chi N \approx 208$, both at room temperature. The stronger chemical interaction might lead to a more pronounced microphase separation, which might appear at an earlier dewetting stage and a different microscopic behaviour in the latter case.

In contrast to the five different phases in bulk (Fig. 6.3), due to the geometrical limitations, in an ultra thin film (thickness $<< D^{lam} / 2$) only two different phases are expected: The lamellar phase and the cylindrical phase, both with phase boundaries perpendicular to the substrate.

The aforementioned arguments on the orientation of the phase boundaries are understood in a qualitative way but a quantitative conclusion on the interactions needed for the unambiguous determination of the phase and the orientation of the phase boundaries is still not possible. Further experiments are needed for a complete understanding of the complex system.

7 Wetting Theory

Wetting is of key importance in many applications ranging from oil recovery and the way pesticides are deposited on plant leaves, to inkjet printing. Adhesion of liquids can be desirable, e.g. paints, or undesirable, e.g. bacterial fouling.

In this chapter, some basic principles of the wetting theory will be discussed. Further information can be found in e.g. [de Gennes'85, de Gennes'04].

7.1 Equilibrium Properties

Wetting refers to the study of how a liquid deposited on a solid (or liquid) substrate spreads out. In the first part of this chapter, it will be assumed that the molecules in the liquid are much smaller than any dimension of the film morphology. Two regimes of wetting can be distinguished (Fig. 7.1). Total wetting, when the liquid has a strong affinity to the substrate, or partial wetting, when the surface-tension term dominates [de Gennes'85]. The spreading parameter S is defined as

$$S = E^{\mathrm{dry}}_{\mathrm{Substrate}} - E^{\mathrm{wet}}_{\mathrm{Substrate}}\,, \tag{7.1}$$

which measures the difference between the specific surface energy of the substrate when dry and wet. Alternatively, S can be defined by the difference between the interface tensions, i.e.

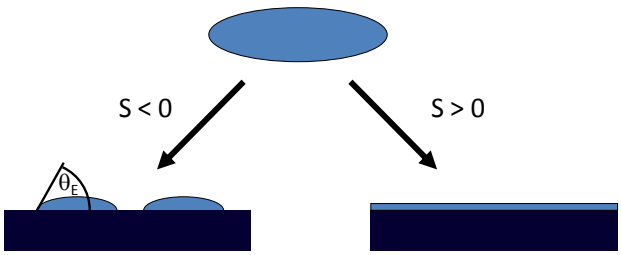

Fig. 7.1: A droplet will wet a substrate partial with a contact angle θ_E (bottom left) or total (bottom right), governed by the spreading parameter S.

$$S = \gamma_{SV} - (\gamma_{SL} + \gamma_{LV}) , \qquad \textbf{(7.2)}$$

where the three coefficients are the surface tension of the solid/vapour, solid/liquid, and liquid/vapour interfaces, respectively. If the parameter *S* is positive, the liquid spreads completely in order to lower its surface energy. In case of a negative parameter *S*, the drop does not spread but, instead, forms at equilibrium a nearly spherical cap resting on the substrate with a contact angle θ_E.

By Youngs equation [Young'05]

$$\gamma_{LV} \cos\theta_E = \gamma_{SV} - \gamma_{SL} , \qquad \textbf{(7.3)}$$

which defines the balances of forces caused by a wet drop on a dry surface, the equilibrium contact angle θ_E is related to the surface tension of the three interfaces. Complete wetting is characterised by a contact angle $\theta_E = 0$, $0 < \theta_E < \pi$ represents partial wetting, and $\theta_E = \pi$ stands for nonwetting, compare Fig. 7.2.

The contact angle of macroscopic droplets can be measured by several methods (e.g., static/dynamic sessile drop method or static/single-fibre Wilhelmy method [de Gennes'04]), whereas at droplets of microscopic size (below the wavelength of visible light) these methods are not applicable.

7.2 Dewetting

Dewetting describes the rupture of a thin liquid film on the substrate (itself liquid or solid) and the formation of droplets. The interface coverage is reduced driven by a transition from the non-equilibrium wetted state towards a partial- or non-wetted equilibrium state on the premise that the spreading parameter of the system is S < 0.

During wetting, when a contact line advances, covering more of the surface with

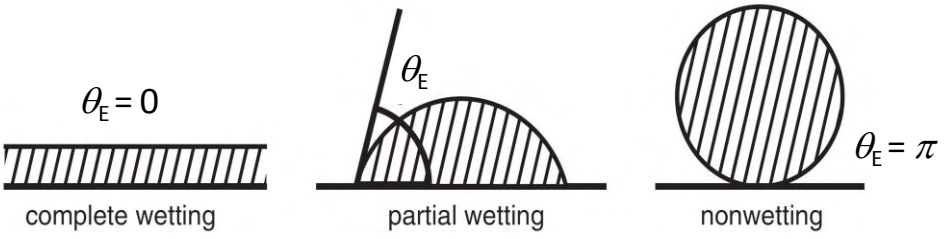

Fig. 7.2: Wetting conditions as a function of the equilibrium contact angle.

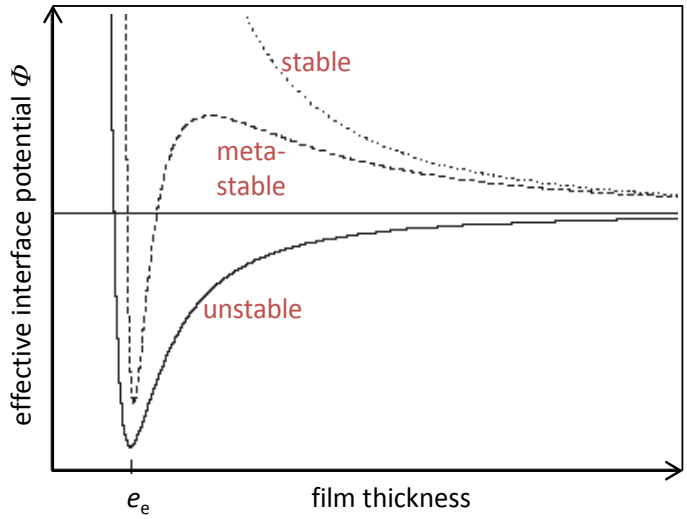

Fig. 7.3: Dependency of the film thickness on the effective interface potential for a stable, meta-stable, and unstable film.

liquid, the contact angle is increasing until the dynamical equilibrium is reached and generally, it is related to the velocity of the contact line. While dewetting, a receding interface likewise has a contact angle that is reduced relative to the static contact angle. The limits of contact angle as velocity approaches zero in the forward and backward directions are not equal, and the range between them defines a range of contact angles that are observed as static contact angles in hysteresis experiments.

The sum of the interfacial energies and the gravitational energy $F(e)$ of a film is

$$F(e) = \gamma_{SL} + \gamma_{LV} + \frac{A_H}{12\pi e^2} + \frac{1}{2}\rho g e^2 \,, \qquad \textbf{(7.4)}$$

where e is the film thickness and A_H the Hamaker constant [Hamaker'37], which is specific to the interaction of both materials at the interface.

Films with S < 0 and thickness above the capillary length

$$l_{cap} = \sqrt{\frac{\gamma_{LV}}{\rho g}} \qquad \textbf{(7.5)}$$

are stabilised by gravity. Films with thickness above the capillary length, where gravity dominates, the curvature of $F(e)$ is positive and the film is metastable. Dewetting only takes place after the nucleation of a dry zone, which will expand

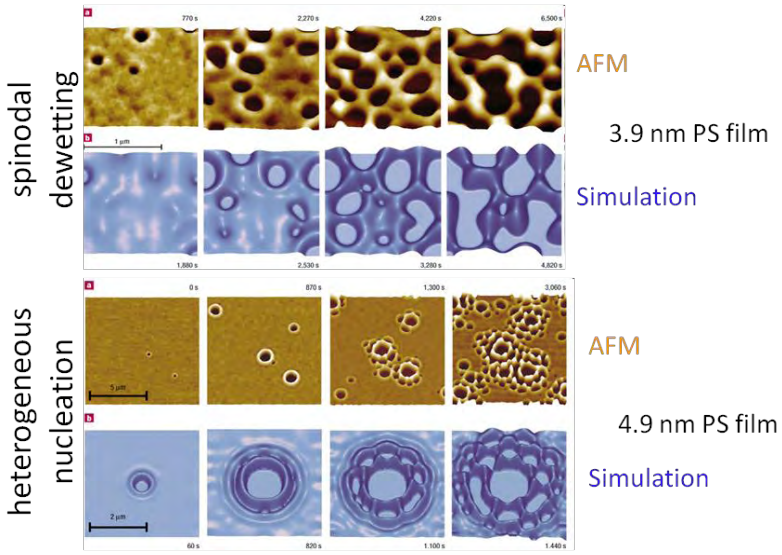

Fig. 7.4: Examples of the spinodal dewetting (top) and heterogeneous nucleation (bottom). In both cases a 2 kg/mol polystyrene film is dewetting. The different dewetting regimes are accessed due to different film thickness (39 Å (top) and 49 Å (bottom). Reproduced from [Becker'03]

if its radius exceeds a critical value. This phenomenon is called the *nucleation and growth* mechanism. For thin, microscopic films the summand with the Hamaker constant is dominating $F(e)$, and the gravitational part is negligible. The film is unstable. Capillary waves can be amplified and the film spontaneously breaks up into a multitude of droplets forming a hexagonal pattern. The regime is called the *spinodal decomposition* regime. The effective interface potential for the different scenarios is plotted in Fig. 7.3. Small deviations in film thickness can lead to different dewetting scenarios as shown by experiment and theory [Becker'03], see Fig. 7.4. For a polystyrene film on a silicon wafer covered by its oxide the oxide layer thickness is influencing the interface potential, see Fig. 7.5. With increasing thickness the oxide layer is destabilising the polystyrene film [Seemann'05]. The Van der Waals contribution to the effective interface potential as a function of the oxide layer thickness d_{ox} is

$$\Phi_{\mathrm{VdW}}(e) = -\frac{A_{\mathrm{SiO}}}{12\pi e^2} + \frac{A_{\mathrm{SiO}}}{12\pi(e+d_{\mathrm{ox}})^2} - \frac{A_{\mathrm{Si}}}{12\pi(e+d_{\mathrm{ox}})^2}. \qquad \textbf{(7.6)}$$

The surface energy of silicon with its natural oxide layer is 49.3 mN/m [Collins'03]. A polystyrene film with a surface tension of 31 mN/m at 20°C [Lee'67] or a polyisoprene film with a surface tension of 40.7 mN/m at 20°C and

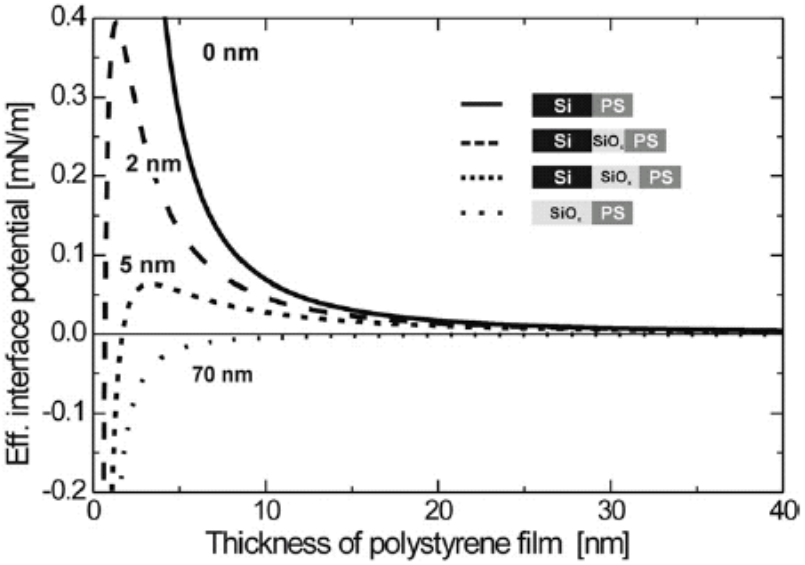

Fig. 7.5: Effect of the silicon dioxide thickness on the effective interface potential. Reproduced from [Seemann'05].

M_w = 40 kg/mol [Wu'70, Lau'72, Lau'73, Lau'74] are stable. Influences, as different surface cleaning procedures, can lead to different interface potentials and hence different dewetting scenarios [Müller-Buschbaum'03b].

In the considerations up to here, the dimensions of the molecules in the liquid were assumed to be far below any dimension describing the film morphology. The behaviour of microscopic films where the dimensions of the molecules are in the order of the film thickness is in addition to the before mentioned phenomenon governed by the size of the (polymer) molecules. A thin polymer film where the film thickness is below twice the radius of gyration of the (polymer) macromolecule will show an additional energy drive towards dewetting, since a spherical Gaussian coil conformation is entropically favourable to a compressed oblate conformation. Hence, the film might rupture and islands of ~$2R_g$ height form. Due to the volume conservation of the polymer film a certain fraction of the substrate will be uncovered [Müller-Buschbaum'05]. The internal microphase separated structure prevents thin diblock copolymer films in many sample systems from dewetting [Fasolka'01].

Examples of the dewetting of diblock copolymer films can be found in [Müller-Buschbaum'99, Müller-Buschbaum'02, Müller-Buschbaum'03a, Müller-Buschbaum'04].

8 Experimental Chamber and Sample Preparation

8.1 Vacuum Chamber

A vacuum chamber (pressure $< 10^{-5}$ mbar) suitable for x-ray and neutron reflectivity and off-specular scattering studies with the option of computer controlled sample heating up to 300°C and regulating the gas pressure of e.g. evaporated toluene was constructed (see Fig. 8.1). The neutron windows are made of 1 mm thick AlMg3 (mass fraction of 95% Al, 3% Mg, and others) as well as the body of the chamber. The x-ray windows are made of Teflon™-coated (12.5 μm on both sides) Kapton™ (38.1 μm). Both windows allow a large accessible angular range of $-6.5° < \alpha_{i,f} < 20°$ in the plane of the direct and specular reflected beam and $-25° < 2\theta < 25°$ in the plane of the sample surface.

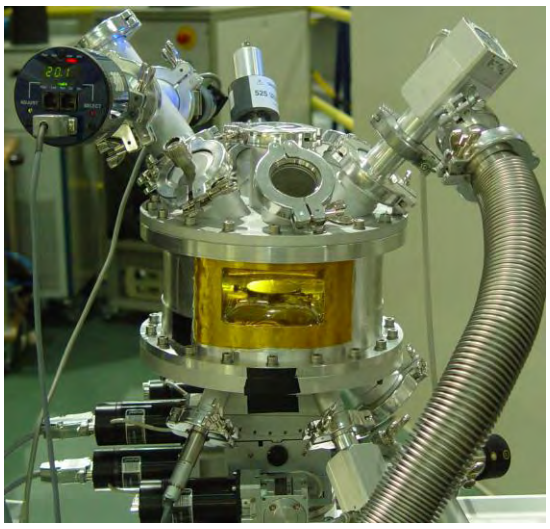

Fig. 8.1: Sample chamber with an aluminium window on the left and right side and a Kapton window at the front- and back-side (yellow). The sample is visible through the Kapton window. The chamber can be evacuated by a turbomolecular pump through the corrugated tube. The toluene reservoir (not visible), the venting valve and the connection to the turbomolecular pump can be closed computer controlled.

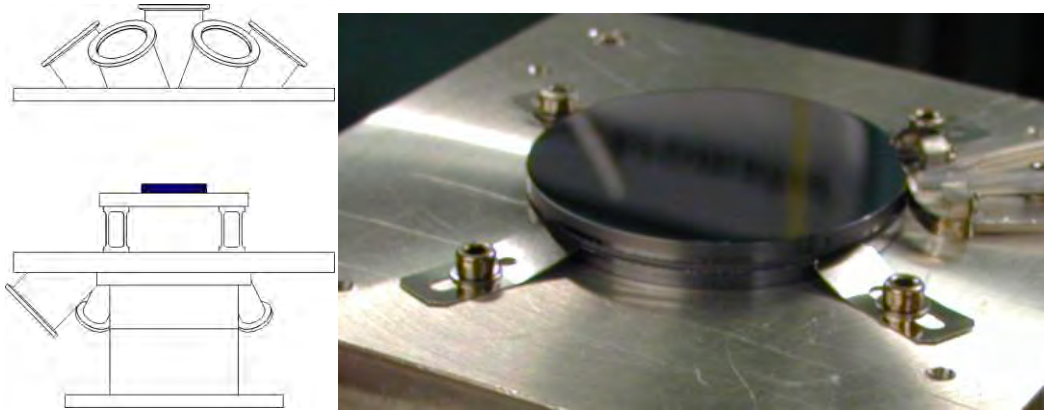

Fig. 8.2: Left: Sample position in the chamber. Right: Sample mounted on the sample table by four flat springs, the sample temperature sensor is mounted at the right side of the silicon slab (only the flat spring and the cable are visible).

AlMg3 is a suitable material for neutron experiments because it does not get radioactive activated in the neutron beam and has a low neutron total cross section. The sample is mounted on a heatable sample table, which is supported by four fourfold feet (all manufactured from AlMg3). The supporting rods in the feet have a suitable heat conductance allowing on one hand heat dissipation with the chamber as heat sink to be able to regulate the sample temperature, and on the other hand are isolating the heatable sample table to a certain degree to allow high sample temperatures. The chamber consists of a bottom, middle, and top part, which are sealed with elastomeric O-rings as well as the KF flanges. The chamber is equipped with ten flanges in total to connect equipment as e.g. the vacuum pump and pressure gauges. Seven KF40 flanges are situated on the top plate, one KF40 and two KF16 flanges on the bottom plate. (KF stands for the norm of the vacuum connection and the number for the inner tube diameter in millimetre).

The silicon substrates have a slit on the side to be fixed with four flat springs to the sample table; see Fig. 8.2. On one side, the sample is flat; here the sample temperature sensor (Pt100) is pressed by a flat spring against the sample. With this set-up, no equipment is exceeding the sample horizon. The holes in the bottom of the sample table serve to fix the sample table, the sample and the sample temperature sensor; see Fig. 8.2 and Fig. 8.3. In the quadratic aluminium sample table, of 10 mm thickness, two heater cartridges (each 50 W) are inserted from the left and right side in the 30 mm holes to provide a centre symmetric heating. Due to the high heat conduction of aluminium, a homogenous sample

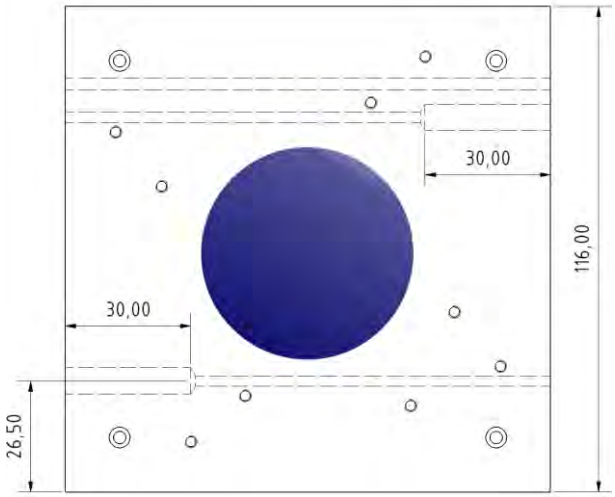

Fig. 8.3: Quadratic aluminium sample table, 10 mm thick. The heater cartridges are inserted from the left and right side in the 30 mm holes to assure a centre-symmetric heating. Due to the high heat conduction of aluminium a homogenous sample temperature can be achieved. The circular holes serve to fix the sample table, the sample and the sample temperature sensor. A second temperature sensor is located next to the right heater cartridge (upper dotted line) to allow a fast feedback circle for temperature regulation. The dimensions are given in millimetres.

temperature can be achieved. A second temperature sensor (Pt100) is located in a hole between the right heater cartridge and the foot (upper dotted line) to allow a fast feedback circle for temperature regulation.

Under basic conditions, the chamber is evacuated with a combination of a membrane pump and a turbomolecular pump system to less than 10^{-5} mbar and the sample temperature is 25°C.

8.1.1 Temperature Control

The temperature of the second temperature sensor is controlled by a Lakeshore 340 proportional-integral-derivative (PID) controller. The temperature at the sample sensors is recorded with a computer. Due to the proximity of the second temperature sensor to a heat sink (foot of the sample table), a temperature dependent temperature offset between both sensors exist, which had to be identified experimentally. By a computer macro, the sample temperature is recorded and the temperature set point is sent to the controller as a function of time to follow a specified heating cycle. The heating time in the following are

specifying the time span of first reaching the specified temperature until the set point was set back to 25°C. The coefficient of linear thermal expansion of aluminium (~$23x10^{-6}$ / K) is significantly larger than that of silicon (~$2x10^{-6}$ / K). This may lead to a potential sample misalignment during heating, making sample realignment necessary after each heating cycle.

8.1.2 Toluene Pressure Control

The pressure in the chamber is monitored with a HPM-2202-OBE vacuum gauge from Teledyne Hasting Instruments. It features two sensors; a patented thin-film Pirani sensor and a piezoresistive sensor (range $1.3x10^{-4}$ mbar to 1.3 bar). The piezoresistive device is a direct force sensor, which works for all kind of gas providing pressure indication from 1.3 bar down to less than 1.3 mbar. The thin film Pirani device is a gas specific (calibrated for nitrogen) thermal conductivity sensor, that provides pressure indication down to less than $1.3x10^{-4}$ mbar. The piezo sensor is used to measure pressure down to 10 mbar, below the Pirani sensor is used.

Toluene of 99.5% purity is stored in a recipient, separated by a computer controlled valve and a flow limiting nozzle from the sample chamber. After filling, the recipient is quickly evacuated through the empty sample chamber and the magnetic vacuum valve is closed. With this procedure, the air toluene mixture in the recipient is removed. The recipient is then filled partly with liquid toluene, partly with toluene vapour at its vapour pressure (29 mbar). The toluene treatment is started by opening the valve situated on top of the recipient to allow the gaseous toluene to flood the chamber. When a pressure of 19.5 mbar is reached, the counting time starts. At a pressure of 20.5 mbar, the valve is closed computer controlled. The toluene pressure is decreasing slowly due to the elastomeric O-rings, which absorb some toluene vapour. When the pressure is reduced to 19.5 mbar, the valve is opened again. This procedure continues computer controlled until the specified time is past. To evacuate the chamber three computer-controlled cleaning cycles with air were performed. Otherwise, the evacuation of the chamber could not be monitored with the Pirani sensor calibrated for nitrogen and in addition, the toluene vapour would affect the

membrane vacuum pump. The cleaning cycle is performed with the membrane pump, the turbo pump switched off. The first step is to evacuate the camber to 5 mbar, then the air valve was opened until a pressure of 150 mbar is reached. In a second step, chamber was again evacuated to 5 mbar. After three cyclers of air flushing, the chamber was completely evacuated with the turbo pump.

8.2 Sample Preparation

To deposit the polymer in a uniform thin film on the silicon substrate, spin-coating is a suitable technique [Bornside'93, Schubert'03]. The polymer is diluted in toluene. Toluene is a suitable solvent due to its properties as a so-called θ-solvent (Section 6.1.1). The polymer toluene solution is dripped on the spinning silicon substrate in order to spread the fluid by centrifugal force. The fluid spins off the edges of the substrate, until the desired thickness of the film is achieved. The applied solvent is volatile, and simultaneously evaporates. The resulting film thickness depends on the concentration of the polymer in the solution, the spinning speed and the spinning time. Typical spinning speeds and times are 1500 – 6000 rpm and a few seconds to several minutes. To insure that residual toluene evaporates entirely, the samples are kept for several hours in a vacuum furnace at 50°C. The polymer samples are spin-coated in the framework of a cooperation by Prof. Hyungjung Kim from the Sogang University in Seoul, South Korea. The polymers are ordered from Polymer Source Inc., Quebec, Canada. After spin-coating, the samples are shipped by airmail in a sealed transport box.

Before spin-coating, the sample were cleaned first with acetone and then with ethanol in an ultrasonic bath during 5 minutes and finally in a Piranha solution (one part 30%-H_2O_2 with two parts 98%-H_2SO_4) during one hour. The Piranha solution stays at 80°C for 20 min, after that it is slowly cooled down to room temperature. In the last step, the silicon wafers are rinsed with deionised water.

In the as received state (after the spin-coating), the film is expected to be homogeneous due to the spin-coating or eventually partially phase separated. This initial phase separation of the diblock copolymer might occur in the time span between the spin-coating process and the removal of the toluene by evaporation.

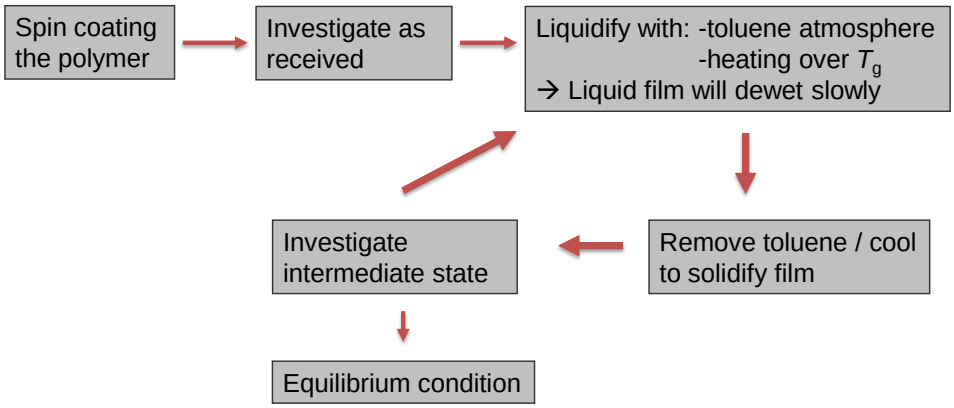

Fig. 8.4: Preparation process of the samples

After the removal of the solvent, it is assumed that the film is stable due to its high viscosity (Section 6.1.2).

To address the different dewetting stages, the polymer film is annealed at a given temperature, respectively exposed to toluene atmosphere for a given time and then the measurements are performed. The toluene treatment is done with constant toluene pressure of 20 mbar (Section 8.1.2). The heat treatment is done at constant temperature for the time specified (Section 8.1.1). During the toluene- or heat-treatment the viscosity of the polymer film is reduced (Chapter 6) and the film is dewetting slowly. The heating or toluene application time is short enough that the sample is dewetting only partly. To solidify the film, the toluene was removed or the sample temperature was decreases, respectively. After each treatment measurements are performed. This iterative dewetting and measurement cycle, illustrated in Fig. 8.4, was performed until no change in the sample morphology is observable any more. All measurements are performed at vacuum pressure ($<10^{-5}$mbar) and at 25°C, if not state otherwise.

9 Results

The results chapter is divided into two parts. In the first part, different SERGIS options are compared on the example of a strongly scattering optical grating. The second part focuses on the self-organisation of diblock copolymer films investigated with SERGIS and several other complementary techniques.

9.1 Comparative Studies of Different SERGIS Options

In the following subsections, the different SERGIS options introduced in Chapter 2 and 3 are compared. For this comparison an optical grating (Section 4.3.1) was investigated with the different types of SERGIS equipment: an NRSE set-up and three triangular-coil versions with different shape.

The optical grating as reference sample has the advantage that in certain directions the scattering signal is much stronger than that obtainable on macroscopically disordered samples (Section 4.3.3). Its disadvantage is the strong dependence of the reflectivity and the off-specular scattering on the relative alignment of the grating and the incident neutron beam. This problem was addressed at the beginning of each experiment by performing an azimuthal alignment scan, which allows to symmetrise the scattering pattern on the detector. As described in Section 4.3.1, the scattering signal is limited to small q_y-values in grazing incidence geometry, which are linked to specific q_z-values and are modified in intensity as described by the transmission function. A further problem is the discrimination of the specular reflected beam and the in-plane scattered intensity using a divergent incident beam.

All SERGIS experiments were performed at the instrument *N-REX*$^+$ at the FRM II in Garching at a wavelength of 5.5 Å.

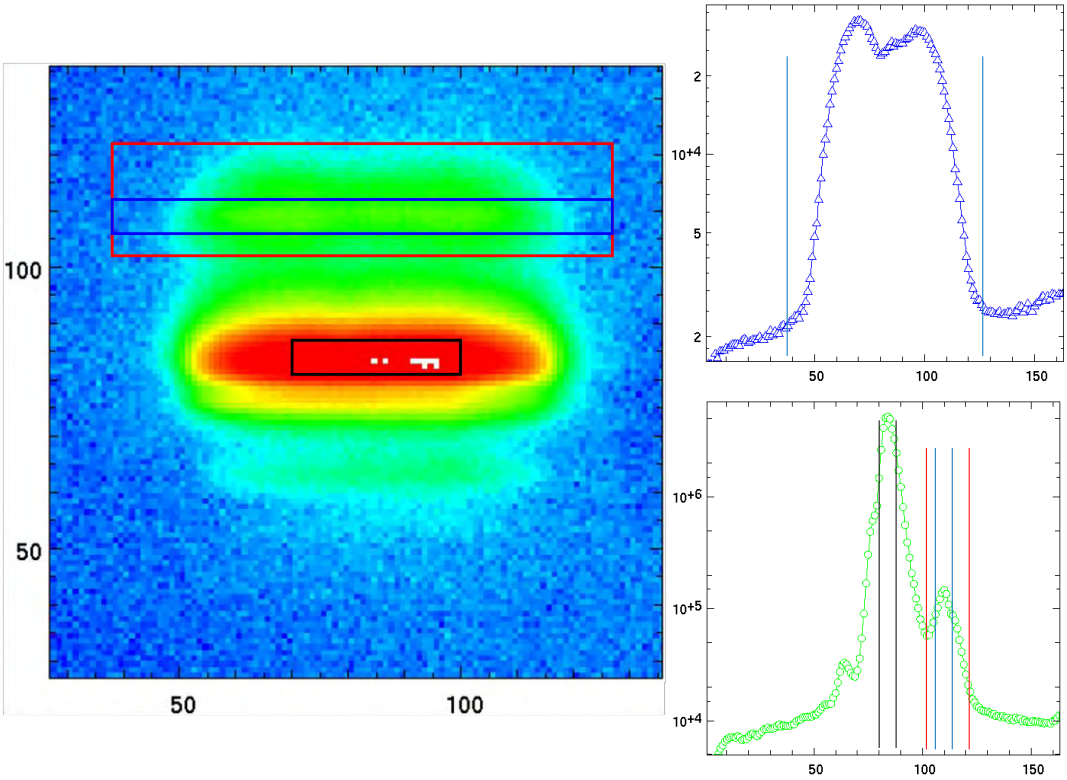

Fig. 9.1: Left panel: Detector image of the scattering from the optical grating recorded with the 45° triangular coil SERGIS set-up. The regions of interest used in the data analyses for the reference beam (black rectangle) and the scattered beam (red and blue rectangle) are indicated. Right panel: Horizontal (blue line) and vertical (green line) projection, integrated over the width and the height of the blue region of interest for the scattered beam, respectively. The marker lines in the top graph indicate the lateral ROI boundaries where the scattered intensity reaches the background level.

9.1.1 General Aspects of the Data Analysis and Interpretation

In this subsection, several general aspects of the SERGIS data analysis and interpretation are discussed. The different aspects are not necessarily related to each other.

For all types of SERGIS equipment investigated in this study, a considerable amount of wire material has to be put into the neutron beam path. This leads to intensity attenuation of the direct and scattered beam and to an enhancement of the overall background level in the detector area. The scattering signal thus is considerably degraded by the SERGIS set-up, as can be verified by comparing the conventional GISANS pattern form the optical grating in Fig. 4.12 (Section 4.3.1)

and the corresponding pattern with the 45° triangular coils in the beam path in Fig. 9.1. The most obvious difference is that sharp features get smeared out.

To determine the polarisation of the scattered beam, several regions of interest need to be defined (cf. Eq. (2.32) and (3.26)). Several regions of interest are indicated as boxes in the left panel of Fig. 9.1. For the SERGIS measurements on the optical grating, either the direct beam or a tail of it was used as reference beam. The region of interest of the reference beam was chosen small enough such that only neutrons, which interact with the sample, are included (black box). The region of interest of the scattered signal must be chosen wider, to cover the entire scattering in the lateral direction (red box). In order to minimize background contributions the right and left border of the region of interest were positioned near the detector pixel column where the scattered signal becomes equal to the background level, see the blue marker lines in the upper right part of Fig. 9.1. In the vertical direction the region of interest of the scattered signal (red box) was extended from the sample horizon to the specular reflected beam, see the red marker lines in the lower right part of Fig. 9.1. Complications arising from averaging over different q_z-values have been discussed in Section 4.3.1 and have to be kept in mind when interpreting the results of such an experiment.

For other samples, where several Fourier components are contributing to the Yoneda peak, the vertical dimension of the region of interest should be chosen small enough so that the integration over different q_z-values can be neglected, but it has to be large enough to obtain a sufficiently high signal intensity. In this case, the specular reflected beam is usually better suited as reference beam, because, compared to the direct beam, its beam path is closer to that of the Yoneda peak intensity (Section 3.3.1). As an example, a second region of interest (blue box) is visualised in Fig. 9.1, and the SERGIS data from the optical grating was evaluated for both regions. The results are shown as full lines in the respective colour in the left part of Fig. 9.2. Since the smaller region of interest (blue line) is only covering a reduced q_z range and thus, as discussed in detail for an optical grating in Section 4.3.1, also a reduced range of in-plane momentum transfers, its SERGIS signal is different to the larger region of interest covering all accessible in-plane momentum transfer in this sample geometry (red line).

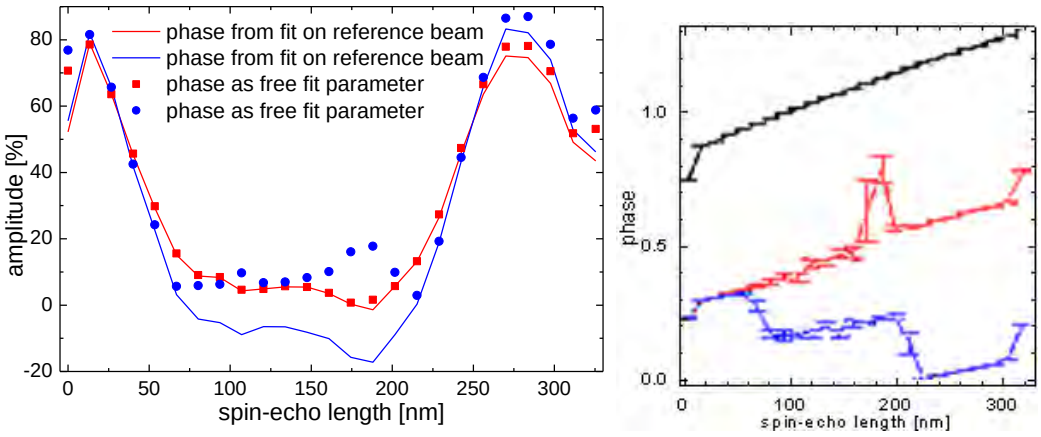

Fig. 9.2: SERGIS scan on the optical grating with 45° triangular coils. The analysis is done using different regions of interest (red and blue), as defined in Fig. **9.1**, with the direct beam as reference. In one case the polarisation of the scattered beam is fitted with the phase of the sine function as free fit parameter (points and squares), in the other case the phase of the reference beam is used for the phase of the scattered beam (solid lines). For the fit with the phase as free parameter the fitted phase is plotted in the right part of the figure. The black line represents the phase of the reference beam. The reference beam contribution and the background contribution were set to zero for the purpose of the data evaluation shown in this figure.

This observation, that limiting the signal integration to a too narrow q_y-range can significantly alter the resulting SERGIS data, can be understood from the scattering theory (Chapter 4). It can also be demonstrated experimentally by performing the data evaluation with an artificially small region of interest, covering only a narrow q_y-range. In this case, high-frequency Fourier components get suppressed and the SERGIS polarisation signal (resp. the generalized Patterson function of the sample) tends to become more sine-like. This effect is visible in Fig. 9.3 when comparing the blue data set obtained for an artificially narrow q_y-range with the red data set obtained for a properly chosen larger q_y-range. The black line represents the polarisation of the reference beam.

As described in Section 3.3.1, the phase of the sine function used to fit the polarisation of the scattered beam as a function of the spin-echo length should be determined on the corresponding signal of the reference beam. To illustrate the influence of this phase, in Fig. 9.2 the results of two different fitting strategies are compared: The results of sine fits with a freely variable phase parameter are indicated as points, as opposed to the solid lines which have been obtained by sine

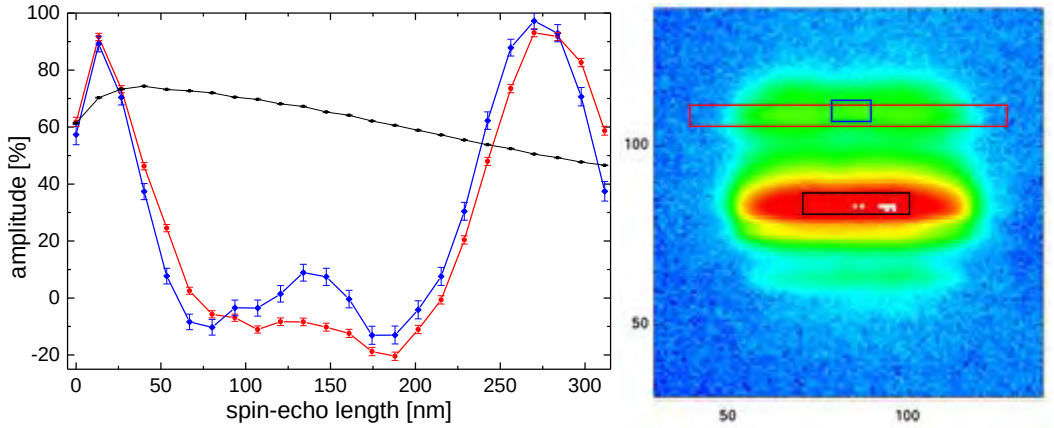

Fig. 9.3: A small region of interest, only covering a very limited q_y-range (blue box), results in a suppression of high frequency Fourier components in the SERGIS polarisation signal (blue data set). In this case an artificial peak appears at half the grating period. The larger region of interest covering a larger q_y-range (red box) is reproducing the known structure of the optical grating more correctly (red data set). The blue and the red curve are both normalised to the reference beam (black curve / box).

fits with the phase parameter set equal to the one fitted on the reference signal. As can be seen in the figure, when the phase is set equal to the one of the reference signal (solid lines), positive polarisation amplitudes are reduced slightly and, in this example, negative polarisation amplitudes appear more clearly.

When interpreting the intensity in the region of interest of the scattered beam, the background contribution and the contribution of in y-direction unscattered neutrons (i.e. tails of the direct or reflected beam) must be accounted for. The background contribution is calculated from the background level at high exit angles, where the scattering signal can be neglected. The contribution of in y-direction unscattered neutrons to the region of interest of the scattered beam is estimated by the peak shape of the reflected and the direct beam as a function of the exit angle. In case of the optical grating, only the direct beam contribution can be estimated from its peak shape, whereas the reflected beam contribution cannot be separated from the scattered beam.

For intensity reasons, the maximum suitable angle of incidence in the SERGIS experiments on the optical grating turned out to be $\alpha_i = 0.3°$. Hence, the maximum in-plane scattering angle was limited to 0.3°. Taking into account this maximum accessible in-plane scattering angle and the sample width of 25.4 mm,

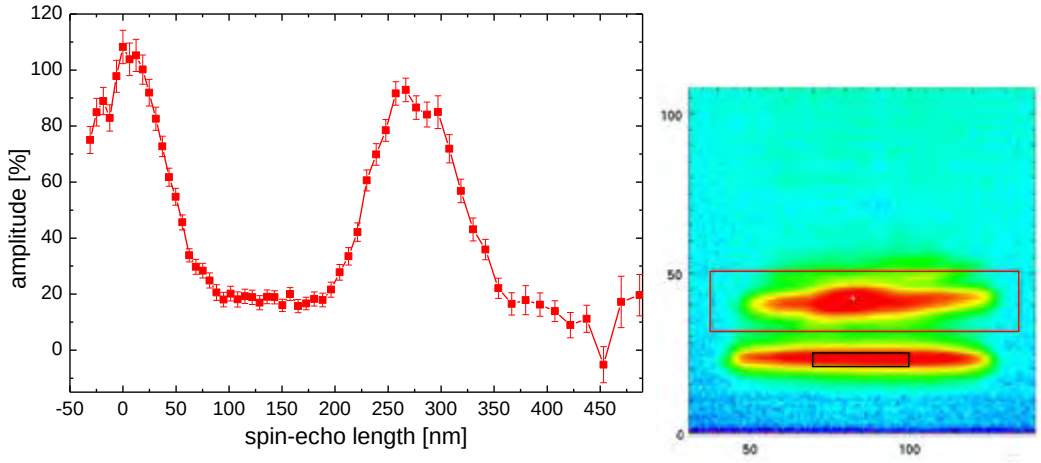

Fig. 9.4: SERGIS scan on the optical grating with NRSE coils. The incidence angle was $\alpha_i = 0.24°$. The reference beam contribution was 4% and the background contribution 1%. The phase for the polarisation fit is taken from the reference beam. The scan was performed by tilting the magnetic-field borders from $\chi = -5$ to $+55°$ in steps of 1°, the polarisation was measured in 11 steps at each spin-echo length with counting times between 20 s ($\chi = -5°$) and 60 s ($\chi = 55°$). The total time for this measurement was 15.3 hours.

the apertures in the various SERGIS set-ups were all wide enough (60 to 120 mm, see Sections 9.1.2 to 9.1.5) and did not pose any additional limitation for the in-plane scattering angle. This can be verified experimentally by comparing the widths of the peaks in the SERGIS data that have been measured with different coils. Thus, the real space resolution was only limited by the scattering geometry, not by the SERGIS equipment.

In the experiments on the optical grating the beam divergence at the sample position was ± 1.0° in y-direction and ± 0.15° in z-direction.

9.1.2 Neutron Resonance Spin-Echo NRSE

Results of SERGIS experiments performed on the optical grating with the NRSE option as introduced in Section 3.1.2 are shown in Fig. 9.4. The incidence angle was $\alpha_i = 0.24°$. In the region of interest of the scattered beam, the intensity contribution of the tail of the primary beam (100% polarisation) is estimated to 4%, and the background contribution (zero polarisation) is 1%. The phase in the sine-fit of the spin-echo scan is set identical to the fitted reference beam phase. The SERGIS measurement was performed by tilting the magnetic-field borders from $\chi = -5$ to $+55°$ in steps of 1°, the polarisation was measured in 11 steps at

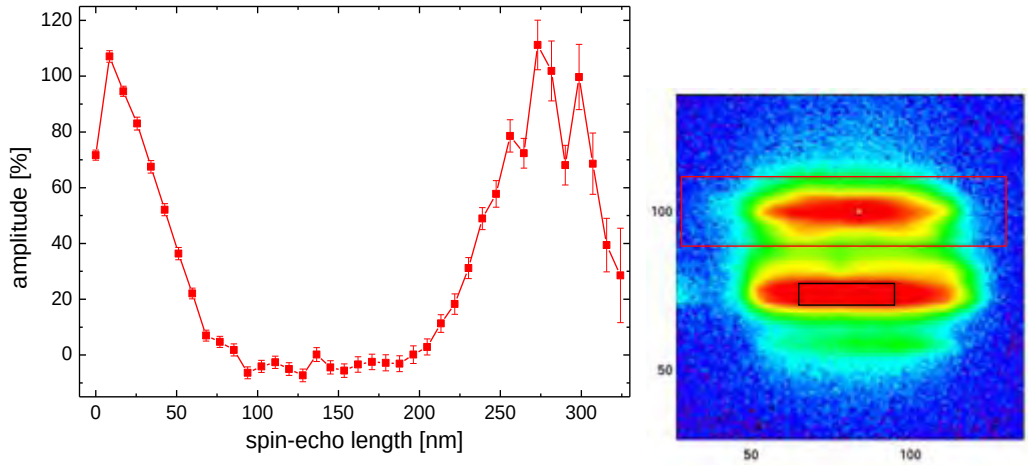

Fig. 9.5: SERGIS scan on the optical grating with 30° triangular coils. The incidence angle was $\alpha_i = 0.29°$. The direct beam contribution (tail) was 8% and the background contribution 2%. The phase shift for the polarisation fit is taken from the reference beam. The polarisation was measured in 14 steps at each spin-echo length with a linear increasing counting time of 10 to 25 s. The total time for this measurement was 5.6 hours.

each spin-echo length with counting times between 20 s ($\chi = -5°$) and 60 s ($\chi = +55°$), compare Fig. 3.24. To account for the loss in polarisation of the reference beam and the resulting larger statistical error bars after normalisation on the reference beam, the counting time is increased linearly with increasing spin-echo length. The total time for this measurement was 15.3 hours. Due to the relatively low incident angle the specular reflected beam intensity is quite strongly contributing to the polarisation of the region of interest. This leads to an elevated polarisation at spin-echo length between 80 and 200 nm. (Since the exact value of the unscattered beam contribution is unknown, no correction for the specular beam intensity was performed at this point.)

9.1.3 30° Triangular Coils

Results of SERGIS experiments performed on the optical grating with 30° triangular coils as introduced in Section 3.1.3 are shown in Fig. 9.5. The incidence angle was $\alpha_i = 0.29°$. A direct beam contribution (tail) of 8% and a background contribution of 2% were accounted for. The phase for the polarisation fit is taken from the reference beam. The polarisation was measured in 14 steps at each spin-echo length with a linearly increasing counting time of 10 to 25 s.

The relatively small inclination angle χ of the magnetic-field borders in the case of this triangular-coil results a in the large horizontal free path, which in turn should result in the best reproduction of the generalized Patterson function of the optical grating in comparison with the other SERGIS options. Also, thanks to the low inclination angle of the coils, the wire thickness in the direction of the neutron beam is minimised. This should yield a low background level and low absorption compared to the other SERGIS options. For this reason, the SERGIS scan could be performed in a relatively short time of 5.6 hours.

As characteristic to all triangular coils, there is no guide field in the triangular coils at zero spin-echo length. This makes a measurement at zero spin-echo length unreliable and the measured polarisation is usually, as in this case, lower than expected. Between the two peaks in the SERGIS scan, a decrease of the polarisation below zero is measured at spin-echo length between 80 nm and 200 nm. This is to be expected since the deviation of the scattering length density from its lateral mean value is observed.

9.1.4 45° Triangular Coils

The SERGIS measurement on the optical grating with 45° triangular coils is shown in Fig. 9.6. Both, the reference beam contribution and the background contribution were 10%. The phase for the polarisation fit is taken from the reference beam. The polarisation was measured in 11 steps at each spin-echo length with a linear increasing counting time of 50 s to 100 s. The total time for this measurement was 11.6 hours.

The 45° version was the first version of triangular coils and not equipped with additional water-cooling in the supporting rods. Consequently, the achievable maximum spin-echo length achievable with these coils is only around 330 nm, i.e. in the same range as the maximum spin-echo length for the (water-cooled) 30° coils.

9.1.5 60° Triangular Coils

The SERGIS measurement on the optical grating with 60° triangular coils was performed at an incident angle of $\alpha_i = 0.3°$. With this coil version, spin-echo

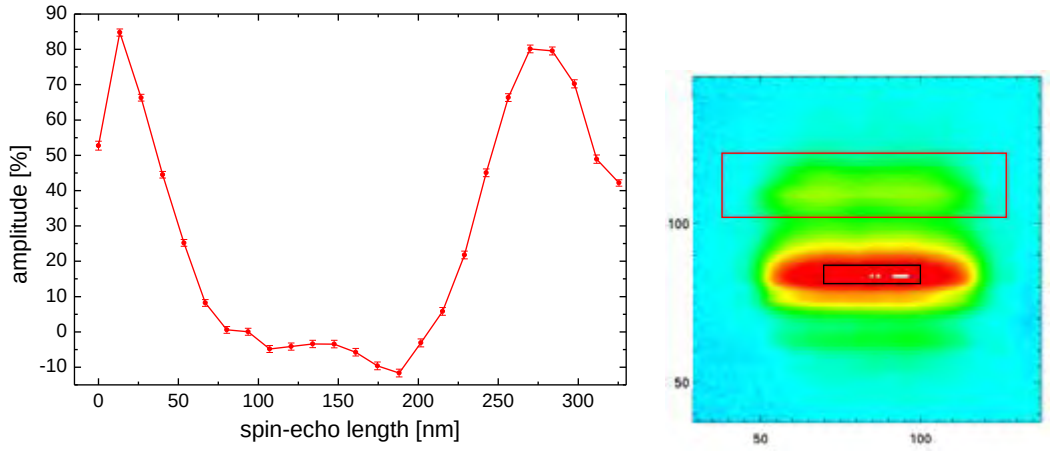

Fig. 9.6: SERGIS scan on the optical grating with 45° triangular coils. The incidence angle was $\alpha_i = 0.30°$. The reference beam contribution was 10%, the background contribution was also 10%. The phase shift for the polarisation fit is taken from the reference beam. The polarisation was measured in 11 steps at each spin-echo length with a linearly increasing counting time of 50 to 100 s. The total time for this measurement was 11.6 hours.

lengths up to 900 nm were accessible, see Fig. 9.7. A direct beam contribution (tail) of 9% and a background contribution of 13% were accounted for in the fit. The phase for the polarisation fit is taken from the reference beam. 90% of the direct beam was blocked to reduce the background level. The polarisation was measured in ten steps at each spin-echo length with a constant counting time of 100 s. The total time for this measurement was 20.5 hours.

The advantage of the 60° triangular coils is the large accessible spin-echo length. Due to experimental problems, during this measurement the reference beam polarisation was only around 30% instead of the usual 60%. This leads, despite the large counting time, to elevated statistical errors after normalisation to the reference beam.

9.1.6 Summary of the Different SERGIS Options

On the optical grating similar results were obtained with the four presented SERGIS options. In the top panel of Fig. 9.8 the SERGIS measurements from Fig. 9.4 to Fig. 9.7 are summarised. As mentioned above, in case of the optical grating, the unscattered beam contribution is unknown. In the bottom panel of Fig. 9.8 the same results are shown again, but here the unscattered beam contribution has been

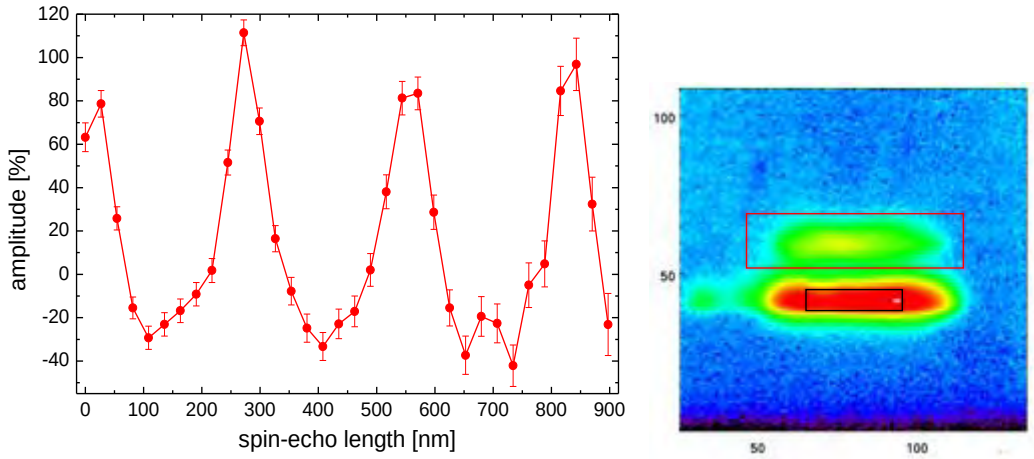

Fig. 9.7: SERGIS scan on the optical grating with 60° triangular coils at an incident angle of $\alpha_i = 0.3°$. The direct beam contribution (tail) was 9% and the background contribution was 13%. The phase shift for the polarisation fit is taken from the reference beam. 90% of the direct beam was blocked. The polarisation was measured in 10 steps at each spin-echo length with a constant counting time of 100 s. The total time for this measurement was 20.5 hours.

chosen manually such as to compensate differences in polarisation amplitude. After this manipulation, the different measurements on the optical grating with the different SERGIS options coincide to a very high degree.

Since the scattering of the optical grating is limited to small angles, the scattered beam does not considerably broaden, and the effects of the different limitation in horizontal free path width of the different SERGIS set-ups do not become apparent. For all used SERGIS coils, the scattering signal of the optical grating is well above the background level, although the absorption and small angle scattering is approximately twice stronger with the NRSE set-up than with the triangular coils. For weakly scattering samples, the triangular-coil set-up is thus the most suitable. Depending on the desired maximum spin-echo length and the desired maximum in-plane scattering angle, triangular coils with a smaller or larger inclination angle might be advantageous. In the next section SERGIS experiments on a weakly scattering diblock copolymer film will be presented, for which 30° triangular coils were used.

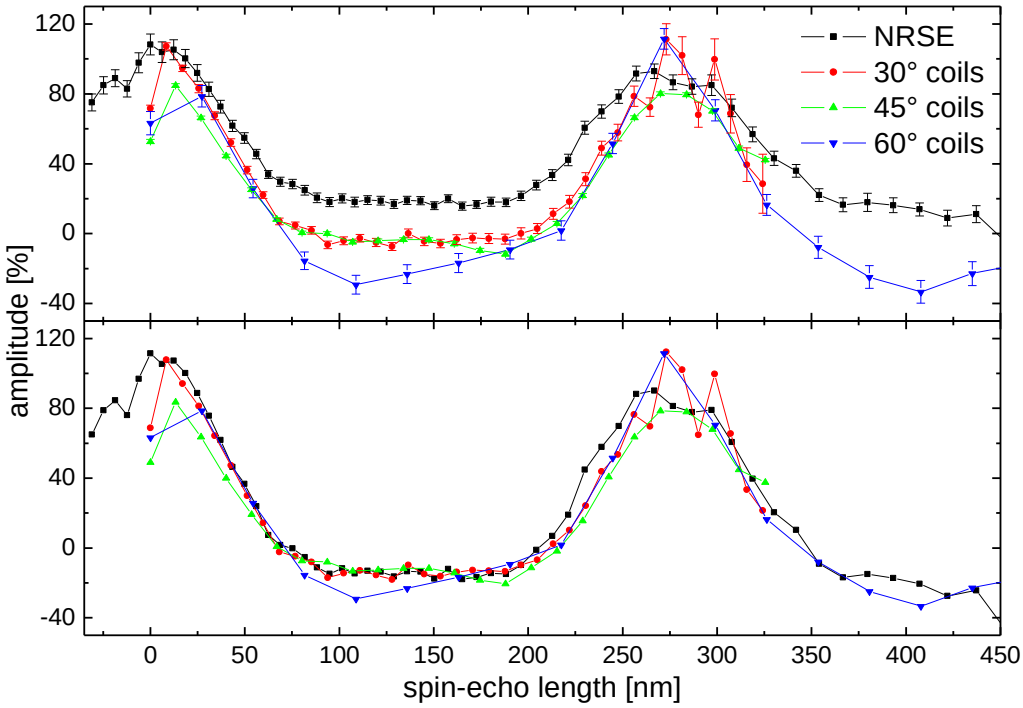

Fig. 9.8: Comparison of the different SERGIS methods. Top: unscattered beam contribution as estimated from the tail of the direct beam. Bottom: unscattered beam contribution set to compensate relative differences in polarisation amplitude. In the lower diagram, the statistical error bars are omitted for clarity.

9.2 Dewetting of Diblock Copolymer Films

The dewetting of polymer films of different thickness (~ 120 Å and ~ 500 Å) was stepwise investigated by means of four complimentary techniques: SERGIS, x-ray reflectivity, neutron reflectivity, AFM, and optical microscopy. Introductions to these techniques can be found in Chapters 2 to 5. Results obtained on different samples are presented in separate sub-sections of this chapter.

At each dewetting step, the measurements are fitted with different model functions to determine the microphase separation as well as the droplet morphology. By means of specular reflectivity measurements, one can distinguish between the two parallel arrangements described in Fig. 9.9 a-b and no ordering (laterally averaged) in the direction perpendicular to the substrate surface (Fig. 9.9 c-d). The scenario of a microphase separation with phase boundaries perpendicular to the substrate and the inter-mixed state cannot be discriminated. SERGIS resolves the scattering length density distribution in the direction parallel

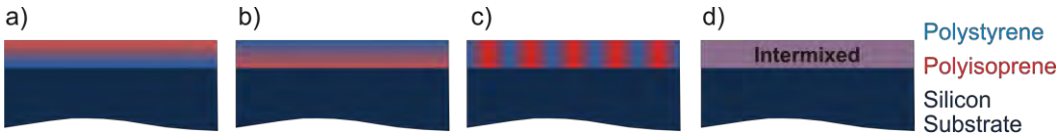

Fig. 9.9: Possible polymer film morphologies (the dewetting is not shown): a) Lamellar ordering with the phase boundaries parallel to the substrate and polystyrene in the top layer, b) Lamellar ordering as in a), but with polyisoprene in the top layer. c) Microphase separation with the phase boundaries perpendicular to the substrate. d) Intermixed state without phase separation of the two polymer constituents.

to the substrate surface hence one can distinguish a microphase separation with phase boundaries perpendicular to the substrate (Fig. 9.9 c) from the three other possible arrangements (Fig. 9.9 a-b and Fig. 9.9 d). Therefore, the combination of both techniques allows identifying the ordering in both directions (perpendicular and parallel to the substrate). Since the in-plane orientation of the microphase separation is on a macroscopic scale randomly distributed in all lateral directions, there is no necessity to measure the scattering length density distribution in more than one lateral direction.

In Section 9.2.0 below, some details of the analysis of the SERGIS and reflectivity data are explained. The following two sections are dedicated to the study of diblock copolymer films of about 100-150 Å initial thickness, which were investigated mainly by SERGIS (Section 9.2.1) and reflectivity (Section 9.2.2). Finally, in Section 9.2.3, SERGIS and reflectivity results obtained on a 450 Å thick film are discussed. All studies are complemented by AFM topography and phase contrast measurements. The measurements are labelled consistently by the employed method (AFM (A), neutron reflectivity (N), x-ray reflectivity (X) and SERGIS (S)) followed by the third digit of the section number and the dewetting step. For example, (A2.3) stands for the AFM measurement on the sample presented in Section 9.2.2 at the 3rd dewetting step.

9.2.0 Data Treatment

9.2.0.1 SERGIS Data Treatment

The diblock copolymers consist of a deuterated polystyrene and a protonated polyisoprene part of nearly identical volume fraction, see Section 6.2. The

deuterated polystyrene part has a high neutron scattering length density, whereas the protonated polyisoprene has a very low neutron scattering length density (see Table 4.1). The microphase separation in the droplets might have a box-like profile as in the bulk: compare Fig. 6.4 in the case of the strong segregation limit (SSL). As a consequence of the confinement in a thin film, also a slight smoothening of this box-like concentration profile might occur. The corresponding correlation functions are a symmetric saw-tooth function or a smoothed symmetric saw-tooth function, which can be approximated by a cosine function. In the experimental data the statistical error bars are too large to be able to make a statement about the concentration gradient at the phase boundaries. Therefore, the following model function is used to fit the data

$$g(Y^{SE}) = A_{mp}\, e^{-D_{mp}Y^{SE}} \cos\left(\frac{2\pi \cdot Y^{SE}}{l_{mp}}\right) + A_d e^{-D_d Y^{SE}}. \qquad \textbf{(9.1)}$$

A cosine function of period l_{mp} and amplitude A_{mp} is used to model the correlation function of the microphase separation as depicted in Fig. 9.9 c. The microphase separation is only correlated over a limited distance along the surface. Therefore the cosine function is decorated with and exponential factor whose decay length D_{mp} corresponds to the correlation length of the microphase separation. In the droplet morphology of a dewetted film, the droplets are assumed to be of elliptic shape with a nearly identical height. The droplet shape is fitted by an exponential function of amplitude A_d and decay length D_d. The decay length of the exponential function can be interpreted as the average droplet diameter. No conclusion about the droplet distance can be drawn from the presented SERGIS scans, since the maximum accessible spin-echo length is smaller than the expected droplet distance. As an example, a model function, according to Eq. (9.1), is plotted in Fig. 9.10. The ratio of A_{mp} and A_d is a complicated function of instrumental settings and the droplet and microphase morphology of the sample.

The SERGIS scans were processed in three different ways. Once, the data were smoothed by locally fitting 15 adjacent data points with a polynomial function of third degree, also called the Savitzky-Golay method [Savitzky'64]. This is a model-independent way of treating the data and allows identifying local maxima

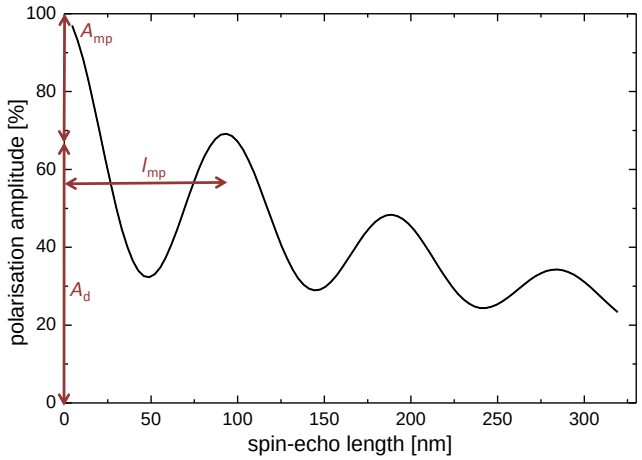

Fig. 9.10: SERGIS fitting function for microphase separated droplets, see Eq. (9.1). The decay in correlation of the microphase separation is fitted by a decaying cosine function, while the droplet shape is only fitted by a simple exponential function. The parameters for the presented example are l_{mp} = 96 nm, A_{mp} = 35%, A_d = 65%, D_{mp} = 0.006 nm^{-1}, D_d = 0.003 nm^{-1}.

and minima. Alternatively, the data were fit by a decaying cosine function plus an exponential decay (Eq. (9.1)). Third, to double check if a fit without assuming a microphase separation with phase boundaries perpendicular to the sample surface gives a better accordance with the data, a fit with a simple exponential decay (Eq. (9.1) with A_{mp} = 0) was performed. The latter two models were compared by means of their $\chi^2_{red.}$ value, see Section 3.3.4.

9.2.0.2 **Specular Reflectivity Data Treatment**

Neutron reflectivity is suitable to probe the inner structure of the investigated diblock copolymer films, since the coherent scattering length densities of both polymer constituents differ by a factor of ~30. The corresponding x-ray scattering length densities differ only by a factor of about 1.4. However, advantages of x-ray reflectivity are the higher dynamic range (between the direct beam intensity and the background level) and the easy access to laboratory x-ray sources. The total film thickness can easily be measured by neutron and x-ray reflectivity. Both methods were used in a complementary way. The reflectivity data were fitted with a three layer model to account for a phase-separated polymer film resting on a silicon substrate covered by a native silicon oxide layer. In case the scattering length densities of the two polymer sub-layers converged or if the thickness of

one polymer sub-layer converged to zero, one polymer sub-layer was removed from the fit model and the fit repeated. The fitted parameters were: the real part of the scattering length density, the layer thickness, and the roughness of each layer. The imaginary part of the scattering length density was calculated based on the distribution of to the real part of the scattering length density and the condition of equal volume fraction of the two constituents of the diblock copolymer. The specular reflectivity data were fitted with the 'winfit' program [Rühm'99].

9.2.1 Dewetting of a 100 Å Thick Diblock Copolymer Film Investigated by SERGIS

A 100 Å thick spin-coated diblock copolymer film of deuterated poly(styrene-block-isoprene) was investigated by means of SERGIS at different dewetting steps as presented in Table 9.1. After certain dewetting steps, the sample was additionally investigated by AFM.

9.2.1.1 Experimental Set-Up and Data Treatment

The SERGIS measurements were performed with the 30° triangular coils

Dewetting step	Annealing temperature [°C]	Annealing time [hours]	Measurements
0	as received at 25	0	SERGIS (S1.0)
1	62	1	SERGIS (S1.1)
2	80	1	SERGIS (S1.2)
3	105	1	SERGIS (S1.3)
4	116	1	SERGIS (S1.4)
5	130	1	SERGIS (S1.5)
6	145	1	SERGIS (S1.6), AFM (A1.6)
7	160	1	AFM (A1.7)
8	176	1	SERGIS (S1.8)
9	189	1	SERGIS (S1.9)
10	203	1	SERGIS (S1.10)
11	215	1	SERGIS (S1.11)
12	25 with 20 mbar toluene	1	SERGIS with 2D supermirror (S1.12a) and ^{3}He analyser (S1.12b), AFM (A1.12)

Table 9.1: Sample treatments (100Å P(S-b-I))

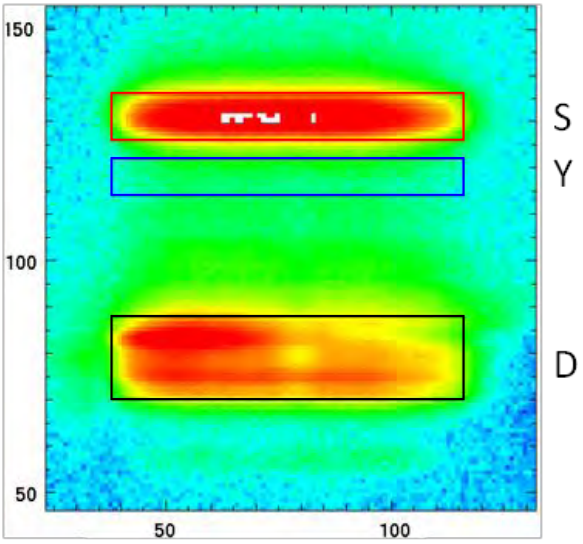

Fig. 9.11: Integrated detector image with regions of interest for the direct beam (D, black rectangle), the Yoneda peak (Y, blue rectangle), and the specular reflected beam (S, red rectangle) (100Å P(S-b-I)).

(Section 3.1.3). The low background contribution and the large horizontal aperture of these coils make them the most suitable SERGIS option. The incident angle of the neutron beam on the sample surface was $\alpha_i = 0.34°$. At this angle, the Yoneda peak can be discriminated well enough from the specular reflected beam. The beam divergence at the sample position was ± 1.1° in y-direction and ± 0.15° in z-direction. During the SERGIS experiments, the sample was kept under constant vacuum below 10^{-4} mbar. The scattered neutrons were measured in a region of interest centred at the Yoneda peak, and the specular reflected beam served as reference, see Fig. 9.11. The direct beam was mostly blocked before reaching the second spin-echo arm in order to reduce the background level. Thus, only a tail of the direct beam reached the detector, which was weaker in intensity than the specular reflected beam. To account for the contribution of neutrons which are not scattered in y-direction (100% polarisation) and the contribution of background neutrons (zero polarisation) to the Yoneda region of interest, the correction factors $I_r/I_{ROI} = I_{back}/I_{ROI} = 0.25$ were used in Eq. (3.27).

9.2.1.2 **Results**

The measured SERGIS data and corresponding fit curves are presented in Fig. 9.12, the obtained fit parameters are shown in Fig. 9.13.

In the as-received state (i.e. after spin-coating) the film surface is expected to be relatively flat. The SERGIS measurement (S1.0) (dewetting step 0) shows a quite smooth decay in polarisation amplitude. A model with microphase separation can be fitted to the data with a small oscillation amplitude, but the fit with the model without microphase separation yields a slightly lower $\chi^2_{\mathrm{red.}}$ value ($\chi^2_{\mathrm{red.}}$ = 1.15 and 1.08, respectively). One can conclude that no microphase separation in the lateral direction, i.e. with phase boundaries perpendicular to the sample surface, existed in the initial state. If such a microphase separation were assumed to exist within a very small fraction of the film, the periodicity could be between 72 nm (local maximum in the smoothed curve) and (62 ± 2) nm (fit result).

During the first annealing step (1 h at 62°C), the sample state does not change noticeably, as revealed by the SERGIS measurement (S1.1). In the following annealing step at 80°C (measurement (S1.2)), a lateral concentration gradient of polystyrene and polyisoprene with phase boundary perpendicular to the sample surface developed. The fitted period amounts to (81 ± 11) nm. In the smoothed curve a local minimum at a spin-echo length of 50 nm becomes apparent. However, although the SERGIS data set (S1.2) shows quite pronounced oscillations, the $\chi^2_{\mathrm{red.}}$ values are nearly identical for both models. This means that the statistical error bars do not permit a discrimination of both scenarios. Perhaps a third scenario, described by a slightly different fitting function, might be able to reproduce the observed oscillation in the smoothed dataset better.

After additional annealing for 1 h at 105°C (dewetting step 3), a distinct phase separation with phase boundaries perpendicular to the substrate surface became apparent in the SERGIS scan (S1.3). The fit with a model assuming a phase separation is much more reliable ($\chi^2_{\mathrm{red.}}$ = 0.93) than a fit with a model assuming homogeneous droplets ($\chi^2_{\mathrm{red.}}$ = 1.34). The resulting periodicity of the phase separation is (96.0 ± 3.1) nm. The decay of the microphase separation (D_{mp}= 0.006 nm^{-1}) is twice faster than the one of the island size (D_{d}= 0.003 nm^{-1}), cf. Eq. (9.1). The larger oscillation amplitude in the SERGIS data (S1.3) might arise from a larger concentration gradient in the phase separated film or from a higher volume fraction of phase separated diblock copolymer in the film. For

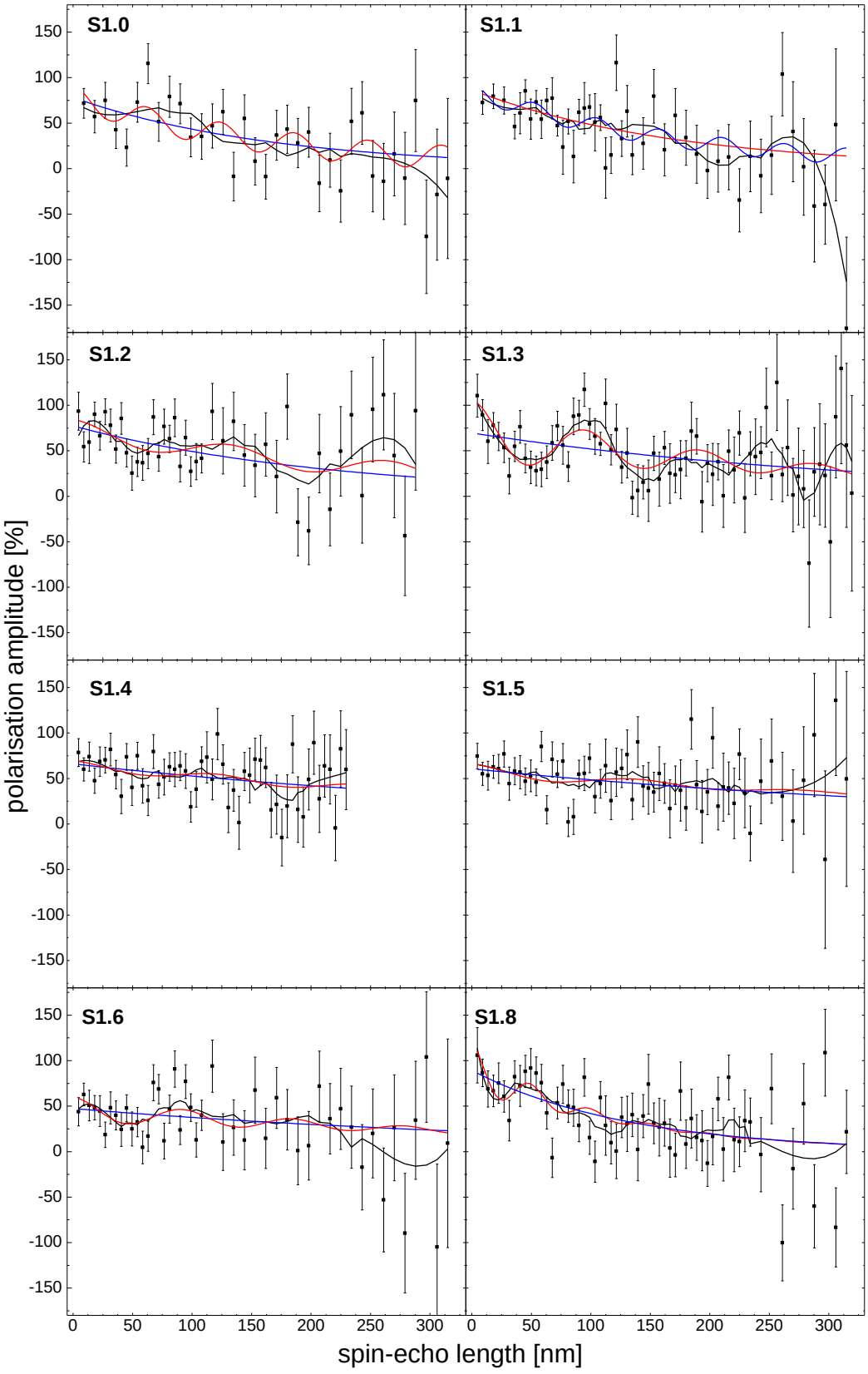

Fig. 9.12a: SERGIS data sets in comparison with three different model curves (see the legend in the second part of the figure on the next page). The number of each SERGIS measurement is indicated in each diagram. The numbers after the period correspond to the dewetting step. For a detailed discussion see the main text.. (100Å P(S-b-I)).

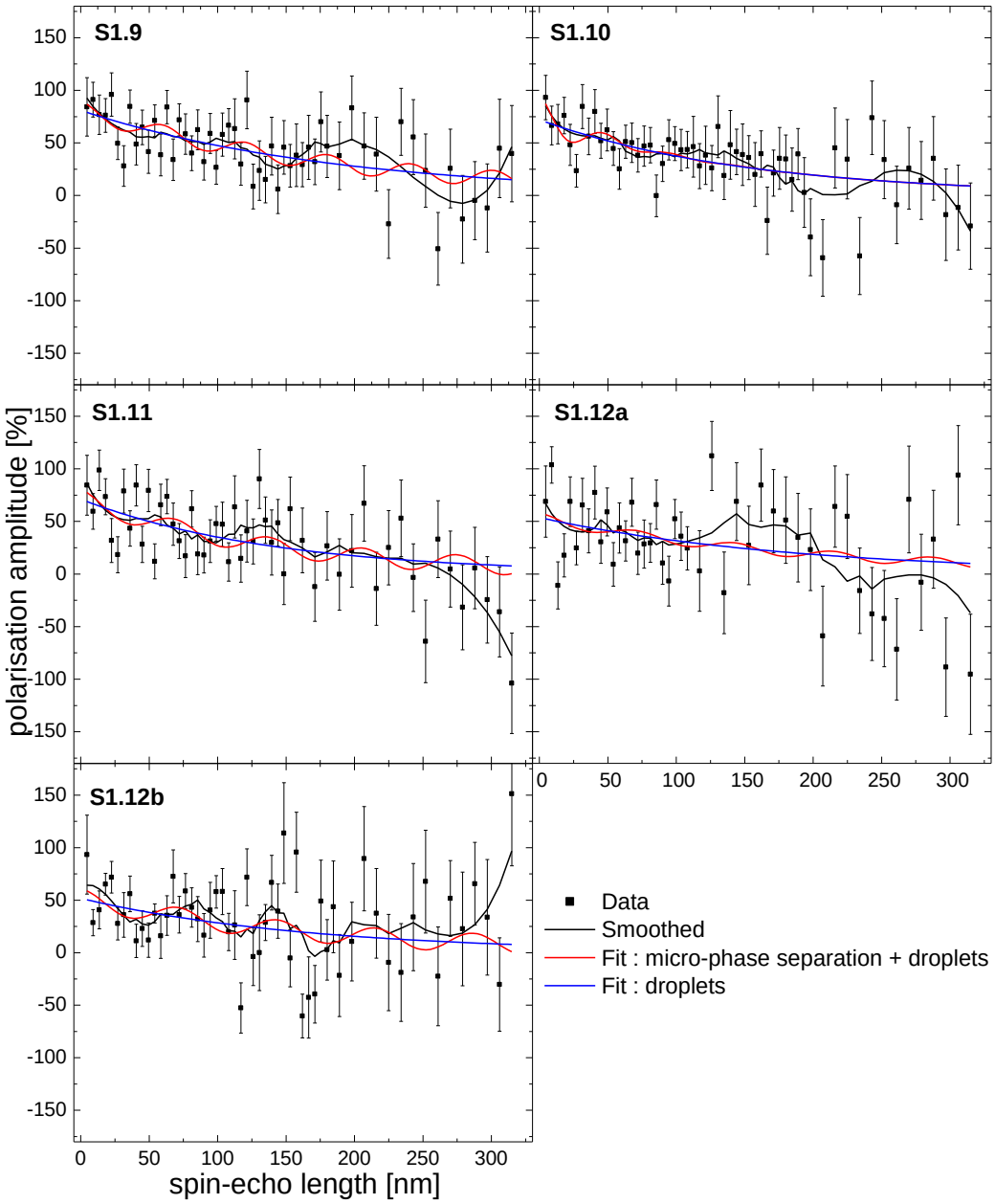

Fig. 9.12b: Continuation from Fig. 9.12a.

spin-echo lengths up to 220 nm the model taking into account the microphase separation coincides very well with the smoothed data, indicating that the model is chosen well.

Further annealing for one hour at 116°C, 130°C, and 145°C (dewetting steps 4 to 6) made the strong lateral phase separation disappear. Both models agree to the same satisfying extent with the three data sets ($\chi^2_{\mathrm{red.}} = 1$ to 1.21). No clear statement can therefore be made based on the SERGIS data sets (S1.4) to (S1.6)

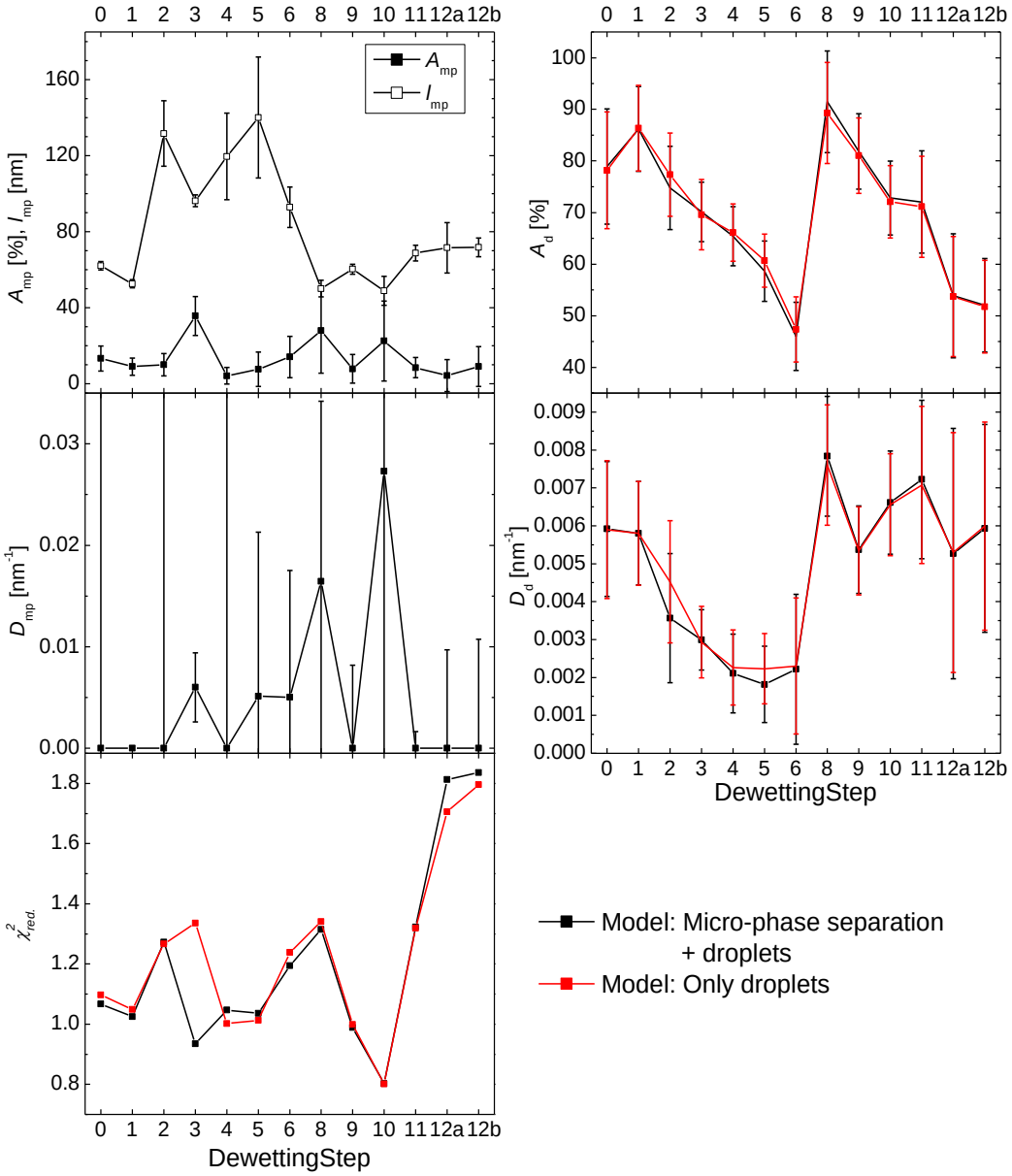

Fig. 9.13: Summary of the fit parameters from the fits shown in Fig. **9.12** (100Å P(S-b-I)).

alone. AFM measurements (A1.6) after the annealing step at 145°C show that circular elevations formed on top of the film (Fig. 9.14). The height of the elevations is approximately 2 nm, i.e. relatively small with respect to the film thickness (10 nm). The high and low regions also give rise to a phase contrast in the AFM phase image, which can be attributed to the two different constituents of the diblock copolymer exposed at the film surface. Since, the viscosity of the film material influences the energy dissipation of the AFM tip and hence the phase shift, it can be concluded that the areas with a smaller phase shift (dark in the

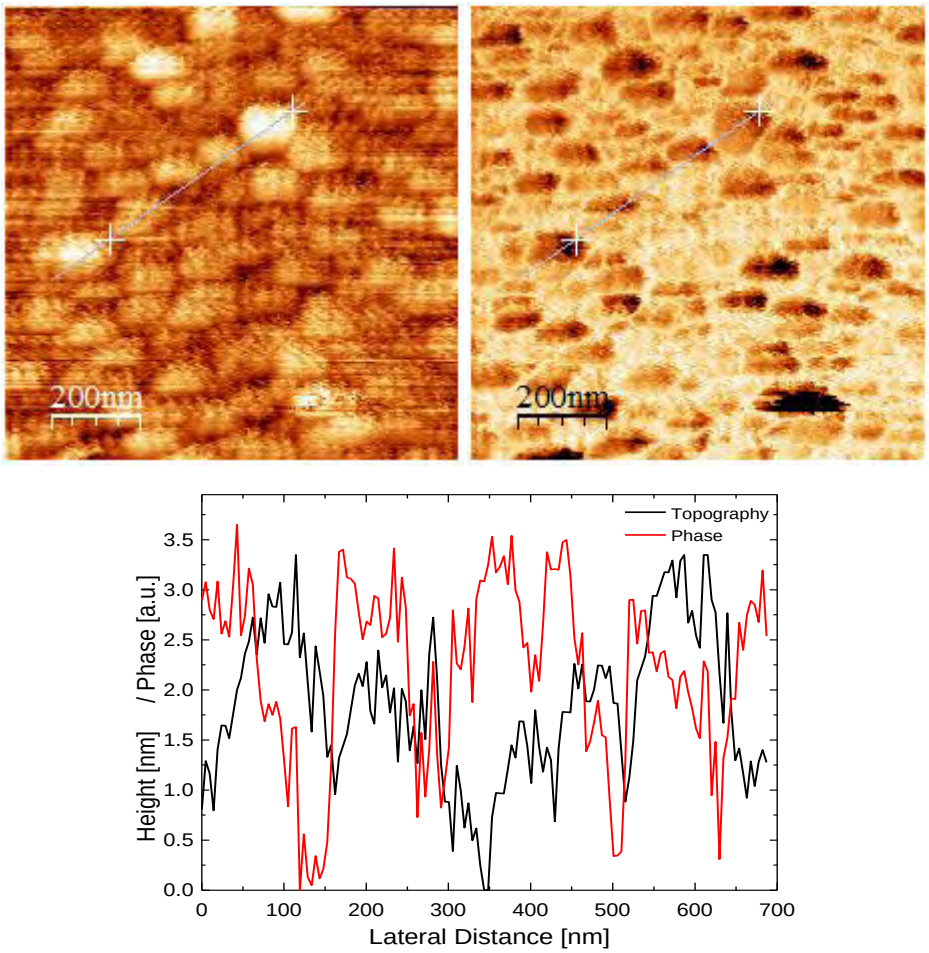

Fig. 9.14: AFM measurement (A1.6) after 1 h annealing at 145°C. In the top panel, the topography and the phase image are displayed. In the graph below, a line cut along the direction indicated in the two images is shown. High regions in the AFM topography (bright circles in the left image) are correlated to regions with a small phase shift (dark circles in the right image). The smaller phase shift indicates a lower energy dissipation. It can thus be concluded that the darker areas in the phase image correspond to the more viscous polystyrene part of the polymer and the brighter areas to the much less viscous polyisoprene part. The height of the elevations is relatively small (2 nm) with respect to the initial total film thickness (10.1 nm) (100Å P(S-b-I)).

phase image) consisted of the more viscous polystyrene part of the diblock copolymer, whereas the areas with a larger phase shift (bright in the phase image) consisted of the much less viscous polyisoprene part.

The phase shift of the cantilever can be interpreted only qualitatively since the absolute energy dissipation depends on ambient conditions, like the air humidity, the average cantilever-sample distance and the oscillation amplitude. From the

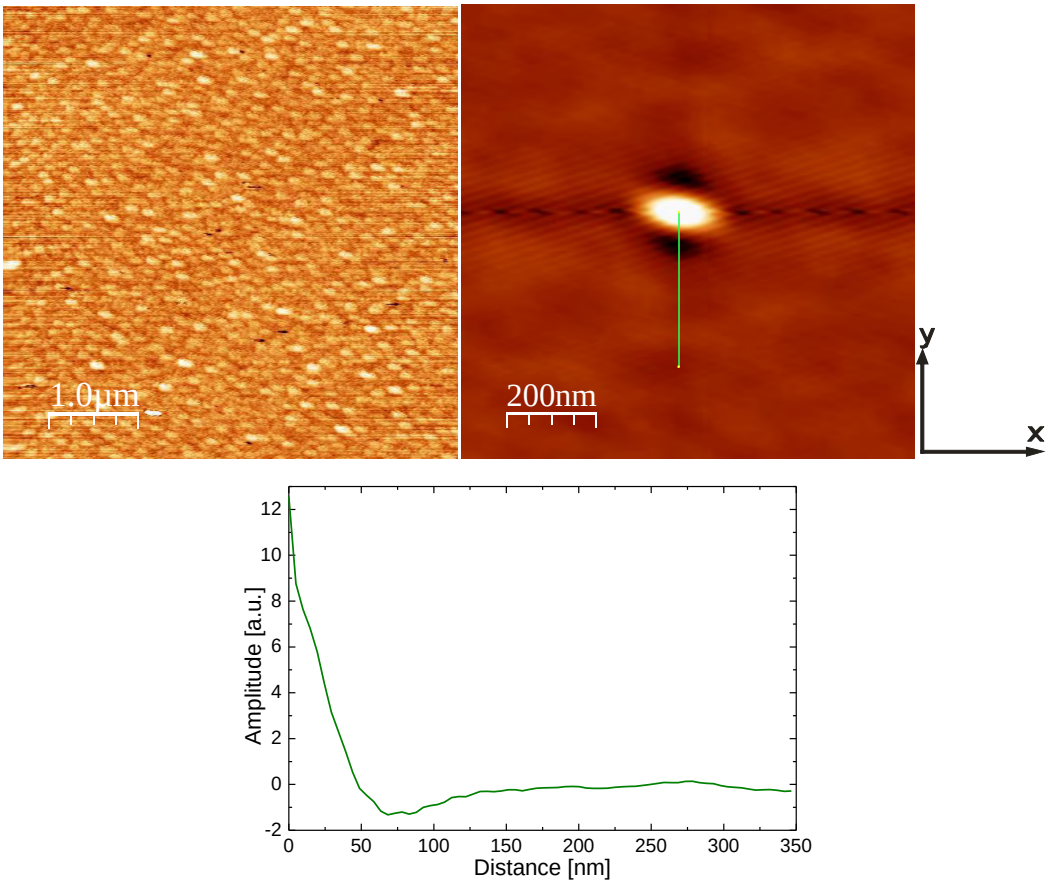

Fig. 9.15: AFM topography measurement (A1.6) after 1 h annealing at 145°C (upper left side). The self-correlation is shown on the right with a line cut in y-direction displayed in the lower part of the figure. The discrepancy of the width of the correlation in the x- and y-direction is an instrumental artefact. The image was scanned in x-direction as the fast scanning direction. The AFM tip is probably enlarged by wear in the x-direction. The convolution of the tip shape gives rise to enlarged features in this direction. The self-correlation is decaying until 60 nm, indicating the elevation diameter (100Å P(S-b-I)).

self-correlated AFM topography image (Fig. 9.15), one can conclude that the average diameter of the elevations is about 60 nm.

One hour of further annealing at 160°C does not change the sample morphology significantly, see the results of the AFM measurement (A1.7) displayed in Fig. 9.16. The elevations are of comparable height as before, and a dominant length scale of approximately 100 nm can be identified in the Fourier transformed topography image and the power spectral density diagram, which is relatively close to the correlations obtained in the SERGIS measurement.

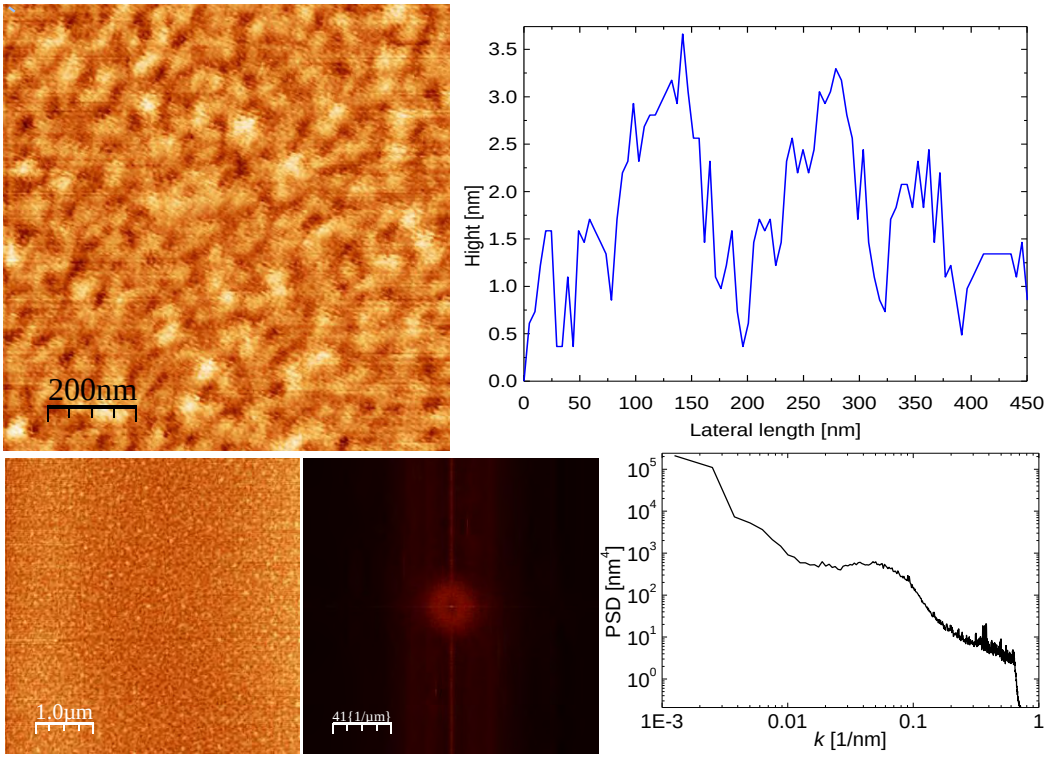

Fig. 9.16: AFM measurement (A1.7) recorded after 1 h additional annealing at 160°C. Top row**:** Topography measurement and line cut. Bottom row: Topography, FFT and power spectral density (100Å P(S-b-I)).

The following five annealing steps at temperatures of 176°C to 215°C (dewetting steps 8 to 11) did not lead to a significant change in the SERGIS signal (Fig. 9.12, measurements (S1.8) to (S1.11)).

After the final toluene treatment for 1 hour at a vapour pressure of 20 mbar (dewetting step 12) some oscillations reappeared in the SERGIS measurements (S1.12a,b). Due to the possibly different surface tensions of the polymer melt and the toluene-polymer solution, the toluene-polymer solution might have different equilibrium conditions, which might for example lead to different boundary conditions regarding the segregation of one polymer component to the film interface. This sample state was measured with both the 2D supermirror (S1.12a) and the ^{3}He cell (S1.12b) as polarisation analyser. The data in the measurement with the ^{3}He cell have a smaller statistical error bar since no absorbing layers were in the beam as in the case of the 2D supermirror analyser (cf. Fig. 3.20). Due to the higher and in particular more homogenous transmission, the ^{3}He cell is more

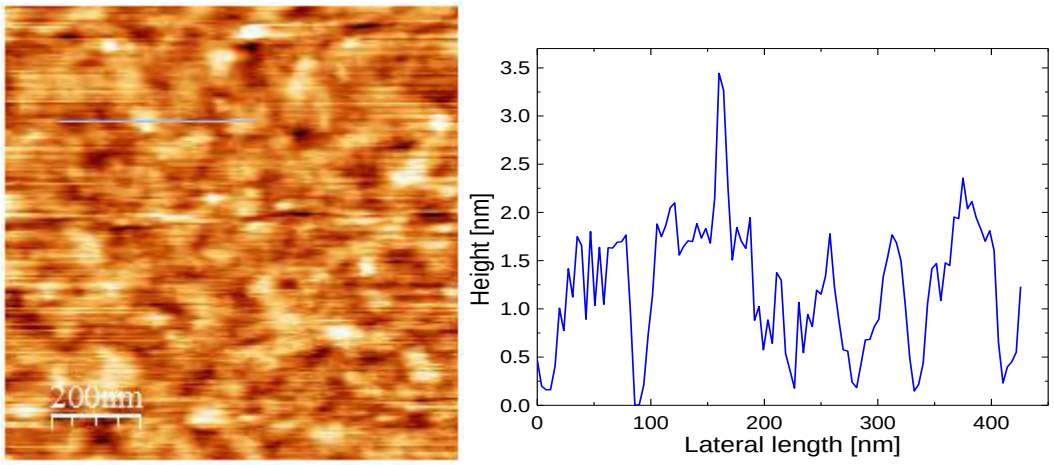

Fig. 9.17: AFM topography measurement (A1.12) and line cut after annealing at temperatures up to 215°C and 1 hour toluene treatment at 25 mbar (100Å P(S-b-I)).

suitable for the measurement, but it was only available at the last stage of the experiment.

The AFM topography image (AFM measurement A1.12, see Fig. 9.17) after the toluene treatment shows still no dewetting of the diblock copolymer film, i.e. no uncovered regions of the underlying substrate, and the topography did not change significantly as compared to the previous state after annealing at 160°C.

9.2.1.3 **Discussion**

The AFM images in Fig. 9.14 and Fig. 9.15 indicate that polystyrene and polyisoprene may have laterally phase separated into a hexagonal structure, with polystyrene cylinders of 60 nm diameter sticking slightly out of the average film surface as sketched in Fig. 9.18. The volume of one such cylinder can comprise approximately 100 polystyrene sub-chains. Taking into account the initial film thickness and the height of the elevations, one can conclude that the polystyrene cylinders are elevated by approximately 25% compared to the thickness of the rest of the film. Taking further into account the equal volume fraction of both polymer constituents, the surface coverage of each polymer constituent and the relative distance of the polystyrene cylinders can be calculated. The resulting surface coverage of the polystyrene cylinders is 43%, the edge length of the hexagons diplayed in Fig. 9.18 is 49.5 nm, the centre-to-centre distance of the cylinders is 86 nm, and the gap between two adjacent cylinders is 26 nm. This hexagonal

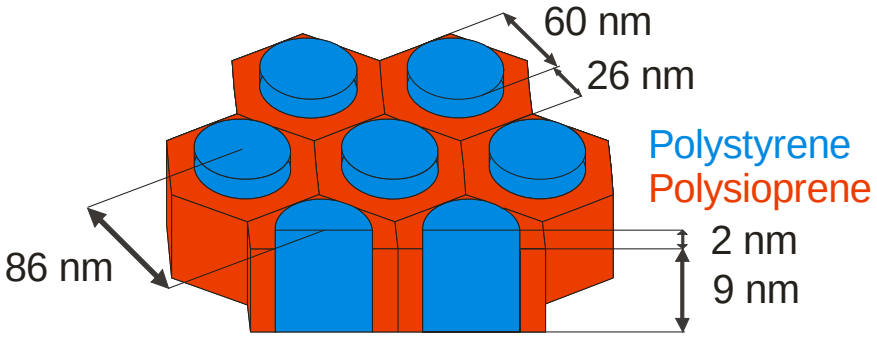

Fig. 9.18: Sketch of the cylinder phase. The polystyrene-rich areas (blue circles) are approximately elevated by 25% compared to the height of the polyisoprene-rich part (red fraction of the hexagon). Since the volume fraction of polystyrene and polyisoprene are identical in the investigated diblock copolymer material, the surface coverage of polystyrene must be approximately 43%. Based on the measured diameter of the cylinders (60 nm), the other parameters, i.e. the cylinder centre to centre distance (86 nm) and the gap between the cylinders (24 nm), have been calculated.

phase does not exist in bulk samples of poly(styrene-block-isoprene) diblock copolymers with equal volume fraction of both constituents. The different phase might be induced by the free interface and the very limited thickness of the film. Note that the film thickness of 100 Å corresponds to only twice the thickness of a lying-down diblock copolymer molecule in bulk (cf. Fig. 6.6).

No AFM images have been taken in this state however in a further dewetting state a cylindrical structure can be observed in the AFM image. It can be expected that this morphology observed in AFM was much more pronounced in the sample state at dewetting step 3, where clear oscillations were observed in the SERGIS measurement S1.3.

9.2.1.4 **Summary**

The film structure only changed significantly during annealing at 105°C and 116°C. The SERGIS data (S1.3) of the initially 100 Å thick poly(styrene-block-isoprene) diblock copolymer film presented in Fig. 9.12 allows to make a clear statement about the existence of a microphase separation with phase boundaries perpendicular to the sample surface and a periodicity of 96 nm at the dewetting step 3, i.e. after annealing the as-grown sample at 62°C, 80°C, and 105°C for one hour each. In all other SERGIS measurements, no oscillation significantly larger

than the statistical error bars is observable, and in these cases, both models fit the data equally well.

9.2.2 Dewetting of a 150 Å Thick Diblock Copolymer Film Investigated by Reflectivity

The dewetting of a 150 Å spin-coated diblock copolymer film of party deuterated poly(styrene-block-isoprene) was investigated by means of neutron and x-ray reflectivity at different dewetting steps as presented in Table 9.2. The final state of the sample was investigated in addition with SERGIS (NRSE option, Section 3.1.2) and AFM.

During the neutron reflectivity measurements and the second x-ray reflectivity measurement (X2.1) the sample was kept in vacuum below 10^{-4} mbar. All other experiments were performed under ambient conditions.

9.2.2.1 Reflectivity Studies

The x-ray and neutron reflectivity measurements are presented in Fig. 9.19 as a function of the dewetting step. For the fitting of the data, a three-layer model was used to allow for surface segregation or phase separation of the two polymer constituents. The fitted film thicknesses are displayed in Fig. 9.20.

During annealing at 53°C, an x-ray measurement (X2.1a) was performed on a sealed tube copper anode x-ray source at the instrument *N-REX*$^+$, see Section 4.1.

Dewetting step	Annealing temperature [°C]	Annealing time	Measurements
0	25	0	x/n reflectivity (X2.0,N2.0))
1a	53	60 min	x reflectivity at annealing temp (X2.1a)
1b	53	48·60 min	n reflectivity at annealing temp (N2.1b)
1c			n reflectivity after cool down (N2.1c)
2	65	4·30 min	n reflectivity (N2.2)
3	91	30 min	n/x reflectivity (N2.3/X2.3)
4	25	1 year	x reflectivity (X2.4), SERGIS (S2.4), AFM (A2.4)
5	25	2 months	x reflectivity (X2.5), SERGIS (S2.5), AFM (A2.5)

Table 9.2: Sample treatments and measurements (150Å P(S-b-I)).

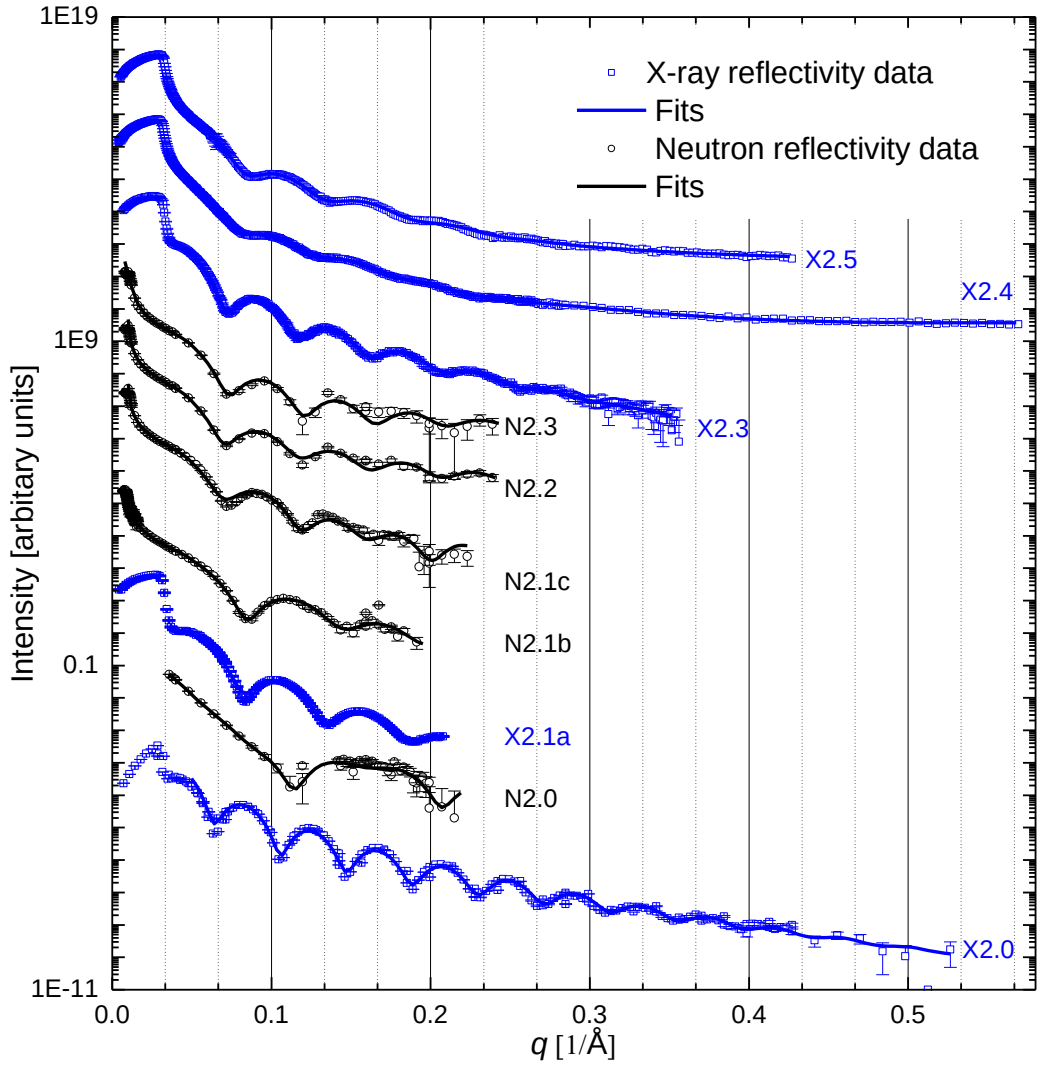

Fig. 9.19: Neutron and x-ray reflectivity. Experimental data (points with statistical error bars) and fits (solid lines) (150Å P(S-b-I)).

The other x-ray reflectivity measurements (X2.0 and X2.3 – X2.5) were performed at a rotating copper anode x-ray source with a micro focus filament at the MPI-MF in Stuttgart. The x-ray wavelength was 1.54 Å in both cases. The neutron wavelength was approximately 5.5 Å. Higher harmonic neutron wavelengths, also Bragg-reflected by the monochromator, were not suppressed. The higher harmonic wavelengths are particularly dominant when using an absorber: In the relevant wavelength range the absorption coefficient is proportional to the wavelength λ, which leads to a higher absorption of longer wavelengths (see also Section 5.2.1). The neutron data were only fitted for

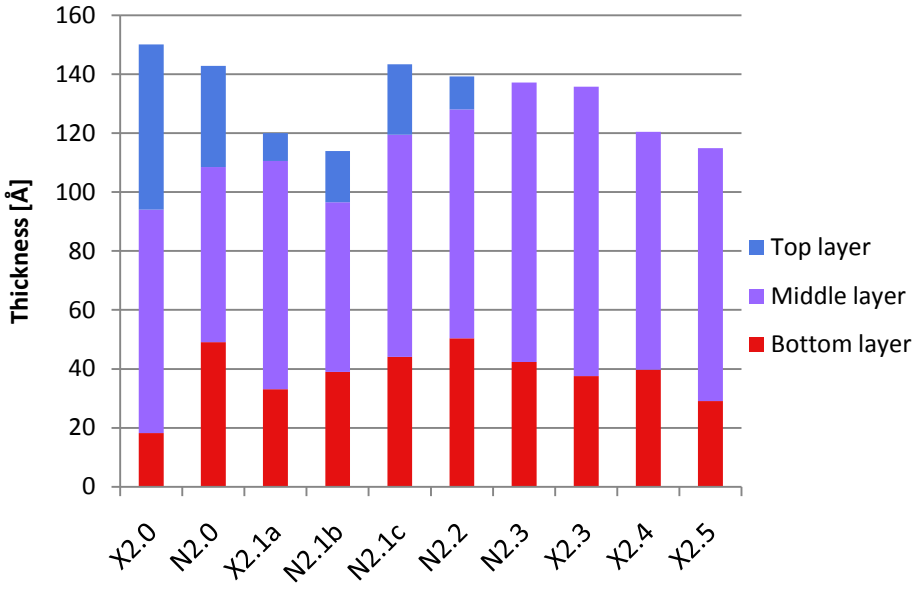

Fig. 9.20: Thicknesses as obtained from the reflectivity fits (150Å P(S-b-I)).

$\alpha_i > 0.4°$, where no absorber was used and the reflectivity of higher harmonic wavelengths is insignificant.

In the as-received state at 25°C, the film had a thickness of 150 Å (x-ray measurement (X2.0)) under ambient conditions and 142 Å (neutron measurement (N2.0)) in vacuum. The difference in thickness might be related to air diffusing into the film and causing it to swell. Another explanation might be a measurement inaccuracy, e.g. a small deviation from the specified neutron wavelength. The fitted scattering length densities of all three layers can be attributed to different mixtures of deuterated polystyrene and protonated polyisoprene. In the middle layer the density of polystyrene is slightly elevated compared to the nominal film stoichiometry, whereas in the top and bottom layers polyisoprene is enriched. The average scattering length density in the film is in very good agreement to the literature value (deviation < 1%).

In the next step, two reflectivity measurements were performed during annealing for 48 hours at 53°C (dewetting step 1). At the beginning of the annealing, a film thickness of 120 Å (X2.1a) was obtained. After 23 hours, another reflectivity measurement was started (N2.1b) and yielded a film thickness of 114 Å. This reduction of the film thickness compared to the initial value of 142 – 150 Å points to a shrinking of the film during annealing. For polymer films a reversible

negative thermal expansion coefficient over a certain temperature range below the glass transition temperature was already reported [Mukherjee'02]. The neutron data (N2.1b) further indicates that the scattering length density of the centre part of the film did not change compared to the as received state, but polystyrene diffused to the top layer and polyisoprene to the bottom layer. The final scattering length density of the top layer can be attributed to polystyrene and the lower part of the film was a polyisoprene-rich mixture with approximately 75% polyisoprene volume fraction.

After cooling down, the total thickness of the film was identical to the state before annealing, as revealed by a neutron reflectivity measurement (N2.1c). This indicates a complete reversibility of the shrinking of the film in the direction perpendicular to the sample surface during annealing at 53°C. By means of reflectivity, no conclusion can be drawn whether the film is still homogeneous or if droplets of equal height formed with a locally enhanced scattering length density.

In the next step, the sample was four times annealed during 30 min at 65°C (dewetting step 2). Between the annealing steps, the sample was cooled down to 25°C. After the last annealing step, the sample was measured at 25°C by means of neutron reflectivity (N2.2). The layered morphology of the film remained unchanged and the total film thickness slightly decreased to 139 Å.

Finally, the sample was annealed for 30 min at 91°C (dewetting step 3) which made the film thickness shrink again slightly to 137 Å, as revealed by the neutron reflectivity measurement (N2.3). At this dewetting step, the polystyrene-rich top layer disappeared and the middle layer grew accordingly, while the polyisoprene-rich bottom layer remained practically unchanged. The layered film morphology and the total thickness found in the neutron reflectivity measurements were confirmed by the subsequent x-ray reflectivity measurement (X2.3) performed under ambient conditions.

9.2.2.2 **In-Plane Measurements at the Two Last Dewetting Steps**

After the reflectivity experiments described in the preceding section, the sample was kept under ambient conditions for 1 year in a sealed container (dewetting

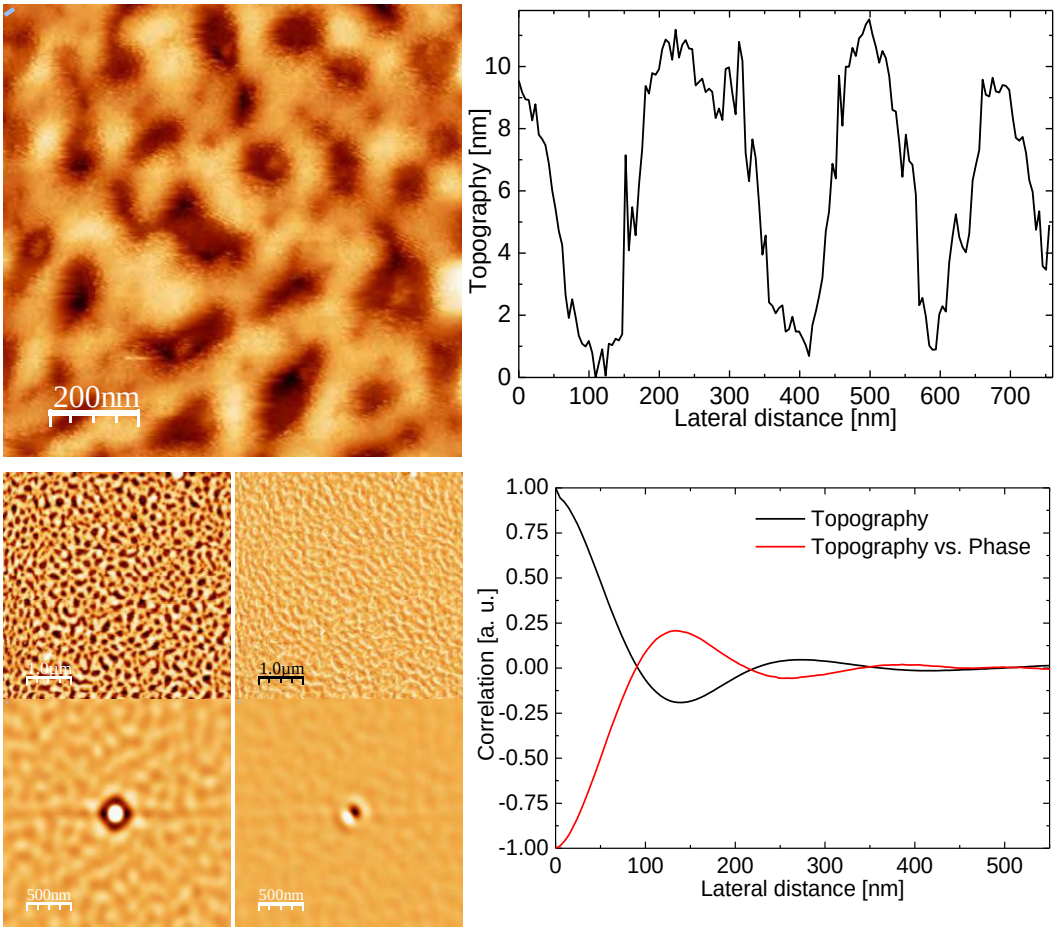

Fig. 9.21: AFM study (A2.4) (dewetting step 4)**.** Top row: AFM topography image and line cut. Bottom left: AFM topography and phase image, together with topography self correlation and cross correlation. Bottom right: Line cuts as indicated in the correlation images on the left (150Å P(S-b-I)).

step 4). In this time, the total thickness decreased to 120 Å as obtained by the fit to the x-ray reflectivity measurement (X2.4). Compared to the last x-ray measurement performed one year before, the scattering length density of the top layer was now found to be reduced by 58%, indicating a possible dewetting of the sample, which could be confirmed by the subsequent AFM measurements (A2.4) as illustrated in Fig. 9.21. Depletions of approximately 10 nm in depth are observed. The AFM topography self-correlation shows a depletion at 142 nm and a peak at 273 nm. The order is decaying until the second neighbour distance. The cross correlation between AFM topography and phase shows that at elevations in the topography are correlated to depletions in the phase signal. Hence, in the depletions polyisoprene is exposed at the film surface and the elevations of the film consist of the more viscous polystyrene. Obviously, the film did not

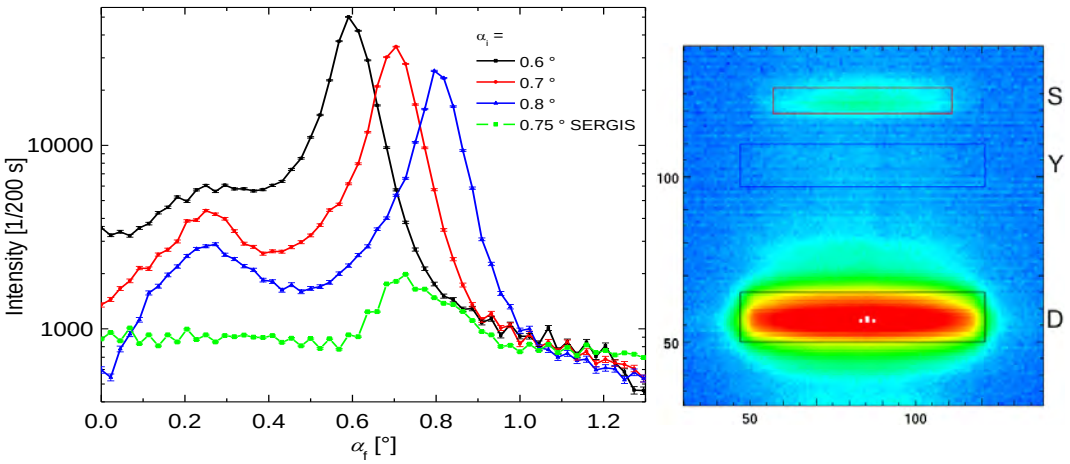

Fig. 9.22: Left: α_f profiles for different incident angles with (green line) and without (other colours) the complete SERGIS-NRSE set-up. The SERGIS set-up includes the polariser, the NRSE- and coupling-coils and the 2D multi mirror analyser. Right: Detector image with SERGIS equipment in the beam path (images corresponds to the green line on the left). The position of the direct beam (D), the Yoneda peak (Y) and specular reflected beam (S) are indicated. The boxes mark the regions of interest for the SERGIS evaluation (150Å P(S-b-I)).

completely dewet, since bare silicon regions would lead to a minimum of the phase shift at the minimum position of the topography signal.

Grazing incidence neutron scattering experiments show a distinct Yoneda peak, as illustrated in Fig. 9.22, indicating a film with high roughness. A repetition of the grazing incidence neutron measurement with the complete SERGIS-NRSE set-up in the neutron beam path reveals that the insertion of the SERGIS equipment leads to strong absorption of the neutron intensity and an, in relation, elevated background.

The two SERGIS measurements (S2.4 and S2.5) presented in the following were performed with the neutron resonance spin-echo set-up (Section 3.1.2), and the multi mirror neutron spin analyser (Section 3.2.2.2).

In the left panel of Fig. 9.23 the SERGIS measurement (S2.4) at the dewetting step 4 is plotted. Due to a relatively large incidence angle of $\alpha_i = 0.75°$ the contribution of in y-direction unscattered neutrons in the Yoneda ROI is negligible ($I_r/I_{ROI} = 0$), but a non-polarised background was taken into account ($I_{back}/I_{ROI} = 0.45$). The fit assuming a droplet morphology with microphase

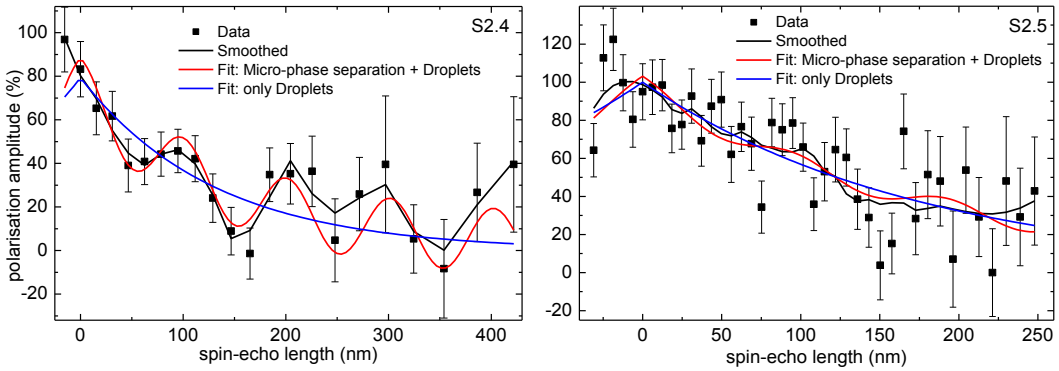

Fig. 9.23: SERGIS measurement (S2.4 and S2.5) obtained with the neutron resonance spin-echo set-up (150Å P(S-b-I)).

separation yields a lower $\chi^2_{\mathrm{red.}}$ value than the fit assuming droplets of homogenous scattering length distribution parallel to the sample surface ($\chi^2_{\mathrm{red.}}$ = 0.65 vs. 1.19). The obtained microphase separation period is (100.6 ± 2.1) nm and the decay parameter of the droplets is (6.9 ± 1.1) 10^{-3} nm^{-1} or (7.7 ± 1.4) 10^{3} nm^{-1} for the fit with and without microphase separation, respectively. The decay parameter translates to an average droplets size of (146 ± 23) nm or (130 ± 25) nm, which is in very good agreement with the first minimum in the AFM topography self-correlation function at 142 nm (Fig. 9.21) which also indicates the droplet diameter. We can presume that a hexagonal structure formed as illustrated in Fig. 9.18. The situation seems to be similar to the one described in Section 9.2.1 in connection with dewetting step 6, but when comparing measurements A1.6 and A2.4 the film appears to be further dewetted in measurement A2.4.

The second SERGIS measurement (S2.5) was performed after a further delay of two months (dewetting step 5) during which the sample was again kept at ambient conditions in a sealed container. The SERGIS data are shown in the right panel in Fig. 9.23. The measurement was performed at an incidence angle of α_i = 0.6°. As opposed to the previous SERGIS measurement, the direct beam was mostly blocked before the second spin-echo arm leading to a lower background level (I_r/I_{ROI} = 0, I_{back}/I_{ROI} = 0.3).

The sample morphology as well as the inner structure changed, as can be seen in the SERGIS data (S2.5). When fitting the data with the model assuming a

microphase separation with phase boundaries perpendicular to the sample surface, no significant difference in the $\chi^2_{\mathrm{red.}}$ value can be observed in comparison with the model without microphase separation ($\chi^2_{\mathrm{red.}}$ = 1.23 vs. 1.18). The decay parameters [$(5.5 \pm 0.9)\ 10^{-3}$ nm^{-1} and $(5.6 \pm 0.8)\ 10^{-3}$ nm^{-1}] correspond to islands with a diameter of (183 ± 30) nm assuming the presence of a lateral microphase separation or (177 ± 27) nm assuming the absence of a microphase separation with phase boundaries perpendicular to the sample surface. When assuming a microphase separation, the fit yields a period of (96 ± 12) nm with an amplitude A_{mp} of (4.5 ± 6.7)%.

An AFM study (A2.5) performed in the final dewetting state (Fig. 9.24) yields an AFM topography self-correlation function with a first minimum at 202 nm, which is in good agreement with the SERGIS data. The first neighbour correlation peak is at 356 nm. In the SERGIS measurement, the polarisation of the reference beam decayed nearly to zero at a spin-echo length of 250 nm, due to limitations of the magnetic-field homogeneity in this specific experiment. Hence, no sign of the first neighbour correlation could be observed in this SERGIS experiment.

The AFM topography and phase images (Fig. 9.24) show that the sample is dewetted further in comparison to the state of the sample two months earlier. The holes have an elongated shape and the height distribution of the film is terrace like. The terrace height corresponds well to the film thickness determined by x-ray reflectivity (X2.5) which is only 5 Å smaller than in the case of the previous measurement (X2.4). Within the holes visible in the AFM image, the silicon substrate seems to be exposed: The elevations in the AFM topography image are correlated with a high phase shift and the depletions with a very low phase shift. The silicon substrate being a very solid crystal is giving rise to the lowest phase shift in the system. No phase contrast indicating polyisoprene or polystyrene on the film surface is visible.

In the final state of the sample, 76% of the substrate surface was still covered by the polymer film. The volume of the film has shrunk by a factor of 2.2 with respect to the as-prepared film. A comparison of all neutron reflectivity results shown in Fig. 9.25 reveals a continuous decrease of the integrated scattering

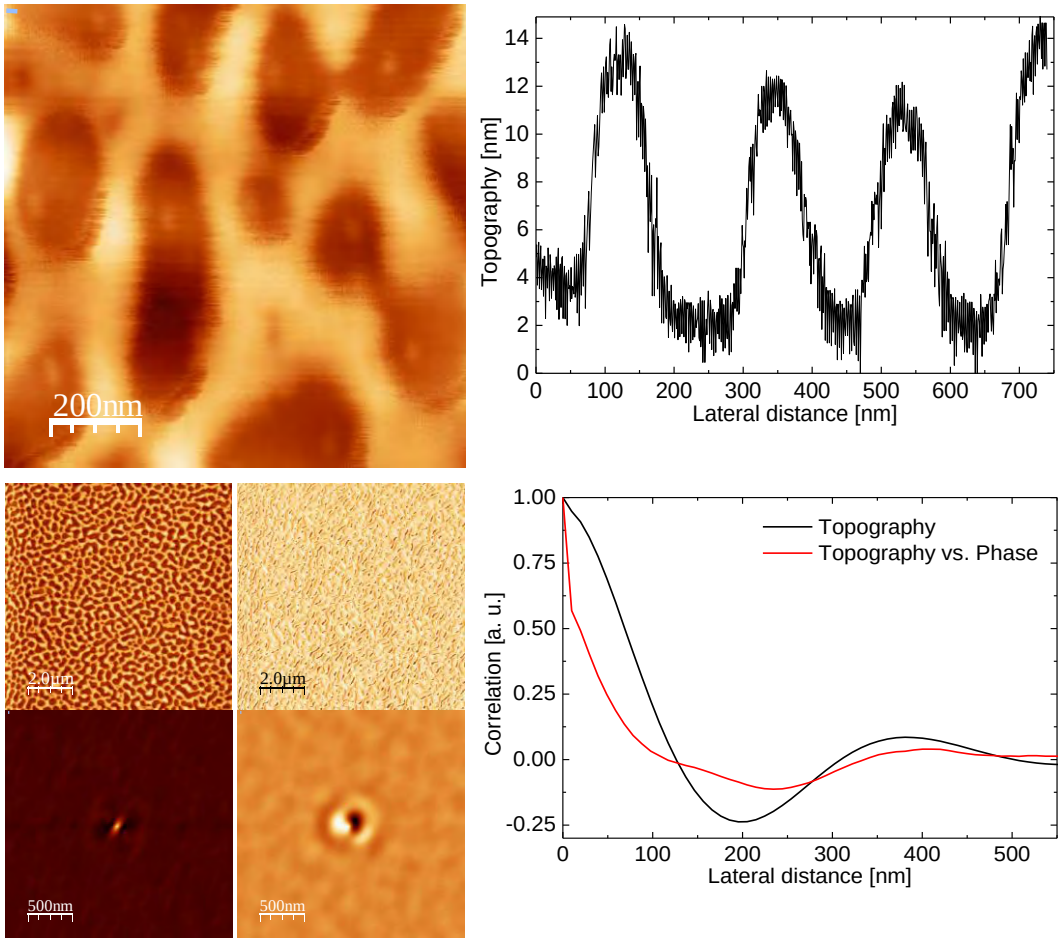

Fig. 9.24: AFM study (A2.5) in the final state of the sample. Top row: AFM topography image with line cut. Bottom left: AFM topography and phase image with topography self correlation and cross correlation. Bottom right: Line cuts as indicated in the correlation images on the left. Where dark areas are visible in the phase image, the tip approached the sample too closely and got into an attractive regime. Hence, the cross correlation is slightly distorted at short distances (< 100 nm) (150Å P(S-b-I)).

length by 20% in the course of annealing in vacuum. This cannot be related to an evaporation of toluene which might still be incorporated in the film after the spin coating process, because the neutron scattering length density of toluene is very low (similar to that of polyisoprene). A loss of polymer molecules by evaporation during the annealing and dewetting of the film might have occurred. The reduction of the integrated x-ray scattering length (Fig. 9.25) from the initial to the final state is in accordance with the material loss apparent from the AFM study. The origin of this loss of material could not be clarified.

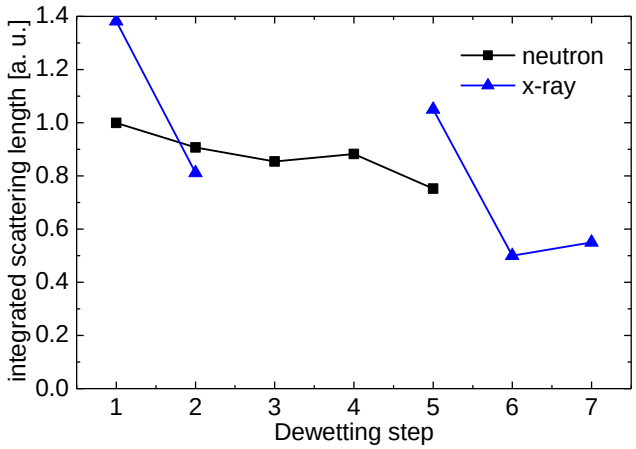

Fig. 9.25: Total scattering length in the polymer film as obtained by neutron and x-ray reflectivity fits (150Å P(S-b-I)).

9.2.2.3 **Summary**

In the initial state, the 150 Å thick film exhibited a layered structure of a polystyrene-rich mixture in the centre, and polyisoprene-rich mixtures at the substrate and the vacuum interface. The morphology changed to a polystyrene-rich top layer, a mixture in the centre, and a polyisoprene-rich bottom layer during mild annealing at 53°C. Further annealing at 91°C made the top polystyrene-rich layer disappear, and the former middle layer grew accordingly. Presumably, the film then dewetted while stored for one year in a sealed container. The SERGIS data presented in Fig. 9.23 allow to make a clear statement about the existence of a microphase separation with phase boundaries perpendicular to the substrate surface with a periodicity of 101 nm. The AFM study shows a morphology in accordance with the SERGIS measurement. Droplets with a diameter of 140 nm were identified in both cases. The elevations consist of polystyrene and the depletions in between of polyisoprene. This indicates a hexagonal structure as illustrated in Fig. 9.18. Further storage for two months resulted in a partially dewetted sample state. The strong microphase separation disappeared as seen in a further SERGIS measurement. The corresponding AFM images show a growth in island diameter, which is in agreement with the SERGIS measurement. In the final state large holes have formed in which the substrate surface is uncovered.

9.2.3 Dewetting of a 450 Å Thick Diblock Copolymer Film

A 450 Å thick spin-coated film of partially deuterated poly(styrene-block-isoprene) was investigated by means of neutron reflectivity, x-ray reflectivity, SERGIS, and AFM studies. The dewetting of the sample was investigated in different steps, see Table 9.3.

9.2.3.1 Experimental Set-Up

The SERGIS experiments were performed with 30° triangle coils and a single analyser mirror (see Section 3.2.2.1), since the other more sophisticated spin analyser options were not available at the time of the experiment. Due to the limited aperture of the mirror unit, only a narrow exit angle (α_f) range of about 0.2° could be recorded at a time. Therefore, neither the direct nor the reflected beam could be observed simultaneously with the Yoneda peak at the incident angles of interest. Hence, an additional spin-echo measurement on a bare silicon wafer was performed and used as reference signal. The 450 Å thick film gives rise to a Yoneda peak with relatively high intensity at advanced dewetting steps, hence the background and the contributions of in y-direction unscattered neutrons could be neglected ($I_r/I_{ROI} = I_{back}/I_{ROI} = 0$). Neutron reflectivity and SERGIS measurements were performed with neutrons of wavelength λ = 5.5 Å. To polarise

Dewetting step	Annealing temperature [°C]	Annealing time [hours]	Measurements
0	25	0	x/n reflectivity (X3.0, N3.0), AFM (A3.0)
1	96	1	SERGIS (S3.1)
2	120	1	n-reflectivity (N3.2)
3	155	1	n reflectivity (N3.3)
4	155	1	n reflectivity (N3.4)
5	155	2	n reflectivity (N3.5)
6	169	1	SERGIS (S3.6), n reflectivity (N3.6)
7	183	1	SERGIS (S3.7), n reflectivity (N3.7), AFM (3.7)
8	183	2	SERGIS (S3.8), x reflectivity (X3.8), AFM (A3.8)

Table 9.3: Sample treatments (450Å P(S-b-I)).

the neutrons for the SERGIS measurements and at the same time suppress higher harmonics, mainly the $\lambda/2$ contribution in the beam, the polarising mirror (see Section 3.2.1) was installed in reflection geometry. Due to time restrictions during the measurement, the polariser mirror was left in the beam for the reflectivity measurements. To assure identical spin-echo conditions in each experiment and due to time limitations, all SERGIS coils were also left in the neutron beam path from the first to the last SERGIS measurement, i.e. also during neutron reflectivity measurements (N3.2 – N3.7). Only the neutron spin analyser was removed for each neutron reflectivity measurement. The SERGIS measurements were performed at an incident angle $\alpha_i = 0.8°$, where the signal to background ratio was optimised with the SERGIS coils inserted into the neutron beam path.

The x-ray measurements were performed at the rotating anode x-ray source at the MPI-MF in Stuttgart at a wavelength of 1.54 Å. Both, the x-ray and AFM studies were performed under ambient conditions. During the neutron experiments (SERGIS and reflectivity) the sample was kept in vacuum below 10^{-4} mbar.

9.2.3.2 **Results**

The reflectivity data measured at different dewetting steps together with the corresponding fits are presented in Fig. 9.26 and the obtained thicknesses are illustrated in Fig. 9.27.

In the as received state, i.e. after spin coating, the total film thickness was 470 Å (X3.0) when measured under ambient condition with x-ray reflectivity and 401 Å (N3.0) when measured with neutron reflectivity in vacuum. AFM studies (A3.0) show that on the film surface droplet-like elevations of approximately 5 nm height have formed (see Fig. 9.28). The AFM topography RMS roughness is 14 Å. This value is identical to the roughness obtained by the x-ray and neutron reflectivity measurements. A correlation between the phase image and the topography can be observed. The elevations seem to be mostly covered with a softer material than the depletions. On one hand, this may indicate that the less viscous polyisoprene is concentrated at the elevations and polystyrene in the valleys. On the other hand, this observation may also be related to a reduced viscosity of the elevations due to missing geometrical constraints. The second explanation is in line with the

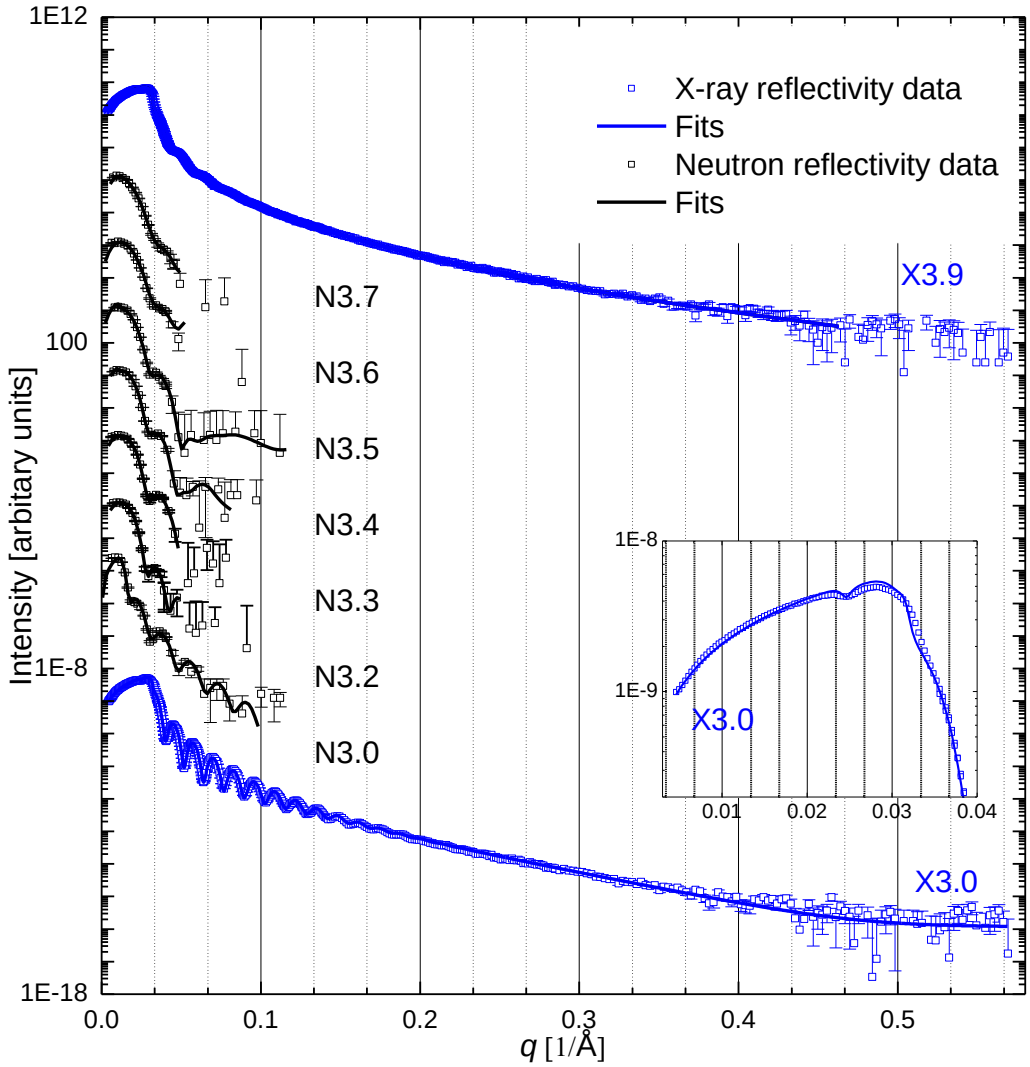

Fig. 9.26: Reflectivity data and fits (450Å P(S-b-I)).

neutron reflectivity fit (N3.0). The neutron reflectivity data can be fitted with a two layer model. Both layers consisted, laterally averaged, of a mixture of polystyrene and polyisoprene. The lower part of the film is approximately 10% richer in polyisoprene, whereas the top layer is richer in polystyrene. The x-ray reflectivity data (X3.0) show two total reflection edges in the area of total reflection ($\alpha_i < 0.23°$ or $q_z < 0.033$ Å^{-1}), which were not observable in the case of the thinner films. These two critical angles of total reflection correspond to the polymer film and the silicon substrate. A two layer fit assuming a polyisoprene rich layer close to the substrate interface and a one layer fit with an intermixed state are both able to reproduce the data in this regime, but not a two layer fit assuming a polyisoprene rich layer adjacent to the vacuum. In the remaining

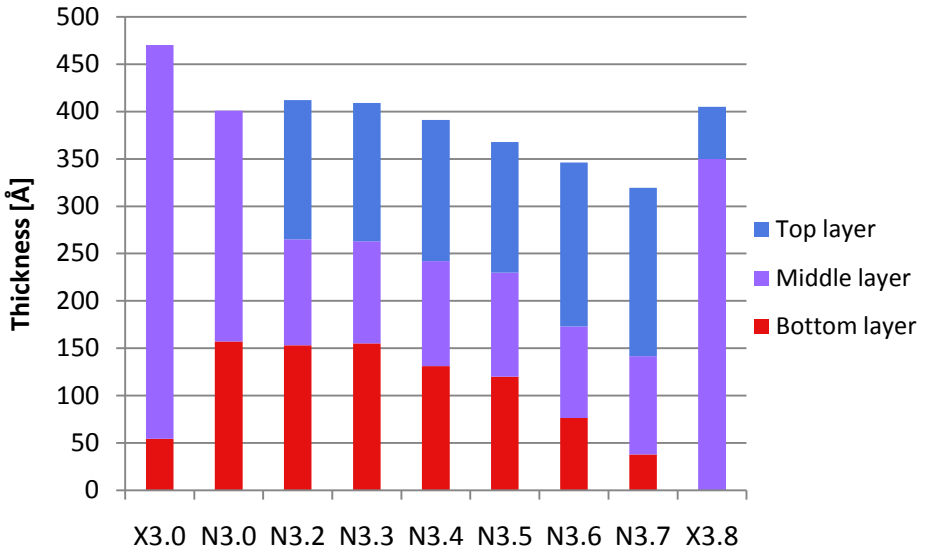

Fig. 9.27: Thicknesses as obtained from the reflectivity fits (450Å P(S-b-I)).

angular range of the reflectivity curve ($q_z > 0.033$ Å^{-1}), the three scenarios cannot be distinguished due to the small scattering length density contrast of polyisoprene and polystyrene using x-rays. Only the fit in agreement with the neutron data is displayed (two layer model with a weak increasing concentration gradient of polystyrene towards the surface).

Simultaneously to the specular neutron reflectivity, the off-specular scattering signal was recorded. The α_i - α_f maps are presented in Fig. 9.29. In the as received state (N3.0) two Yoneda wings at $\alpha_i = \alpha_c$ and $\alpha_f = \alpha_c$ can be observed very well above the background level. This neutron reflectivity measurement was performed without the SERGIS equipment in the neutron beam. With the SERGIS equipment in the neutron beam, the background is expected to increase and the signal to be partly absorbed. Unfortunately, the SERGIS measurement in the as received state gave no result due to technical difficulties. A second SERGIS measurement (S3.1) was performed after the first annealing for 1h at 96°C (dewetting step 1). The strong off-specular scattering was not observable any more. Hence, there was not sufficient off-specular intensity to evaluate the SERGIS data.

The neutron reflectivity fit (N3.2) reveals, that the concentration gradient of polystyrene and polyisoprene in the direction perpendicular to the substrate surface became very pronounced after annealing the sample for 1 h at 96°C and 120°C (dewetting step 2). A distinct layering formed with nearly pure polystyrene

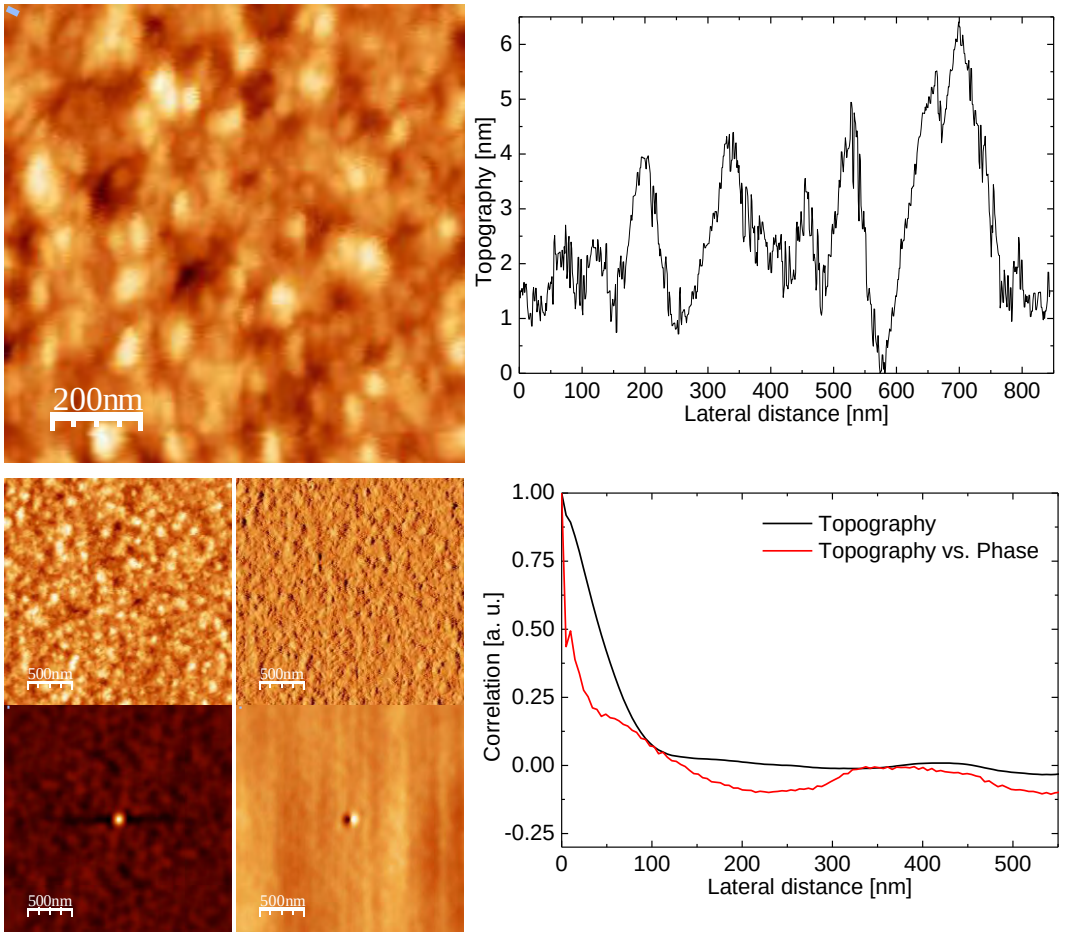

Fig. 9.28: AFM study (A3.0) in the as received state. Top: AFM topography image with line cut. Bottom: AFM topography, phase, topography self correlation, and cross correlation image, line cuts on the right as indicated (450Å P(S-b-I)).

in the top layer and a polyisoprene concentration of 80% in the layer adjacent to the substrate. In between the polystyrene top layer and the polyisoprene-rich bottom layer, an intermixed layer had to be introduced to fit the data. Compared to the as received state the total reflection edge is clearly shifted to higher angles. The data could be fitted only when assuming a layered system with polystyrene on top. The middle layer has a thickness slightly larger than those of the polystyrene and the polyisoprene-rich layer (top layer 112 Å, middle layer 153 Å, bottom layer 113 Å). As can be seen in the neutron α_i - α_f map (N3.2), the two Yoneda wings at the critical angle are not observable any more. Since in this neutron reflectivity measurement the SERGIS equipment was in the neutron beam, no direct comparison with the previous neutron reflectivity can be made with respect to the off-specular scattering intensity.

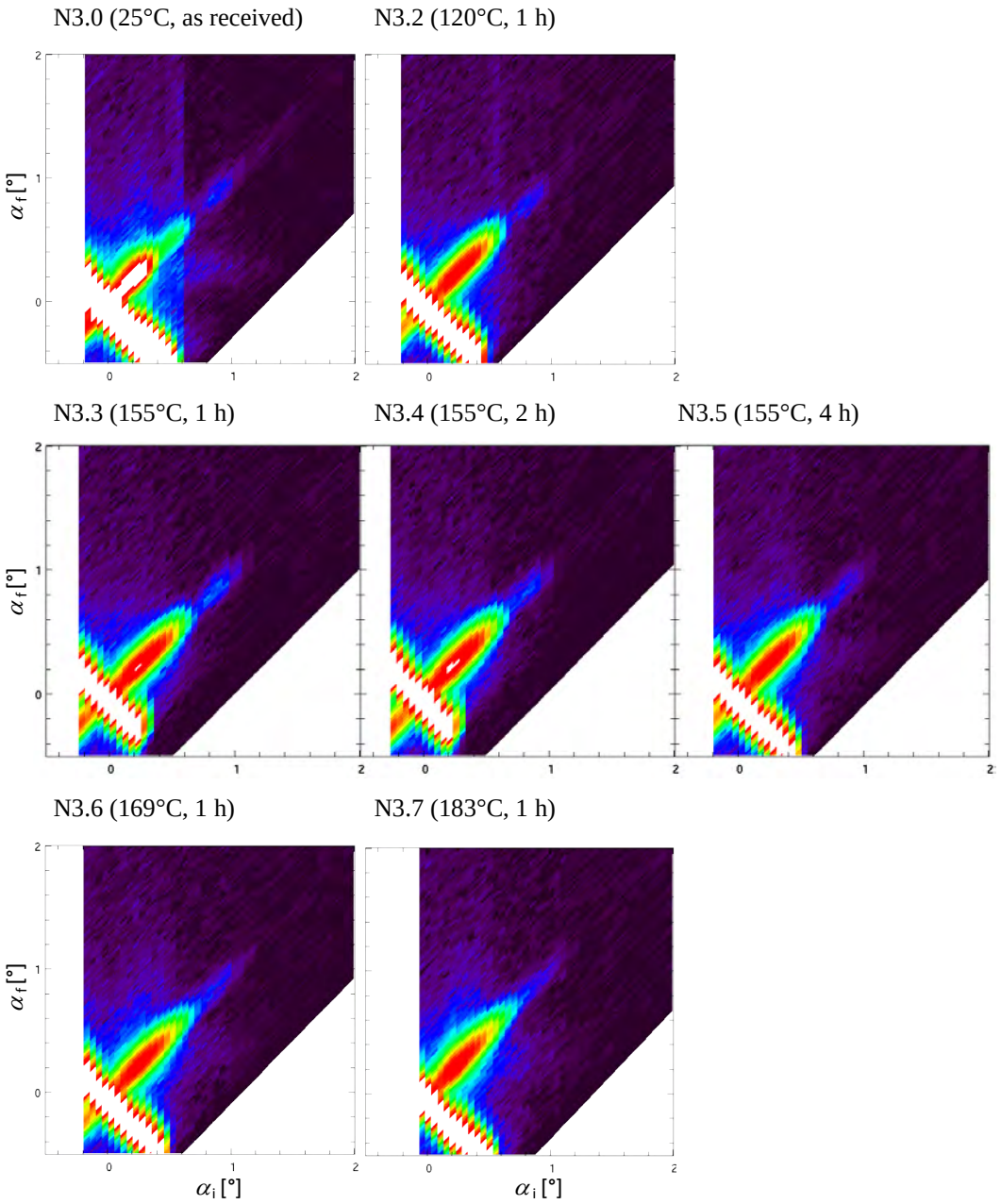

Fig. 9.29: Neutron reflectivity, α_i-α_f maps. At the angles α_i where the direct beam ($-0.2° < \alpha_i < 0.6°$) is recorded on the detector the background is elevated. At higher incident angles the direct beam is absorbed by a piece of boron rubber after the sample position. The white stripe is the very high intensity of the direct beam and the mainly red line is the area of total reflection in specular reflectivity. The first neutron reflectivity was recorded without, the following measurements with the SERGIS equipment in the neutron beam (450Å P(S-b-I)).

After the initial annealing steps at 96°C and 120°C, the sample was annealed three times at 155°C, twice for one hour and then once for two hours (dewetting steps 3 - 5). The amplitudes of the oscillations in the neutron reflectivity data

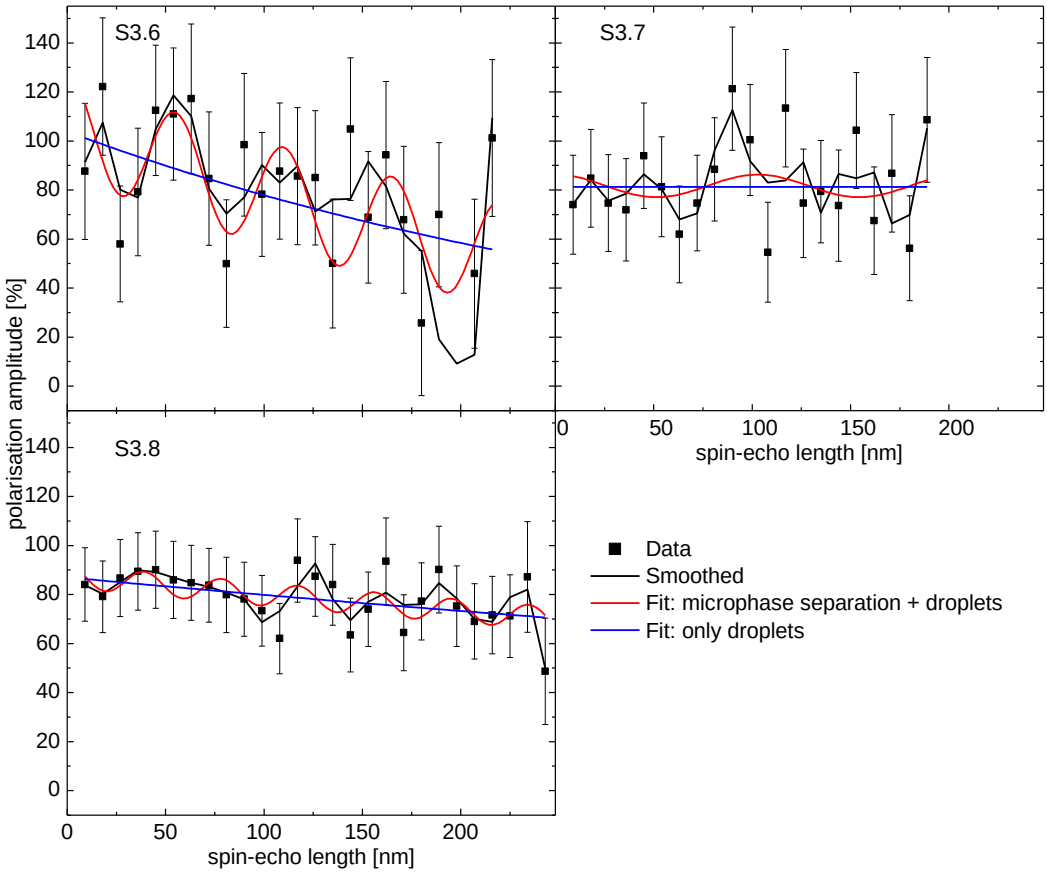

Fig. 9.30: SERGIS measurement (S3.6-8). The fit parameters are given in the text (450Å P(S-b-I)).

(N3.3 - N3.5) became less pronounced by further annealing the sample. In the α_i - α_f map (N3.5), an increase in the Yoneda intensity is clearly visible after the third annealing step at 155°C (dewetting step 5). However, the intensity level was not yet sufficient to perform a SERGIS measurement with acceptable statistics in a sensible time interval of about 12 h. The neutron reflectivity measurements (N3.3 – N3.5) reveal that the scattering length density of the middle layer decreased by about 35% and the thickness of the bottom layer decreased by about 20% from the first to the third annealing step at 155°C. The other layer thicknesses and scattering length densities stayed constant. The total thickness decreased from 409 Å to 368 Å.

The sample was further annealed for 1 h at 169°C (dewetting step 6). The model fit of the neutron reflectivity (N3.6) yields a decrease of the total film thickness (346 Å) due to a further decrease in thickness of the polystyrene rich layer adjacent to the substrate (76 Å). The α_i - α_f map shows two increasing Yoneda

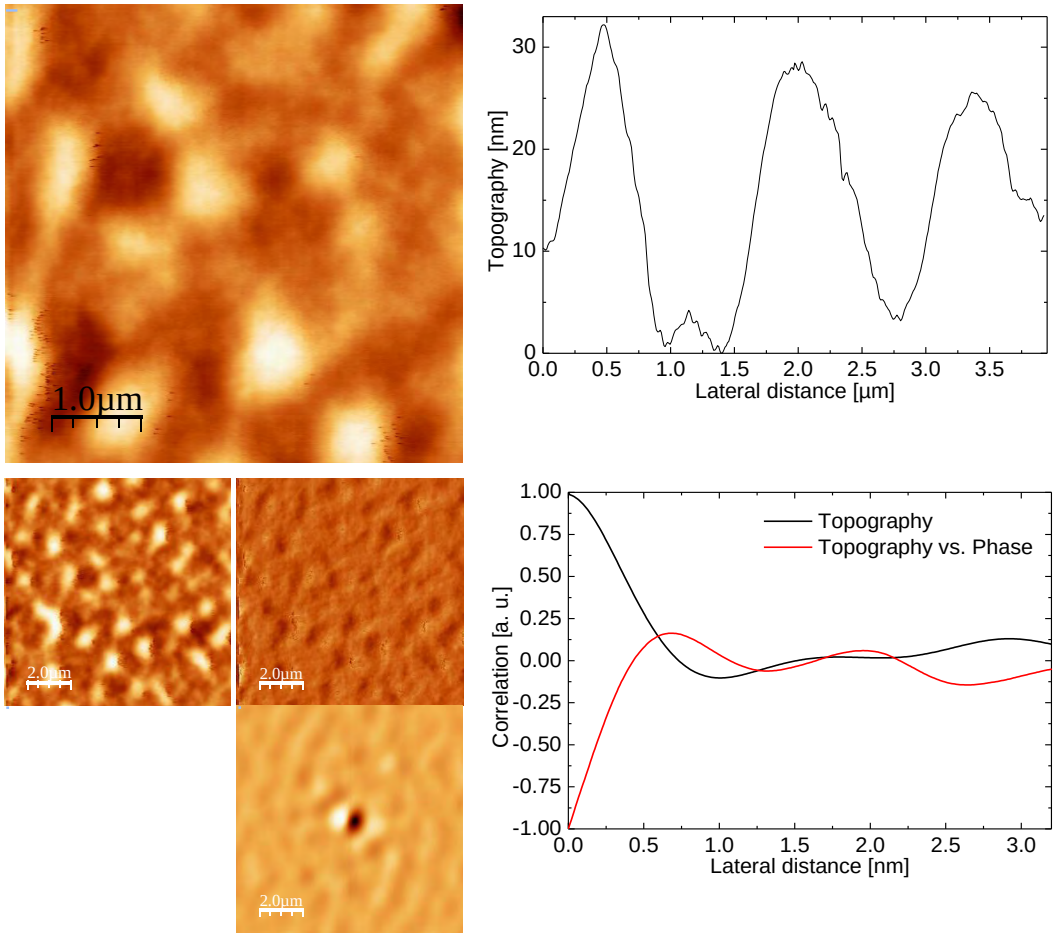

Fig. 9.31: AFM study (A3.7) after annealing 1h at 183°C. Top: AFM topography image with line cut. Bottom: AFM topography and phase image with topography self correlation and cross correlation and line cuts as indicated (450Å P(S-b-I)).

wings whose intensity level allowed performing a SERGIS measurement (S3.6). The SERGIS measurements are presented in Fig. 9.30 The slightly better fit to the SERGIS data with a $\chi^2_{red.}$ value of 0.96 is achieved with the model representing a microphase separation with phase boundaries perpendicular to the substrate surface, compared to a model without microphase separation in this direction. According to the fitting result, the islands could be described by a decay parameter of (3.1± 1.24) 10^{-3} nm^{-1}, indicating a diameter of (323 ± 154) Å. The internal microphase separation had a periodicity of (55.0± 1.5) Å. The fits assuming homogeneous islands without internal structure result in only slightly worse $\chi^2_{red.}$ value of 1.13. Therefore, no conclusion on the existence of a microphase separation with phase boundaries perpendicular to the substrate surface can be made based on the SERGIS data. The neutron reflectivity data

indicate a micro phase separation with phase boundaries parallel to the substrate surface. Hence, if a microphase separation with phase boundaries perpendicular to the sample surface existed, it was most likely limited to a small fraction of the film or it was characterized by a low concentration gradient.

In a further dewetting step the sample was annealed for 1 h at 183°C (dewetting step 7). According to the fit of the neutron reflectivity data (N3.7), the thickness of the polyisoprene-rich layer decreased further during this heat treatment. The total film thickness decreased to (346 Å). The corresponding α_i - α_f map (N3.7) shows two increasing Yoneda wings, which allowed performing a SERGIS measurement. The $\chi^2_{red.}$ value is only slightly lower for the model assuming no microphase separation than in the model with microphase separation with phase boundaries perpendicular to the substrate surface (0.68 vs. 0.78). The amplitude of the microphase separation was three times smaller than its error bar. Hence, a microphase separation with phase boundaries perpendicular to the substrate surface can be excluded. The average island diameter cannot be calculated since the decay parameter converges to zero. As the AFM measurement (A3.7) shows (Fig. 9.31), the sample was in an advanced dewetting state with islands of approximately 30 nm in height and a diameter of approximately 1 μm. The phase image is inversely correlated with the topography image. This might indicate that the surface of the elevations consisted of the more viscous polystyrene and the surface of the space in between of the less viscous polyisoprene. The film was still covering the substrate completely.

Subsequently, the sample was heated during 2 h to 183°C (dewetting step 8). The model with the homogeneous droplets fits the SERGIS data (S3.8) exactly to the same extent as the model with islands and microphase separation with phase boundaries perpendicular to the substrate surface ($\chi^2_{red.} = 0.33$). The average island diameter was determined to be (1167 ± 538) Å from the fit without microphase separation and (1125 ± 490) Å from the fit assuming a microphase separation with phase boundaries perpendicular to the substrate surface. Taking into account the layered morphology deduced by the neutron reflectivity fit (N3.8), the existence of a microphase separation with phase boundaries perpendicular to the substrate can be excluded. Hence, it can be concluded that

droplets formed on the substrate without a marked modulation in scattering length density in the direction parallel to the substrate surface within the droplets. A fit to the x-ray reflectivity data (X3.8) recorded in this state of the sample results in a larger film thickness (405 Å) than obtained by the neutron reflectivity fit (N3.8) (320 Å). This could be explained by: a) the low accuracy of the parameters obtained from the neutron reflectivity fit (due to the very limited accessible *q*-range), or b) by eventual changes in the sample morphology during the delay of one week after the SERGIS measurement until the x-ray reflectivity and the AFM measurement were performed, or c) by the different sample states, vacuum and ambient conditions, under which the measurements were performed. The x-ray reflectivity fit (X3.8) indicates a disappearance of the bottom layer.

The AFM image (A3.8) in Fig. 9.32 shows droplets whose height are in accordance with the thickness obtained by the x-ray reflectivity fit (X3.8). The diameter of the islands is in line with the average island diameter measured with SERGIS. From the correlation of the AFM topography and phase image one can conclude that the droplets partly dewet from the silicon substrate (the substrate has a much larger viscosity than the droplets). In the optical microscope image, the droplet ordering over large surface areas can be seen nicely. The brighter areas between the droplets might correspond to the substrate surface as already assumed before. It has to be mentioned that a thin polymer layer with homogenous thickness is transparent for optical microscopy. 77% of the substrate is still covered with polymer droplets (Fig. 9.33), but the volume of the film decreased by a factor of six (final volume: $8.30 \cdot 10^8$ nm^3 on a sample surface of 100 µm^2) as shown in the AFM images. This change of volume might to a certain extent go hand in hand with an increase in density. The reflectivity fits do not indicate a loss in the laterally averaged scattering density. In addition, an increase of a factor of six seems to be unrealistic.

9.2.3.3 **Summary of the 450 Å Thick Diblock Copolymer Film Dewetting**

The as prepared 450 Å thick film consisted of a relatively homogeneous mixture of polystyrene and polyisoprene with a slight enhancement of the polyisoprene concentration near the substrate interface, as revealed by neutron reflectivity

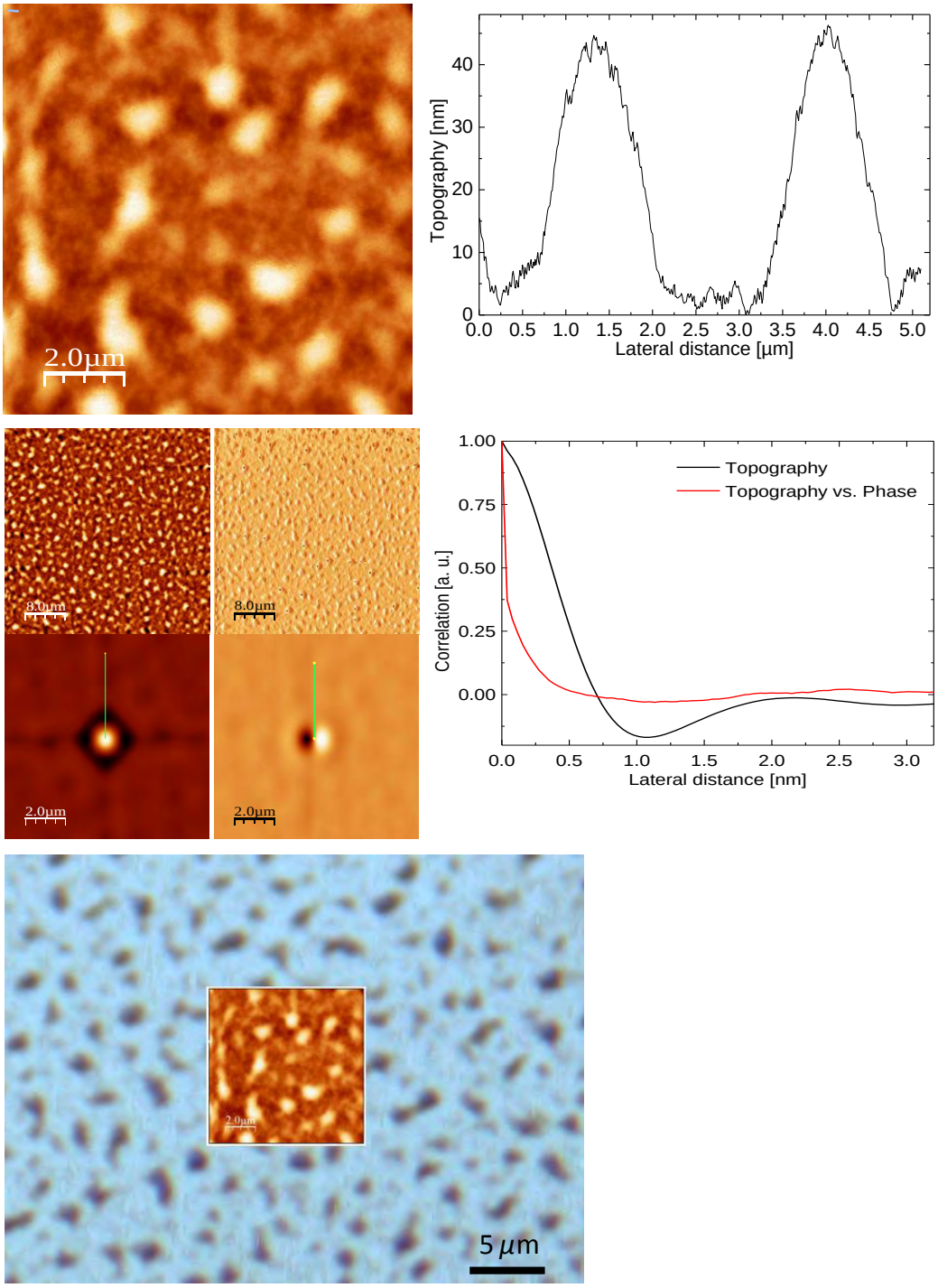

Fig. 9.32: AFM and microscopy study (A3.8) after annealing 3h at 183°C. Top: AFM topography image with line cut. Middle: AFM topography and phase image with topography self correlation and cross correlation and line cuts as indicated. Bottom: Optical microscope image with AFM topography inlet (450Å P(S-b-I)).

measurements. Annealing of the sample induced a pronounced microphase separation with phase boundaries parallel to the substrate surface. A polystyrene-

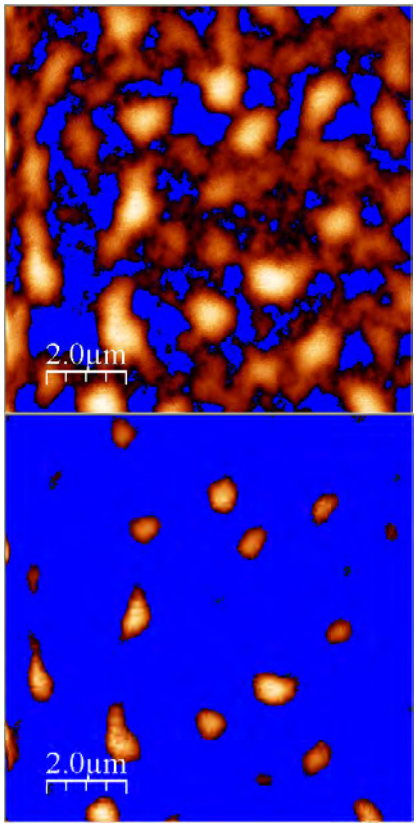

23	islands
1.71	μm average distance
7.67765	μm flooded area
1.427	μm average island diameter
2.49 10^6	nm³ average volume per island over 25 nm height

Fig. 9.33: AFM image (A3.8) with the substrate flooded (upper image) and area below 25nm over the substrate level flooded (lower image) and some data to the lower image (450Å P(S-b-I)).

rich layer formed at the film surface and a polyisoprene layer at the substrate interface with a transition layer in between. In the final dewetting stage, after two hours of annealing at 183°C, the film was dewetted, i.e. the substrate coverage had become incomplete. Since the droplets were too large to be measured in the accessible spin-echo length range up to 250 nm and since AFM images were recorded only after the two final dewetting steps, no conclusion can be made on the onset of the dewetting. The microphase separation with phase boundaries parallel to the substrate persisted also in the dewetted state.

9.2.4 Discussion of the Polymer Self Assembly Results

The self-organisation in ultrathin diblock copolymer films with thicknesses between 100 Å and 450 Å was studied by means of SERGIS, neutron and x-ray reflectivity, optical microscopy, as well as AFM. In Fig. 9.34, the observed structures are summarised. As indicated in the context of Fig. 6.6, the unperturbed dimensions of a single molecule of the diblock copolymer poly(styrene-block-

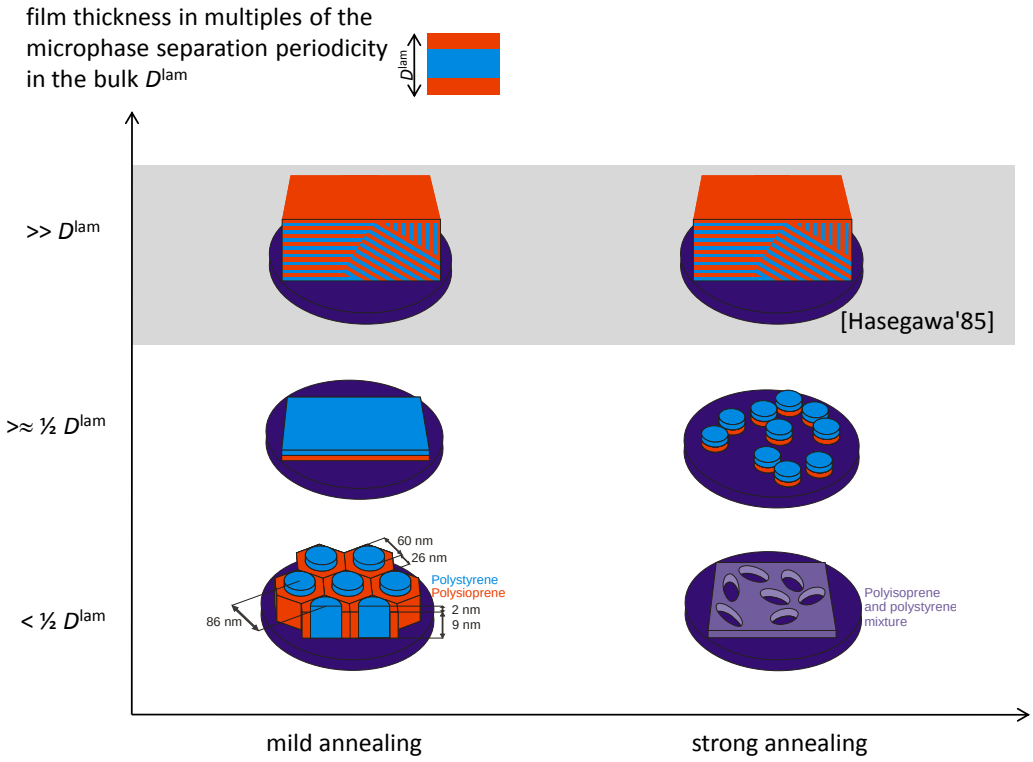

Fig. 9.34: Self organisation of poly(styrene-block-isoprene) diblock copolymer films as a function of the film thickness. Substantial differences exist in films of thicknesses below (bottom row) and above (middle row) the unperturbed length of the polymer molecules (½D^{lam} = 319 Å) in the phase separated state. For comparison the bulk phase is plotted in the top row [Hasegawa'85].

isoprene) in the microphase separated state is 309 Å in the direction perpendicular to the phase boundaries and approximately 50 Å parallel to the phase boundaries. As expected from the strong restriction of the film thickness compared to the unperturbed molecule length (309 Å), in the films with a thickness of 100-150 Å, only a micro phase separation with phase boundaries perpendicular to the substrate surface could be observed. While bulk studies on poly(styrene-block-isoprene) diblock copolymer samples have shown a micro phase separation in form of a lamellar phase [Khandpur'95], in our ultrathin films we observed a cylindrical phase. This phase is composed of polystyrene cylinders within a polyisoprene matrix (Fig. 9.34, bottom left image). The polystyrene-rich cylinders stick out of the film surface of the matrix regions. In the volume in between the substrate and the surface of the polyisoprene matrix, the volume fraction of polystyrene is reduced with respect to a corresponding bulk sample (50%) and amounts to approximately 45%. For a polystyrene volume fraction of 45%,

however, a lamellar phase would still be observed in the bulk (see Fig. 6.3). This implies that additional interface effects are influencing the structure in ultrathin films. In films with a thickness of 450 Å, i.e. larger than the unperturbed length of a diblock copolymer molecule, a lamellar phase separation with phase boundaries parallel to the substrate was observed. This result is in line with the observation in bulk samples [Khandpur'95]. Since the film thickness was not commensurate with the bulk lamella period, the observed lamella period was increased slightly to match the film thickness. Upon mild annealing, phase separation occurs in the investigated films. Dewetting, resulting in an only partly covered substrate surface, only occurred after annealing at higher temperatures or much longer annealing times.

10 Summary and Conclusions

This thesis focused on two main objectives: First, the clarification of the prospects of the spin-echo resolved grazing incidence neutron scattering method (SERGIS) for the investigation of buried interfaces. And second, the investigation of the self-organisation (i.e. microphase separation and dewetting) of ultrathin poly(styrene-block-isoprene) diblock copolymer films on silicon substrates by means of SERGIS and complementary techniques.

SERGIS is a novel neutron scattering technique which was implemented and further developed at the new neutron / x-ray reflectometer *N-REX*$^+$ at the FRM II (Garching, Germany). In contrast to conventional small-angle scattering methods, SERGIS characterises the lateral structure and morphology of interfaces and thin-film systems in real space. The technique uses a polarised primary beam, and the measured quantity is the integral polarisation of the scattered beam. By decoupling the measurement resolution and the beam divergence (in a first approximation), SERGIS aims at a good resolution and a good measurement statistics simultaneously.

In Chapter 2, the depolarisation of the initially polarised neutron beam due to the scattering by the sample is calculated for a SERGIS set-up within the framework of the first Born approximation. It is shown, that by making simplifying assumptions as in current literature some inherent limitations of the SERGIS method are overlooked. The influence of beam divergence and limitations of the accessible momentum transfer are discussed in detail. Deviations from the proportionality of the SERGIS signal to the correlation function of the scattering length contrast in the sample surface region are shown and discussed. For example, as shown in Section 2.4, higher order neighbour correlations are systematically suppressed in the SERGIS signal. It is shown, however, that

SERGIS is a suitable technique to measure first neighbour correlations of relatively large length scales in buried structures. Restrictions for very small and very large lateral structures, which arise from the grazing incidence scattering geometry under which SERGIS measurements are performed, are discussed in Chapter 4.

SERGIS is based on the spin precession in two parallelogram shaped magnetic field areas with opposite field orientation. Two different technical realisations of these magnetic field areas are presented in Chapter 3: neutron resonance spin-echo (NRSE) systems and birefringent magnetic prisms (triangular coils). NRSE is a wavelength specific technique, which allows to address relatively large spin-echo lengths with the trade-off of high signal absorptions and high background levels. For technical reasons, the angle of the magnetic field borders is scanned to address different spin-echo lengths, whereas in the case of the birefringent magnetic prisms the magnetic induction is scanned instead. The high complexity of the NRSE set-up limits the cooling options, constraining the range of reachable spin-echo lengths. As a further development of the SERGIS technique, easy to handle triangular coils with 30°, 45° and 60° magnetic field border inclinations were constructed. The birefringent prism set-up generates less background and the absorption is reduced with respect to the NRSE set-up. An elaborate cooling system was installed in the 30° and 60° coils. Thereby the range of accessible spin-echo lengths, which in the case of a birefringent prism set-up is intrinsically by a factor of two smaller than in the NRSE case (for identical parameters like inclination and length of the magnetic-field areas), could be maintained by correspondingly higher magnetic inductions.

An experimental comparison of the aforementioned SERGIS options, applied to an optical grating as strongly scattering test sample, is presented in Section 9.1. In this particular case, only low-frequency Fourier components of the scattering length distribution can be addressed due the grazing angle scattering geometry (Section 4.3.1). It was shown, that under this constraint the autocorrelation function of the sample is equally well reproduced by the SERGIS signal of the four set-ups. However, the NRSE set-up gives rise to stronger signal attenuation, requiring longer measurement times to compensate for the weaker signal.

Two principle limitations of the SERGIS technique have been identified: a limited spin-echo range and the low intensity signal of weakly scattering samples. The accessible spin-echo range depends on the design parameters of the different set-ups. The triangular SERGIS option with 60° inclined birefringent magnetic prisms provides the largest accessible spin-echo range. Structures of large length scales up to 900 nm could be investigated, a sufficient neutron scattering length density contrast provided (Section 9.1.5). The instrumental limitations in this case are dominated by the signal degradation (attenuation and scattering) induced during the passage of the neutron beam trough the magnetic coil wire material, and also by undesired depolarisation due to magnetic field inhomogeneities. Weakly scattering ultrathin polymer films (of about 100 Å thickness) were investigated with the SERGIS option with 30° inclined birefringent magnetic prisms (Section 9.2.1). Lateral structures from 25 nm up to 350 nm could be accurately measured. The limitation of the SERGIS method for the investigation of weakly scattering films is dominated by the absorption and the background contribution from the magnetic coil wire material in the trajectory of the neutron beam.

As a first systematic application of SERGIS to a real physical problem, the dewetting and internal structure of ultrathin poly(styrene-block-isoprene) diblock copolymer films were studied by means of SERGIS and complementary surface sensitive techniques, namely neutron and x-ray reflectivity and atomic force microscopy (AFM) (Section 9.2.). Reflectivity studies unveiled the scattering length distribution in the direction perpendicular to the sample surface in contrast to the lateral characterisation provided by SERGIS. AFM provides information on the topography and viscosity of the surface. The polymer films were spin-coated to thicknesses below and above the unperturbed dimension (319 Å) of the long axis of the diblock copolymer chain in the phase-separated state. The dewetting was induced by tempering or toluene treatment in an in-situ vacuum neutron / x-ray chamber constructed in the framework of this project (Chapter 8). Substantial differences exist in films of thickness below and above the unperturbed dimension of the polymer. For films of 100-150 Å thickness evidence of a hexagonal phase is obtained, which does not exist in the bulk state of diblock copolymers with equal volume fraction of both components. Hexagonally arranged

polystyrene rich cylinders oriented perpendicular to the substrate stand out of the average surface. On the other hand, the film of 450 Å thickness showed a lamellar structure with phase boundaries parallel to the substrate surface. This phase is also observed in bulk samples. For all studied film thicknesses, the microphase separation occurs at milder annealing conditions than the dewetting of the film.

In conclusion, SERGIS opens the possibility to investigate lateral structures up to relatively large length scales on conventional neutron reflectometers, requiring only moderate modifications of the instrument. SERGIS thereby represents a convenient alternative to conventional GISANS instruments due to its easy installation and limited space requirements. Limitations of SERGIS for thin and therefore weakly scattering films due to signal absorption and small-angle scattering in the magnetic coils in the neutron beam path can possibly be overcome in the future by a more sophisticated coil design (e.g. the wire material that defines the magnetic field borders may be replaced by thin superconducting foils). For experiments with a limited divergence and width of the incident beam in the direction of interest, the magnetic field borders could be slightly curved to compensate for the deviations of the SERGIS signal from the idealised theory as discussed in Chapter 2.4.3. A SERGIS set-up with ideal magnetic field borders (i.e., very well defined, non-absorbing, and slightly curved field borders) will permit to balance the measurement intensity versus resolution in a much more favourable way than possible with grazing incidence small-angle neutron scattering (GISANS).

For the understanding of the influence of confinement on diblock copolymer films, two crucial results have been pointed out: First, a transition from a lamellar structure to a hexagonal structure was observed when reducing the film thickness to a value below the size of the diblock copolymer molecule. Second, microphase separation was shown to occur during mild annealing, whereas dewetting only occurs after intense annealing. This makes a separation of both processes possible, which is crucial for potential technological applications that will require stable films in most cases. Thus ultrathin diblock copolymer films might indeed become an important partner in the endeavour to produce and master self-organised structures on the nanoscale.

11 Bibliography

[Arend'04] **N. Arend, R. Gähler, T. Keller, R. Georgii, T. Hils, and P. Böni.** "Classical and quantum-mechanical picture of nrse - measuring the longitudinal stern-gerlach effect by means of tof methods." Physics Letters A 327(1): 21-27, (2004).

[Badurek'79] **G. Badurek, H. Rauch, A. Wilfing, U. Bonse, and W. Graeff.** "Perfect-crystal neutron polarizer as an application of magnetic prism refraction." Journal of Applied Crystallography 12(Apr): 186-191, (1979).

[Bates'99] **F.S. Bates, and G.H. Fredrickson.** "Block copolymers - designer soft materials." Physics Today 52(2): 32-38, (1999).

[Becker'03] **J. Becker, G. Grun, R. Seemann, H. Mantz, K. Jacobs, K.R. Mecke, and R. Blossey.** "Complex dewetting scenarios captured by thin-film models." Nature Materials 2(1): 59-63, (2003).

[Bevington'69] **P. Bevington.** Data reduction and error analysis for the physical science, McGray-Hill Book Company, (1969).

[Binnig'86] **G. Binnig, C.F. Quate, and C. Gerber.** "Atomic force microscope." Physical Review Letters 56(9): 930-933, (1986).

[Binning'82] **G. Binning, H. Rohrer, C. Gerber, and E. Weibel.** "Surface studies by scanning tunneling microscopy." Physical Review Letters 49(1): 57-61, (1982).

[Bloch'40] **F. Bloch, and A. Siegert.** "Magnetic resonance for nonrotating fields." Physical Review 57(6): 522-527, (1940).

[Bornside'93] **D.E. Bornside, R.A. Brown, P.W. Ackmann, J.R. Frank, A.A. Tryba, and F.T. Geyling.** "The effects of gas-phase convection on mass-transfer in spin coating." Journal of Applied Physics 73(2): 585-600, (1993).

[Bouwman'99] **W.G. Bouwman, W. Kraan, and M.T. Rekveldt.** "Spin echo small angle neutron scattering experiment." Physica B 268: 79-83, (1999).

[Bouwman'00] **W.G. Bouwman, M. van Oossanen, O. Uca, W.H. Kraan, and M.T. Rekveldt.** "Development of spin-echo small-angle neutron scattering." Journal of Applied Crystallography 33(1): 767-770, (2000).

[Bouwman'04] **W.G. Bouwman, W. Stam, T.V. Krouglov, J. Plomp, S.V. Grigoriev, W.H. Kraan, and M.T. Rekveldt.** "Sesans with a monochromatic beam or with time-of-flight applied on colloidal systems." Nuclear Instruments & Methods in Physics Research Section a-Accelerators Spectrometers Detectors and Associated Equipment 529(1-3): 16-21, (2004).

[Bouwman'08] **W.G. Bouwman, J. Plomp, V.O. De Haan, W.H. Kraan, A.A. van Well, K. Habicht, T. Keller, and M.T. Rekveldt.** "Real-space neutron scattering methods." Nuclear Instruments & Methods in Physics Research Section a-Accelerators Spectrometers Detectors and Associated Equipment 586(1): 9-14, (2008).

[Brandt'99] **S. Brandt.** Datenanalyse. Heidelberg, Berlin, Sepktrum Verlag, (1999).

[Breiner'98] **U. Breiner, U. Krappe, E.L. Thomas, and R. Stadler.** "Structural characterization of the "Knitting pattern" In polystyrene-block-poly(ethylene-co-butylene)-block-poly(methylmethacrylate) triblock copolymers." Macromolecules 31(1): 135-141, (1998).

[Broseta'90] **D. Broseta, G.H. Fredrickson, E. Helfand, and L. Leibler.** "Molecular-weight and polydispersity effects at polymer polymer interfaces." Macromolecules 23(1): 132-139, (1990).

[Busch'06] **P. Busch, M. Rauscher, D.M. Smilgies, D. Posselt, and C.M. Papadakis.** "Grazing-incidence small-angle x-ray scattering from thin polymer films with lamellar structures-the scattering cross section in the distorted-wave born approximation." Journal of Applied Crystallography 39: 433-442, (2006).

[Buzza'99] **D.M.A. Buzza, I.W. Hamley, A.H. Fzea, M. Moniruzzaman, J.B. Allgaier, R.N. Young, P.D. Olmsted, and T.C.B. McLeish.** "Anomalous difference in the order-disorder transition temperature comparing a symmetric diblock copolymer ab with its hetero-four-arm star analog a(2)b(2)." Macromolecules 32(22): 7483-7495, (1999).

[Buzza'00] **D.M.A. Buzza, A.H. Fzea, J.B. Allgaier, R.N. Young, R.J. Hawkins, I.W. Hamley, T.C.B. McLeish, and T.P. Lodge.** "Linear melt rheology and small-angle x-ray scattering of ab diblocks vs a(2)b(2) four arm star block copolymers." Macromolecules 33(22): 8399-8414, (2000).

[Cheng'01] **J.Y. Cheng, C.A. Ross, V.Z.H. Chan, E.L. Thomas, R.G.H. Lammertink, and G.J. Vancso.** "Formation of a cobalt magnetic dot array via block copolymer lithography." Advanced Materials 13(15): 1174-+, (2001).

[Claesson'83] **S. Claesson, J.L. Mcatee, and S. Ali.** "Pressure-dependence of the viscosity of dilute polystyrene solutions in toluene." Journal of Polymer Science Part B-Polymer Physics 21(9): 1873-1881, (1983).

[Clery'02] **D. Clery, and M. Lavine.** "Skimming the surface - introduction." Science 297(5583): 961-961, (2002).

[Collins'03] **S. Collins, I.W. Hamley, and T. Mykhaylyk.** "An atomic force microscopy study of ozone etching of a polystyrene/polyisoprene block copolymer." Polymer 44(8): 2403-2410, (2003).

[de Gennes'71] **P.G. de Gennes.** "Reptation of a polymer chain in presence of fixed obstacles." Journal of Chemical Physics 55(2): 572-&, (1971).

[de Gennes'85] **P.G. de Gennes.** "Wetting - statics and dynamics." Reviews of Modern Physics 57(3): 827-863, (1985).

[de Gennes'04] **P.G. de Gennes, F. Bouchard-Wyart, and D. Quéré.** Capillarity and wetting phenomena: Drops, boubbles, pearls, waves. New-York, Springer, (2004).

[Dosch'92a] **H. Dosch.** "Critical phenomena at surfaces and interfaces - evanescent x-ray and neutron-scattering." Springer Tracts in Modern Physics 126, (1992a).

[Dosch'92b] **H. Dosch, K.A. Usta, A. Lied, W. Drexel, and J. Peisl.** "The evanescent neutron-wave diffractometer - on the way to surface sensitive neutron-scattering." Review of Scientific Instruments 63(12): 5533-5542, (1992b).

[Egami'03] **T. Egami, and S.J.L. Billinge.** Underneath the bragg peaks. Amsterdam, Boston, Heidelberg, London, New York, Oxford, Paris, San Diego, San Francisco, Singapore, Sydney, Tokyo, Pergamon, (2003).

[Eigler'90] **D.M. Eigler, and E.K. Schweizer.** "Positioning single atoms with a scanning tunneling microscope." Nature 344(6266): 524-526, (1990).

[Falus'06] **P. Falus, A. Vorobiev, and T. Krist.** "Test of a two-dimensional neutron spin analyzer." Physica B-Condensed Matter 385-86: 1149-1151, (2006).

[Fasolka'01] **M.J. Fasolka, and A.M. Mayes.** "Block copolymer thin films: Physics and applications." Annual Review of Materials Research 31: 323-355, (2001).

[Felcher'02] **G.P. Felcher, S. te Velthuis, J. Major, H. Dosch, C. Anderson, K. Habicht, and T. Keller**. Spin-echo resolved grazing incidence scattering (sergis) of cold neutrons. Conference on Advances in Neutron Scattering Instrumentation, Seattle, Wa, Spie-Int Soc Optical Engineering, (2002).

[Flory'41] **P.J. Flory.** "Thermodynamics of high polymer solutions." Journal of Chemical Physics 9(8): 660-661, (1941).

[Forte'80] **M. Forte, B.R. Heckel, N.F. Ramsey, K. Green, G.L. Greene, J. Byrne, and J.M. Pendlebury.** "1st measurement of parity-nonconserving neutron-spin rotation - the tin isotopes." Physical Review Letters 45(26): 2088-2092, (1980).

[Fredrickson'87a] **G.H. Fredrickson.** "Surface ordering phenomena in block copolymer melts." Macromolecules 20(10): 2535-2542, (1987a).

[Fredrickson'87b] **G.H. Fredrickson, and E. Helfand.** "Fluctuation effects in the theory of microphase separation in block copolymers." Journal of Chemical Physics 87(1): 697-705, (1987b).

[Gähler'88] **R. Gähler, and R. Golub.** "Neutron resonance spin-echo, bootstrap method for increasing the effective magnetic-field." Journal De Physique 49(7): 1195-1202, (1988).

[Gähler'92] **R. Gähler, R. Golub, and T. Keller.** "Neutron resonance spin-echo - a new tool for high-resolution spectroscopy." Physica B 180: 899-902, (1992).

[Gähler'96a] **R. Gähler, and R. Golub.** "Neutron spin optics: A thought experiment with applications." Physics Letters A 213(5-6): 239-244, (1996a).

[Gähler'96b] **R. Gähler, R. Golub, K. Habicht, T. Keller, and J. Felber.** "Space-time description of neutron spin echo spectrometry." Physica B 229(1): 1-17, (1996b).

[Giessibl'06] **F.J. Giessibl, and C.F. Quate.** "Exploring the nanoworld with atomic force microscopy." Physics Today 59(12): 44-50, (2006).

[Glatter'82] **O. Glatter, and O. Kratky.** Small angle x-ray scattering. London, New York, Paris, San Diego, San Francisco, Sao Paulo, Sydney, Tokyo, Toronto, Academic Press, (1982).

[Golub'94] **R. Golub, R. Gähler, and T. Keller.** "A plane-wave approach to particle-beam magnetic-resonance." American Journal of Physics 62(9): 779-788, (1994).

[Grigoriev'06] **S.V. Grigoriev, W.H. Kraan, M.T. Rekveldt, T. Kruglov, and W.G. Bouwman.** "Spin-echo small-angle neutron scattering for magnetic samples." Journal of Applied Crystallography 39: 252-258, (2006).

[Grigoriev'07] **S.V. Grigoriev, Y.O. Chetverikov, V.N. Zabenkin, W.H. Kraan, M.T. Rekveldt, and N. van Dijk.** "Spin-echo small-angle neutron scattering study of the domain structure of an ni layer on a cu substrate." Journal of Applied Crystallography 40: S111-S115, (2007).

[Hamaker'37] **H.C. Hamaker.** "The london - van der waals attraction between spherical particles." Physica 4: 1058-1072, (1937).

[Hamley'05] **I.W. Hamley.** Introduction to soft matter. Chichester, New-York, Weinheim, Brisbane, Singapore, Toronto, John Wiley & Sons, LTD, (2005).

[Harrison'98] **C. Harrison, M. Park, P.M. Chaikin, R.A. Register, and D.H. Adamson.** "Lithography with a mask of block copolymer microstructures." Journal of Vacuum Science & Technology B 16(2): 544-552, (1998).

[Hasegawa'85] **H. Hasegawa, and T. Hashimoto.** "Morphology of block polymers near a free-surface." Macromolecules 18(3): 589-590, (1985).

[Hashimoto'80] **T. Hashimoto, M. Shibayama, and H. Kawai.** "Domain-boundary structure of styrene-isoprene block co-polymer films cast from solution .4. Molecular-weight dependence of lamellar microdomains." Macromolecules 13(5): 1237-1247, (1980).

[Heil'99] **W. Heil, J. Dreyer, D. Hofmann, H. Humblot, E. Lelievre-Berna, and F. Tasset.** "He-3 neutron spin-filter." Physica B-Condensed Matter 268: 328-335, (1999).

[Helfand'72] **E. Helfand, and Y. Tagami.** "Theory of interface between immiscible polymers .2." Journal of Chemical Physics 56(7): 3592-&, (1972).

[Helfand'89] **E. Helfand, S.M. Bhattacharjee, and G.H. Fredrickson.** "Molecular-weight dependence of polymer interfacial-tension and concentration profile." Journal of Chemical Physics 91(11): 7200-7208, (1989).

[Henke'93] **B.L. Henke, E.M. Gullikson, and J.C. Davis.** "X-ray interactions - photoabsorption, scattering, transmission, and reflection at e=50-30,000 ev, z=1-92." Atomic Data and Nuclear Data Tables 54(2): 181-342, (1993).

[Holden'65] **G. Holden.** "Viscosity of polyisoprene." Journal of Applied Polymer Science 9(8): 2911-&, (1965).

[Holy'99] **V. Holy, U. Pietsch, and T. Baumbach.** High-resolution x-ray scattering from thin films and multilayers. Berlin, Heidelberg, New-York, Barcelona, Hong Kong, London, Milan, Paris, Singapore, Tokyo, Springer-Verlag, (1999).

[Huang'98a] **C.I. Huang, B.R. Chapman, T.P. Lodge, and N.P. Balsara.** "Quantifying the "Neutrality" Of good solvents for block copolymers: Poly(styrene-b-isoprene) in toluene, benzene, and thf." Macromolecules 31(26): 9384-9386, (1998a).

[Huang'98b] **E. Huang, L. Rockford, T.P. Russell, and C.J. Hawker.** "Nanodomain control in copolymer thin films." Nature 395(6704): 757-758, (1998b).

[Huang'98c] **E. Huang, T.P. Russell, C. Harrison, P.M. Chaikin, R.A. Register, C.J. Hawker, and J. Mays.** "Using surface active random copolymers to control the domain orientation in diblock copolymer thin films." Macromolecules 31(22): 7641-7650, (1998c).

[Huggins'41] **M.L. Huggins.** "Solutions of long chain compounds." Journal of Chemical Physics 9(5): 440-440, (1941).

[Jeoung'01] **E. Jeoung, T.H. Galow, J. Schotter, M. Bal, A. Ursache, M.T. Tuominen, C.M. Stafford, T.P. Russell, and V.M. Rotello.** "Fabrication and characterization of nanoelectrode arrays formed via block copolymer self-assembly." Langmuir 17(21): 6396-6398, (2001).

[Johnson'95] **J.M. Johnson, J.B. Allgaier, S.J. Wright, R.N. Young, M. Buzza, and T.C.B. Mcleish.** "Linear rheological behavior of polyisoprene-polystyrene hetero-star and linear diblock copolymer melts." Journal of the Chemical Society-Faraday Transactions 91(16): 2403-2409, (1995).

[Just'73] **W. Just, Schneide.Cs, Ciszewsk.R, and C.G. Shull.** "Refraction of thermal-neutrons by shaped magnetic-fields." Physical Review B 7(9): 4142-4145, (1973).

[Kampf'70] **G. Kampf, M. Hoffmann, and H. Kromer.** "Conformation, supermolecular structure and wide-range order in non-crystalline and non-steroespecific polymers .1. Visible supermolecular structure and wide-range order in non-crystallien block copolymers." Berichte Der Bunsen-Gesellschaft Fur Physikalische Chemie 74(8-9): 851-&, (1970).

[Keddie'94] **J.L. Keddie, R.A.L. Jones, and R.A. Cory.** "Interface and surface effects on the glass-transition temperature in thin polymer-films." Faraday Discussions(98): 219-230, (1994).

[Keller'95] **T. Keller, R. Gähler, H. Kunze, and R. Golub.** "Features and performance of an nrse spectrometer at bensc." Neutron News 6(3): 16-17, (1995).

[Kellogg'96] **G.J. Kellogg, D.G. Walton, A.M. Mayes, P. Lambooy, T.P. Russell, P.D. Gallagher, and S.K. Satija.** "Observed surface energy effects in confined diblock copolymers." Physical Review Letters 76(14): 2503-2506, (1996).

[Khandpur'95] **A.K. Khandpur, S. Forster, F.S. Bates, I.W. Hamley, A.J. Ryan, W. Bras, K. Almdal, and K. Mortensen.** "Polyisoprene-polystyrene diblock copolymer phase diagram near the order-disorder transition." Macromolecules 28(26): 8796-8806, (1995).

[Klenke'08] **J. Klenke**. (21.08.2009). "Mephisto." from http://www.frm2.tum.de/en/science/fundamental-amp-particle-physics/mephisto/index.html, (2008).

[Knoll'02] **A. Knoll, A. Horvat, K.S. Lyakhova, G. Krausch, G.J.A. Sevink, A.V. Zvelindovsky, and R. Magerle.** "Phase behavior in thin films of cylinder-forming block copolymers." Physical Review Letters 89(3): 4, (2002).

[Kobayashi'05] **H. Kobayashi, H. Takahashi, and Y. Hiki**. Temperature dependence of the viscosity through the glass transition in metaphosphate glasses and polystyrene. 14th International Conference on Internal Friction and Mechanical Spectroscopy (ICIFMS-14), Kyoto, JAPAN, (2005).

[Koppe'99] **M. Koppe, M. Bleuel, R. Gähler, R. Golub, P. Hank, T. Keller, S. Longeville, U. Rauch, and J. Wuttke.** "Prospects of resonance spin echo." Physica B-Condensed Matter 266(1-2): 75-86, (1999).

[Kraan'03] **W.H. Kraan, S.V. Grigoriev, M.T. Rekveldt, H. Fredrikze, C.F. de Vroege, and J. Plomp.** "Test of adiabatic spin flippers for application at pulsed neutron sources." Nuclear Instruments & Methods in Physics Research Section a-Accelerators Spectrometers Detectors and Associated Equipment 510(3): 334-345, (2003).

[Kratky'84] **O. Kratky, and H. Stabinger.** "X-ray small-angle camera with block-collimation system an instrument of colloid research." Colloid and Polymer Science 262(5): 345-360, (1984).

[Krouglov'03] **T. Krouglov, I.M. de Schepper, W.G. Bouwman, and M.T. Rekveldt.** "Real-space interpretation of spin-echo small-angle neutron scattering." Journal of Applied Crystallography 36: 117-124, (2003).

[Laschitsch'99] **A. Laschitsch, C. Bouchard, J. Habicht, M. Schimmel, J. Ruhe, and D. Johannsmann.** "Thickness dependence of the solvent-induced glass transition in polymer brushes." Macromolecules 32(4): 1244-1251, (1999).

[Lau'73] **W.W.Y. Lau, and C.M. Burns.** "Kinetics of spreading - polystyrene melts on plane glass surfaces." Journal of Colloid and Interface Science 45(2): 295-302, (1973).

[Lau'74] **W.W.Y. Lau, and C.M. Burns.** "Effect of temperature and molecular-weight on rate of spreading of polystyrene melts on plane soda lime glass surfaces." Journal of Polymer Science Part B-Polymer Physics 12(2): 431-439, (1974).

[Lau'72] **W.Y. Lau, and C.M. Burns.** "Pendent drop-sessile drop approach for determination of surface-tension." Surface Science 30(2): 478-&, (1972).

[Lee'67] **L.H. Lee.** "Adhesion of high polymers .2. Wettability of elastomers." Journal of Polymer Science Part a-2-Polymer Physics 5(6PA2): 1103-&, (1967).

[Leibler'80] **L. Leibler.** "Theory of microphase separation in block co-polymers." Macromolecules 13(6): 1602-1617, (1980).

[Levine'89] **J.R. Levine, L.B. Cohen, Y.W. Chung, and P. Georgopoulos.** "Grazing-incidence small-angle x-ray-scattering - new tool for studying thin-film growth." Journal of Applied Crystallography 22: 528-532, (1989).

[Liang'88] **K.S. Liang, E.B. Sirota, K.L. Damico, G.J. Hughes, and S.K. Sinha.** "The step roughening transition of a cu(113) surface studied by surface x-ray-scattering." Journal of Vacuum Science & Technology a-Vacuum Surfaces and Films 6(3): 654-655, (1988).

[Liu'01] **K. Liu, S.M. Baker, M. Tuominen, T.P. Russell, and I.K. Schuller.** "Tailoring exchange bias with magnetic nanostructures." Physical Review B 63(6): 4, (2001).

[Lopes'01] **W.A. Lopes, and H.M. Jaeger.** "Hierarchical self-assembly of metal nanostructures on diblock copolymer scaffolds." Nature 414(6865): 735-738, (2001).

[Lopes'02] **W.A. Lopes.** "Nonequilibrium self-assembly of metals on diblock copolymer templates." Physical Review E 65(3): 14, (2002).

[Maier'04] **R. Maier.** Aufbau und test einer neutronen-spin-echo-reklektometrie-anordnung. Max-Planck-Institut für Metallforschung and Institut für Theoretische und Angewandte Physik, Universität Suttgart. Diplomarbeit, (2004).

[Major'03] **J. Major, H. Dosch, G.P. Felcher, K. Habicht, T. Keller, S.G.E.T. Velthuis, A. Vorobiev, and M. Wahl.** "Combining of neutron spin echo and reflectivity: A new technique for probing surface and interface order." Physica B-Condensed Matter 336(1-2): 8-15, (2003).

[Major'09] **J. Major, A. Vorobiev, A. Rühm, R. Maier, M. Major, M. Metzger, M. Nülle, H. Dosch, G.P. Felcher, P. Falus, T. Keller, and R. Pynn.** "A spin-echo resolved grazing incidence scattering (sergis) set-up for the neutron interrogation of buried nanostructures." Review of Scientific Instruments 80, (2009).

[Martin'87] **Y. Martin, C.C. Williams, and H.K. Wickramasinghe.** "Atomic force microscope force mapping and profiling on a sub 100-a scale." Journal of Applied Physics 61(10): 4723-4729, (1987).

[Masalovich'07] **S. Masalovich.** "Method to measure neutron beam polarization with 2 x 1 neutron spin filter." Nuclear Instruments & Methods in Physics Research Section a-Accelerators Spectrometers Detectors and Associated Equipment 581(3): 791-798, (2007).

[Masson'02] **J.L. Masson, and P.F. Green.** "Viscosity of entangled polystyrene thin film melts: Film thickness dependence." Physical Review E 65(3): -, (2002).

[Matsen'94a] **M.W. Matsen, and M. Schick.** "Stable and unstable phases of a linear multiblock copolymer melt." Macromolecules 27(24): 7157-7163, (1994a).

[Matsen'94b] **M.W. Matsen, and M. Schick.** "Stable and unstable phases of a diblock copolymer melt." Physical Review Letters 72(16): 2660-2663, (1994b).

[Matsen'94c] **M.W. Matsen, and M. Schick.** "Microphase separation in starblock copolymer melts." Macromolecules 27(23): 6761-6767, (1994c).

[Matsen'96] **M.W. Matsen, and F.S. Bates.** "Origins of complex self-assembly in block copolymers." Macromolecules 29(23): 7641-7644, (1996).

[Mezei'72] **F. Mezei.** "Neutron spin-echo - new concept in polarized thermal-neutron techniques." Zeitschrift Fur Physik 255(2): 146-&, (1972).

[Mezei'78] **F. Mezei**. Proceedings of a symposium on neutron inelastic scattering. Neutron Inelastic Scattering, Vienna, (1978).

[Mori'85] **K. Mori, H. Hasegawa, and T. Hashimoto.** "Small-angle x-ray-scattering from bulk block polymers in disordered state - estimation of x-values from accidental thermal fluctuations." Polymer Journal 17(6): 799-806, (1985).

[Morkved'97] **T.L. Morkved, and H.M. Jaeger.** "Thickness-induced morphology changes in lamellar diblock copolymer ultrathin films." Europhysics Letters 40(6): 643-648, (1997).

[Mukherjee'02] **M. Mukherjee, M. Bhattacharya, M.K. Sanyal, T. Geue, J. Grenzer, and U. Pietsch.** "Reversible negative thermal expansion of polymer films." Physical Review E 66(6), (2002).

[Müller-Buschbaum'99] **P. Müller-Buschbaum, J.S. Gutmann, and M. Stamm.** "Dewetting of confined polymer films: An x-ray and neutron scattering study." Physical Chemistry Chemical Physics 1(17): 3857-3863, (1999).

[Müller-Buschbaum'02] **P. Müller-Buschbaum, J.S. Gutmann, C. Lorenz-Haas, O. Wunnicke, M. Stamm, and W. Petry.** "Dewetting of thin diblock copolymer films: Spinodal dewetting kinetics." Macromolecules 35(6): 2017-2023, (2002).

[Müller-Buschbaum'03a] **P. Müller-Buschbaum.** "Dewetting and pattern formation in thin polymer films as investigated in real and reciprocal space." Journal of Physics-Condensed Matter 15(36): R1549-R1582, (2003a).

[Müller-Buschbaum'03b] **P. Müller-Buschbaum.** "Influence of surface cleaning on dewetting of thin polystyrene films." European Physical Journal E 12(3): 443-448, (2003b).

[Müller-Buschbaum'04] **P. Müller-Buschbaum, N. Hermsdorf, J.S. Gutmann, M. Stamm, S. Cunis, R. Gehrke, and W. Petry.** "Dewetting of confined diblock copolymer films." Journal of Macromolecular Science-Physics B43(1): 29-42, (2004).

[Müller-Buschbaum'05] **P. Müller-Buschbaum, E. Bauer, O. Wunnicke, and M. Stamm.** "The control of thin film morphology by the interplay of dewetting, phase separation and microphase separation." Journal of Physics-Condensed Matter 17(9): S363-S386, (2005).

[Müller-Buschbaum'06] **P. Müller-Buschbaum, E. Bauer, E. Maurer, and R. Cubitt.** "Fast swelling kinetics of thin polystyrene films." Physica B-Condensed Matter 385: 703-705, (2006).

[Müller-Buschbaum'07] **P. Müller-Buschbaum, E. Bauer, E. Maurer, A. Nelson, and R. Cubitt.** "In-situ neutron reflectometry probing competitive swelling and de-swelling of thin polystyrene films." Physica Status Solidi-Rapid Research Letters 1(2): R68-R70, (2007).

[Nickel'01] **B. Nickel, A. Ruhm, W. Donner, J. Major, H. Dosch, A. Schreyer, H. Zabel, and H. Humblot.** "Spin-resolved off-specular neutron scattering maps from magnetic multilayers using a polarized he-3 gas spin filter." Review of Scientific Instruments 72(1): 163-172, (2001).

[Papadakis'97] **C.M. Papadakis, K. Almdal, K. Mortensen, and D. Posselt.** "A small-angle scattering study of the bulk structure of a symmetric diblock copolymer system." Journal De Physique Ii 7(12): 1829-1854, (1997).

[Park'97] **M. Park, C. Harrison, P.M. Chaikin, R.A. Register, and D.H. Adamson.** "Block copolymer lithography: Periodic arrays of similar to 10(11) holes in 1 square centimeter." Science 276(5317): 1401-1404, (1997).

[Parratt'54] **L.G. Parratt.** "Surface studies of solids by total reflection of x-rays." Physical Review 95(2): 359-369, (1954).

[Pickett'93] **G.T. Pickett, T.A. Witten, and S.R. Nagel.** "Equilibrium surface orientation of lamellae." Macromolecules 26(12): 3194-3199, (1993).

[Plomp'07a] **J. Plomp, V.O. de Haan, R.M. Dalgliesh, S. Langridge, and A.A. van Well.** "Neutron spin-echo labelling at offspec, an isis second target station project." Thin Solid Films 515(14): 5732-5735, (2007a).

[Plomp'07b] **J. Plomp, V.O. de Haan, R.M. Dalgliesh, S. Langridge, and A.A. van Well.** "Time-of-flight spin-echo small-angle neutron measurements." Physica B-Condensed Matter 397(1-2): 76-78, (2007b).

[Pukite'85] **P.R. Pukite, C.S. Lent, and P.I. Cohen.** "Diffraction from stepped surfaces .2. Arbitrary terrace distributions." Surface Science 161(1): 39-68, (1985).

[Pynn'80] **R. Pynn**. Neutron spin echo and three-axis spectrometers. Neutron Spin Echo. Proceedings of a Laue-Langevin Institut Workshop, Grenoble, France, Springer-Verlag, (1980).

[Pynn'92] **R. Pynn.** "Neutron-scattering by rough surfaces at grazing-incidence." Physical Review B 45(2): 602-612, (1992).

[Pynn'02] **R. Pynn, M.R. Fitzsimmons, M.T. Rekveldt, J. Major, H. Fritzsche, D. Weller, and E.C. Johns.** "Optimization of neutron scattering instrumentation using neutron spin echo: Application to the discrimination of diffuse scattering in neutron reflectivity experiments." Review of Scientific Instruments 73(8): 2948-2957, (2002).

[Pynn'03] **R. Pynn, M.R. Fitzsimmons, H. Fritzsche, J. Major, and M.T. Rekveldt.** "Does beam divergence matter for neutron reflectometry?" Physica B-Condensed Matter 336(1-2): 1-7, (2003).

[Pynn'05] **R. Pynn, M.R. Fitzsimmons, H. Fritzsche, M. Gierlings, J. Major, and A. Jason.** "Neutron spin echo scattering angle measurement (sesame)." Review of Scientific Instruments 76(5): -, (2005).

[Pynn'08a] **R. Pynn, M.R. Fitzsimmons, W.T. Lee, V.R. Shah, A.L. Washington, P. Stonaha, and K. Littrell.** "Spin echo scattering angle measurement at a pulsed neutron source." Journal of Applied Crystallography 41: 897-905, (2008a).

[Pynn'08b] **R. Pynn, W.T. Lee, P. Stonaha, V.R. Shah, A.L. Washington, B.J. Kirby, C.F. Majkrzak, and B.B. Maranville.** "The use of symmetry to correct larmor phase aberrations in spin echo scattering angle measurement." Review of Scientific Instruments 79(6): -, (2008b).

[Ramsey'56] **N.F. Ramsey.** Molecular beams. Oxford, Clarendon Press, (1956).

[Reiter'94] **G. Reiter.** "Dewetting as a probe of polymer mobility in thin-films." Macromolecules 27(11): 3046-3052, (1994).

[Rekveldt'96] **M.T. Rekveldt.** "Novel sans instrument using neutron spin echo." Nuclear Instruments & Methods in Physics Research Section B-Beam Interactions with Materials and Atoms 114(3-4): 366-370, (1996).

[Rekveldt'97] **M.T. Rekveldt.** "Neutron reflectometry and sans by neutron spin echo." Physica B 234: 1135-1137, (1997).

[Rekveldt'00] **M.T. Rekveldt.** "Novel instrumentation concepts using polarised neutrons." Physica B 276: 55-58, (2000).

[Rekveldt'01] **M.T. Rekveldt, T. Keller, and R. Golub.** "Larmor precession, a technique for high-sensitivity neutron diffraction." Europhysics Letters 54(3): 342-346, (2001).

[Rekveldt'03a] **M.T. Rekveldt.** "Spin-echo small-angle neutron scattering in neutron reflectometry." Journal of Applied Crystallography 36: 1301-1306, (2003a).

[Rekveldt'03b] **M.T. Rekveldt, W.G. Bouwman, W.H. Kraan, T.V. Krouglov, and J. Plomp.** "Larmor precession applications: Magnetised foils as spin flippers in spin-echo sans with varying wavelength." Physica B-Condensed Matter 335(1-4): 164-168, (2003b).

[Rekveldt'05] **M.T. Rekveldt, J. Plomp, W.G. Bouwman, W.H. Kraan, S. Grigoriev, and M. Blaauw.** "Spin-echo small angle neutron scattering in delft." Review of Scientific Instruments 76(3): -, (2005).

[Rekveldt'06] **M.T. Rekveldt, N.H. van Dijk, S.V. Grigoriev, W.H. Kraan, and W.G. Bouwman.** "Three-dimensional magnetic spin-echo small-angle neutron scattering and neutron depolarization: A comparison." Review of Scientific Instruments 77(7): -, (2006).

[Rieger'96] **J. Rieger.** "The glass transition temperature of polystyrene - results of a round robin test." Journal of Thermal Analysis 46(3-4): 965-972, (1996).

[Rosedale'95] **J. Rosedale, F.S. Bates, K. Almdal, K. Mortensen, and G.D. Wignall.** "Order and disorder in symmetrical diblock copolymer melts." Macromolecules 28(5): 1429-1443, (1995).

[Rouse'53] **P.E. Rouse.** "A theory of the linear viscoelastic properties of dilute solutions of coiling polymers." Journal of Chemical Physics 21(7): 1272-1280, (1953).

[Rühm'99] **A. Rühm, B.P. Toperverg, and H. Dosch.** "Supermatrix approach to polarized neutron reflectivity from arbitrary spin structures." Physical Review B 60(23): 16073-16077, (1999).

[Rühm'06] **A. Rühm, U. Wildgruber, J. Franke, J. Major, and H. Dosch.** N/x materials science reflectometer at frm-ii in garching. Neutron reflectometry: A probe for materials surfaces. Vienna, IAEA, (2006).

[Russell'89] **T.P. Russell, G. Coulon, V.R. Deline, and D.C. Miller.** "Characteristics of the surface-induced orientation for symmetric diblock ps/pmma copolymers." Macromolecules 22(12): 4600-4606, (1989).

[Savitzky'64] **A. Savitzky, and M.J.E. Golay.** "Smoothing + differentiation of data by simplified least squares procedures." Analytical Chemistry 36(8): 1627-&, (1964).

[Schaerpf'89] **O. Schaerpf.** "Comparison of theoretical and experimental behavior of supermirrors and discussion of limitations." Physica B-Condensed Matter 156: 631-638, (1989).

[Schäffer'00] **E. Schäffer, T. Thurn-Albrecht, T.P. Russell, and U. Steiner.** "Electrically induced structure formation and pattern transfer." Nature 403(6772): 874-877, (2000).

[Schubert'96] **D.W. Schubert, and M. Stamm.** "Influence of chain length on the interface width of an incompatible polymer blend." Europhysics Letters 35(6): 419-424, (1996).

[Schubert'03] **D.W. Schubert, and T. Dunkel.** "Spin coating from a molecular point of view: Its concentration regimes, influence of molar mass and distribution." Materials Research Innovations 7(5): 314-321, (2003).

[Sears'92] **V.F. Sears.** "Neutron scattering lengths and cross sections." Neutron News 3(3): 26-37, (1992).

[Seemann'05] **R. Seemann, S. Herminghaus, C. Neto, S. Schlagowski, D. Podzimek, R. Konrad, H. Mantz, and K. Jacobs.** "Dynamics and structure formation in thin polymer melt films." Journal of Physics-Condensed Matter 17(9): S267-S290, (2005).

[Silberberg'82] **A. Silberberg.** "Distribution of conformations and chain ends near the surface of a melt of linear flexible macromolecules." Journal of Colloid and Interface Science 90(1): 86-91, (1982).

[Sinha'88] **S.K. Sinha, E.B. Sirota, S. Garoff, and H.B. Stanley.** "X-ray and neutron-scattering from rough surfaces." Physical Review B 38(4): 2297-2311, (1988).

[Sinha'94] **S.K. Sinha.** "X-ray diffuse-scattering as a probe for thin-film and interface structure." Journal De Physique Iii 4(9): 1543-1557, (1994).

[Smith'06] **G.S. Smith, and C.F. Majkrzak.** International tables for crystallography. E. Prince, Springer. C: Mathematical, physical and chemical tables: 126-146, (2006).

[Squires'96] **G.L. Squires.** Introduction to the theory of thermal neutron scattering. Mineola, New York, Dover Publications, Inc., (1996).

[Stommer'96] **R. Stommer, U. Englisch, U. Pietsch, and V. Holy.** "X-ray and neutron diffuse scattering from multilayers of fatty acid salt molecules." Physica B 221(1-4): 284-288, (1996).

[Tang'91] **H. Tang, and K.F. Freed.** "Interfacial studies of incompressible binary blends." Journal of Chemical Physics 94(9): 6307-6322, (1991).

[Theodorou'88] **D.N. Theodorou.** "Structure and thermodynamics of bulk homopolymer solid interfaces - a site lattice model approach." Macromolecules 21(5): 1400-1410, (1988).

[Thurn-Albrecht'00a] **T. Thurn-Albrecht, J. Schotter, C.A. Kästle, N. Emley, T. Shibauchi, L. Krusin-Elbaum, K. Guarini, C.T. Black, M.T. Tuominen, and T.P. Russell.** "Ultrahigh-density nanowire arrays grown in self-assembled diblock copolymer templates." Science 290(5499): 2126-2129, (2000a).

[Thurn-Albrecht'00b] **T. Thurn-Albrecht, R. Steiner, J. DeRouchey, C.M. Stafford, E. Huang, M. Bal, M. Tuominen, C.J. Hawker, and T.P. Russell.** "Nanoscopic templates from oriented block copolymer films." Advanced Materials 11(15): 787-791, (2000b).

[Tolan'99] **M. Tolan.** X-ray scattering from soft-matter thin films - materials science and basic research, Springer-Verlag, Berlin, Heidelberg, (1999).

[Usta'91] **K.A. Usta, H. Dosch, A. Lied, and J. Peisl.** "Depth controlled grazing angle neutron-diffraction." Physica B 173(1-2): 65-70, (1991).

[Usta'92] **K.A. Usta, H. Dosch, A. Lied, and J. Peisl.** "Neutron diffraction under grazing incidence: Recent results from the evanescent wave diffractometer." Springer Proceedings in Physics 61: 239-245, (1992).

[Vineyard'82] **G.H. Vineyard.** "Grazing-incidence diffraction and the distorted-wave approximation for the study of surfaces." Physical Review B 26(8): 4146-4159, (1982).

[Wahl'02] **M. Wahl.** Aufbau einer messanordnung zur neutronenreflektometrie. Max-Planck-Institut für Metallforschung and Institut für Theoretische und Angewandte Physik, Universität Stuttgart, (2002).

[Walheim'99] **S. Walheim, E. Schäffer, J. Mlynek, and U. Steiner.** "Nanophase-separated polymer films as high-performance antireflection coatings." Science 283(5401): 520-522, (1999).

[Wood'63] **L.A. Wood, and F.L. Roth.** "Creep of pure-gum rubber vulcanizates from indentation-time measurements." Rubber Chemistry and Technology 36(3): 611, (1963).

[Wu'70] **S. Wu.** "Surface and interfacial tensions of polymer melts .2. Poly(methyl methacrylate), poly(normal-butyl methacrylate), and polystyrene." Journal of Physical Chemistry 74(3): 632-&, (1970).

[Xia'99] **Y.N. Xia, J.A. Rogers, K.E. Paul, and G.M. Whitesides.** "Unconventional methods for fabricating and patterning nanostructures." Chemical Reviews 99(7): 1823-1848, (1999).

[Yoneda'63] **Y. Yoneda.** "Anomalous surface reflection of x rays." Physical Review 131(5): 2010-&, (1963).

[Young'05] **T. Young.** "An essay on the cohesion of fluids." Philosophical Transactions of the Royal Society of London 95: 65-87, (1805).

[Zabel'94] **H. Zabel.** "Spin-polarized neutron reflectivity of magnetic-films and superlattices." Physica B 198(1-3): 156-162, (1994).

Acknowledgments - Danksagung

Abschließend möchte ich allen danken, die mich während der Doktorarbeit begleitet und unterstützt haben.

Herrn **Prof. Dr. Helmut Dosch** möchte ich für die freundliche Aufnahme in seine Abteilung am Max-Planck-Institut für Metallforschung, die ständige Diskussions- und Hilfsbereitschaft, sowie die Möglichkeit meine Arbeit auf internationalen Konferenzen vorzustellen, danken.

Mein Dank gilt **Dr. Janos Major** und **Dr. Adrian Rühm** für die Betreuung und Korrektur dieser Doktorarbeit. Viele ausführliche wissenschaftliche Diskussionen, und die Unterstützung während Messzeiten haben zu dieser Arbeit beigetragen.

Herrn **Prof. Dr. Ulrich Stroth**, danke ich für die freundliche Übernahme des Mitberichts und dem Interesse an dieser Arbeit.

Thanks to **Prof. Hyungjung Kim** from the Sogang University in Seoul, South Korea for the spin-coating of the samples and interesting discussions at the Warren Symposium.

Jörgen Franke und **Dr. Marton Major** möchte ich für die Unterstützung während der Experimente an *N-REX*$^{+}$ danken.

Der ITAP Werkstatt unter Leitung von **Hr. Michael Schäfer** gebührt mein Dank für das große Engagement bei der sehr präzisen und bei Bedarf sehr schellen Fertigung der Probenkammer und weiteren Bauteilen. Auch auf die Hilfe von **Frank Adams**, **Peter Schützendübe**, **Ralf Weigel**, **Annette Weißhardt** und **Taufan Zimmer** konnte ich immer zählen.

I want to thank **Dr. Esther Barrena**, **Dr. Carmen Munuera,** and **Dr. Tobias Krauss** for the help with the AFM interpretation.

I am grateful to **Dr. Alejandro Dias-Ortiz** and **Dr. Ingo Ramsteiner** for proofreading the introduction and conclusion of this thesis.

Für die gute Atmosphäre im und außerhalb des Instituts möchte ich **Claus Ellinger**, **Dr. Matthias Denk**, **Dr. Dimas Garcia de Oteyza Feldermann**, **Dr. Ulrich Gebhardt**, **Navid Khorshidi**, **Ruslan Kurta, Felix Maye**, **Dr. Phillipp Nolte, Florian Rödl**, **Mathias Schmidt**, **Dr. Heiko Schröder**, **Dr. Ayse Turak**, **Dr. Alexander Udyansky**, **Dr. Alina Vlad** und allen Mitarbeitern der Abteilung Dosch danken.

Meinen Eltern danke ich für die Unterstützung während meinem Studium und darüber hinaus.

Finally, I want to thank **Mélissa** for her love and her constant support during my thesis.